Modelling the Zambezi River plume using the Regional Oceanic Modelling System

Fialho Paloge Juma Nehama

Thesis presented for the Degree of
Doctor of Philosophy

Oceanography Department
Faculty of Science
University of Cape Town

South Africa
April, 2012

Modelling the Zambezi River plume using the Regional Oceanic Modelling System

Fialho P.J. Nehama

Abstract

The Zambezi River constitutes an important source of freshwater to the Sofala Bank in the western Mozambique Channel, where it is believed that the outflow from the river influences the secondary production of coastal waters. Observational data is analyzed alongside simulation outputs to describe the main features of the Zambezi River plume, and its response to ambient factors. These plumes spread over both the downstream and upstream coasts, with the downstream part remaining attached to the shoreline and confined to the region onshore from the 50 m isobath. The plume naturally penetrates downstream beyond the City of Quelimane, but only under a strong buoyancy input or an ambient current oriented equatorward do the plume waters spread further north (beyond the mouth of the Licungo River). The upstream portion of the plume consists of a tongue of brackish water leaving the mouth and spreading poleward and offshore, beyond the 50 m isobath. Plume waters occupy the entire water column in the region immediately seaward from the delta, to a distance of about 30 km from the coast, where they become limited to the top 10 m.

In the absence of wind, tides, and ambient current, a sizable unsteady plume forms under a constant-slope bathymetry and straight shoreline, consisting of a bulge that grows continually as it re-circulates anti-cyclonically (counter-clockwise) in front of the mouth, and a coastal current that flows equatorward along the coast. Under realistic geometry and bathymetry, the multiple mouth Zambezi River generates a surface-advected plume with diminished upstream penetration. The plume response to constant impulsive winds is characterized by a change of the shape into either a "coastal current" that moves equatorward along the coast or a "large bulge" that spreads seaward and poleward, depending on whether the wind field is equatorward or poleward. Asymmetric sea-breezes and tides deepen the plume, hence changing the plume structure from surface-advected to bottom-advected. Strong poleward ambient current forces the plume water in the far-field region to spread southward beyond 20^oS at times when the water in the near-field region is transported downstream.

April 2012

Contents

Declaration

This dissertation is being submitted in fulfillment of the requirements for the Degree of Doctor of Philosophy at the University of Cape Town, South Africa.

This work has not been previously accepted in substance for any degree and is not being concurrently submitted for any degree.

This thesis report is the result of my own independent work, except where otherwise stated.

Other sources are acknowledged in the text giving explicit references, also a bibliography is appended.

I hereby give consent for my dissertation, if accepted, to be made available for photocopying and for inter-library loan, and the title and summary to be made available to outside organizations.

Signed
(Candidate)

Acknowledgements

This research was funded by the Carnegie Corporation through the Western Indian Ocean Regional Initiative for Sciences and Education (WIO-RISE) network. And I would like express my gratitude to the people at the WIO-RISE for continually providing the necessary means that allowed me to do this research. These people include Dr Margareth Kyewalyanga (the academic director, who replaced Prof. Alfonse Dubi), Dr Musa Chacha (the technical director), Prof. Antonio Hoguane and Prof. Chris Reason (the leaders of the UEM and UCT nodes of the network, respectively).

I would like to thank the people who in different occasions helped me to collate and process scientific data with paramount importance for this work, and that includes Bernardino Malauene, who provided hydrographic data for the Sofala Bank, Genito Maure, who provided simulation-based atmospheric data, Onilda Dovelo and Teles Benjamim, who ventured going down the Zambezi River with me, and Dr Bjorn Backeberg, who showed me some matlab tricks right at the beginning of my Ph.D. Many people have helped me during my stay in Cape Town in too various ways to detail. My very appreciations belong to: Obadias Cossa, Steve Kemanke, Ana Cristina Godinho, Clousa Chevane, Izidine Pinto, Antonio Beleza, Arlindo Meque, and Claudio Paulo.

My special thank belongs to my supervisor, Prof. Chris Reason, for the continued guidance and great recommendations.

Great thanks go to my parents for making every effort to provide me with the best education possible. I thank my wife and mommy-to-be, Alice B. Marques Nehama, with infinite love and patience gave me strength to survive my time in Cape Town.

Last but not the least, I thank God, in all His forms, for shining the torch in the tunnel - Nothing about this would have been possible without Him.

"When the only tool you have is a hammer, it is tempting to treat everything as if it were a nail" (A. Maslow)

List of Figures

List of Tables

Chapter 1

Introduction

1.1 Background

Freshwater discharges from river runoff into the ocean have an important influence on the dynamics of many coastal regions worldwide. In these regions, the input of buoyancy is responsible for generating a distinct physical regime very often called "plume", which is characterized by a surface layer of less saline water flowing over the denser ambient water. Depending on the region where the mixing between fresh and saline water primarily occurs, be it the estuary or the coastal sea immediately offshore from the river mouth, the resulting plumes are termed "estuarine" or "river" plumes.

Following the plume generation, a large range of dissolved and suspended substances reach the ocean and can cause a variety of impacts, the strongest of which occurs within the limits of the plume. These impacts vary from the physical alteration of the coastline, to changes in the availability of biological resources. For example, evidence of seaward motion of the Zambezi Delta in geological timescales caused primarily by high sediment flux is presented in Walford et al. (2005), and the impact of the Zambezi freshwater on the secondary production, in particular the shrimp fisheries in the adjacent coastal sea, is discussed by Mann and Lazier (1996). For a better understanding of these changes, an accurate description of the dispersion of plume waters as well as of the plume structure is of great importance.

The Zambezi is the largest river flowing into the Indian Ocean from Africa, it is 2750 km long (Bourgeois et al., 2003), and has its origin in Zambia. Its connection to the ocean is made through an extensive delta with numerous river mouths, located in the central Mozambique. The Zambezi outflow has a mean rate of $3000\,\mathrm{m^3 s^{-1}}$ (Gammelsrød, 1992), and is believed to have an influence not only the near-shore hydrodynamics and ecosystems, but also on the offshore mesoscale circulation at times when the freshwater from runoff dominates the water masses within the continental

shelf (Schumann, 1998; Sætre and da Silva, 1984). A concise review of the coastal features along the coast of Mozambique has been offered by Lutjeharms (2006), who presented evidence that the seaward intrusion of freshwater from the Zambezi River can reach up to 50 km offshore, being confined to a water column of $15-30$ m depth.

A typical structure for river or estuarine plumes does not seem to exist, since idealized models very often produce a small gyre in front of the river mouth, rarely present in real systems, and attached to a density-driven current trapped in the coast, while observations show plumes significantly deflected by the Coriolis force with horizontal and vertical dimensions varying due to a number of factors. Hence, the main controlling factors for the primary dispersion of specific plumes have been found to be the wind-stress (Brakel, 1984; Fong et al., 1997; Manikiam et al., 1993), the buoyancy input (Geyer et al., 2004; Münchow and Garvine, 1993), the ambient currents in the vicinity of the river mouth (Warrick et al., 2007; Nikiema et al., 2007), the topography (Mestres et al., 2007), and the combination of some of these factors (Münchow and Garvine, 1993; Warrick et al., 2004a). Most of the current knowledge on river plumes was gained through the use of numerical models, which evolved from very idealized bi-dimensional ones to tri-dimensional models capable of giving a more realistic simulation. Here, the Regional Oceanic Modelling System (ROMS) is used since it is reasonably well suited for coastal applications, and it is capable of performing realistic and idealized simulations with a minimum of modifications. The observations of plumes around the world indicate the existence of great variations in the ways in which selected forcing acts on the plume water dispersal; thus, restraining the worldwide use of the existing models as they become merely local or regional.

Previous studies on the Zambezi River plume were mostly based on field campaigns and yet, they do not provide a succinct description of the plumes in this region. For instance, data from the cruise undertaken on board of the R/V Dr. Fridtjof Nansen by (IMR, 1978a,b) indicated that, during the rainy season, the freshwater tended to move seawards, while it moved primarily northeastwards along the downstream coast in the dry season. Siddorn et al. (2001) have examined cruise data collected towards the end of the rainy season in 1998 and found the plume water to spread northeastwards.

This study is motivated by the need to understand the dynamics of the Zambezi River plume, in particular, the issue of how the local settings (bathymetry, geometry, forcings) contribute to modify the plume patterns from the theoretical predictions for an outflow oriented eastwards in the Southern Hemisphere. In this case, a number of theoretical studies suggest that in the absence of a strong external forcing, a re-circulating bulge of brackish water forms immediately offshore from the river mouth, and the surface flow turns cyclonically (anticlockwise in the Southern Hemisphere) due to the Coriolis force and develops into a coastal current.

Although there is an increasing number of oceanographic studies conducted along the Mozambican coast, little or no attention has been paid to the structure and dynamics of plumes of the numerous rivers that meet the Indian Ocean in this region, particularly the Zambezi River.

1.2 Objectives

It is the intention of this thesis to examine the dispersion patterns and structure of the Zambezi River plumes. The main goal is to describe the main features of the plume and the plume response to selected ambient factors. In particular, the study addresses the following questions:

1. **Structure of the Zambezi River plume:** What are the typical cross-shore and alongshore plume dimensions? What depth does the freshwater usually reach? Is salinity the unique parameter indicating the limits of the Zambezi plume? What is the distribution of physical properties in the vicinity of the river mouth? Is there a clear separation between the Zambezi plumes and the plumes from the rivers further south and north?

2. **Effects of ambient factors on the plume structure and dynamics:** What is the role played by local winds, tides, bathymetry, and coastal circulation on the plume structure and dynamics? What is the influence of the relatively large size of the delta on the plume features?

1.3 Research methodology and thesis outline

Two different approaches were used to address the objectives and questions mentioned in the previous section, namely, the collation and interpretation of observational data, which essentially provided the means to describe the plume morphology; and numerical modelling of the plume, which through a number of idealized and realistic simulations provided the means to increase insight into the plume response to selected factors and its dynamics.

The thesis is organized into 7 chapters. Chapter 1 provides an introduction that includes the scientific background, motivation, and the objectives. Chapter 2

documents the plume structure based on observational data. Chapter 3 presents the general model configuration. Chapter 4 and 5 present the results from an idealized and a realistic simulation of the plume, respectively, as well as the modifications made to the general model configuration used in each numerical experiment. The results in Chapter 5 are divided into three sections in which the first two cover the experiments with a coarse and finer resolution bathymetry, while Section 5.3 presents a discussion of results presented in the entire chapter. Chapter 6 explores different scales of plume variation using results from a hindcast simulation whose configuration is presented in Section 6.1. Chapter 7 presents a synthesis of the thesis, which include the methodological constraints, and the main findings.

Chapter 2

Plume morphology from CTD observations

In this chapter, observations of the Zambezi River plumes are presented. They constitute the ground-truth for the numerical simulations presented in the following chapters. The discussion starts by introducing the general oceanographic settings of the region that are meaningful for this study, and then provides a review of past studies on the Zambezi plumes (given in Section 2.2). The sampling methodology and results are given in Section 2.3, and a discussion is presented in Section 2.4.

The main objective of the chapter is to document the Zambezi plumes based on all published reports and the available *in situ* data. The patterns of dispersion highlighted a feature of the Zambezi plume that have not been explored in previous studies. It consists of the tendency for the plume to progressively propagate upstream (poleward) as well as downstream (equatorward), which means that the Zambezi River plume is one of the very few plumes across the globe that propagate in the direction opposite to the sense of a Kelvin wave. Through visual inspection of the salinity distribution, the Zambezi plume was found to be super-critical (indicative of a faster freshwater inflow compared to the long internal waves), as well as surface-advected (bottom-advected) at times when the freshwater discharge rate measured at Tete was less than (more than) $\sim 2000\,\mathrm{m}^3/\mathrm{s}$.

A clear distinction was found between the plumes of the Zambezi and Licungo (located further north) rivers, characterized by a seaward bending of the salinity contours as the Zambezi freshwater flows downstream past the mouth of the Licungo River. In contrast, no clear distinction was found between the plumes from the Zambezi and Pungoe/Buzi (located further south) rivers.

2.1 Regional oceanographic context

The Zambezi River outlet is located in the Sofala Bank, on the western margin of the Mozambique Channel, around 18.7^oS. The bank constitutes an offset in the coastline between $17^oS - 20^oS$, and is characterized by an estuarine environment with a large range of salinity variability. There are records of salinity as low as 20.0 in extensive regions of the bank taken during the rainy season, when the salinity near the shelf break if slightly above 35.0 (IMR, 1978b; Lutjeharms, 2006).

The hydrodynamics of the channel is dominated by a number of highly variable anticyclonic eddies propagating poleward. These remarkably large eddies (>300 km wide) are formed roughly every 8 weeks (i.e., $6 \sim 7$ eddies per year) in the northern part of the channel, following a pulse in the volume transported westward by the South Equatorial Current (Backeberg and Reason, 2010). The frequency of these mesoscale features decreases in the central and southern parts of the channel to 4 per year (Schouten et al., 2003), likely induced by anomalies emanated from the western coast of Madagascar (Huisman, 2006). Based on the transport estimates reported in the literature, de Ruijter et al. (2002) and Asplin et al. (2006) have suggested that the poleward residual current at 15^oS carries about 5 Sv ($1\,\text{Sv} = 10^6\,\text{m}^3\text{s}^{-1}$), a significant contribution to the global thermohaline circulation.

The existence of large anticyclonic eddies in the offshore region implies a modified poleward (equatorward) current along the Mozambique (Madagascar) side of the channel. According to Lutjeharms (2006), these currents induce cyclonic lee eddies when moving past a shelf offset, as it is believed to be the case in Angoche, (i.e., north of the Sofala Bank) and Delagoa Bight. Amongst other characteristics, the lee eddies are known to drive a significant upwelling at the shelf edge, which is likely to be an intermittent feature given the variability of the poleward current and lee-eddy generation.

Despite all the uncertainty about the circulation in the Mozambique Channel, one fact is seemingly unarguable: the intensity of current variability on the eastern side is noticeably lower than on the western side of the channel. Here, the shelf circulation is mainly influenced by the passing eddies and their secondary effects, namely: coastal upwelling, lee-eddy generation, and extraction of water to mid-channel. In addition to the passing eddies, the Sofala Bank located at the centre of this region is strongly influenced by tides (Hoguane, 2007). The central and northern parts of the bank are also influenced by river runoff, while the southern part exhibits high salinities in the dry season presumably due to the excess of evaporation over precipitation (Lutjeharms, 2006; Hoguane, 2007).

The importance of tides in the Mozambique Channel was initially believed to be limited to the shallow zones of the shelf (Lutjeharms, 2006), where the tidal

currents play a role in the subsurface mixing, but recent studies have extended this importance to the offshore region in virtue of observations of seaward propagation of internal solitary waves and internal tides once generated at the shelf break (da Silva et al., 2009). Tidal amplitude computed from altimetry data for the central part of the channel is presented in Figure 2.1. There is a gradual increase in tidal range from each end towards the central part, which is likely due to the double standing wave system (Pugh, 2004) created by the interaction between the tide and the channel morphology. The entire channel has essentially semi-diurnal tides, as evidenced by the values of the Form factor ($F = \frac{K1+O1}{M_2+S_2}$) smaller than 0.25. The maximum tidal range in the channel is about 7 meters (da Silva et al., 2009) and it occurs during spring tides in the Sofala Bank, in a spot where the contribution of M_2 alone to the elevation is $\sim 1.8\,\mathrm{m}$.

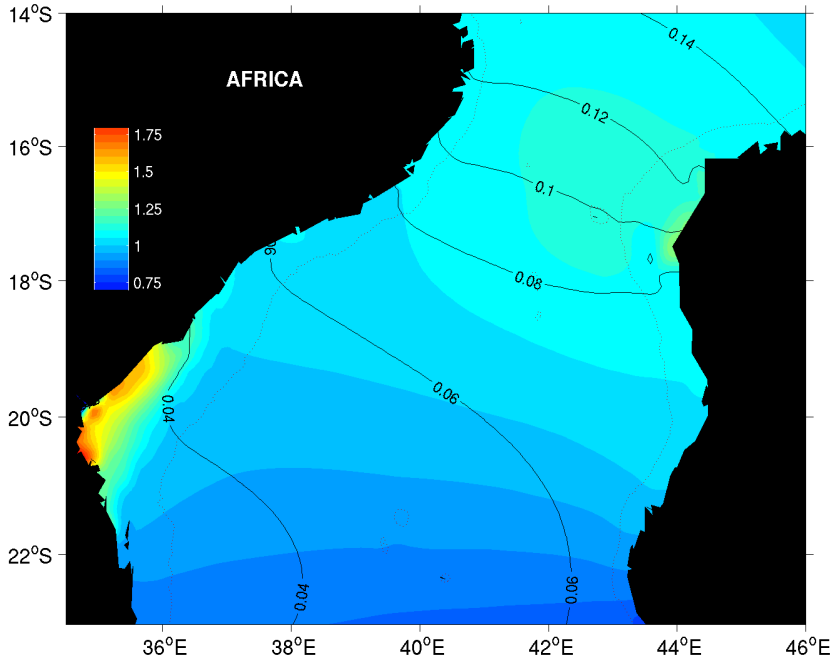

Figure 2.1: Tides in the central Mozambique Channel: distribution of M_2 amplitude (colours), overlaid by contours of Form factor, based on data from the Oregon global model v7.

2.2 Previous studies on the Zambezi plume

Between 1977 and 1979, a total of three cruises were conducted on board the *R/V Dr. F. Nansen* with the aim of surveying the fish resources and fishing potential along the Mozambican coast. The sampling included hydrographic stations throughout the coast and the results were presented by the IMR (1977, 1978a,b) and also used to formulate the tentative circulation patterns for the Mozambique Channel by Sætre and da Silva (1984). Based on these records, one finds a great deal of variability in the distribution of surface waters near the Zambezi Delta. Data collected in the first cruise in late September 1977 (IMR, 1977) clearly show a tongue of less saline water leaving the delta and moving polewards, at times when the ship drift indicated a weak equatorward surface current in the near-shore region between the delta and the city of Beira (20^oS), and a strong poleward current at the shelf break.

Observations of ship drift made towards the end of January 1978 revealed surface currents similar to the above described currents, except for small differences in the magnitudes (IMR, 1978a). However, the salinity distribution did not present any distinct directionality, and the most striking feature was the seaward bending of isohalines in front of the delta, suggesting the existence of a large bulge. Another interesting feature was the minimum in surface salinity (i.e., $<$30.0) observed directly offshore from the City of Beira where the shelf has its maximum extension, with values of salinity increasing from there towards the Zambezi Delta. However, the surface current did not support either the concept of a re-circulating bulge, or a poleward transport of the less saline plume waters. On the other hand, vertical salinity profiles taken along the central line of the delta reveal a stratified water column with ambient water (i.e., $>$35.0) at the bottom layers overlaid by less saline (i.e., $<$33.5). The vertical structure north of this line is only slightly different, but stratification reduces considerably in the southern part, where most of the water column consists of ambient water, confirming the equatorward transport of plume waters.

In early May 1978, a third cruise was undertaken along the coast (IMR, 1978b), and despite the fact that currents were not directly observed by any means, the horizontal distribution of salinity pointed to an equatorward motion of plume waters, given that the region between the delta and the city of Quelimane ($\sim 18^oS$) displayed the minimum values of salinity (below 20.0). North of Quelimane, the salinity contours of $20.0 - 34.5$ bended landwards, suggesting a limit for the direct influence of freshwater from the Zambezi River. As noted by the authors of the cruise report (IMR, 1978b), plume waters occupied the entire water column down to ~ 50 m in the four transects located near the delta, and the highly stratified structure observed in January of the same year had been substituted by isohalines extending from surface

to the bottom, with a slight seaward inclination, and no ambient water in the shelf zone.

The northern limit of the direct influence of the Zambezi freshwater has previously been noted by Siddorn et al. (2001), who used cruise and satellite data to assess the potential of satellite imagery in determining plume properties. The cruise data in that study was collected in the beginning of April 1998 in a 12-day field campaign that surveyed the transects A through J displayed in Figure 2.2. The sampling of salinity was then made using a ship-lowered Valeport CTD, and calibrated using a Guildline portable salinometer. A region of maximum salinity was found along the coast between the city of Quelimane and the mouth of the Licungo River, from where the salinity decreased towards the Zambezi Delta in the southern part, as well as towards a second source of freshwater in the northern part. The surface salinity in the vicinity of the Zambezi delta increased with the distance offshore having values between < 20.00 and 35.50, and the plume appeared to be moving northeastwards beyond the city of Quelimane, but never really reaching the mouth of the Licungo River.

2.3 Observational program

2.3.1 CTD sampling

Between 2004 and 2007, the Mozambican National Institute of Fisheries Research carried out an oceanographic cruise once every year, over the Sofala Bank region, on board vessels from the semi-industrial shrimp fishery fleet. The measurements comprise hydrographic data collected at the stations illustrated in Figure 2.2, which usually are sampled over a period of about 10-15 days time. The goal of these cruises is to assess the shrimp recruitment prior to the onset of the fishing season, which occurs in mid March every year, and apart from the biological sampling, a ship-lowered enhanced Seabird CTD system (conductivity, temperature, depth, turbidity, dissolved oxygen, and fluorescence sensors) was used to record physical properties of the water. At each station, the first measurement was taken as close to the surface as possible, and subsequent readings were taken in profiling mode and averaged every 2 decibars. No calibration of salinity or temperature was performed on-board, and the post-processing and archiving was undertaken at the institute headquarters. These data have not previously been presented in any written form, and here the focus is the measurements of salinity, temperature and turbidity. The latter was measured through an optical back-scattering sensor (OBS, D&A Instruments Inc.)

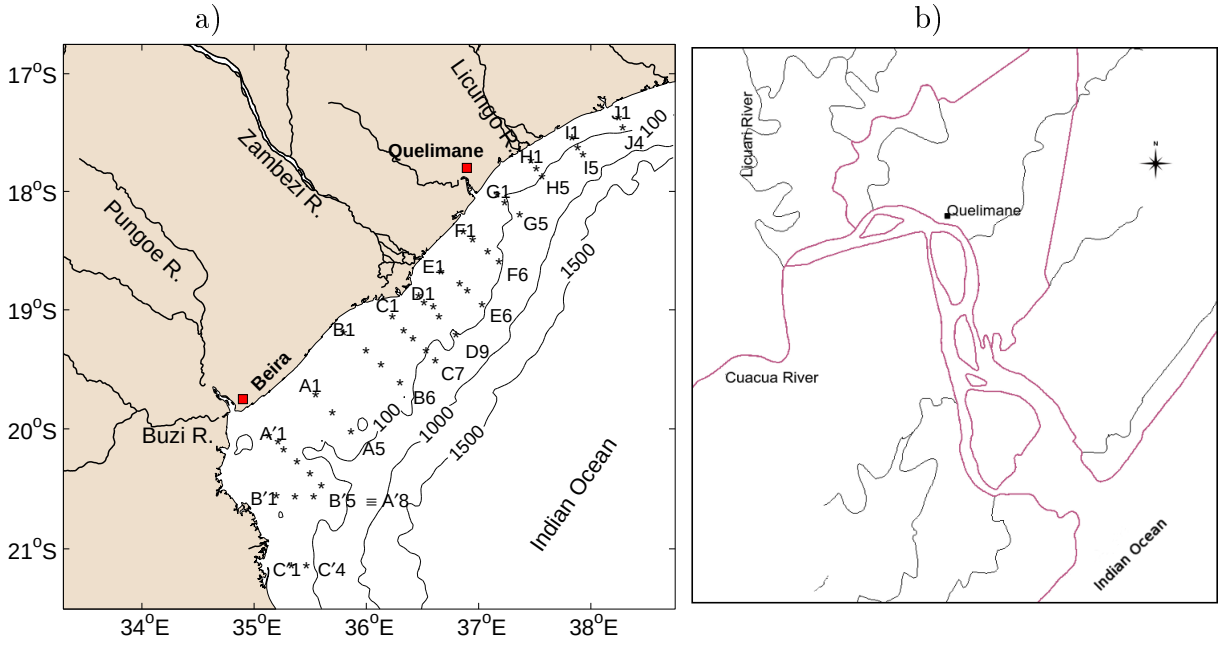

Figure 2.2: CTD stations in the Sofala bank. Also shown are the 100 m and 1000 m isobaths taken from ETOPO2 global dataset, along with the place and river names referred to in the text. The left panel shows details of the region around Quelimane city, with the Licuari and Cuacua Rivers combining to form the Bons Sinais Estuary.

with sensitivity reported in NTU based on factory calibration.

2.3.2 Auxiliary data

River discharge

Freshwater transport measured on a regular basis at an upriver station located in Tete, about 440 km from the river mouth, is presented in Figure 2.3. The seasonal variation of river discharge is characterized by two periods: a) a rise period spanning the months of September to February (near the end of the rainy season) with a maximum monthly-mean discharge of 3039 m^3s^{-1}; and b) a fall period between March-August (dry season) with a minimum of 1633 m^3s^{-1}. According to Beilfuss and dos Santos (2001), the rainfall in the Zambezi catchment region is strongly influenced by the movement of the Inter-Tropical Convergence Zone, and specially for the delta region, this movement translates to a rainy season 4-6 months long between October and April. This region is also highly susceptible to torrential rain from cyclones that can occur anytime between November and April (Mavume et al., 2009). It is worth mentioning that the river discharges presented in Figure 2.3 do not include the effects of rainfall and storms in the low-laying lands and the delta region. However, it does include a substantial part of the freshwater flowing through

the Cuacua River, a distributary of the Zambezi whose estuary is located by the city of Quelimane, north of the Zambezi delta.

Apart from the Cuacua waterway, the lower Zambezi and the delta region are characterized by a dense branch network, where three particular branches are important for this study because they constitute the main drainage for the Zambezi freshwater, as follows. Firstly, the Mucelo River branches off at about 55 km from the coast and follows a meandering path to the sea in the southern part of the delta. Secondly, the Chinde River branches off at about 30 km from the coast and flows north. Lastly, the Zambezi main course in the central part of the delta. During peak discharges, these distributaries spill overbank forming a broad channel to the ocean. This pattern is enhanced during spring tide, as high tide levels retreat river water (Beilfuss and dos Santos, 2001). During the dry season, tidal influence is still noticed 80 km upriver, as verified during a field work in September 2009 carried out in the context of the present study. The maximum depth in the delta is about 8 m and it occurs in a very small distributary.

Another smaller but important source of freshwater in the Sofala Bank is the Licungo River whose basin constitutes the northern bound for the Zambezi River basin in the low-laying lands. The entire Licungo basin is located in Mozambican territory, and therefore the river discharges give a better indication of the rainfall regime in the region. As can be seen in Figure 2.3, there are significant differences in the timing of maximum and minimum discharges between the Licungo and Zambezi rivers. In general, the Zambezi reaches its peak discharges earlier compared to the Licungo River, and the lag is about one month and 2 months in the case of maximum and minimum discharges, respectively.

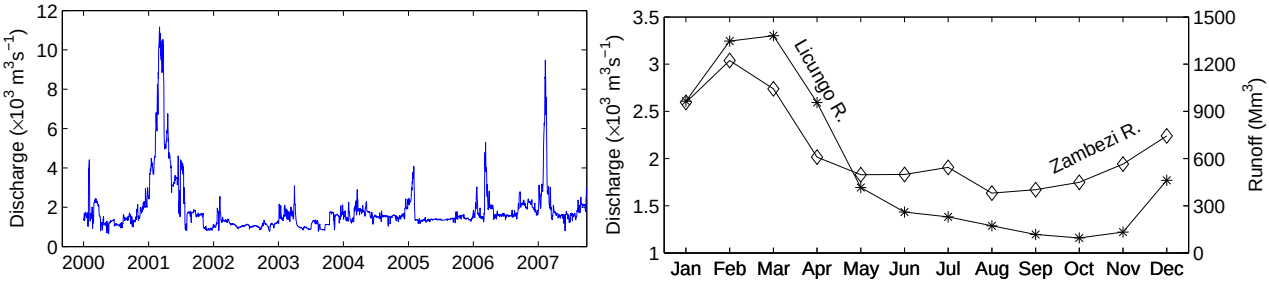

Figure 2.3: *Left:* Daily river discharge measured at Tete during years 2000-2007, with the time tags referring to 1st January. *Right*: Seasonal variation of the Zambezi discharges (left axis) based on the 1976-2007 dataset, and Licungo runoff (right axis) based on the data measured at Mocuba in the period 1970-2001 (from Langa, 2002).

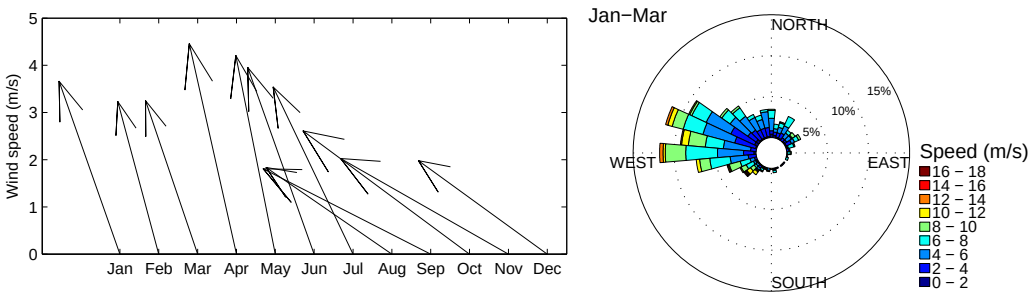

Figure 2.4: *Left*: Monthly-mean estimates of wind field for the period 2000-2008 based on QuikSCAT. *Right:* Wind rose plotted from daily JFM data for the period 2000-2008, using the oceanographic notation "*blowing towards*".

Winds

Wind data have been extracted from the QuikSCAT dataset, for a $2^o \times 2^o$ box centered at the river mouth. Monthly means for the period 2000-2008 are presented in Figure 2.4 , which indicates a predominance of northwestward winds throughout the year, with a significant change in direction from August to December. The monthly mean intensity is nearly constant during the year, however, the dominant frequencies returned by a power spectrum based on the daily wind magnitudes observed during the period of CTD data collection (results not shown) revealed patterns of variation at the scale of 6, 12, and 182 days, with the 12-day period representing the highest peak in a periodogram.

A close look at the daily wind data for the period of peak river discharges (i.e., January to March) displayed in Figure 2.4 points the westward, followed by northwestward, as the most frequent orientation of the winds. Since the coastline in the delta region is oriented in the SW-NE direction, this pattern implies that the synoptic northwestward winds blow nearly perpendicular to the shoreline. No information regarding the sea/land breezes is available for this region, provided that the local meteorological services collect wind data from a ground station only three to four times a day.

2.3.3 Results: plume patterns

The plume observed during 11.02-01.03.2004

During 2004, the recorded river discharges were lower than the monthly climatological discharge for February or March, and even in the rise season they never reached the annual mean value ($\sim 3000\,\mathrm{m^3 s^{-1}}$). The maximum transport of about $2900\,\mathrm{m^3 s^{-1}}$ was observed towards the end of March, and during the time of CTD sampling it varied between 1200 and $1500\,\mathrm{m^3 s^{-1}}$. The wind field was very weak during that particular time, corresponding to the intensity of a gentle breeze in the Beaufort scale blowing from no predominant direction, but rather changing between easterly, southeasterly, and northeasterly winds (Figure 2.5). However, prior to the plume observation, the winds blew at about 12 m/s from the southwest then weakened and changed to southeasterly winds.

The hydrographic data recorded for this period is presented in Figure 2.6. Salinity varied between <33 psu near the northernmost tip of the delta to >35 psu at the most offshore stations, as well as at the coastal stations offshore from the city of Beira. Temperature varied between <30 °C near the river mouth to about 28 °C at the northernmost transects. Attached to the downstream coast there is a pool of estuarine waters, characterized by the lowest observed salinities and highest temperatures. This pattern suggests the existence of a density-driven coastal current flowing northwards and reaching the regions beyond the city of Quelimane. The vertical profiles taken at the transect I (Fig. 2.7), located about 200 km north of the river mouth, exhibit a structure that is consistent with the simulation results of a

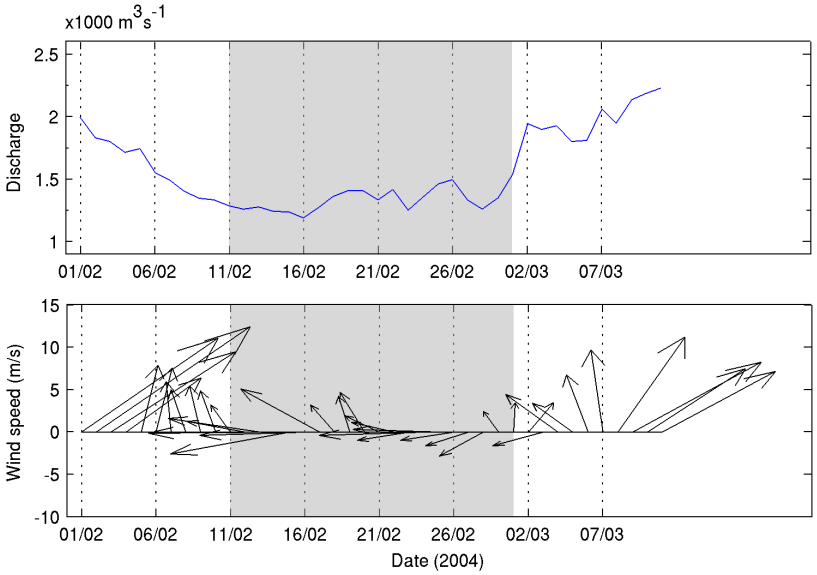

Figure 2.5: River discharge (*top*) from the Tete gauge station, and QuikSCAT winds (*bottom*) during February and March/2004. The shaded area corresponds to the period of CTD data collection.

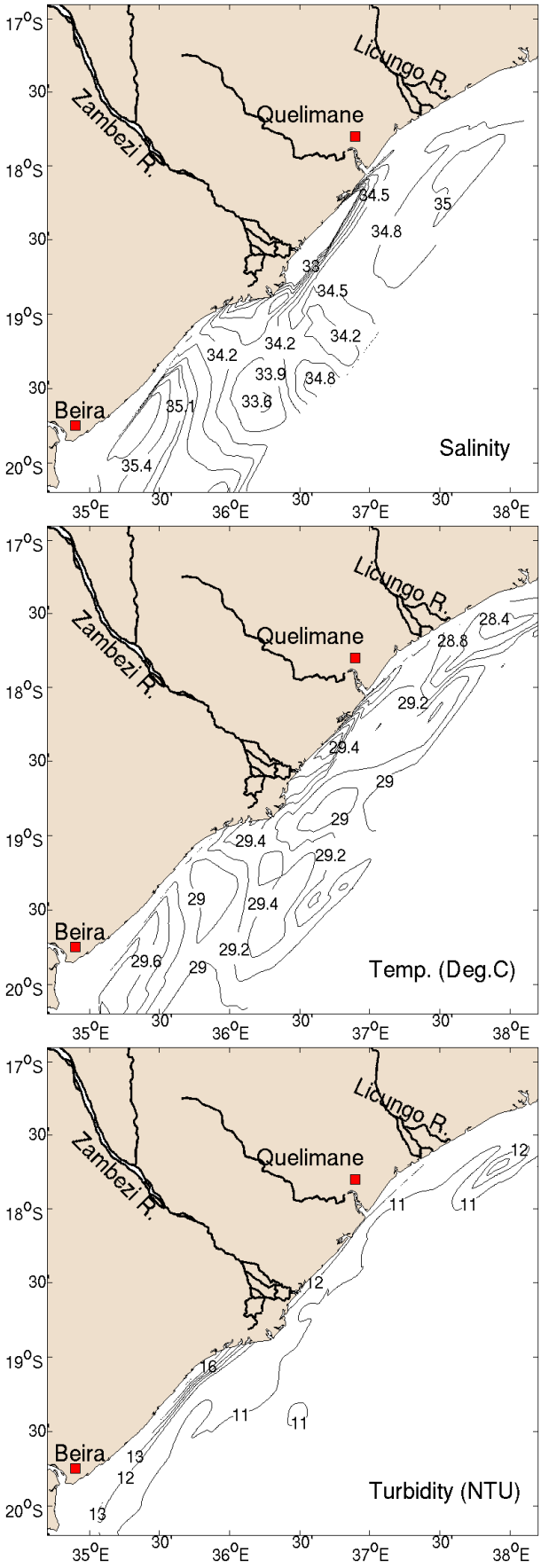

Figure 2.6: Near surface salinity, temperature, and turbidity from shipboard castings taken between 11.02 and 01.03.2004.

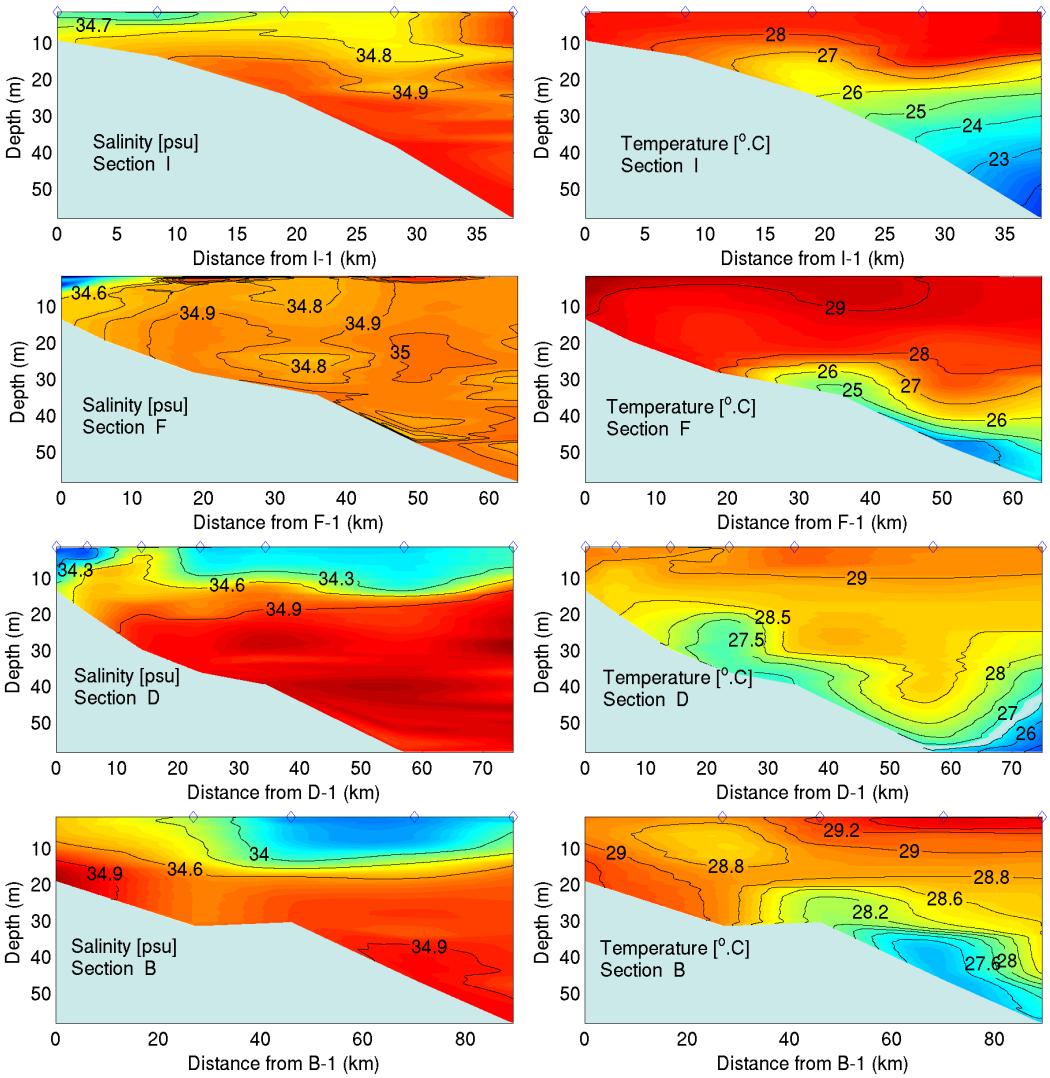

Figure 2.7: Vertical profiles of salinity (*left*) and temperature (*right*) recorded in 2004, along transects I, F, D (at the river mouth), and B. The values for the spaces between sampled station were filled using cubic interpolation. Note the different horizontal scales on the sections.

flow attached to the coast driven primarily by buoyancy, and consists of a two layer coastal ocean with a relatively high geostrophic shear, and a top layer made of lighter water moving in the downstream direction (Garvine, 1999).

The horizontal distributions of either salinity or temperature contain another feature marked by plume waters, with salinity as low as 33.6 psu and temperatures as high as 29 °C, apparently spreading southwards and reaching as far south as 20 °S. The orientation of the patch of lighter water is not consistent with the theory of buoyancy-driven flow, and can only be explained by the combined action of other forcing. Turbidity varied between <11.00 NTU at the offshore stations and >16.00 NTU at the Zambezi mouth, more specifically at the southern outlet. Judging by the area bounded by the 11.00 NTU contour and the coastline, it is suggested that the majority of suspended sediments coming from the the Zambezi

River were transported poleward along with a portion of freshwater, followed by a smaller amount of sediments transported equatorward in the coastally-trapped density-driven flow.

The data from transect D (i.e., at the river mouth), indicates that plume waters occupy the surface layers of all the stations, all the way to the isobath $100-1000\,\mathrm{m}$, which is about 100 km away from the coast. A re-circulating bulge is not evident in neither the horizontal nor the vertical distributions of salinity and temperature.

The plume observed during 22.01-08.02.2005

In 2005, the maximum discharge measured at Tete occurred during the time of CTD sampling, and it reached $4000\,\mathrm{m^3 s^{-1}}$, about two times greater than the maximum in the previous year during plume observation. It is interesting to note that following the peak discharge on the 31st January, it took only one week for the discharge to drop down to its minimum corresponding to the mean value for the fall season in that year (Fig. 2.8). This sudden change of the river discharge is very likely a consequence of the river regulation upstream. The winds were predominantly moderate with orientation changing from southeasterly prior to plume observation, to northerly and northwesterly in the first two days of observation, to southwesterly in the following 5 days, and to southeasterly for the rest (majority) of the sampling period.

The horizontal plume structure (see Figure 2.9) is similar to that observed in 2004, except for the extent of the southward motion of plume waters that is greater

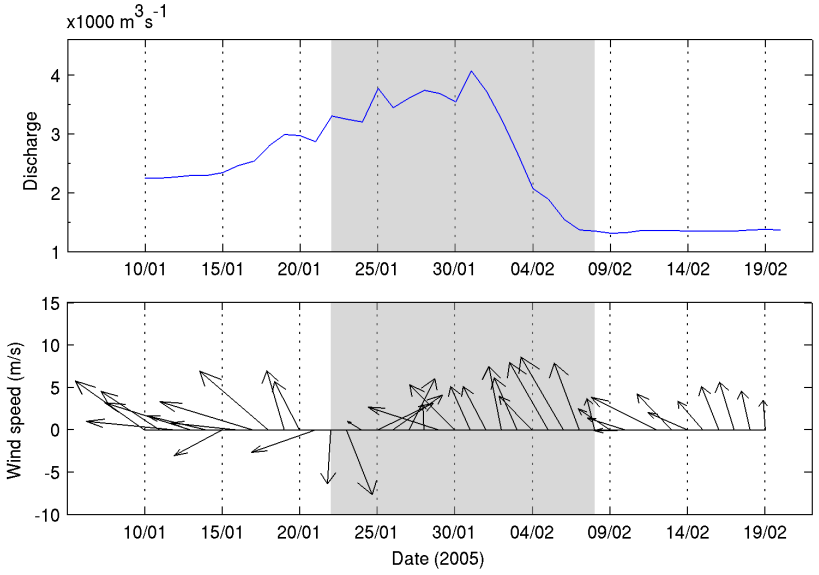

Figure 2.8: River discharge (*top*) from the Tete gauge station, and QuikSCAT winds (*bottom*) for the period January-February/2005. The shaded area corresponds to the period of CTD data collection.

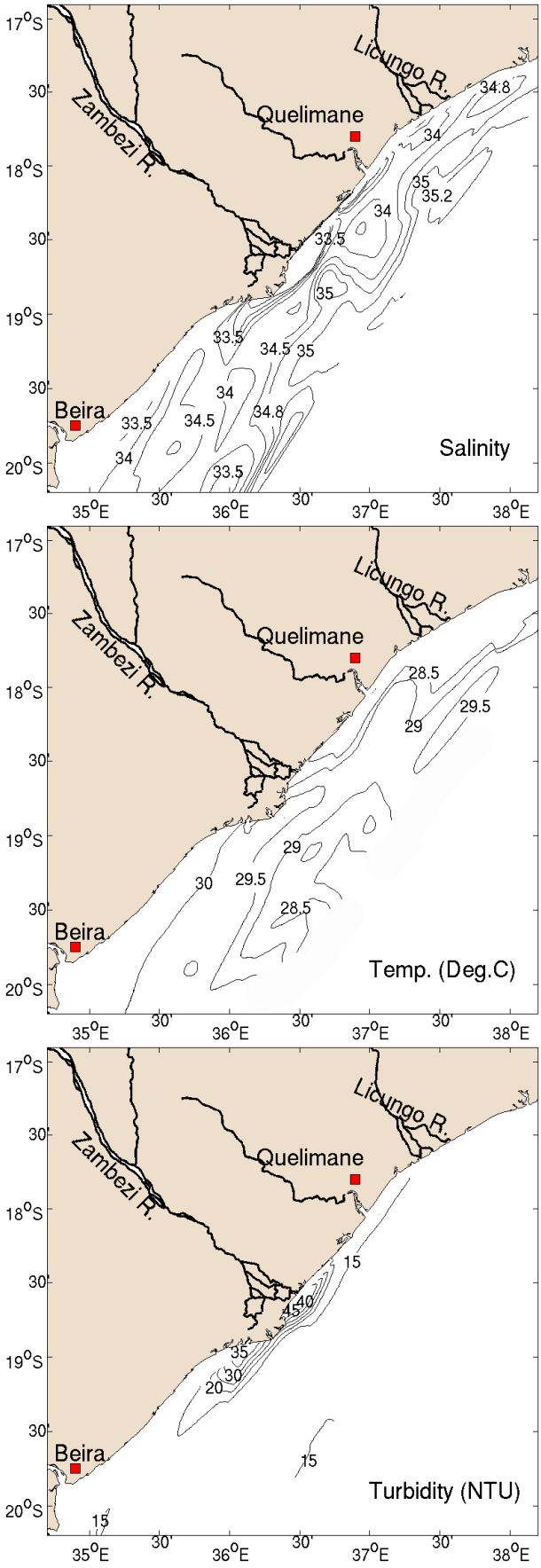

Figure 2.9: Near surface salinity, temperature, and turbidity from shipboard castings taken between 22.01 and 08.02.2005.

in the current case. The salinity distribution shows that due to freshwater contribution from the Licungo River the isohalines bend seawards to form a second bulge and plume connected to the northward flowing portion of the Zambezi plume. The implications of this second bulge on the coastal current still need to be determined. The distribution of turbidity is nearly homogeneous in the offshore stations, but in the periphery of the delta it increases gradually from 15.00 to 45.00 NTU at the northern outlet of the river. However, the turbidity distribution is fairly well balanced between the northern and southern regions relative to the delta centreline, and hence it gives no clear hint about the preferential direction for sediment transport.

The offshore plume extent displayed in the vertical distribution of salinity (Fig. 2.10) is considerably smaller in the periphery of the river mouth, when compared to the 2004 plume. The plume maintains contact with the bottom near the river mouth

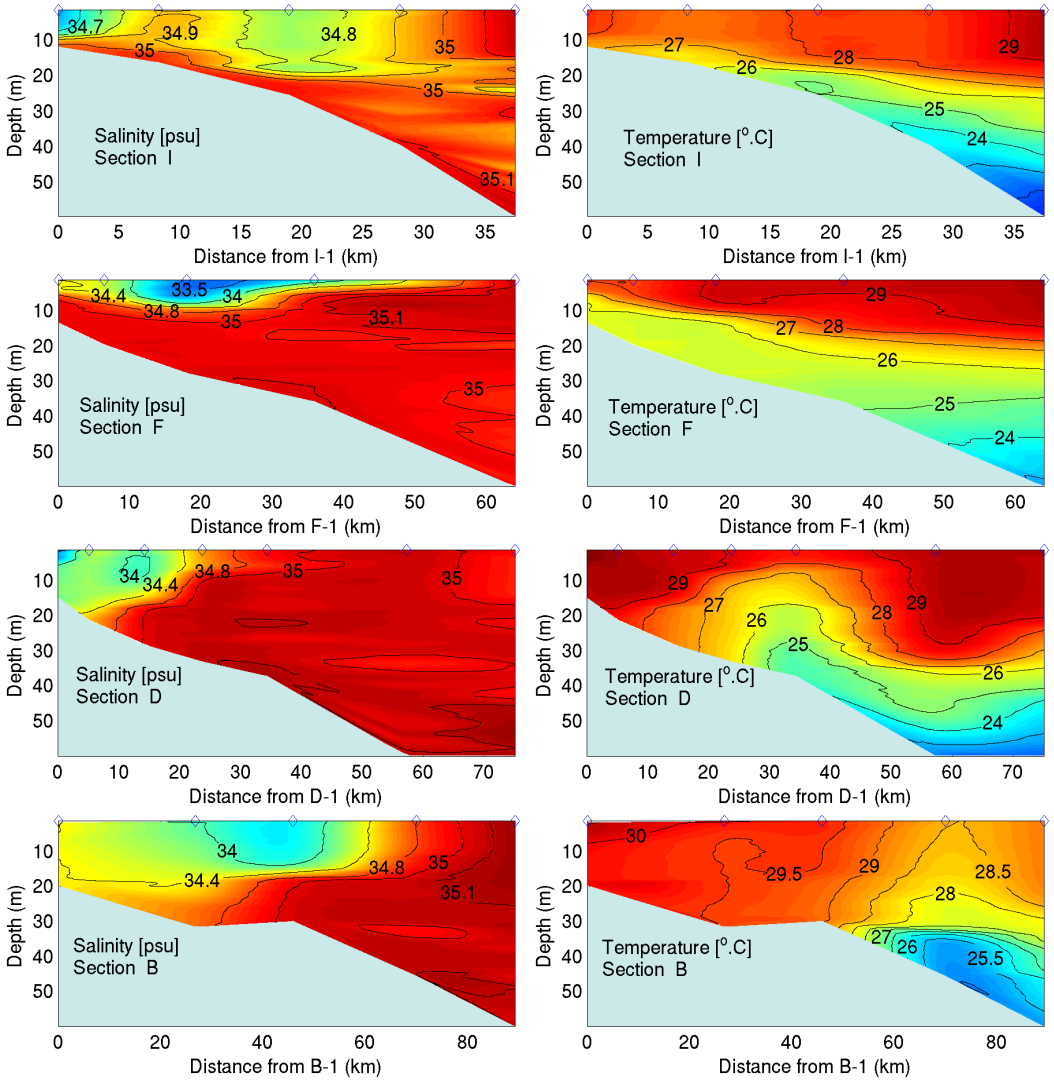

Figure 2.10: Same as Fig. 2.7, except for the data collected in 2005.

(transects B and D), in contrast to the 2004 plume in which the contact exists in all regions. The coastal northward current seems to attain its maximum depth at about 25 km from the coast (since station F1 is located 7 km from the coast), as evidenced in the data from transect F.

The plume observed during 01.02-12.02.2006

The rise period in river discharge for the year 2006 started in December 2005 and was marked by a drop in discharge towards the end of January, before reaching the peak at the end of March (*cf.* Figure 2.3). No information regarding discharge rates for that period is available for the Licungo (in the north) and Pungoe/Buzi (in the south) Rivers. However, the CTD sampling took place during the time when the discharges fell (see Fig. 2.11) , and hence, it is very likely that the observed plume carries some signature of the peak discharge from the preceding days. On the other hand, the wind field during the sampling period was characterized as follows. Prior to plume observation, the winds blew particularly from southeast with moderate intensity, and during the observation there was no predominant direction. However, the winds blowing from the southwest and northeast were a lot more intense than those blowing from southeast in the last two days of sampling.

The surface views of salinity, temperature, and turbidity are presented in Figure 2.12. As can be seen, low salinity (<35.00) waters are found almost everywhere, but in contrast to the previous plumes, the lowest value recorded for surface salinity ($\sim$ 32.50) did not occur exactly in the vicinity of the Zambezi mouth. It was located

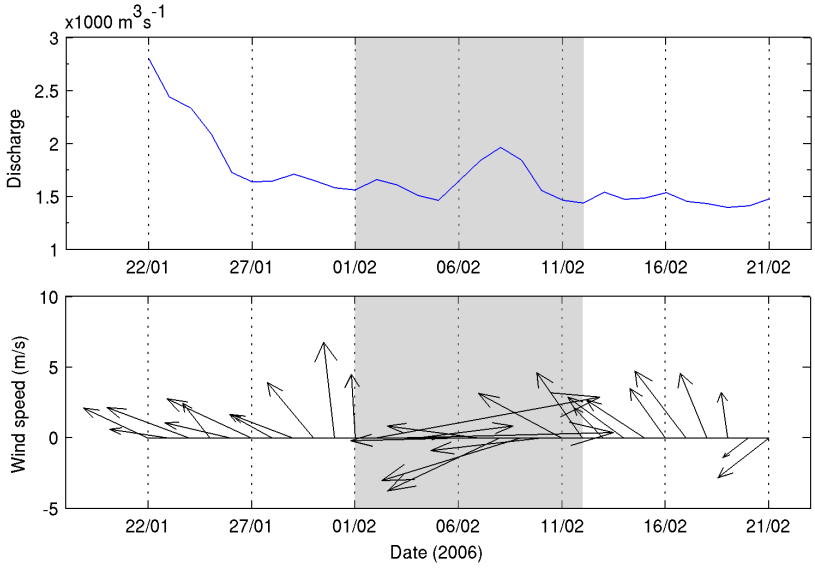

Figure 2.11: River discharge (*top*) from the Tete gauge station, and QuikSCAT winds (*bottom*) for the period January-February/2006. The shaded area corresponds to the period of CTD data collection.

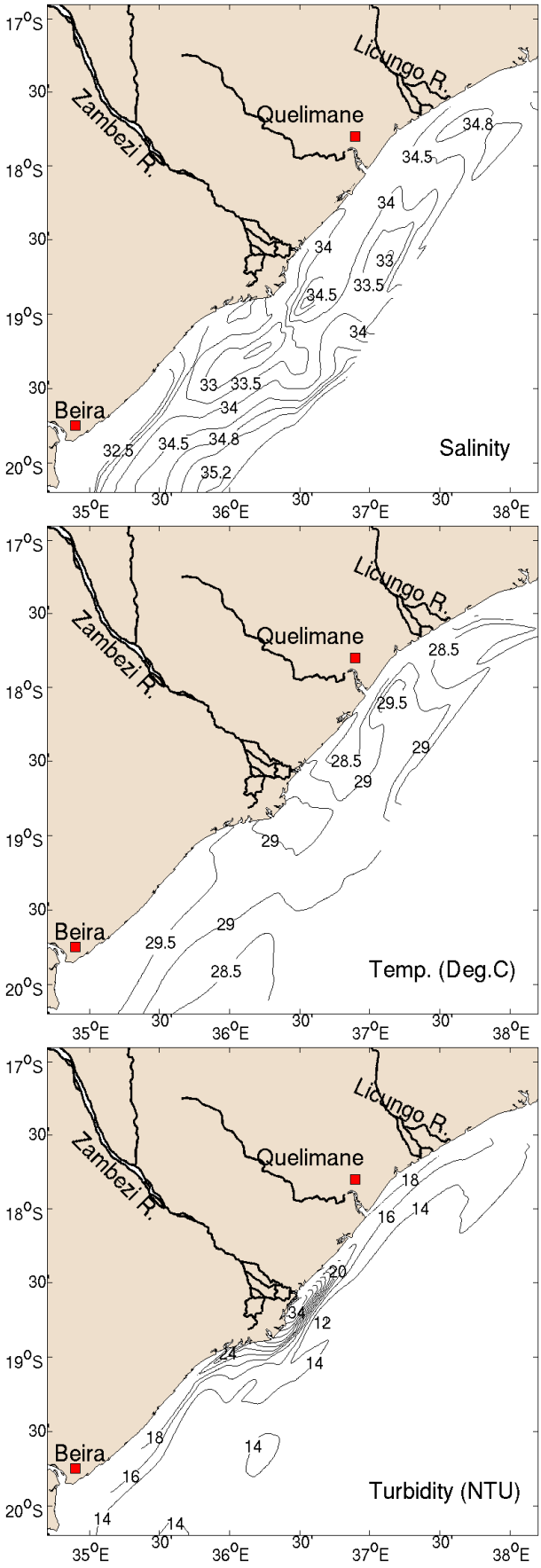

Figure 2.12: Near surface salinity, temperature, and turbidity from shipboard castings taken between 01-12.02.2006.

further south at the coast, directly offshore from the city of Beira where the Pungoe and Buzi Rivers seem to be the major contributors to the freshwater input. It appears that the equatorward movement of Zambezi plume waters near the coast is strongly reduced in the current case, in favour of the offshore transport, suggesting a plume movement detached from the coast. In spite of this behaviour, the distribution of turbidity indicates that sediments are transported primarily equatorward given that the gradients are higher in this direction, and the maximum turbidity is found north of the river mouths. In contrast to the previous two cases, the current plume exhibits a more complex horizontal structure in which the patchiness in the freshwater distribution makes it difficult to clearly infer the directionality and dimensions of the plume.

The vertical profiles (Fig. 2.13) indicate that the plume water is limited to the surface layer, which is relatively thinner near the river mouth (see transect D), in

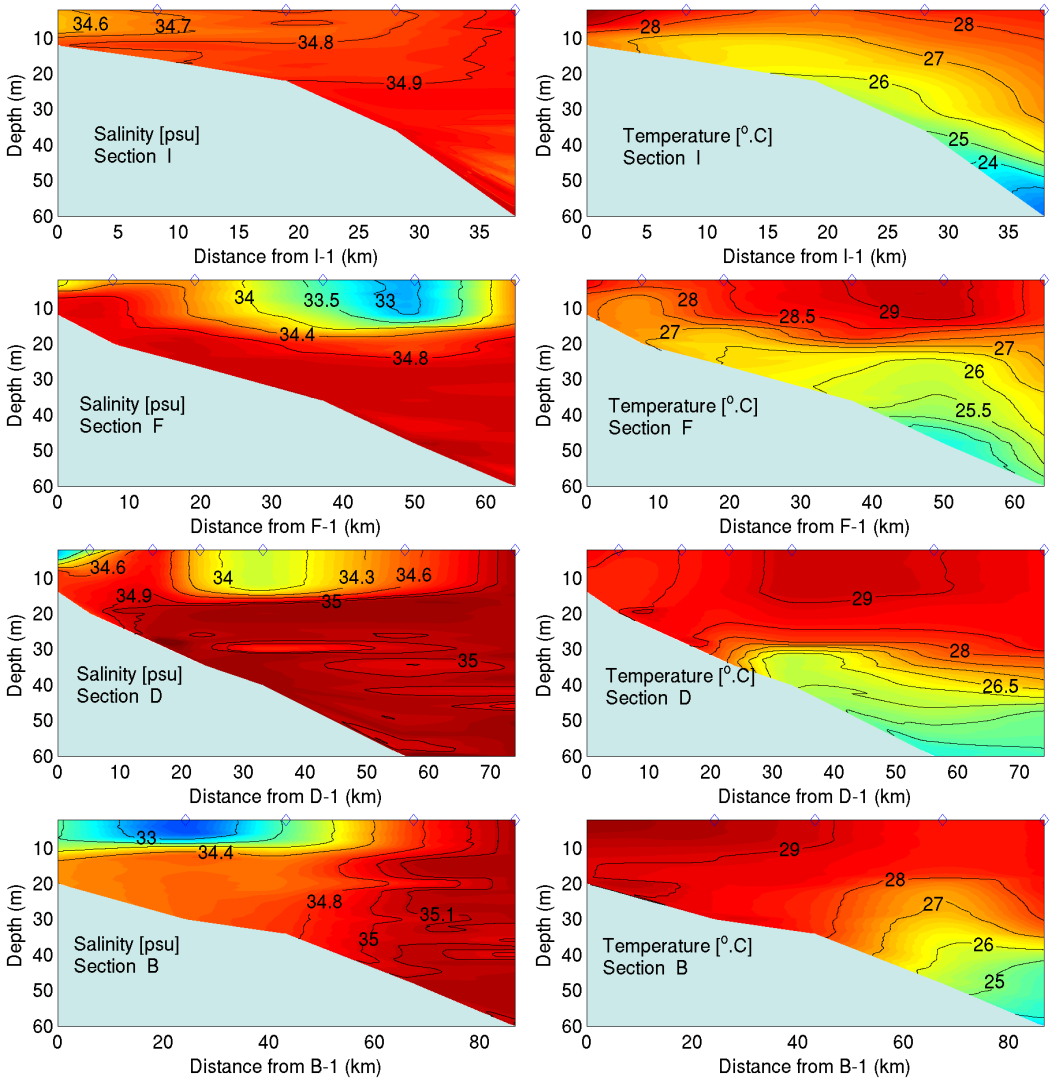

Figure 2.13: Same as Fig. 2.7, except for the data collected in 2006.

comparison with the remaining transects where the plume waters maintain contact with the bottom. Despite the fact that surface plots do not show a strong evidence of a downstream coastal current as the plumes observed previously, the vertical structure at transect I is identical for all the plume observations, except that the surface layer containing lighter water is notably much deeper in the 2006 plume. The large plume thickness is typical for excessive buoyancy under negligible mixing, or a moderate discharge under enhanced mixing conditions attributable to either a strong wind field or stronger influence of tides. However, the data from the remaining transects do not support this.

The plume observed during 30.01-11.02.2007

The second largest discharge of the decade occurred during 2007. According to readings from the Tete gauge station, it reached a maximum of 9.480 m^3s^{-1} just the day before the 13-day CTD sampling was terminated (Fig. 2.14). The discharge rate was about 4.000 m^3s^{-1} on the first day of sampling, and it even doubled during the sampling. Also, the winds were blowing predominantly from the southeast with weak to moderate intensity during all the sampling period. Prior to the CTD sampling, river discharges were below 4.000 m^3s^{-1} and some moderate to strong southerly winds were observed.

Figure 2.15 presents the horizontal distributions of surface salinity, temperature, and turbidity for the plume observed in 2007. Light water having very low salinities (< 31.0) and high temperature bounds the coast from the delta region to the region

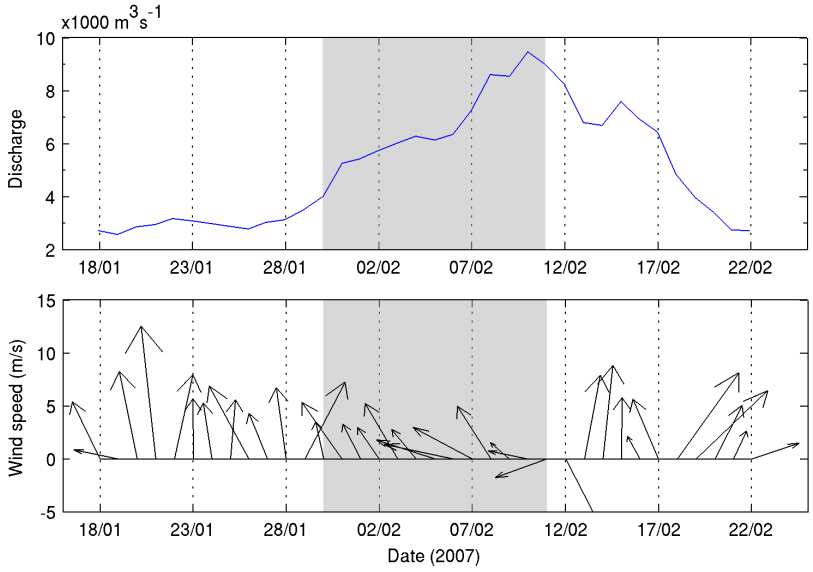

Figure 2.14: River discharge (*top*) from the Tete gauge station, and QuikSCAT winds (*bottom*) for the period January-February/2007. The shaded area corresponds to the period of CTD data collection.

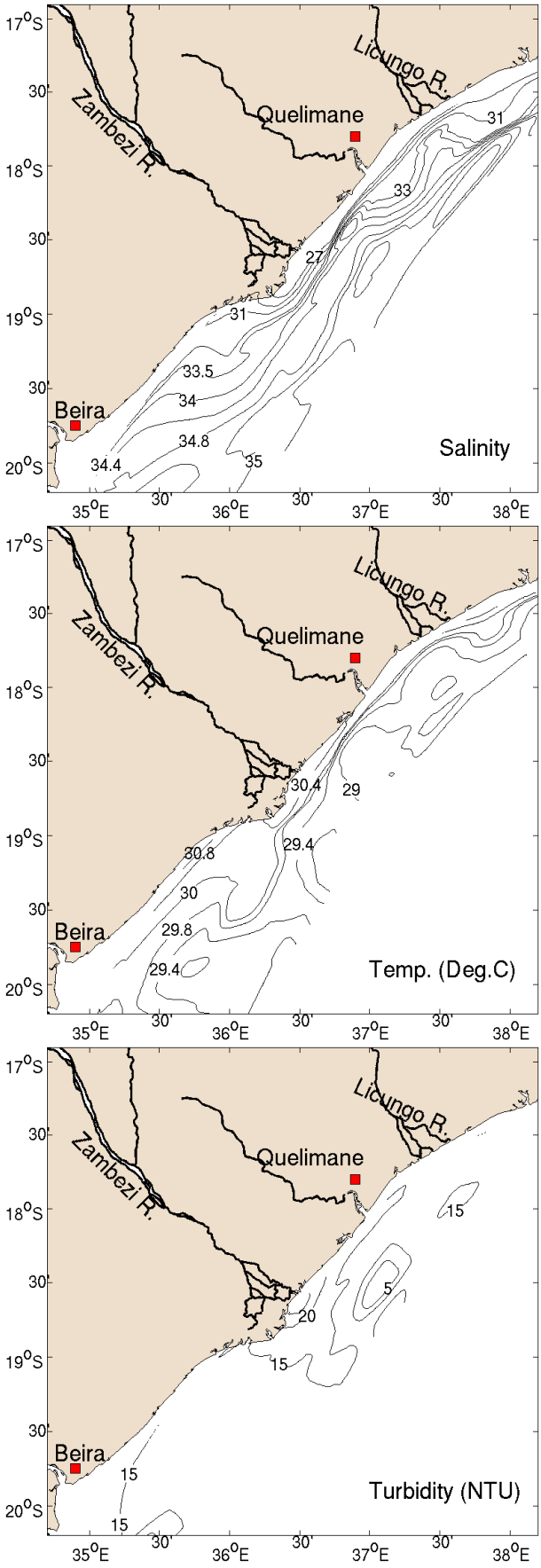

Figure 2.15: Near surface salinity, temperature, and turbidity from shipboard castings taken between 30.01 and 11.02.2007.

north of the Zambezi delta, depicting the existence of a strong buoyancy-driven flow along the coast, which extends beyond the limits of the sampled area. Contours of salinity and temperature bend seaward in the regions near the mouths of the Cuacua (flows through Quelimane) and Licungo Rivers, increasing considerably the width of the buoyancy-driven flow. This increase is more salient for the Licungo River than the Cuacua River. It turns out that if the density-driven flow is parallel to the salinity contours (top panel of Figure 2.15), then a region of intensified alongshore current will exist between these river mouths. Turbidity is uniformly distributed over the southern part of the plume, with values around 15.0 NTU. The northern region on the other hand, displays some rather large gradient as the values decrease from about 25.0 NTU at the northern outlet to $\sim$ 15.0 NTU in a area that extends beyond the city of Quelimane. In addition, there is a fairly large amount of suspended sediment transported directly offshore from the river mouth, which might be the

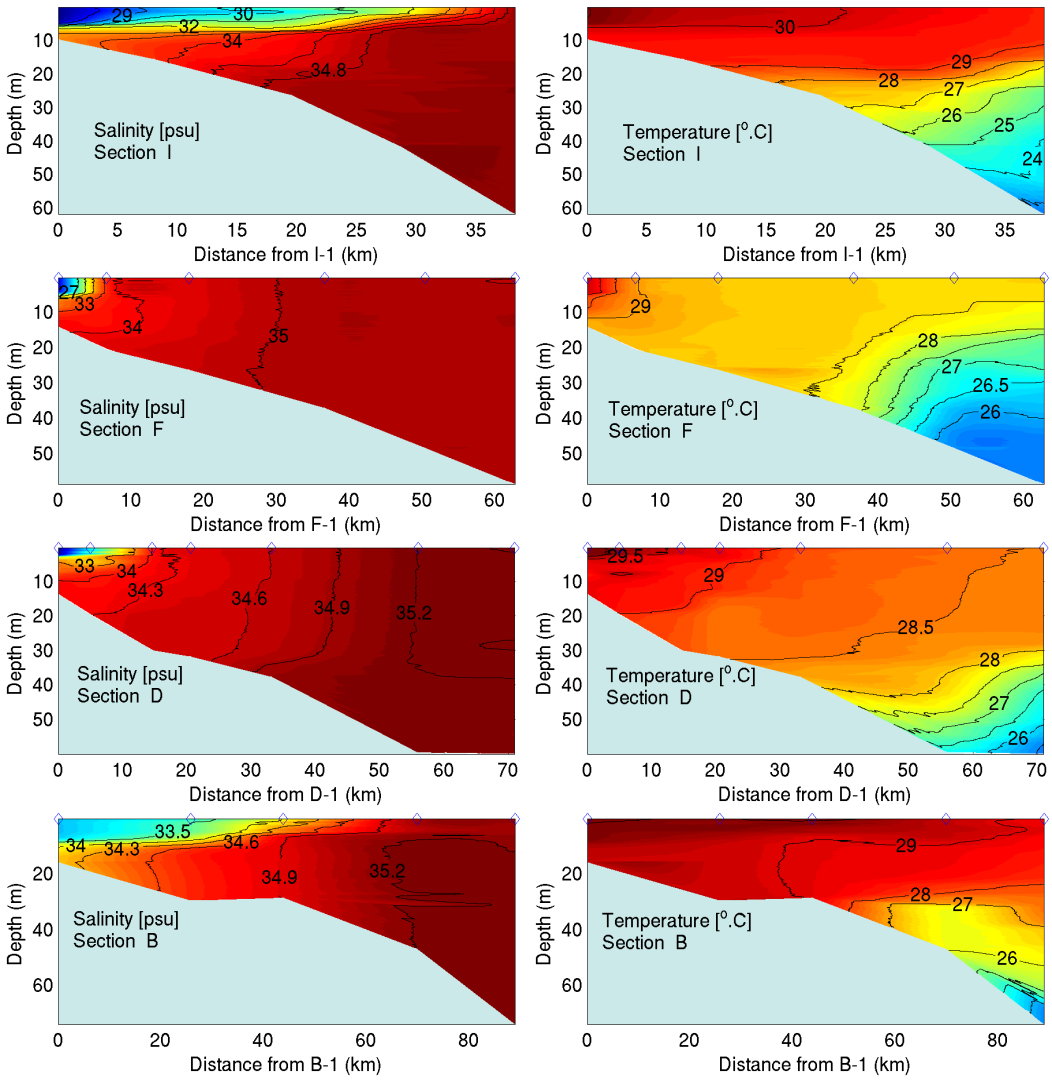

Figure 2.16: Same as Fig. 2.7, except for the data collected in 2007.

consequence of a presumably enhanced inertial flow at the river mouth.

To the south of the Zambezi River mouth, it appears that although the amount of plume water is reduced in comparison with the previous observations, there is still some plume water with the previously described tendency of moving poleward (*cf.*, isohalines $33.00 - 34.8$ psu and isotherms $29.8 - 30.0\,^{\circ}$C).

The vertical profiles for this plume are presented in Figure 2.16. As can be seen, plume waters occupy the entire water column from the coast to $20 - 30$ km offshore, and the surface layer in the coastal stations in all transects I, F, D (river mouth) is made up of estuarine water. However, the seaward extension of this pool of estuarine water is relatively smaller in transects D and F than in transect I, where there is an additional freshwater input from the Licungo River.

2.4 Discussion

The Zambezi River plume as it is known today, is characterized as an estuarine plume that turns northward and proceeds along the coast (Mann and Lazier, 1996; Hoguane, 1997; Siddorn et al., 2001). These earlier studies used either satellite data or single-cruise *in situ* observations to establish this conclusion. The data presented in the previous section, which represent four plume events separated by a period of about a year, suggest that the above mentioned northward turn and subsequent equatorward flow of plume water might be a feature more prevalent during high discharge periods, and more importantly, a feature observable in years of extremely high discharge when the buoyancy effects dominates the dynamics. During the periods of plume observation, the average discharge varied between 1300, 2500, 1600, and $6000\,\mathrm{m^3 s^{-1}}$ in consecutive years since 2004, and the transport of plume waters oriented predominantly northeastwards (equatorward) was only found in the year 2007. The freshwater transport could not be directly determined from the available dataset since no current measurement was made, hence the transport analysis presented here is based on the position of density contours or patchiness in the horizontal distribution of density.

In contrast to the general consensus of a northward density-driven flow, the plumes were found to advect not only northwards but also polewards in a great number of observations, which includes also the historical data reported in IMR (1977), and IMR (1978a,b). An exception to the above mentioned pattern is the plume event recorded in 2007 (Fig. 2.15), which features only a northeastward spreading. It must be noted that the poleward transport (opposite to a Kelvin wave direction) of less saline waters differs from the upstream intrusion of plume waters discussed in a number of previous simulation-based studies. For instance, Chapman

and Lentz (1994) found a coastally-trapped upstream flow that was negligible in comparison with the downstream transport of plume waters. Garvine (1999) and the references therein have found similar results and hypothesized that under a flat bottom little or no upstream intrusion occurs, while even for a gentle slope the plume waters would significantly penetrate upstream. Other features of the upstream intrusion that seemingly are not found in the Zambezi influenced waters are the anticyclonic turn and subsequent downstream flow present in the simulations by Garvine (1999), and the quasi-steady state attained when a moderate mean ambient current was applied (Yankovsky and Chapman, 1997; Garvine, 2001).

The dynamical basis for the upstream propagation was analyzed not long ago through numerical simulations of the Suo-Nada river plume (Seto Inland Sea, Japan) by Magome and Isobe (2003), whose results support earlier findings that suggested the vortex line stretching as the main driver for the upstream intrusion. The upstream intrusion of freshwater has been observed in only a few real systems, namely, the Changjiang River (East China Sea; Beardsley et al., 1985), major Siberian rivers (Arctic; Weingartner et al., 1999), the Mississippi River (Walker et al., 1994), and the Suo-Nada outlet (Seto Inland Sea, Japan; Magome and Isobe, 2003). The results presented here justify the inclusion of the Zambezi River in this short list, although the existing model results can not be applied in this case, as they link the upstream flow with re-circulation in front of the bulge or the turning of the upstream flow to join the downstream counterpart, which has not being observed in the Zambezi River plume system.

A number of classification schemes have been proposed in the literature as an attempt to generalize the plume features, most of which relate the observed/simulated features to the most dominant forcing in the generation or evolution of the plume. Therefore, the velocity field within the plume is a vital parameter for the implementation of these classification schemes (Chao, 1988a; Garvine, 1995; Kourafalou et al., 1996b; Yankovsky and Chapman, 1997). However, a few exceptions do exist, in which case the density field is used to describe the plume instead of the velocity field. These include the approach proposed by Chao (1988a), which characterize the plume as *super-critical* (*sub-critical*) if the width of the bulge is greater (smaller) than the width of the coastal current. This scheme was later explored by Kourafalou et al. (1996b) who recognized its ability to appropriately characterize the plumes. In addition, it is possible to distinguish the plume using the terminology introduced by Yankovsky and Chapman (1997), according to which a plume can be either a *surface-advected* if the plume spreading occurs with little or no contact between the

lighter water at surface and the seabed, or *bottom-advected* if the contact with the bottom is sustained well offshore and the density front extends from the surface to the bottom.

On this basis, the plumes presented in the previous section can be characterized as *super-critical* since the plume width decreases from the bulge region towards the downstream coast. Notice that the portion of plume waters that spreads upstream in not used to derive this classification, and in some cases it represents the majority of plume water (*cf.* data collected in 2006). According to Kourafalou et al. (1996b), a super-critical plume implies that the speed of the freshwater inflow exceeds that of the long internal waves.

With respect to the vertical structure directly offshore from the sources, the plumes observed in 2005 and 2007 are classified as *bottom-advected*, while those observed in 2004 and 2006 fall into the category of *intermediate.* The intermediate plumes are predominantly vertically stratified, yet with a small degree of homogeneity near the river mouth. The bottom-advected plumes exhibit a higher tendency for homogeneity throughout its cross-shore extension, in spite of fact that the density front is located further offshore at the surface compared with the bottom layers. All available observations indicated that the base of the plume is located 15 to 30 km from the shoreline, in the region immediately seaward from the centre of the delta (transect D in the images of vertical structure). This distance is considerably greater in the southern region (transect B), and highly variable in the northern region, where in some occasions the plume becomes limited to a thin surface layer (i.e., a base connected to the bottom is absent).

The above mentioned plume classification based on the plume vertical structure, gives a rough idea of the balance between the forces promoting the stratification due to freshwater discharge, and the tendency for homogeneity due to mixing. By inspecting the discharge during the sampling period, one finds that the *intermediate* plumes observed in 2004 and 2006 are connected with a river discharge $\leq 2000\,\mathrm{m^3 s^{-1}}$, while *bottom-advected* plumes occurred under a larger discharge. The plumes observed in 1978 (IMR, 1978a,b), were classified according to their vertical structure as surface-advected in January, and bottom-advected in May of that year. The daily discharge was low during the plume observation in January ($2700 \sim 4000\,\mathrm{m^3 s^{-1}}$), reached its peak in late March ($18500\,\mathrm{m^3 s^{-1}}$), and during the field campaign in the beginning of May it was still elevated ($8800 \sim 9100\,\mathrm{m^3 s^{-1}}$). The patterns of plumes observed in 1978, a time when the river discharges were considerably higher compared to today's rates, suggests that the freshwater accumulated prior to plume observation had a strong impact on the plume dispersion during proceeding days.

In general, the horizontal distribution of temperature offers no clear distinction between the Zambezi River influenced waters and the surroundings, in contrast

with the vertical distribution. In this case, the bending in the temperature contours suggests an upward movement of ambient waters near the base of the plume, or at the plume offshore boundary, a feature present in most of the observations. This type of vertical motion is presumably driven by topographical effects induced by either an alongshore current (Lill, 1979), or a landward current running up-shelf (Lu et al., 2006). This tendency for upward movement was notably greater during relatively moderate discharges (data from 2004, 2005, and 2006), suggestive of a reduced seaward advection of freshwater induced by river-inertia.

Freshwater discharges from the Pungoe (located near the city of Beira) and Licungo (located north of Quelimane) Rivers constitute an important contribution for the overall buoyancy forcing along the coast. A vast majority of the data presented in this chapter displayed a seaward bending of salinity contours in the vicinity of the Licungo River, which is an indication of a clear distinction between the Zambezi and the Licungo River plumes, in agreement with observations of Siddorn et al. (2001). The data presented in this study further suggests that the Licungo plumes will limit the equatorward spreading of the Zambezi plumes during periods of low Zambezi discharges, and it will generate a protuberance along the course of the plume waters during periods of high discharge. On the other hand, no clear distinction was found between the Zambezi and Pungoe plumes, as they merge seamlessly in the shallows of the bank.

In summary, the analysis in this chapter allowed for the general classification of the structure of the Zambezi River plume. It was shown that the plume is part of a small group of real plume systems that are known to penetrate large distances upstream (opposing the sense of a Kelvin wave), when the expected spreading (according to the theory of buoyancy-driven flows with freshwater being the main source of buoyancy), should occur primarily in the downstream direction. The analysis in the following chapters will attempt to find plausible explanations for this spreading pattern through numerical simulations of the plume. The strategy consists of simulating a plume in the absence of external forcings, and then add the forcing successively in to order to determine their relative influence on the plume structure. To that extent, the general configuration of the model is presented next.

Chapter 3

Model description and configuration

The Regional Ocean Model System (ROMS) is a three-dimensional, free-surface, terrain-following model widely used by the scientific community. It makes use of high-order numerical schemes, and the conservative and constancy preserving barotropic/baroclinic coupling to generate accurate solutions, while keeping the computational costs as reasonable as possible for today's standards (Shchepetkin and McWilliams, 2005). The model solves the momentum and transport equations discretized in a three-dimensional frame. The model equations are expressed according to the well-documented Boussinesq approximation. While a third-order upstream biased advection-diffusion scheme is used for the momentum equations, the transport of tracers (i.e., salinity and temperature) is implemented using a fourth-order centered scheme.

ROMS have showed to perform fairly well in the simulation of river plumes either in idealized cases (Hetland, 2005), or in realistic cases (Li et al., 2005). Based on that, two simulations of the Zambezi River plumes were performed, one using an idealized configuration and the other using a realistic configuration. Due to the large number of similar features in the two configurations, the idealized configuration is presented first, and the alterations made in the realistic configuration will be presented later in Chapter 5.

Figure 3.1 illustrates a part of the lower Zambezi River and the coastal area surrounding the river mouth, which is the archetype used for the idealized model configuration. Also shown is the bathymetry in the Sofala Bank region. The larger outlets of the river are displayed in the inset map of the delta, which indicates clearly that the distance between the southernmost and northernmost points of the delta is slightly larger than half a degree of latitude. Amongst others, the coastline in the idealized configuration is assumed to be a straight line parallel to the meridians, with a hypothetical estuary located at 18.83 °S, and the coastal bathymetry is assumed to have a constant slope.

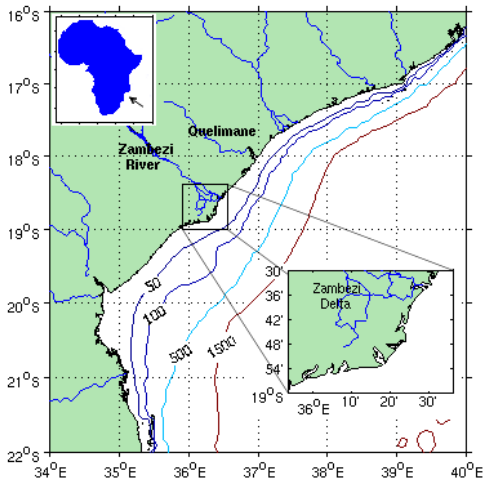

Figure 3.1: Study site. Bathymetry contours of 50 m, 100 m, 500 m, and 1500 m are plotted. The subset area shows the various mouths of the Zambezi River.

3.1 Model domain and grid

The model domain is made of a river attached to a coastal ocean (Figure 3.2). A constant depth of 10 m is assumed for the river member, which is 40 km long and about 3 km wide. The chosen length of the river is nearly half the maximum distance of tidal influence, and therefore believed believed to be sufficient to allow the gravitational adjustment between the fresh and salty waters to occur before the river flow reaches the coastline, ensuring that the freshwater enters the sea through a correct number of vertical gridpoints. The river occupies 5 gridpoints in the y-direction, and its mouth is located at the origin of the horizontal grid, i.e. (x,y) = (0 km,0 km).

The coastal ocean has a western wall 10 m deep, and the topography decreases from this wall to the eastern boundary with a constant slope $\alpha = 1/1800$. This slope is very close to the realistic one, particularly in the region between the coastline and the 70 m isobath near the river mouth, and it results in a maximum water depth of about 100 m along the eastern boundary. The ocean is 210 km × 660 km with the estuary centre-line located 160 km from the southern boundary.

There are 140 × 260 horizontal gridpoints with the resolution focused near the river mouth (Figure 3.2), where the grid size is less than a kilometer. The grid is orthogonal (maximum orthogonality error = 2.5), and is projected into an f-plane

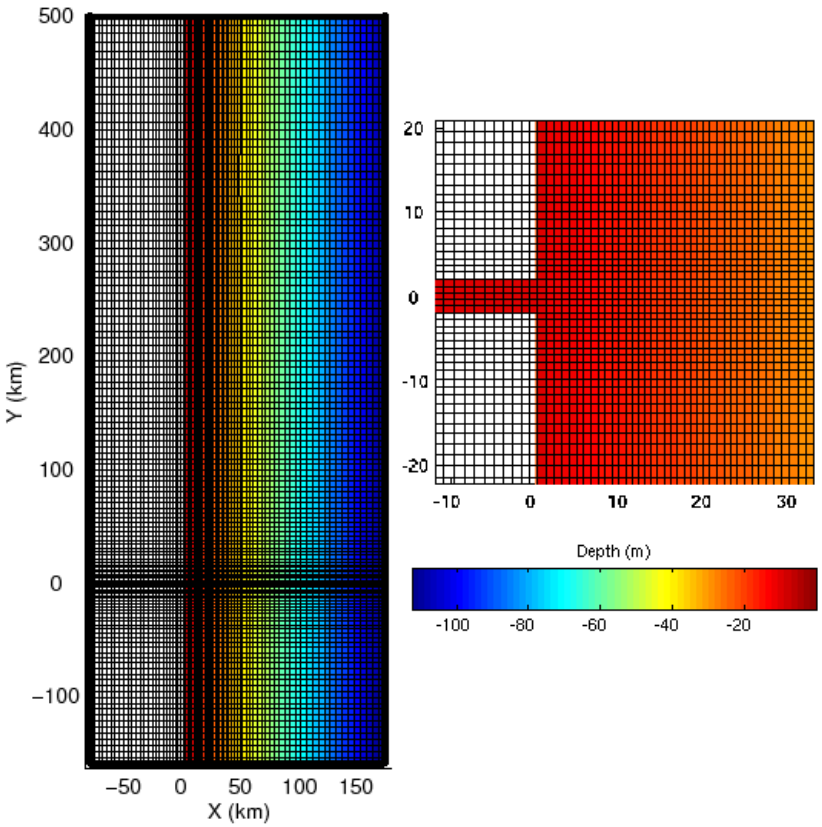

Figure 3.2: Model domain consisting of a river/estuary ~ 3 km wide and 40 km long. Depth in the ocean varies from 10 m at the coastal wall to about 90 m at the eastern boundary. The grid is focused near the river mouth, resulting in grid resolution of about 620 m near the river mouth and about 3.5 km at the eastern boundary. A detail of the region near the river mouth is displayed on right side.

($f = 2\Omega sin\phi$, $\phi = -18.83^o$), with ϕ set constant over the entire domain and equal the latitude of the Zambezi River mouth. The implementation of this grid follows the analysis of Hetland (2005), which points that simulations using poorer resolution or low-order advection scheme often result in a spurious freshwater source at the surface, in some cases reaching 10% of the real (specified) source. The resolution in that study varied between $0.5 \sim 3.0$ km.

Twenty sigma-layers are used in the vertical (Figure 3.3), with the resolution focused near the surface. The sigma-coordinate control parameters are as follows: $\theta_s = 5.0$ for the free-surface, $\theta_b = 0.1$ for the ocean bottom, and $h_c = 10$ m for the vertical dimension. These parameters result in a vertical grid that is uniform within the river member, and it has a resolution of about a meter in the upper 5 m of the water column, over the coastal ocean.

All four horizontal boundaries are set open, as to allow tides to propagate through the eastern boundary, as well as to allow freshwater to be introduced through the western boundary. It is worth mentioning that in experiments with river discharge

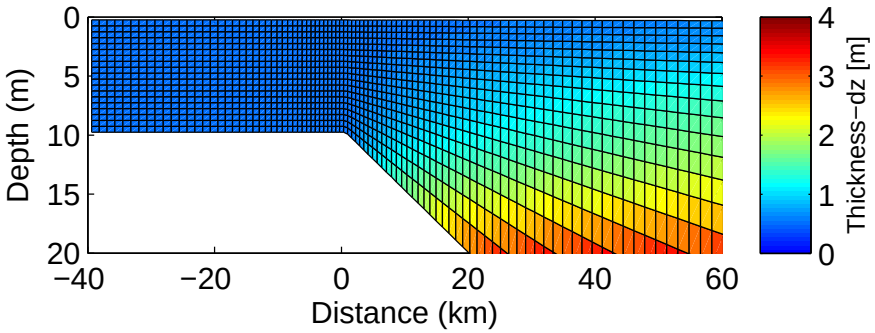

Figure 3.3: Vertical grid consisting of 20 sigma layers focused at the surface. Depth varies from 10m within the river member to 110m at the eastern boundary. Only the upper 20 meters are showed, to a distance of 60 km from the coastline.

specified as point sources (not presented here), the western boundary were closed while others remain opened. The physical conditions specified at each boundary are presented in Section 3.3.

3.2 Initial conditions and external forcing

At the beginning of each simulation it is assumed no motion as well as no vertical displacement of the water surface. Temperature is uniformly distributed over the model domain, and it is kept constant (29 °C) throughout the simulation. This way, only the variations in potential density due to changes in salinity are considered and analyzed. The initial distribution of salinity (Figure 3.4) is such that within the river member it varies gradually from the value prescribed for the river head (typically 20.5 psu) to 35.5 psu at the river mouth. This choice of a non-zero initial salinity in the upstream end of the river implies a diminished time for the estuarine (geostrophic) adjustment, and it can be argued by the need to simulate an estuarine

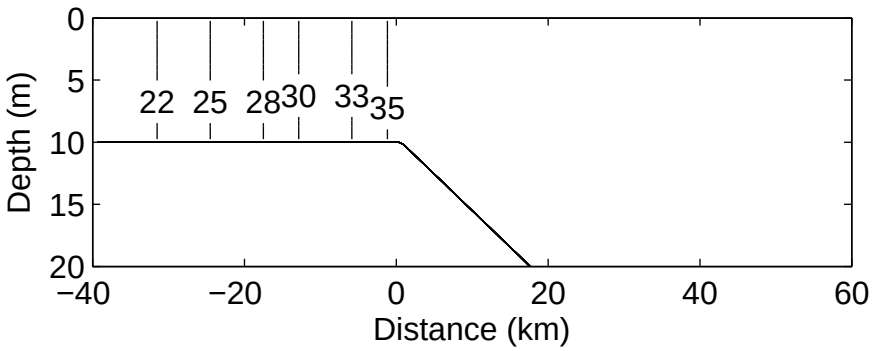

Figure 3.4: A transect along the river member illustrating the initial distribution of salinity in the upper 20 m.

plume rather than a river plume. It has been noted in parallel experiments (results not discussed here) that using an 80-km long river member and/or zero-salinity at the upstream river head the model produced plumes with spurious distributions of salinity (i.e., values as low as 15 psu in the region immediately offshore from the mouth).

For the remaining part of the model domain, the initial salinity was set uniform ($S = 35.5$ psu), and with no vertical gradients.

Buoyancy forcing

The buoyancy forcing in the idealized simulations is associated to the input of freshwater from a river member, and the freshwater is introduced as a boundary condition by specifying a lateral flux of momentum and tracers at the western boundary. The river contribution to momentum is specified as a steady depth-averaged flow that is allowed to change with the local surface elevation according to:

$$\overline{U}_{river} = \frac{Q_{river}}{L\left(\overline{H} + \eta_{west}\right)}, \tag{3.1}$$

where $\overline{U}$ is the velocity function per unit width, $\overline{H}$ is the average depth at the boundary (set to 10 m), η_{west} is the model surface elevation at the western boundary, L is the width of river, and Q_{river} is the volumetric transport of freshwater by the river, here taken as constant throughout the simulation (yet varying between 1000 through 8000 m^3s^{-1} in different simulations). The river transport is ramped through a hyperbolic tangent function (Figure 3.5), over the first inertial period (i.e. 1.55 days) to avoid high frequency oscillations excited by a sudden turning of the forcing. Apparently, a criteria to choose the period over which the forcing is ramped in river plume simulations is yet inexistent, and reported values chosen randomly lie in the range of a few hours to a few days. In addition, the river contributes to the transport of tracers as water of lower potential density is introduced at the boundary, and this transport is accomplished in the model by prescribing constant values of tracers (temperature and salinity) at the western boundary.

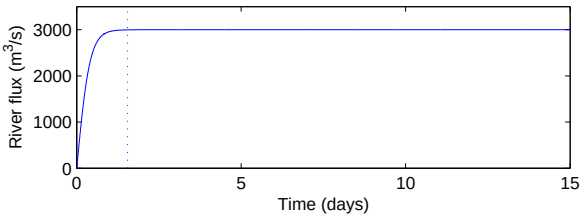

Figure 3.5: River discharge ramped over the fist inertial period. The dotted vertical line depicts the inertial period in the time axis.

Surface and bottom flux of momentum

The model is forced with spatially uniform winds of varying intensity and direction, which in general are spun-up over the first inertial period and then sustained until the end of simulation (Figure 3.6). In one set of model runs, the sustained winds were kept constant throughout the simulation, which implies the assumption that only the effects of daily mean winds are accounted. In a second set, a diurnal component was added to the mean wind field in order to consider the effects of both the daily mean wind and the sea-breeze on the plume dynamics.

The kinematic surface flux of momentum was expressed in terms of the wind-stress, parametrized through the quadratic friction law (Equation 3.2),

$$(\tau_x\,,\,\tau_y) = \rho_{air} C_d \left(\sqrt{u^2+v^2}\right)(u\,,\,v)\,, \tag{3.2}$$

where τ_x and τ_y are the $x-$ and $y-$ stress components, ρ_{air} is the air density here taken as $\rho_{air} = 1.2\,\mathrm{kgm}^{-3}$. u_s and v_s are the wind velocity components at the surface level, and C_d is the drag coefficient here taken as constant $C_d = 0.0013$. In this configuration, all these parameters were set uniform over the entire model domain.

Our parametrization of sea-breeze follows the analysis of Hyder et al. (2002), who suggested that the windstress can be represented by the sum of a two components, i.e., a daily mean, τ_0, and an oscillating part having amplitude τ_1, and phase

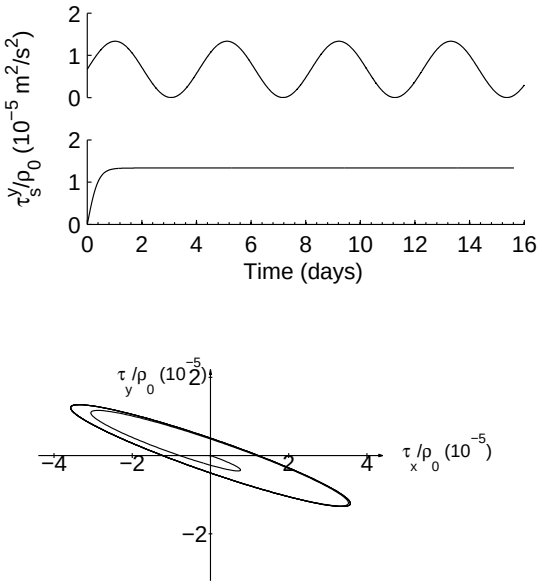

Figure 3.6: Windstress calculated for southeasterly winds of intensity 5 m/s. From top to bottom: 4-day period oscillating winds, constant winds, 24-hour period oscillating winds.

difference ϕ_τ, as follows,

$$\begin{cases} \tau_x = & \tau_{0x} + \tau_{1x}\cos(\omega t + \phi_{\tau_x}) \\ \tau_y = & \tau_{0y} + \tau_{1y}\cos(\omega t + \phi_{\tau_y}) \end{cases} . \tag{3.3}$$

The daily mean stress components τ_{0x} and τ_{0y} can be calculated by averaging low frequency wind data over a relatively long period, and the amplitude and phase of the sea-breeze component can be derived from a regression analysis of high frequency wind data. The periodic components in Eq. (3.3) result in a vector whose orientation throughout the 24-h cycle describes an ellipse, and therefore, it is possible to choose the ellipse phases (ϕ_{τ_x} and ϕ_{τ_y}) so that the orientation of the major axis matches the observed predominant wind direction.

The flux of momentum at the bottom is expressed in terms of the quadratic friction law (Eq. 3.2), substituting the air density, ρ_{air}, by the Boussinesq approximation mean density of seawater, ρ_o (taken as $\rho_o = 1025\,\mathrm{kgm}^{-3}$), and the wind velocity components by the model velocity components at the bottom gridpoint. The drag coefficient used for bottom stress follow the logarithmic formulation and is given by

$$C_d = k^2 \left(\ln \frac{z_b}{z_0} \right)^{-2} , \tag{3.4}$$

where k is the vonKarman's constant, z_b is the distance from the seafloor to the bottom u or v grid point, and z_0 is the bottom roughness specified as 1 cm. This formulation combined with the resolution scheme applied to the sigma-layer vertical grid results in a constant bottom stresses along the river member, and a variable stress in the adjacent coastal ocean. A minimum bottom drag coefficient ($C_{d,min} = 0.0010$) is applied to prevent the law-of-the-wall to extend indefinitely, and the maximum allowed drag coefficient was arbitrarily set to $C_{d,max} = 0.0045$.

3.3 Boundary conditions

Boundary conditions (BC's) imposed at the free surface include a constant flux of momentum (windstress) and no flux of heat and salt. Also, no flux of heat and salt is allowed at the bottom, and the model uses a logarithmic profile at the lowest gridpoint and a specified roughness height, z_0, to compute the typical stress boundary condition (Eq. 3.2).

As stated before, all horizontal boundaries are set open, however, only the eastern and western boundaries are active. The horizontal boundary condition for the free surface is set to zero-gradient ($\eta_{b\pm1} = \eta_b$) in the active as well as in the passive

boundaries, meaning that the surface displacement is not altered at the boundaries.

The surface gravity waves in the model are computed based on the normal barotropic velocity at the boundaries (Marchesiello et al., 2001), and their propagation into the domain occurs seamlessly under the Flather boundary conditions. These boundary conditions are an extension to the radiation BC's, and therefore all quantities are allowed to propagate in/out with the minimum interaction with the boundary (i.e., non-reflexive condition). The general form of this condition is given by Eq. (3.5), and it can be derived by considering the propagation of the free-surface at a speed given by the long wave phase speed, $c = \sqrt{gH}$, (where g is the gravitational acceleration and H is the local water depth), and a one-dimensional approximation of the continuity equation applied to the outwardly normal direction at an open boundary (Marchesiello et al., 2001; Carter and Merrifield, 2007). This gives,

$$\overline{v}_{n,b} = \overline{v}_n^{ext} \pm \sqrt{\frac{g}{H}} \left(\eta_{b\pm1} - \eta^{ext}\right), \tag{3.5}$$

where the $\overline{v}_n$ is the barotropic normal component of the velocity, the subscript b denotes a boundary point, and $\overline{v}^{ext}$ and η^{ext} are the externally prescribed velocity and surface elevation. The positive sign applies to the north and east boundaries, and negative for south and west. The term in parenthesis indicates that the propagation of any difference between the model prediction and external data is always outward.

In this idealized model configuration, the passive boundaries use the traditional Orlanski radiation conditions for all fields, while the active boundaries use the Flather BC's for the normal and Chapman conditions for the tangential component of the barotropic velocity. Furthermore, the external barotropic velocity, $\overline{v}^{ext}$, which could represent the ambient current, was set null everywhere except at the west boundary where it matches the velocity imposed by the river discharge (i.e., the velocity calculated by Eq. 3.1).

The BC's for the baroclinic velocity components and tracers are set to Orlanski everywhere, except at the western boundary where the tracer BC's are set to *upwind*. The upwind open boundary conditions combine the clamped conditions (i.e. prescription of external values) applied when a water particle is entering the domain, with the Orlanski conditions applied when the particle is leaving the domain. This condition is accomplished in the model by applying changes to the tracer field depending on the sign of the normal component of the baroclinic velocity at the boundary .

This implementation of boundary conditions are summarized in Table 3.1, and it performed well in two important tests, as follows. It resulted in a barotropic flow that was nearly uniform in the alongshore direction in experiments with both the river discharge and the windstress turned off (results not shown). And, it also

Table 3.1: Implementation of the open boundary conditions.

Variables	Passive regime	Active regime
u, v, η	Orlanski	Orlanski
T, S	Orlanski	upwind
$\overline{u}$, $\overline{v}$ - Tangential	Orlanski	Orlanski
$\overline{u}$, $\overline{v}$ - Normal	Orlanski	Flather

resulted in longshore density-driven currents that could flow smoothly across the downstream boundary.

3.4 Lateral and vertical mixing

The lateral mixing of both momentum and tracers is performed using the Laplacian Smagorinsky diffusion formula

$$A = C_a \cdot \Delta x \Delta y \left[\left(\frac{du}{dx} \right)^2 + \left(\frac{dv}{dy} \right)^2 + \frac{1}{2} \left(\frac{du}{dy} + \frac{dv}{dx} \right)^2 \right]^{\frac{1}{2}}, \tag{3.6}$$

applied on the iso-sigma levels. The constant was taken equal to $C_a = 0.1$, and the background horizontal viscosity and diffusivity coefficients were both set to $50\,\mathrm{m^2 s^{-1}}$. Values of the latter coefficients used in other modeling studies were in general much smaller, however they resulted in numerical instabilities and model crash due to infinitely large/small mechanical energy, when used with the current model configuration.

Vertical mixing is achieved through the K-Profile Parametrization (KPP), which was first proposed by Large et al. (1994) and later amended and made suitable for shallow water systems by Durski et al. (2004). The KPP mixing formulation works in a way to match separate parametrizations to the surface layer, the ocean interior, and since recently also the bottom layer. At the surface layer, the viscosities and diffusivities are determined as functions of the product of a length scale (from boundary layer similarity theory), a turbulent velocity scale, and a shape function (Durski et al., 2004). At the ocean interior, mixing through this scheme accounts for the effects of shear mixing and internal wave-generated mixing, and is achieved through the gradient Richardson number formulation (Large et al., 1994; their equation 28). At the bottom layer, the mixing formulation is similar to that applied at the surface, with small but important amendments. For instance, the bottom boundary layer depth is determined using the bulk Richardson number rather than the gradient one,

as the latter would predict high levels of mixing near the bottom, resulting from the strong velocity shear.

The performance of the KPP scheme has been evaluated in Durski et al. (2004) for three different model setups (including a two-dimensional coastal upwelling), and it was compared with other mixing schemes in Li et al. (2001), and Li et al. (2005). The results point to a great job done by KPP, although not very different from the other available schemes (i.e., second-order turbulence models including the classic formulation of Mellor-Yamada).

Summary

In this Chapter, the general configuration of the model that will be used for the analysis in the following chapters was presented. A discussion of the implementation of external forcings, initial conditions, and BC was given. The description of the experiments and the approach used in the analysis of an hypothetical plume is presented in Chapter 4, along with mode results.

Chapter 4

Plume structure in a uniformly sloping shelf

To illustrate the basic structure of a river plume fed by a moderate discharge, this chapter presents the analysis of buoyancy-driven and wind-driven flows in a highly-idealized model configuration. It is aimed in particular at addressing the following questions:

- What is the typical plume thickness, as well as the typical cross-shore and longshore extents that a moderate-discharge plume would reach in the absence of complicating factors?
- What is the structure of the circulation and how much freshwater is transported by this simplified plume? And,
- What distinct physical processes may account for the creation of the simplified plume structure?

The analysis is divided in two parts. Section 4.1 deals purely with an unforced plume, or in other words the coastal circulation driven solely by the freshwater buoyancy input. The plume evolution is presented in time-series of offshore and alongshore penetration of brackish water, together with snapshots of the circulation in front of the river mouth. These results showed clearly that the plume does not reach a steady state in the 100 days of simulation, yet the $1000\,\mathrm{m^3 s^{-1}}$ freshwater discharge generated a plume confined to a surface layer not deeper than 4 m, with a downstream and offshore penetration of about 300 km and 75 km, respectively.

The second part of the chapter deals with plume response to moderate winds, and is presented in Section 4.2. The plume structure is displayed in horizontal maps of surface salinity anomaly, as well as vertical profiles of salinity and velocity. These

results indicated that in response to the impulsive westward or northwestward wind, significant portions of the plume turn poleward and form a pool of brackish water in the upstream direction.

4.1 The standard case

The standard case comprises a mean buoyancy source emptying into a coastal ocean under no influence of either tides or winds. Table 4.1 summarizes the set of parameters used in the standard case simulation. The bottom slope was chosen to roughly mimic the slope immediately offshore from the Zambezi mouth observed in CTD field campaigns as well as the slope retrieved from the ETOPO2 global dataset. The prognostic variables are the free surface elevation, η; barotropic horizontal velocity components $(\overline{u}, \overline{v})$; baroclinic horizontal velocity components (u, v); and tracers, which throughout this report will always refer to temperature and salinity.

The model was run for 100 days, and the buoyancy-induced flow did not reach the northern boundary of the domain during this period, as can be seen in the variation of the plume width and length, presented in Figure 4.1. These plume dimensions along with the different regions of the plume are analyzed in terms of the salinity anomaly, s, defined according to Garvine (1999) as,

$$s = \frac{S_a - S}{S_a - S_m} \tag{4.1}$$

where S_a is the reference (shelf) salinity initially set uniform ($S_a = 35.5\,\text{psu}$), S is the model computed salinity, and S_m is the surface salinity at the river mouth. Although the latter varies in time and space, a constant value is taken from the average salinity of the gridpoints defining the river mouth (five in total). For practical purposes, the isopleth $s = 0.1$ at the surface will be defined as the effective boundary of the plume.

Most of the isopleths in Figure 4.1 show a much more accentuated variation in the first 20 days, what characterizes the rapid development of the plume, and is followed by the geostrophic adjustment shortly after that. Between days 15 and

Table 4.1: Standard case parameters

Parameter	Name	Value
f	Coriolis parameter	$-4.695 \times 10^{-5}\,\text{s}^{-1}$
α	Shelf bottom slope	5.56×10^{-4}
q_{river}	Clamped volumetric transport of river	$1000\,\text{m}^3\text{s}^{-1}$
W_{10}	Wind speed and direction	$0\,\text{m/s}$
T_a, S_a	Ambient temperature and salinity	$29\,^\circ\text{C}$, $35.5\,\text{psu}$
T_0, S_0	Temperature and salinity upriver	$29\,^\circ\text{C}$, $20.5\,\text{psu}$

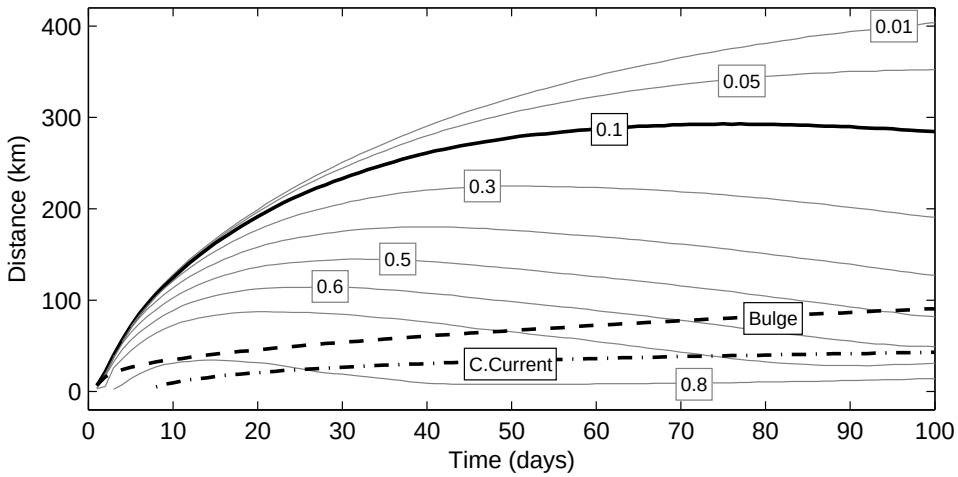

Figure 4.1: Time variation of salinity anomaly showing the plume's advance. Solid lines indicate the advance of coastal current in the alongshore direction, and the dot-dashed line shows the evolution of its width at $y = 100\,\text{km}$. The seaward advance of the bulge is indicated by the dashed line. The distances were calculated from the river mouth (coastal wall) in the case of alongshore (offshore) advance.

30, the leading nose of the plume, as indicated by the isopleth $s = 0.1$, undergoes a rapid reduction in speed that can be attributed to the adjustment. Also, as a consequence of the adjustment, the position of higher salinity anomaly contours (i.e., fresher water masses, $s > 0.1$) ceases the motion towards the positive-y values (northern model boundary), and even retreats towards the river mouth.

However, it should be noted that the non advance of salinity contours in Figure 4.1 does not imply a negative alongshore velocity component, since the velocity of brackish water in the downstream coast is always positive, as indicated by the arrows in Figures 4.2 and 4.3. The alongshore advance of the leading nose of the plume continues until day 70, when the position of salinity contours in the entire plume are retreating towards the southern model boundary. In fact, the inner salinity contours start retreating between days 11-15 (i.e., contours $s = 0.7$, $s = 0.8$), and only few days later the others follow. Outside the plume region ($s < 0.1$), no retraction is evident throughout the simulation, what reveals a certain ambiguity in the choice of a particular salinity anomaly as the plume limit. Therefore, it is speculated here that the maximum distance in selected contours of salinity anomaly in Figure 4.1 is related either with the lateral mixing within the plume that tends to decrease in time as the salinity gradient weakens, or with the circular motion within the bulge that forces freshwater particles to move southwards near the coast. Notice that the bulge grows offshore monotonically from around day 10 to the end of simulation, and the coastal current nearly stabilizes from $t = 40\,\text{days}$ when its width ceases to increase seawards. However, this analysis indicates that, by the time $t = 50\,\text{days}$,

the state of the simulated plume is considered to be fully-developed. Therefore, the forthcoming results correspond to 50 days from the beginning of simulation, unless otherwise stated.

Figure 4.2 presents the surface views of the salinity and velocity fields for the unforced plume at the time $t = 50$ days. The area encompassed by the coastline and the plume limit ($s = 0.1$) depicts a plume system composed by a large bulge and a coastal current, whose width decreases gradually towards the northern model boundary. Note that the contour of velocity 2 cm/s penetrates further North than the contour of salinity anomaly $s = 0.05$. The flow within the bulge is circular and anticyclonic, with the inner water particles describing a full circle before being exported to the coastal current, which has a nearly unidirectional flow oriented northwards.

The volumetric river discharge of $1000\,\mathrm{m^3 s^{-1}}$ used in this simulation produces a freshwater transport by the river of $Q_{fr} = 992.6\,\mathrm{m^3\,s^{-1}}$on day 50, as estimated using the Eq. 4.2, applied to a cross-sectional area of the river located immediately upriver from the coastline ($x = 0$ km). Here, the volumetric river discharge differs slightly from the freshwater transport of the river at all times because the salinity

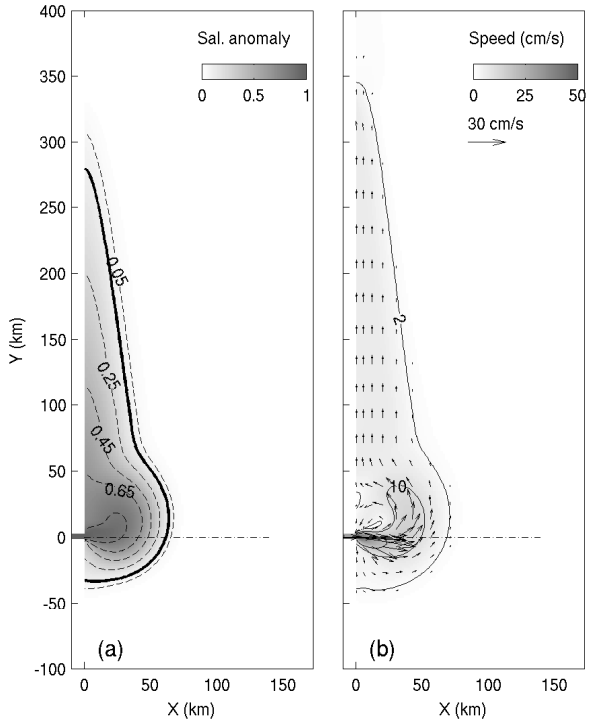

Figure 4.2: (a) Horizontal distribution of surface salinity anomaly, s, with darker (lighter) areas representing fresher (saltier) waters. The anomaly contours are plotted at 0.2 interval (dashed lines), and the plume boundary ($s = 0.1$) is represented by the thick solid line. (b) Map view of the surface velocity simulated for time $t = 50$ days. Plotted are the contours for 2 and 10 m/s.

at the river mouth is never equal to zero.

$$Q_{\mathrm{fr}} = \int u \left(\frac{S_a - S}{S_a} \right) d\mathrm{A} \tag{4.2}$$

Here, the expression in parentheses represent the fraction of freshwater, and A is the area normal to the flow at the river mouth. The water released at the river-head barely mixes with the saltier water within the estuary, and so, the distribution of salinity within the river is uniform at all times except at the early stages when the initial salt gradient exists (results not shown).

Previous studies of Pichevin and Nof (1997), and Nof (2005) have shown that the circulation of an unforced river plume never reaches an equilibrium state in either a f-plane or $\beta-$plane (Nof and Pichevin, 2001), because of the impossibility of balancing the alongshore momentum flux. These authors have considered that an inviscid outflow that turns left (in the Southern Hemisphere) due to effects Earth rotation, and proceeds as an unsteady coastal current cannot exist, since the downstream momentum flux do not find any opposing forces to balance it (see Figure 1 of Nof, 2005). Different approaches were offered as possible means of solving the imbalance, and that include the shedding of eddies that eventually migrate upstream (Nof, 2005), and the continuous growth of the bulge region (Nof and Pichevin, 2001). As a consequence of the imbalance, numerical simulations of buoyant plumes often produce a relatively weak alongshore current and a re-circulating bulge that grows continually Garvine (1999); Fong and Geyer (2002); Cheng and Casulli (2004); Isobe (2005); and Hetland and Signell (2005). Such is the case of the plumes simulated in the current standard case, which attain a structure similar to the one described above in less than 10 days of model time, and are discussed further below.

4.1.1 The bulge circulation

The bulge in the present study consists of an anticlockwise gyre that grows in size continuously, generated around days 3 and 5, the centre of which migrates primarily seawards, as depicted in Figure 4.3. This way, the centre of rotation changes from nearly-connected to detached from the coast. The offshore growth of the bulge is often referred to as "ballooning", and has been suggested to be the immediate consequence of the momentum imbalance in the alongshore direction (Pichevin and Nof, 1997; Nof and Pichevin, 2001; Isobe, 2005). This form of bulge growth has been observed in laboratory experiments of unforced river plumes by Avicola and Huq (2003) and Horner-Devine et al. (2006), although evidences based on *in-situ* observations have not been reported to date. However, there is plenty

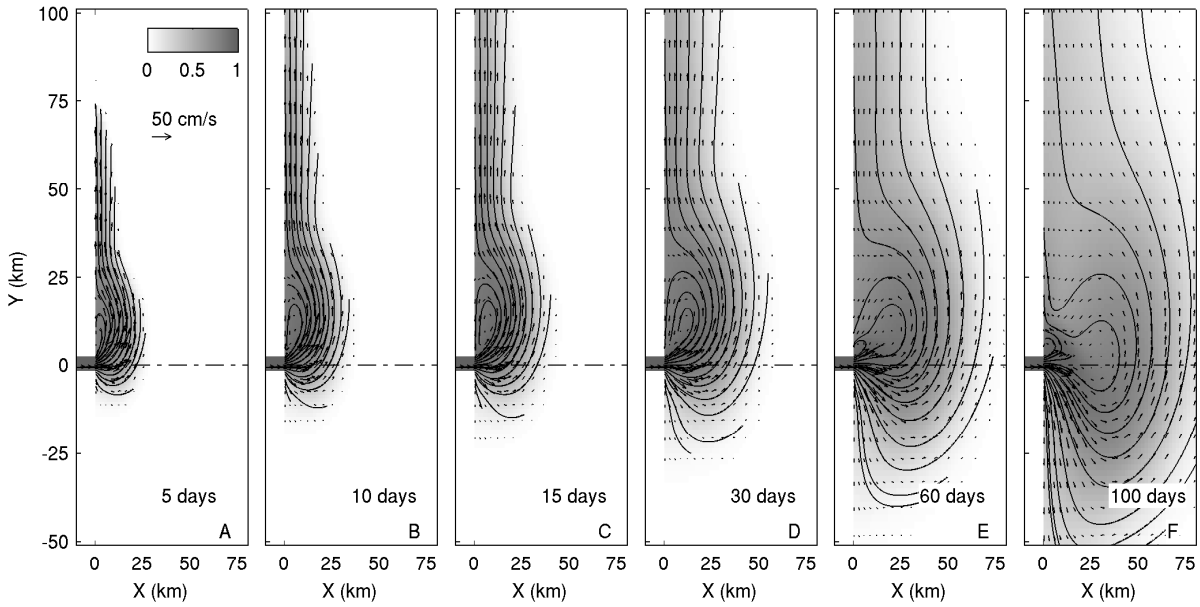

Figure 4.3: Snapshots of bulge migration. The shaded colors indicate salinity anomaly, which are overlaid by streamlines leaving the river mouth.

of recent observational evidence of the existence of bulges in real plume systems (Chant et al., 2008; Horner-Devine, 2009; Hickey et al., 2010; Warrick and Stevens, 2011), and yet no records of the plume growing process have been reported, most likely due to the fact that wind events introduce disruptions in the measurement of plume growth.

On the other hand, the imbalance of momentum flux in the alongshore direction in unforced plumes also results in the generation of an upstream flow, opposing the direction of a Kelvin wave (Pichevin and Nof, 1997), that is generally weaker than the downstream counterpart. It has also been noted that a valid and possible alternative for the imbalance problem could be the generation of anticyclonic eddies (instead of a steady current), followed by their propagation upstream due to the β effect.

A close inspection of the plume evolution (Figure 4.3) reveals that after the generation of the circular motion withing the bulge, the centre of rotation moves in the alongshore direction, initially towards the northern boundary, and after the buoyancy-driven flow crosses the northern model boundary the centre of rotation moves towards the southern boundary. Thus, it is very likely that the upstream migration of the bulge is a product of some inconsistency in the boundary conditions, even though the current did not reflect at the boundary.

The structure of the bulge circulation at $t = 50$ days is displayed in Figure 4.4. The across-shelf and alongshore velocity components of the top-layer, estimated at some random locations near the bulge's centre, exhibit a quasi-linear trend in the vicinity of the centre, confirming the existence of a core region of constant

vorticity. The maximum velocity occurs at the edge of the core region, from where it decreases to nearly zero at the centre of the bulge's anticyclonic gyre, as well as towards the plume outer border ($s = 0.1$), where the average speed is about $3.5\,\mathrm{cms}^{-1}$. This horizontal velocity structure is similar for the layers underneath the surface, although with small differences in the velocity magnitude and diameter of the core region. This feature is more evident in Figure 4.5, which presents the vertical structure of the flow along a transect parallel to the coast (landward view). In general, the current speed decreases with the depth, and it appears that the position of the centre of rotation in the surface layers containing brackish water tilts towards the negative y-direction. Shown in Figure 4.5 is the cross-shore component of velocity, which displays a vertical structure that mimics that of the alongshore component (results not shown), except for the relatively higher velocities.

If re-circulating bulges can be found in nature, then the core region of constant vorticity is likely to be an interesting feature in these plumes. In Figure 4.6 this region is surrounded by the contour of zero relative vorticity, and is marked by a weak gradient of relative vorticity, and a rather strong gradient of potential vorticity. Following the analysis of Horner-Devine (2009), the radius of the core region was estimated by finding the distance between the gyre's centre and the edge of the core (point of maximum velocity between the centre and the plume's outer border). For the model time $t = 50\,\mathrm{days}$, the data in Figure 4.4 was used to determine the position of the gyre's centre at the surface layer as the point where the velocity components along a randomly selected transect change their orientation, and it resulted in $(x, y) = (19.1, 12.7)$ in kilometers. Using a similar approach for the edge

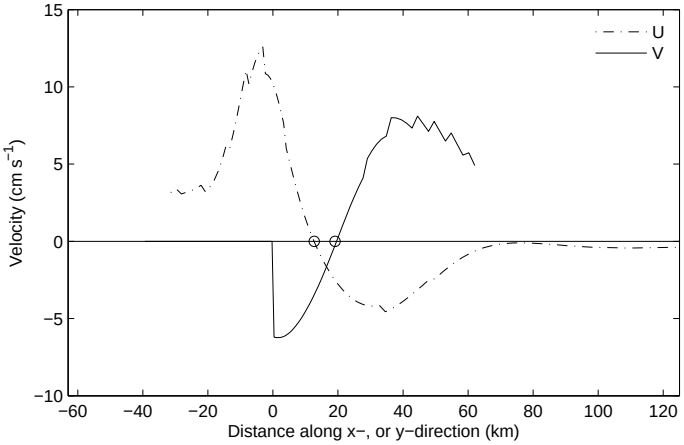

Figure 4.4: Determination of bulge dimensions. Diagrams of a cross-shore (dotted line) and alongshore (solid line) surface velocity as functions of the distance $[u(x = const, y)$ and $v(x, y = const)]$, in the vicinity of bulge centre. The location of the bulge's centre of rotation is marked with circles ($x = 19.1\,\mathrm{km}$, $y = 12.7\,\mathrm{km}$).

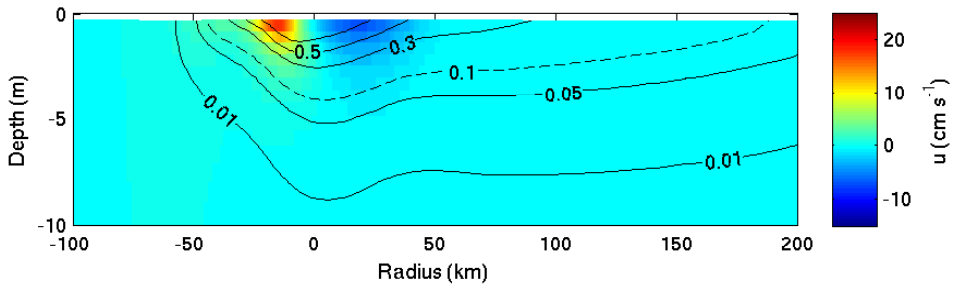

Figure 4.5: Numerical cross-sectional structure of the circulation at the bulge at $t = 50$ days. Colors represent the cross-shore velocity component, $u\,(\mathrm{cms}^{-1})$, at an alongshore transect crossing the centre of the gyre (radius =0). Contours shows the salinity anomaly within the re-circulating gyre. Actual plume thickness is indicated by the dashed line.

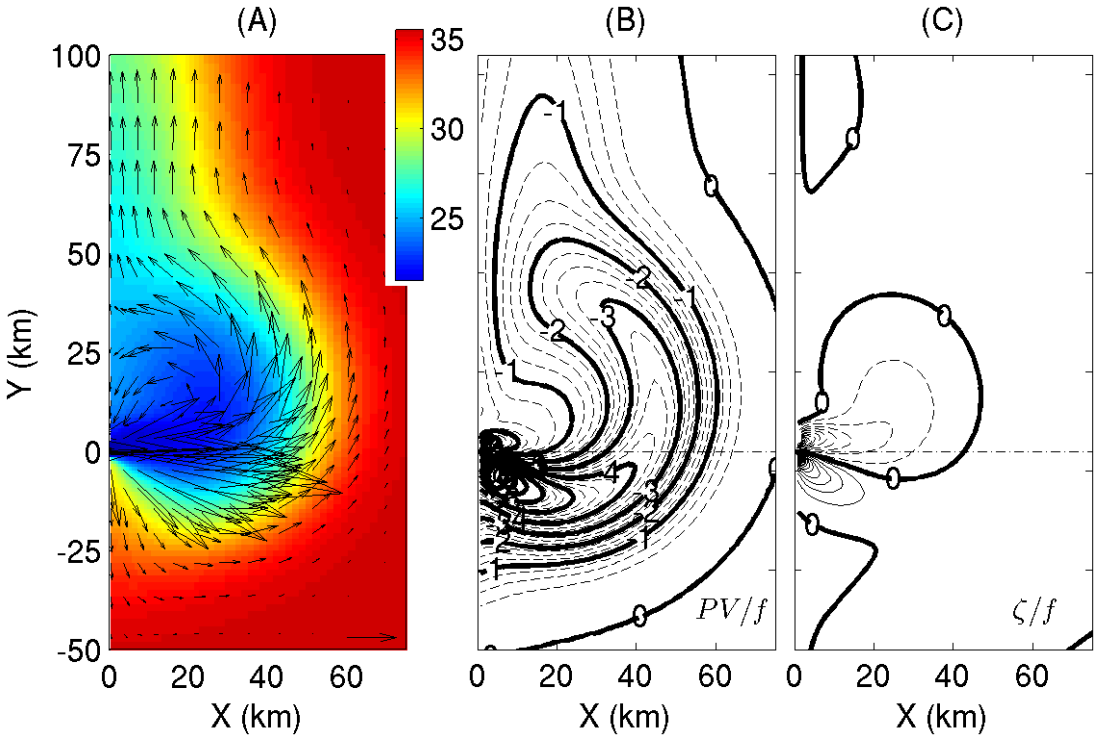

Figure 4.6: Horizontal distributions of properties at day 50. (A) Surface salinity (colours) and velocity vectors (the horizontal vector at the bottom right corresponds to 10 cm/s). (B) Surface (Ertel's) potential vorticity scaled by the planetary vorticity (contours are separated by $0.25 \times 10^{-3}\,\mathrm{m}^{-1}\mathrm{s}^{-2}$). (C) Surface relative vorticity, $\zeta = \frac{\partial v}{\partial y} - \frac{\partial u}{\partial x}$, non-dimensionalized by the planetary vorticity (contours separated by 0.25; solid lines depict positive values, and dashed lines depict negative values).

of the core region, the radius of the region of constant vorticity was determined for the panels (B) through (F) in Figure 4.3, which resulted in 11.3 km, 13.7 km, 14.6 km, 16.1 km, and 21.4 km, respectively. These values indicate that the size of

the core region also grows as the bulge balloons in time.

It is a common practice to use non-dimensional numbers to categorize and compare plumes. The Rossby number (Ro) is one of the numbers found in the literature, and according to Fong and Geyer (2002) it relates the bulge shape and coastal current transport to the inlet parameters, and is defined as $Ro = \frac{U_0}{fL}$. Here, U_0 represents the exiting velocity of freshwater at the river mouth, and L is the characteristic length scale, here taken as the width of the river mouth. The Rossby number calculated at model day 50 was found to be $Ro = 0.27$ (corresponding to $U_0 = 0.04\,\mathrm{m/s}$ and $L = 3.11\,\mathrm{km}$). This small value of Ro suggests that the shape of the bulge is semicircular (with the center of the bulge located close to the shore), with a fairly large transport downstream at the coastal current (McCreary et al., 1997; Fong and Geyer, 2002).

Another non-dimensional number is the Kelvin number, $K = \dfrac{L}{L_r}$, defined as the ratio of the is the characteristic length scale (L), and the baroclinic Rossby radius, $L_r = C/f$. Here, C is the phase speed associated with the first baroclinic mode, and is obtained by computing the eigenvalues for the normal mode equation on the model grid (Chelton et al., 1998). f is the Coriolis parameter. Therefore, K offers a measure of the length scale where the inertial and Coriolis forces are still important. When the characteristic length scale is taken equal to the channel width (measured at the river mouth), the resulting K gives the relative importance of the inertia and rotational forcing at the river mouth (Geyer et al., 2000; Warrick et al., 2004b). If, however, the characteristic length scale is taken equal to the across-shore extent of the plume then K gives a measure of the overall importance of Earth's rotation within the plume (Garvine, 1995; Kourafalou et al., 1996a). Based on this, the following parameters were calculated: $L = 3.11\,\mathrm{km}$, $C = 17.9\,\mathrm{cm/s}$, $L_r = 3.81\,\mathrm{km}$, and $K = 0.22$ for the river mouth, and $L = 33.5\,\mathrm{km}$, $C = 11.8\,\mathrm{cm/s}$, $L_r = 2.50\,\mathrm{km}$, and $K = 13.4$ for the plume as whole.

These values indicate that at the mouth, inertial effects are considerably larger than the rotational effects (since $K_{mouth} \ll 1$), while Earth rotation are important in the remaining parts of the plume. In the classification of buoyant plumes it is customary to combine the K_{plume} with the Froude number, defined according to Kourafalou et al. (1996b) as the ratio of discharge speed and the celerity of long internal waves ($F = U_0/c = 0.22$). By these means, a large value of K_{plume} and a small value of F are associated with "large-scale" buoyant discharges (Garvine, 1995), which implies a slow flow (i.e., weak advection terms) and fairly strong influence of Earth rotation. As a consequence, the alongshore extent of the coastal current become very large compared to the bulge width, and the plume shape in general is largely influenced by mixing processes (Marsaleix et al., 1998). On the other side,

the plume falls into the "subcritical" category, since the Froude number is smaller than unity (Chao, 1988a), implying that the plume shape shall be marked by a bulge only slightly wider than the coastal current.

The plume thickness was estimated as the depth of the salinity anomaly contour $s = 0.1$. As can be visualized in Figure 4.5, the thickness is maximum at the centre of the bulge where it reaches about 4 m, and it could be described by a order 2 polynomial. However, the estimation through the salinity anomaly contour leads to a miscalculation in the region where the gyre and the coastal current interact.

Momentum balance

In order to increase insight into processes acting over the shelf and driving the plume movements, the various terms of the momentum balance equation need to be analyzed. Within the river member, the flow is in geostrophic balance if the effects of tides and winds are neglected (Mann and Lazier, 1996; Geyer et al., 2000). As the freshwater modes down the river, the margins of the estuary counteract the Coriolis force that tends to deflect the motion to the side causing the water surface to be tilted. In the open ocean, the flow is not in geostrophic balance, and the Coriolis force causes the flow to turn to the left in the Southern Hemisphere and proceed along the coast (see Figure 4.7). As the Coriolis force pushes the plume water to

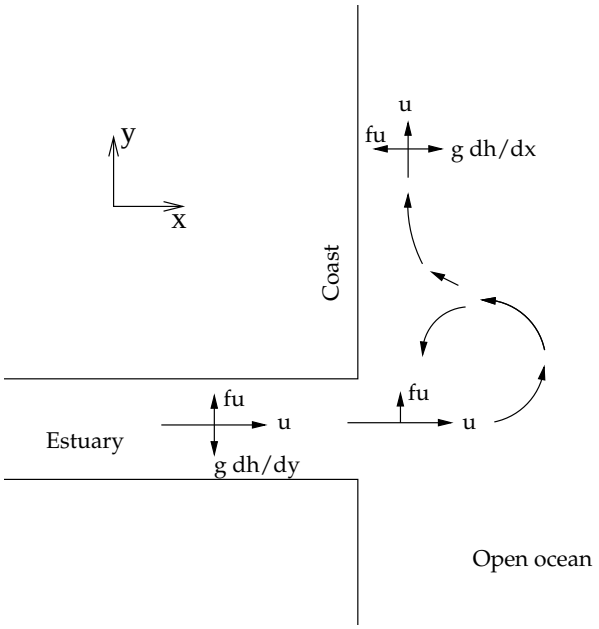

Figure 4.7: Schematic of freshwater fluxes in/out the bulge and balance of forces based on the hydrostatic, Boussinesq, f-plane equations (outflow in the Southern Hemisphere). The speed of the freshwater is represented by "u". Adapted from Mann and Lazier (1996).

the left, the blocking coastline causes an opposing pressure gradient in the form of a slight slope in sea level. Part of the buoyant water continues as a coastal current largely in geostrophic balance parallel to the coast, and another part recirculates in the bulge region in front of the river mouth (Fong and Geyer, 2002).

Very often, the circulation within the bulge is assumed to be in gradient-wind (*or cyclostrophic*) balance, with the centrifugal and Coriolis accelerations balancing the pressure gradient (Yankovsky and Chapman, 1997; Horner-Devine et al., 2006; Isobe, 2005). The momentum equation in the radial direction written in cylindrical polar coordinates takes the form (Kundu, 1990):

$$\frac{\partial v_r}{\partial t} + v_r\frac{\partial v_r}{\partial r} + \frac{v_\theta}{r}\frac{\partial v_r}{\partial \theta} - \frac{v_\theta^2}{r} - fv_\theta = -g\prime\frac{\partial h}{\partial r} + \nu_e\left[\nabla^2 v_r - \frac{v_r}{r^2} - \frac{2}{r^2}\frac{\partial v_\theta}{\partial \theta}\right] \tag{4.3}$$

where v_θ and v_r are the azimuthal and radial velocity components, respectively. $g\prime$ is the reduced gravity ($g\prime = g\frac{\triangle\rho}{\rho_o}$), h is the plume thickness, and $\nu_e = \frac{\mu}{\rho}$ is the coefficient of kinematic viscosity (μ is the dynamic viscosity).

The vertically-integrated momentum equation for this balance reduces to,

$$\frac{v_\theta^2}{r} + fv_\theta = g\prime\frac{\partial h}{\partial r} \tag{4.4}$$

where v_θ is the depth-averaged azimuthal velocity, and the right-hand-side is the pressure gradient term. Evidences of this type of balance have been reported in laboratory experiments (Horner-Devine et al., 2006), as well as in the recent field observations of the Columbia River plume reported by Horner-Devine (2009).

The terms in the momentum balance integrated from the surface to the depth h (plume thickness) along a longitudinal transect that crosses the centre of the bulge ($x = 19.1\,\text{km}$, see Fig. 4.4) are plotted in Figure 4.8, with the terms from the gradient-wind balance plotted separately in panel D. The pressure gradient term was computed directly from the thickness gradient, $\frac{\partial h}{\partial r}$, using a non-uniform reduced gravity estimated from the model-computed density field. A running-average with a window size of 2 gridpoints was applied to smoothen the resulting data. The time derivative of radial velocity is calculated numerically using $\Delta t = 1\,\text{hr}$ (i.e., the time spacing used to record model data for post-processing).

As can be seen, the centrifugal acceleration has smaller influence on the gradient-wind balance when compared with the two other terms, which turn out to mimic each other throughout the transect under examination. The error of gradient-wind balance ($\frac{v_\theta^2}{r} + fv_\theta - g\prime\frac{\partial h}{\partial r}$) is plotted in panel E, and the remaining error terms in panel F. The error in the gradient-wind balance is relatively high, with its maximum occurring at the edge of the core region. The remaining error terms are an order of magnitude smaller than the terms in the gradient-wind balance, which means

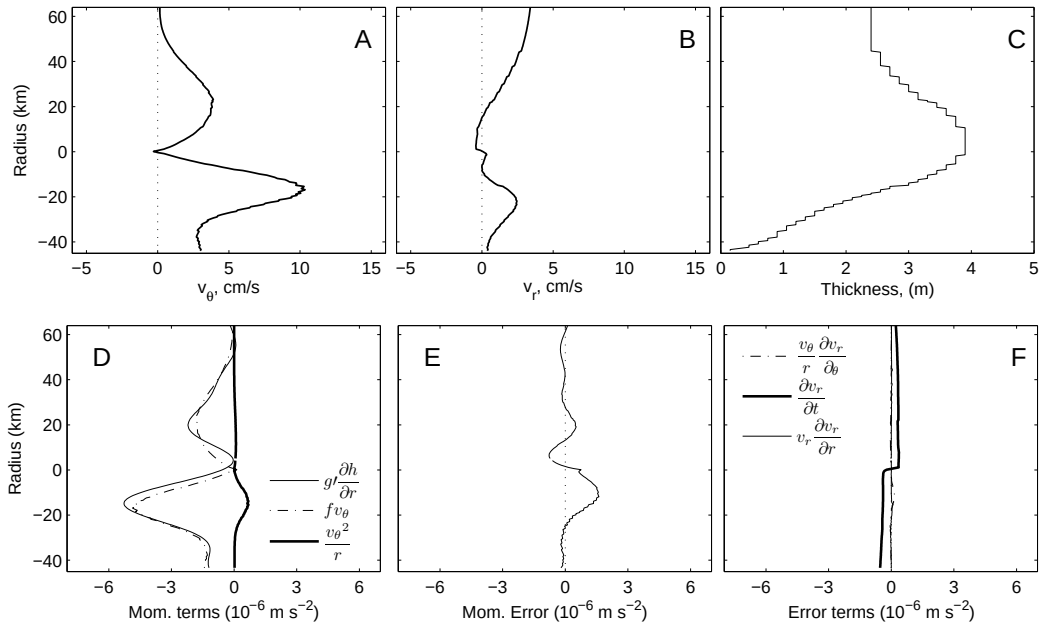

Figure 4.8: Bulge's momentum balance at time $t = 50$ days. The velocities in panels A and B have been averaged over the plume thickness. The pressure gradient term in panel D and the the $v_r \frac{\partial v_r}{\partial r}$ term panel F have been smoothen out using an ideal filter that absorbed the high frequency data. The error in the gradient-wind balance, $\frac{v_\theta^2}{r} + f v_\theta - g\prime \frac{\partial h}{\partial r}$, is plotted in panel E.

that none of these terms can explain the discrepancy in the gradient-wind balance, not even when all terms are combined. The leading two error terms are the radial acceleration $\frac{\partial v_r}{\partial t}$ and the $\frac{v_\theta}{r}\frac{\partial v_r}{\partial \theta}$ term, both relating to the changes in the radial velocity (i.e., changes along the circular orbit, and over the time), which in turn is linked to the bulge growth and expansion. All the diffusive terms are considerably smaller than the terms presented in panel F, and for this reason they were not presented. The small but nonzero radial acceleration is an indication of the bulge expansion through time, and also the plume's tendency to reach a steady condition. These results suggest that bulge growth is an important process in the bulge's momentum balance, yet insufficient for completing the balance.

Freshwater transport

The growth of the bulge in time is accompanied by accumulation of freshwater within the bulge area. Based on the assumption of a bulge that is *a priori* much wider than the coastal current, Nof and Pichevin (2001) suggested that the rate of freshwater input to the bulge, Q_{fb}, in the case of bulge with nonzero potential vorticity ($\gamma < 1$)

can be given by,

$$Q_{fb} = Q_{fr}\frac{2\gamma}{(1+2\gamma)} \tag{4.5}$$

where $\gamma = -\omega_b/f$ is the bulge's average vorticity scaled by the Coriolis frequency. In their analysis they showed that this solution is consistent with that of an intense flow corresponding to a zero potential vorticity bulge ($\gamma = 1$), where the analytically determined rate Q_{fb} is steady and equal to $^2/_3$ of the outflow freshwater discharge, Q_{fr}. It then follows from Eq.(4.5) that a vast majority of the freshwater volume in weaker outflows (those with small relative vorticity, $\alpha \ll 1$) goes into the coastal current and only a small portion goes into the bulge. In the present study, the rate of freshwater input to the bulge (Figure 4.9) was computed in two different ways, one using the velocity field and the other using the density field, as explained below.

Firstly, the rate of freshwater was estimated using the analytical solution presented in Eq.(4.5), where the bulge average vorticity was determined from the vorticity equation in plane polar coordinates (Kundu, 1990; page 623) assuming axial symmetry, $(\partial/\partial\theta = 0)$. This yielded $\omega_b = 2\omega_0$, with ω_0 being a constant equal to the angular velocity of each fluid particle about the gyre centre (i.e., the origin). This constant was evaluated as the slope in the linear fit to the profile of azimuthal velocity (similar to that shown in Figure 4.4), using only the data points located in the core region. As can be seen on the left panel of Fig. 4.9, the average bulge vorticity (here scaled by the Coriolis parameter) decreases towards the end of simulation, apparently due to frictional effects, and so does the rate of freshwater going

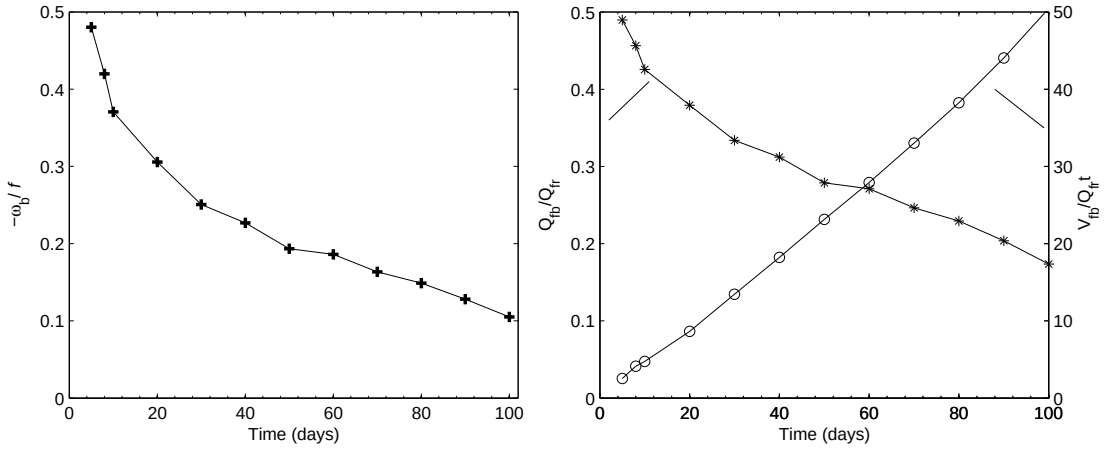

Figure 4.9: *Left*: Non-dimensional bulge average vorticity (scaled by the Coriolis parameter) used to compute the rate of freshwater going into the bulge according to the Nof and Pichevin (2001) formulation. *Right*: Rate of freshwater input to the bulge (Q_{fb}) normalized by the outflow discharge (Q_{fr}), and volume accumulated in the bulge as a function of the filling time of the plume (V_{fb}) normalized by the outflow discharge integrated over 24 hours.

to the bulge (here scaled by the outflow freshwater discharge, Q_{fb}/Q_{fr}), which is shown on the right panel of Fig. 4.9. The average value of this ratio, using the data points marked by asterisks, is 31.7%, which is within the limit of typical values for weak outflows. The weakness of this approach is the fact that the vorticity of the core region was applied for the entire bulge, and the strength is the applicability of the approach to *in situ* data.

Secondly, the rate of freshwater input to the bulge was estimated directly through the volume accumulated in the bulge during the simulation time. Following Horner-Devine (2009), the this volume can be computed as the integral of freshwater fraction, given by,

$$V_{fb} = \int_{-H}^{\eta} \int_{0}^{R} \int_{0}^{2\pi} \left(\frac{S_a - S}{S_a} \right)_{s>0.1} \mathrm{d}\theta \mathrm{d}r \mathrm{d}z \tag{4.6}$$

where S_a is the reference (shelf) salinity, η is the surface level, H is the level of the seafloor, and the integral is computed for water particles whose salinity anomaly is greater than 0.1. Here, a circular bulge is assumed, with its radius taken from the origin to the upstream position of the contour $s = 0.1$, along a line crossing the centre of rotation.

The volume V_{fb} determined by these means was then scaled by the net freshwater transport (Q_{fr}), estimated for a section of the river using equation 4.2. It was found that Q_{fr} (at the river mouth) is nearly constant throughout the simulation with a mean value of $991.9 \pm 13.8\,\mathrm{m^3\,s^{-1}}$. On the other hand, the V_{fb} (in the bulge) increases monotonically at the rate of about $479.1\,\mathrm{m^3 s^{-1}}$ (left panel of Figure 4.9, right axis). This transport implies that on average 48.3% of the freshwater volume discharged at the river goes into the bulge, which is considerably greater than the analytical estimate (Eq. 4.5). Either way, it seems that in the absence of external forcing, the model lacks an efficient mechanism to remove the freshwater from the bulge region, given that the volume in the bulge increases nearly steadily. The removal could occur through either advection to the coastal current or mixing with ambient waters, and either process would result in a reduced time scale (a few days) for the accumulation of freshwater in the bulge, as reported from field observations of the Columbia River plume (Horner-Devine, 2009).

According to Nof and Pichevin (2001), an intense outflow (relative vorticity in bulge equal to $-f$) dumps most of its mass in the bulge that grows in time, while a weak outflow ($\varsigma \ll f$) dumps most of its mass in the coastal current and only a small fraction goes into the bulge. Yet, the bulge in the weak outflow case grows faster than in the former. From the analysis of vorticity in the bulge region (Figure 4.6), one finds that the current case corresponds to a weak vorticity (averaged over the bulge), meaning that the results of freshwater rates qualitatively agree with these

earlier findings.

4.1.2 The near-shore buoyancy-driven circulation

Judging from the horizontal and vertical velocity fields presented in Figures 4.2 and 4.5, the time-dependent coastal current on simulation day 50 is unidirectional, confined to the upper layer, and has a width of about 19 km, which is one third of that of the bulge. Let us consider a transect perpendicular to the flow to evaluate the flow structure and the freshwater transport through it. Figure 4.10 presents the cross-shore section of salinity and alongshore velocity measured at $y = 200$ km. There is a relatively strong vertical shear that clearly distinguishes the region of buoyancy-driven circulation from the offshore region (ambient current). There is also a portion of water that flows southwards (i.e., opposing flow in the upper layer) in the bottommost layer with speeds not exceeding 1 cm/s.

A number of studies report the dynamics of the coastal current to be in cross-shore geostrophic balance, where the Coriolis acceleration balances the pressure gradient (Fong and Geyer, 2002; Lentz et al., 2003; Horner-Devine et al., 2006). For simplicity, and given the fact that the flow is unidirectional over the constant slope bottom, the alongshore momentum balance equations is considered in Cartesian coordinates. The depth-averaged momentum equation in the x-direction reads (Kundu, 1990; Hedström, 1997):

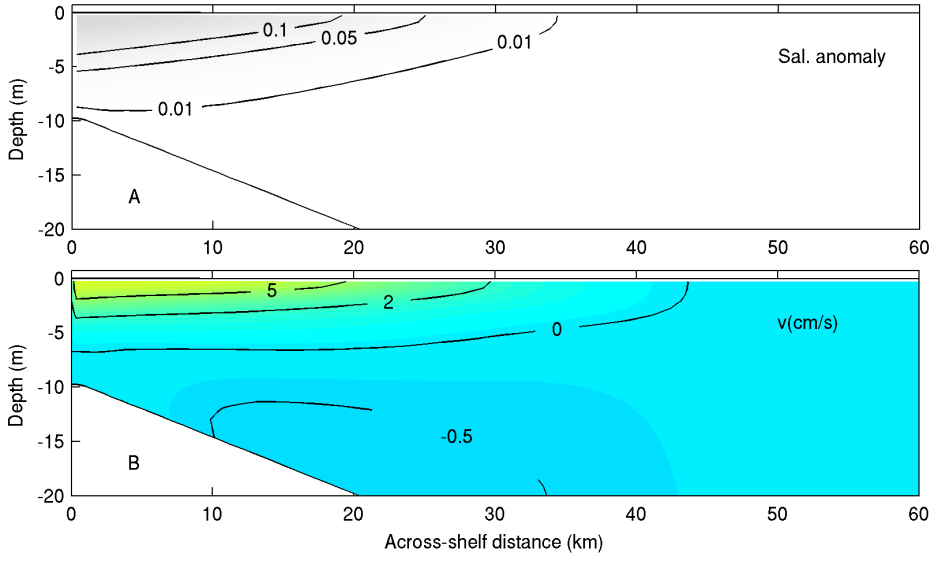

Figure 4.10: Simulated vertical section of salinity anomaly (top) and alongshore velocity component (bottom) at $y = 200$ km at model time $t = 50$ days. The alongshore velocity v(cm/s) was averaged over 12 hours at the beginning of day 50.

$$\frac{\partial \bar{u}D}{\partial t} + \frac{\partial \bar{u}^2 D}{\partial x} + \frac{\partial \overline{uv}D}{\partial y} - f\bar{v}D = \frac{1}{\rho_o}(\tau_s^x - \tau_b^x) - \int_{-h}^{\eta} \frac{\partial \phi}{\partial x}\mathrm{d}z + D\overline{F_u} \tag{4.7}$$

where the overbar denotes a vertically averaged quantity, $D = (h+\eta)$ is the brackish water layer thickness, $\phi = (P/\rho_o)$ is the dynamic pressure, $P = \rho g z$ is the total pressure at level z, and F_u represents the effect of dissipation. The terms in Eq. 4.7 represent (from left to right) the local acceleration, the x and y advection of alongshore momentum, the Coriolis acceleration, the surface and bottom stress, the pressure gradient, and the horizontal diffusion. The horizontal diffusion term is, according to Blumberg and Mellor (1987), given by:

$$D\bar{F}_u = \frac{\partial}{\partial x}(2A_M \frac{\partial \bar{u}D}{\partial x}) + \frac{\partial}{\partial y}A_M(\frac{\partial \bar{u}D}{\partial y} + \frac{\partial \bar{v}D}{\partial x}) \ ,$$

where A_M is the horizontal mixing coefficient, whose typical values in continental shelf waters according to Kourafalou et al. (1996b) are $10 - 100\,\mathrm{m^2 s^{-1}}$. For the current configuration, values computed using Eq. (3.6) varied between $50.1 \sim 55.3\,\mathrm{m^2 s^{-1}}$, which are on the extreme high side of the reasonable values. Note that, the higher the mixing coefficients the higher the friction velocity, which then influences the time evolution of the bulge in long simulations.

The pressure gradient term in Eq. (4.7) can be expressed as,

$$\begin{aligned} -\int_{-h}^{\eta} \frac{\partial \phi}{\partial x}\mathrm{d}z &= -gD\frac{\partial \eta}{\partial x} - \frac{g}{\rho_o}\frac{\partial}{\partial x}\int_{-h}^{\eta}\int_{z'}^{0} \rho(x,y,z',t)\mathrm{d}z'\mathrm{d}z \\ &= -\frac{\partial}{\partial x}\int_{-h}^{\eta}(P_{bot} - R)\,\mathrm{d}z \\ &= -\frac{\partial}{\partial x}\left\{D(P_{bot} - \bar{R})\right\} \ , \end{aligned} \tag{4.8}$$

and it accounts for both the barotropic and the baroclinic components of the pressure gradient. Here, $P_{bot} = \int_{-h}^{\eta} \phi \mathrm{d}z$ is the dynamic pressure at the bottom of the plume, and $R = \int_{-h}^{z'} g\rho/\rho_o \mathrm{d}z$ is the buoyancy force integrated from bottom of the plume to a level z'.

It turns out that at the cross-shore transect $y = 200\,\mathrm{km}$, the momentum in x-direction is governed by the geostrophic terms, consistent with previous studies. The terms in the vertically-integrated momentum balance equations are presented in Figure 4.11, and as can be seen in panel B, the bottom-pressure component leads the geostrophic balance, followed by the buoyancy forcing. With no exception, the remaining terms present in the Eq. (4.7), namely the local acceleration, advection, bottom stress, and diffusion, are very small in comparison with the geostrophic

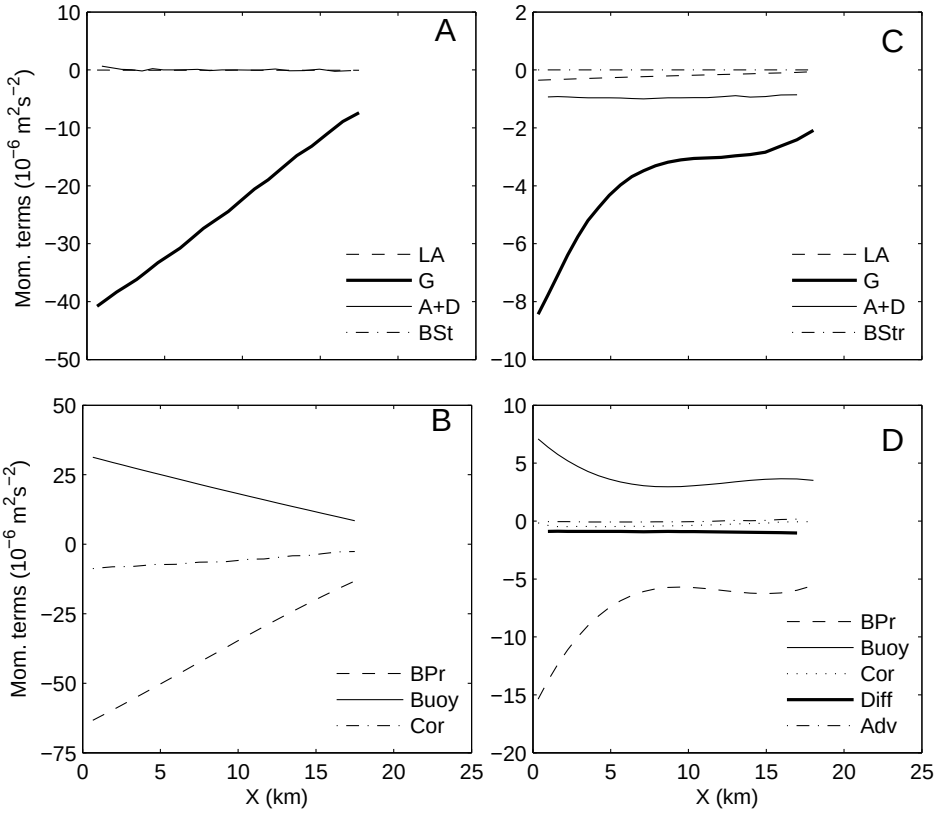

Figure 4.11: Vertically-integrated momentum terms estimated for t=50 days in a cross-shore transect located at $y = 200\,\text{km}$. The left (right) panel presents the momentum in the x-direction (y-direction). For each case, the top panels present all the terms involved in the balance, while the lower panels show details of only the most significant terms. Velocities and densities were averaged over the plume thickness. LA=Local acceleration, G=geostrophic, A+D=Advection and Diffusion, BS=bottom stress, BPr=Bottom pressure, Buoy=Buoyancy and Cor=Coriolis. The sign notation is such that the local acceleration is equal to the sum of the other terms.

terms, which are a few orders of magnitude larger. The Coriolis term (fu) presented in panel D indicates that the across-shore velocity component is very small and positive. Since the only positive term in the geostrophic balance is the buoyancy forcing, the cross-shore movement is determined by the buoyancy forcing. Also, the fact that the local acceleration is relatively small indicates that the flow in this direction is nearly in steady state, in contrast to the momentum along the y-direction (panels C and D) and the bulge region.

The momentum along the y-direction is also leaded by the geostrophic terms, but contrary to the x- direction the contribution of the diffusive terms is considerably large. The local acceleration decreases from the wall to the offshore boundary, and the term appears to be too large to be neglected. The Coriolis and the advection

terms have smaller magnitude, and hence lesser influence in the balance.

The magnitude of the transport of freshwater by the coastal current, Q_{fcc}, influences directly the physical extent and the velocity scales of the downstream penetration, and according to Fong and Geyer (2002) it is defined as ,

$$Q_{fcc} = \int\int v\frac{\Delta S}{S_a}dA \tag{4.9}$$

where v is the alongshore component of velocity, ΔS is the salinity difference between the plume and ambient waters, and the area integral is computed over the cross-shore section. For the standard case, the transport of freshwater at $y = 200\,\mathrm{km}$ is $191.2\,\mathrm{m^3s^{-1}}$, which is equivalent to 19.3% the freshwater transported by river member. The mass conservation law requires that the freshwater released at the river mouth during a period of time is either stored in the bulge, advected away by the coastal current or mixed with ambient waters to constitute the water parcels with small anomalies ($0 < s < 0.1$), in other words, $q_{river} = Q_{fb} + Q_{fcc} + Q_{amb}$. From these simple calculations it is then suggested that there is more freshwater being accumulated in the growing bulge (48% of the river inflow), and the remaining is either mixed with the ambient water (32.4%), or transported in the coastal (19.3%). These estimates are based on (i) a volumetric freshwater transport at the river head of 1000m3/s, (ii) the 100-days average of volume of freshwater accumulated in the bulge (Eq. 4.6), and (iii) the volume of freshwater that crosses the line $y = 200\,\mathrm{km}$ on day 50, assuming that the transport there remains invariant throughout the simulation time.

4.1.3 Sensitivity to river discharge

In order to evaluate the plume sensitivity to varying river discharge, a number of model runs were performed where the freshwater transport at the river mouth was varied. By changing the volumetric transport of freshwater and the salinity difference separately it was possible to get the net freshwater flux at the mouth varying from about 1000 to $8000\,\mathrm{m^3s^{-1}}$, which has produced the plumes presented in Figure 4.12. At the model time $t = 50$days no significant difference was found in the structure of plumes produced in all the cases, apart from the fact that larger freshwater discharge produces slightly larger plumes and so, enhance the freshwater availability in the near-shore. As the size of the bulge increases, the amount of freshwater in the region to the south of the river mouth also increases, yet the brackish water in this region is part of the re-circulating bulge and it is always attached to the coast. This pattern contrasts the results from previous studies (Garvine, 1999) in which the simulated upstream penetration comprised brackish water that actually underwent

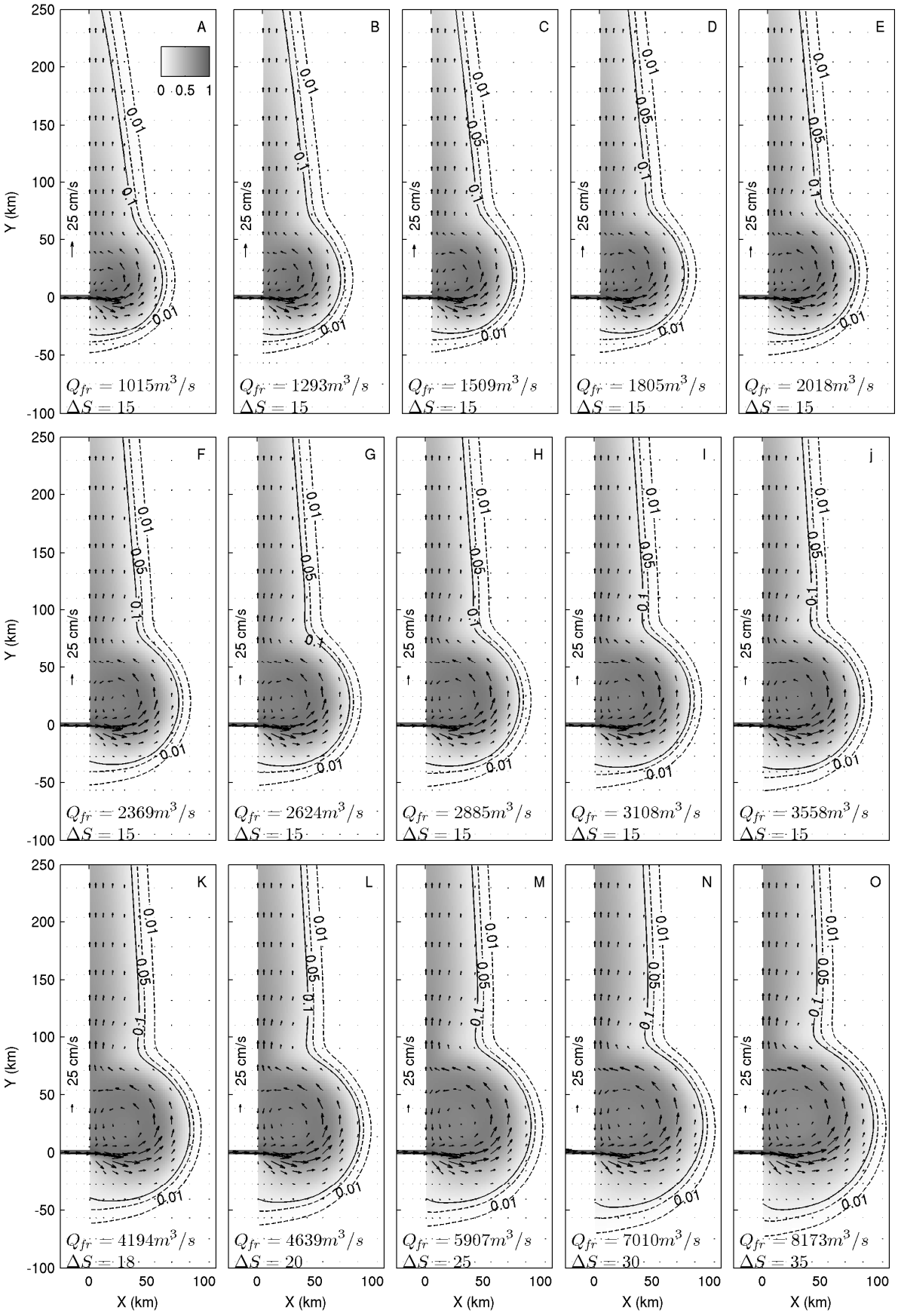

Figure 4.12: Surface salinity anomaly and velocity field at time $t = 50$ days, for clamped discharge varying between $1000 - 10000 \mathrm{m^3 s^{-1}}$ (panels A-J), and varying salinity difference with fixed $Q_{fr} = 10000 \mathrm{m^3 s^{-1}}$ (panels L-O).

a turn towards the upstream direction, and also the field data presented in Chapter 2 that revealed the presence of brackish water to the south of the river mouth but in some cases away from the coastline. Although, the differences in plume structure are very small to offer a quantitative analysis on the effect of buoyancy forcing, it become clear that the river discharge is unlike to promote the upstream spreading of plume waters beyond 50 km from the river mouth.

4.2 Wind effects on the plume structure

4.2.1 Wind forcing in the four main directions

Windstress have long been considered the main controlling factor on the circulation of both freshwater and sediment buoyant plumes. In order to examine the plume structure under different wind conditions, a number of model runs were performed using the parameters presented in Table 4.1, except that a nonzero windstress was considered. Two different wind intensities were used separately, representing weak (5 km/h) and moderate (12 km/h) wind conditions, both oriented along one of the four major directions, combining to a total of eight model runs.

The theory on wind-driven currents in infinitely deep ocean predicts surface water movements at 45 degrees to left of the wind in the Southern Hemisphere, although the few available observations of Ekman drift report substantially smaller angles (5^o to 20^o; (Cushman-Roisin and Beckers, 2009). The discrepancy is sometimes attributed to the fact that the water column is not deep enough to allow the full development of the Ekman spiral.

The simulation results presented in Figure 4.13 are consistent with the theory everywhere far from the coastal walls, except in the regions highly influenced by freshwater. In these regions the surface flow is oriented approximately at 45 degrees to the left of wind, regardless of the water depth. The primary response of buoyant freshwater plumes to wind forcing have been previously described by Chao (1988b), based on results from a numerical simulation and the analytical solution of the linearized steady-state momentum equations in shallow waters. This solution was analyzed considering separately an alongshore (F^y) and cross-shore wind forcing (F^x), and has the form (Chao, 1988b),

$$\begin{cases} u = & \frac{\epsilon F^x}{\epsilon^2+f^2}\left(1-e^{-(\epsilon^2+f^2)^{1/2}\cdot x/c}\right) \\ v = & \frac{fF^x}{\epsilon^2+f^2}\left(-1+e^{-(\epsilon^2+f^2)^{1/2}\cdot x/c}\right) \end{cases}, \tag{4.10}$$

$$\begin{cases} u = & \frac{fF^y}{\epsilon^2+f^2}\left(1-e^{-(\epsilon^2+f^2)^{1/2}\cdot x/c}\right) \\ v = & \frac{\epsilon F^y}{\epsilon^2+f^2}\left(1+\frac{f^2}{\epsilon^2}e^{-(\epsilon^2+f^2)^{1/2}\cdot x/c}\right) \end{cases}, \tag{4.11}$$

where f is the Coriolis parameter, ϵ is the Rayleigh friction coefficient (or Newtonian cooling coefficient when used in the continuity equation), and c is the speed of gravity waves characterizing the stratification.

Highly stratified waters imply (i) an elevated value of c, (ii) a reduced friction (i.e., low values of ϵ) between an upper layer containing plume water and a bottom layer, and (iii) a greatly reduced Ekman drift (since stratification hinders vertical motion). Equations 4.10 and 4.11 are valid for an upper layer moving on top of an

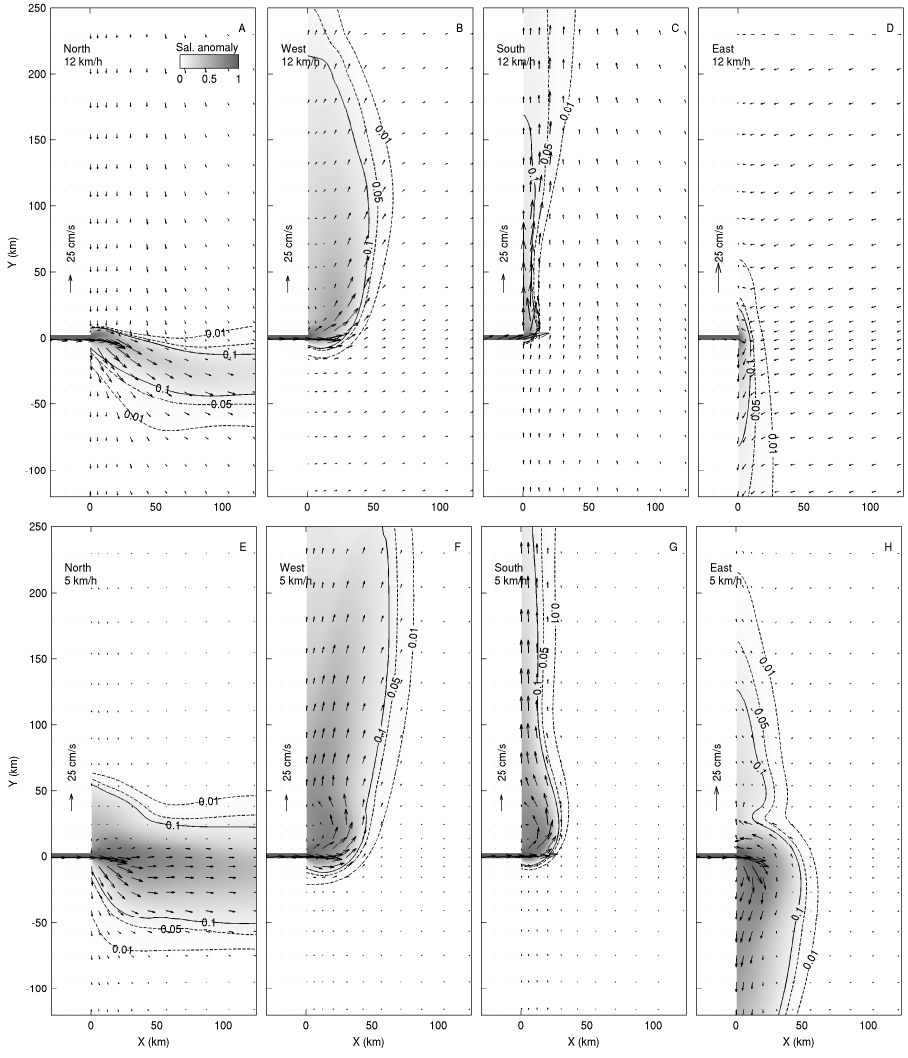

Figure 4.13: Surface velocity and salinity fields at the time $t = 50$ days, simulated under moderate (top) and weak (bottom) wind conditions. Plotted are the velocity (arrows), salinity anomaly (shaded colours), and three contours of salinity anomaly (i.e., 0.01, 0.05, and 0.1). A colour scale for salinity anomaly is given in panel A, and the coastline is located at $X = 0$ km. The wind blows from the direction indicated in each panel.

inert lower layer, and describe a flow field composed by a surface Ekman drift and a geostrophic current that varies with the offshore distance from coastline ($x = 0$). Using those two equations one finds the following plume responses to the wind forcing based on the current model configuration:

Northerly winds (upwelling-favourable) cause the seaward motion of the plume waters, and consequently a massive weakening of the near-shore stratification. Under moderate winds, a coastal jet/current is unlike to develop since a density-driven current would oppose the wind direction, and the resulting flow field is characterized by a tongue of plume waters leaving the river mouth and fading out offshore due to mixing with ambient waters. For weak winds, the enhanced Ekman drift persists in the near-shore, but since the offshore wind mixing is now reduced, offshore stratification increases and the plume waters can be carried downstream (i.e, in the sense of the Kelvin waves). Depending on the degree of offshore stratification, possible scenarios include a pool of plume waters spreading offshore along the estuary axis and/or downstream (panel E of Figure 4.13), and plume waters being transported downstream in either an offshore or coastally-trapped density-driven current. A situation like this where the current opposes the mean wind direction has been observed in the shelf off the Delaware Bay (Münchow and Garvine, 1993).

Westerly winds (seaward) enhance the freshwater export from the river/estuary system onto the shelf, enhance stratification, and so reduce the Ekman drift. The combination between the density-driven current and the reduced Ekman drift result in plume waters being drifted downstream, with significant differences in the offshore/near-shore velocities. Moderate winds will produce offshore velocities higher than near-shore, rendering a surface plume structure that appears to be detaching from coast. Under weak winds the velocity gradually decreases seaward from the coastline, and the downstream extension of the plume exceeds the limits of the model domain.

Southerly winds (downwelling-favourable) induce a wind-driven coastal current by pulling the plume water against the downstream coast. The coastal current remains attached to the coast and is highly non-uniform, meaning that, the flow at the coast is parallel to the wall, while it changes from unidirectional to meandering towards the offshore plume border. This particular aspect that can be described as a meandering of the coastal current has not been given much attention in previous studies in spite of its presence in a number of reported surface plume structures. An example of earlier studies with the presence of the meandering is the simulations of plumes over a sloping bottom by Chao (1988b) and Garvine (1999), and plumes over a flat bottom by Fong and Geyer (2002). The coastal current has its smallest width and it is relatively stronger immediately offshore from the bulge region.

Easterly winds (shoreward) promote the withdrawal of freshwater from the

shelf, weaken the near-shore stratification, and therefore enhance the Ekman drift. The Ekman drift causes the set-up of the sea-surface against the upstream coast, which could drive a geostrophic flow if the wind forcing is weak. The plume water is carried upstream by virtue of the Ekman transport, and it forms either a pool of less dense water in the case of moderate winds (panel D of Figure 4.13), or a coastally-trapped right-bounded flow in the case of weak winds (panel H of Figure 4.13). In the latter case, a portion of lighter water is also found in the downstream coast flowing at a much lower speed in the sense of a Kelvin wave. Following the region of intense river inertia off the river mouth, the freshwater flow is bifurcated by the action of the easterly winds, and so most of the water turns right to form the wind-driven coastal current, while the remaining turns left and proceed as a buoyancy-driven flow. These results show in fact that, irrespective of its magnitude, a easterly wind can deflect the motion of a buoyant plume up to 180^o. This is so because, in the absence of other forcings (i.e., tides, currents) the windstress dominates in the surface layer over the pressure gradient and Coriolis that would combine together to move the plume northeastwards. In this case, a wind-driven surface flow oriented shoreward is deflected to left due to Earth rotation, and ultimately the water flows southwards.

It is worth mentioning that very often the simulations using wind intensity larger than 12 km/h were not stable, but since the moderate wind conditions still produced a wind-driven system, the effects of a strong wind field can be inferred from the results for a moderate wind. No gyre or re-circulating bulge was observed in the case of moderate winds, and the orientation of the plume waters was found to be consistent with the predictions of surface movement in the Ekman theory. This behaviour indicates that for the current model configuration, the plumes behave like a surface layer of freshwater in an infinitely deep ocean. On the other hand, re-circulation within the bulge was observed to occur in all cases simulated with weak winds (characterizing a density-driven system). In general, the results show that the horizontal spreading of the freshwater is very sensitive to either the magnitude or the direction of wind forcing.

The vertical structure of plumes forced by winds blowing from the four main directions are presented in Figure 4.14. Under strong winds the mixing between plume and ambient water is enhanced. The maximum plume thickness at about 10 − 15 km from the coast rarely exceeds 5 m, except when the plume is forced by seaward (westerly) winds. In wind-driven systems, plumes with the largest breadth were generated under the action of winds blowing from the north, followed by the seaward winds, which also originate plumes with the largest thickness (deepest penetration of freshwater). On the other hand, in buoyancy-dominated systems, broader plumes are also generated under winds blowing from the north, however, with no significant

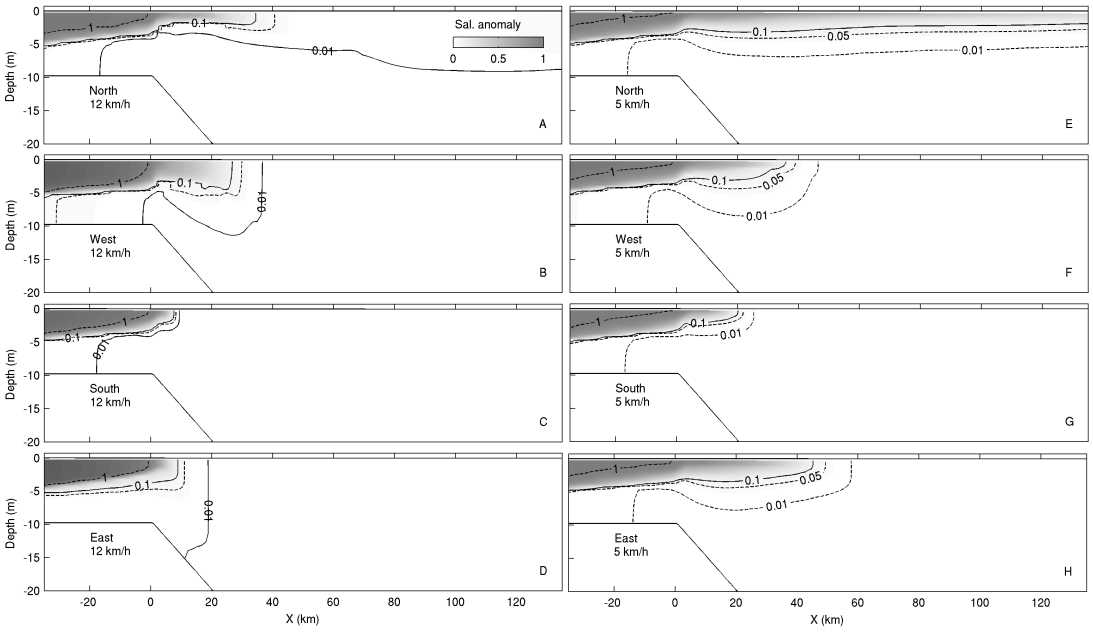

Figure 4.14: Simulated vertical distribution of salinity anomaly at $t =$ 50 days, along a transect perpendicular to the coast and located in the estuary central axis. The 12 km/h (left) and 5 km/h (right) winds blow *from* the directions indicated by the text in each panel.

difference in the plume thickness in all the cases.

Southerly winds inhibit the near-shore stratification by exporting fresher water to the downstream coastal current, and simultaneously they induce an enhanced flow of ambient waters in the bottom layers within the river member (results not shown). In these wind conditions, the resulting plumes are much narrower when compared with the plumes produced when the winds blow from the other directions. It also appears that moderate winds blowing from the east promote the vertical mixing of near-shore plume waters.

In general, the plumes forced by weak winds are a few centimeters deeper and a number of kilometers wider than its correspondent for moderate winds, except for seaward blowing winds, which originate a much deeper plume under strong winds. The dynamics of these plumes is apparently density-driven, however, the vertical and horizontal plume features are determined by the interaction between the buoyancy and the wind forcing. For almost all the cases analyzed so far, the water column at the river mouth is made of plume waters at the top (salinity anomaly varying between zero and unity), and ambient water at the bottom layers, indicating the existence of a rather high degree of stratification. Velocity profiles for all the cases (not presented) show a landward movement of ambient water in the base of plume, at a much lower speed than the seaward movement of the plume waters on top.

4.2.2 Plume structure under southeasterly winds

During the months of maximum river discharge (i.e., January-March), the wind field in the Sofala Bank is predominantly southeasterly, meaning that the cross-shore and alongshore components of windstress get into play simultaneously. It is then expected that the structure of the resulting plume contains features comparable with those observed when either southerly or easterly wind forcing is applied. In order to test this hypothesis a simulation was conducted using all model parameters as described before, except the wind field that was changed as follows. Three different wind directions were used, all corresponding to southeasterly winds, namely, wind blowing from 280^o, 310^o, and 340^o, and the same two magnitudes used in the previous experiment corresponding to either weak or moderate conditions. Note that these angle measures are relative to a 0^o oriented along the positive x-axis.

Figure 4.15 presents the surface views of salinity and velocity simulated for the model time $t = 50$ days, with the wind direction indicated by the numbers in the top left corner in each panel. The vertical features for these configurations are presented in Figure 4.16. In general, plumes exhibit horizontal and vertical features similar to those of a plume forced by southerly winds, with some minor differences in the length scales. Some features that are typical of plumes under easterly winds appeared in the case of winds blowing from 340^o, which include the enhanced mixing in the offshore region.

In addition, the weak southeasterly winds blowing from 340^o produced plumes whose structure contains a re-circulating bulge, a buoyancy-driven current in the downstream, and a large portion of water in the upstream direction, similar to what was found under the action of weak and moderate easterly winds. This pattern suggests that wind fields having a negative cross-shore component and null/positive longshore component tend to force the plume waters upstream, and this tendency for upstream dispersion becomes less noticeable as the negative cross-shore component decreases in magnitude (i.e., as winds changes from easterly to southerly). The vertical profiles of salinity indicate no significant difference in the features between the three directions considered here, except for the plume breadth that increases as the wind changes towards easterly winds.

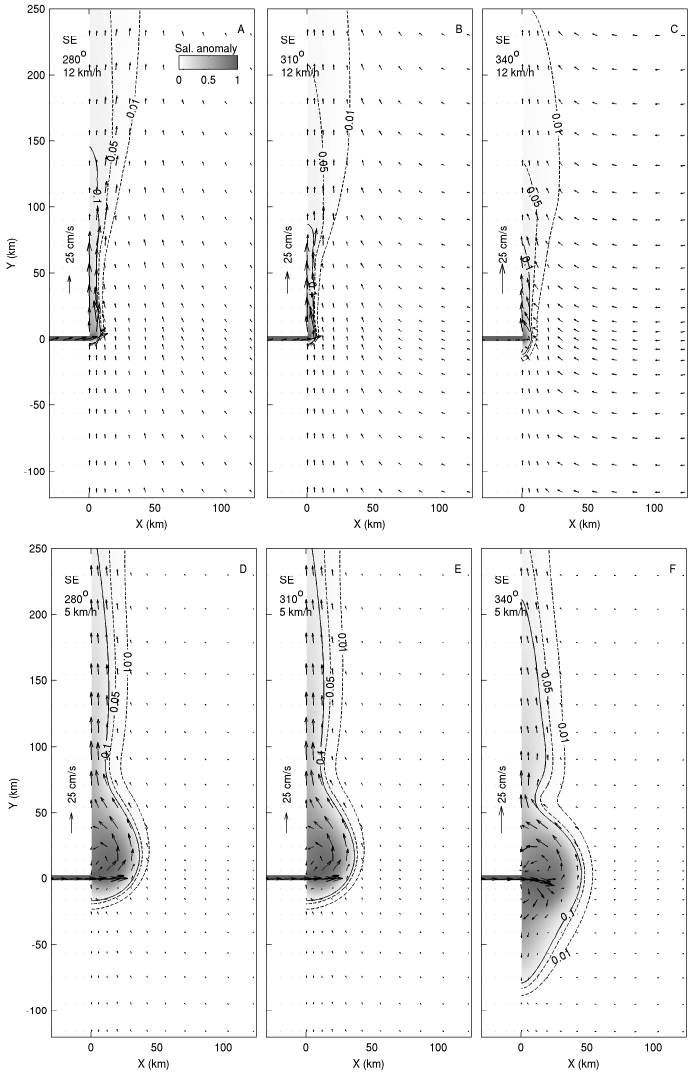

Figure 4.15: Same as in Figure 4.13, except for southeasterly winds blowing *from* the directions indicated by the text in each panel.

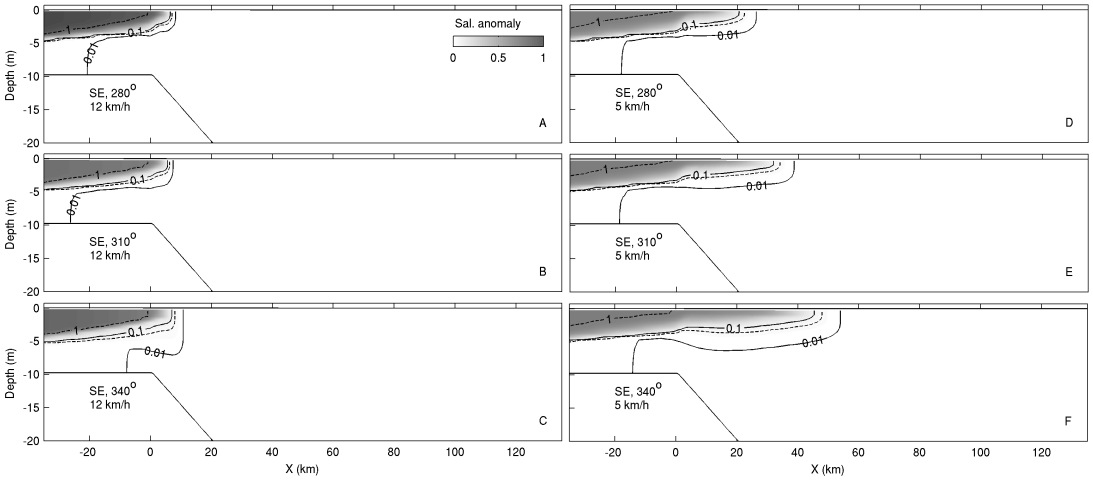

Figure 4.16: Same as in Figure 4.14, except for southeasterly winds blowing *from* the directions indicated by the text in each panel.

Response to a shift in the wind speed

Southeasterly winds are the most frequent winds in study site, and yet large differences were found for the plumes under weak and moderate wind conditions. This feature has raised the question of how do the plumes respond to a change in the wind speed, which presumably occurs quite often in the real system. And particularly, it is interesting to know the time scales associated with the adjustment between different wind conditions. This feature was evaluated in two separate runs, where the wind speed was either intensified to the moderate conditions (12 km/h) or weakened to the weak conditions (5 km/h). A ramp function was used to smoothen the shift during half an inertial period ($T_i = 1.55$ days), and the experiment started from the end of the previous experiment (i.e., 50 days), meaning that the results (Figure 4.17) describe the response of a pre-existing plume.

Following the wind speed intensification, the plume gradually adjusts to the change by substituting the large and extensive pool of freshwater by a narrower bulge, typical of plumes under the action of a moderate windstress. The increased windstress acts in a way to strengthen the current field in the entire domain, and ultimately to erode the offshore stratification in the bulge region. This behaviour results in a plume that is deeper than those found when the strong and weak winds were considered separately. On the other hand, the relaxation of windstress resulted in an enhancement of the stratification near the river mouth followed by flow separation within the bulge, also typical for plumes under the action of weak winds. In both cases, a signature of the previous plume is still noticeable in the surface fields

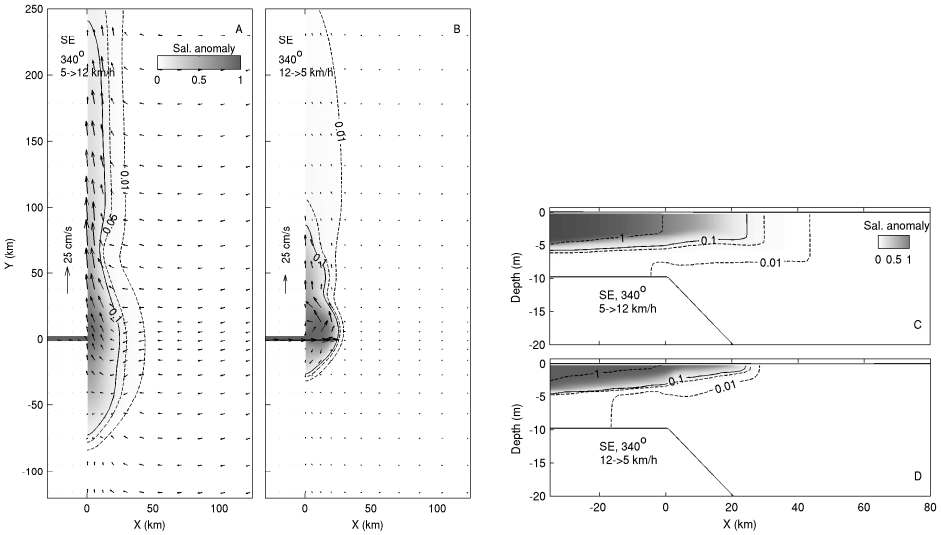

Figure 4.17: Horizontal and vertical plume structure 7 days after intensification/relaxation of wind conditions. Shaded colors indicate the variation of salinity anomaly, which is equal to unity at the surface layer in the river mouth.

recorded 7 days after the shift in the wind intensity, suggesting that a complete change in the plume structure is likely to take longer than 7 days to occur. This result is particularly interesting because the analysis of wind intensity in the region surrounding the Zambezi Delta (i.e., presented in Section 2.3.2) has indicated that, the most dominant synoptic frequency is once every 12 days followed by once every 6 days. Therefore, it is found that the surface features of real plumes at any given time is a consequence of the wind conditions observed during the few days prior to plume observation.

Response to oscillating winds

The next step involved the simulation of a plume under the action of a high-frequency varying wind field, which aimed at evaluating the effects of an oscillating wind field on the plume structure. This task was accomplished in a different set of model runs that used similar parameters to the standard case, except that the speed and orientation of the wind forcing were allowed to vary periodically, using the windstress field described by Eq. (3.3). Here, the windstress vector describes an ellipsoid with its major axis representing the sea-breeze predominant direction, chosen to be oriented along 340^o. In separate runs, the maximum intensity of sea-breeze was varied between 5, 12, 18, and 26 km/h, which according to the Beaufort scale it corresponds to slight breezes, gentle breezes, moderate breezes, and fresh breezes, respectively.

In Figure 4.18 , the surface features of plumes forced by sea-breezes are compared with those produced by the weak constant wind forcing. As can be seen, the near-shore stratification increases considerably in response to the periodic wind field, and that is accompanied by an enhance mixing in the portions of the plume located further offshore. The surface features in the plume forced by slight breezes (5 km) seem to be the least affected by the the windstress, as the distribution of salinity and velocity are much closely related to the unforced plumes (standard case) than to any of the wind forced plumes. In other words, the horizontal features of a plume forced by slight breezes have no appreciable difference when compared with the unforced plumes, however the bulge and coastal current of these plumes are considerably larger in comparison with the plumes forced by a weak southeasterly constant wind.

Conversely, massive changes occur in the horizontal structure of plumes forced by gentle to fresh breezes ($12 - 26$ km/h), when compared with the features of a plume forced by weak southeasterly constant winds. The dynamics of the system is dominated by the Ekman drift at times when the breezes are oriented predominantly seaward or landward, and it changes to purely geostrophic when the winds are aligned with the coast. The low-salinity water appears to spread primarily in the

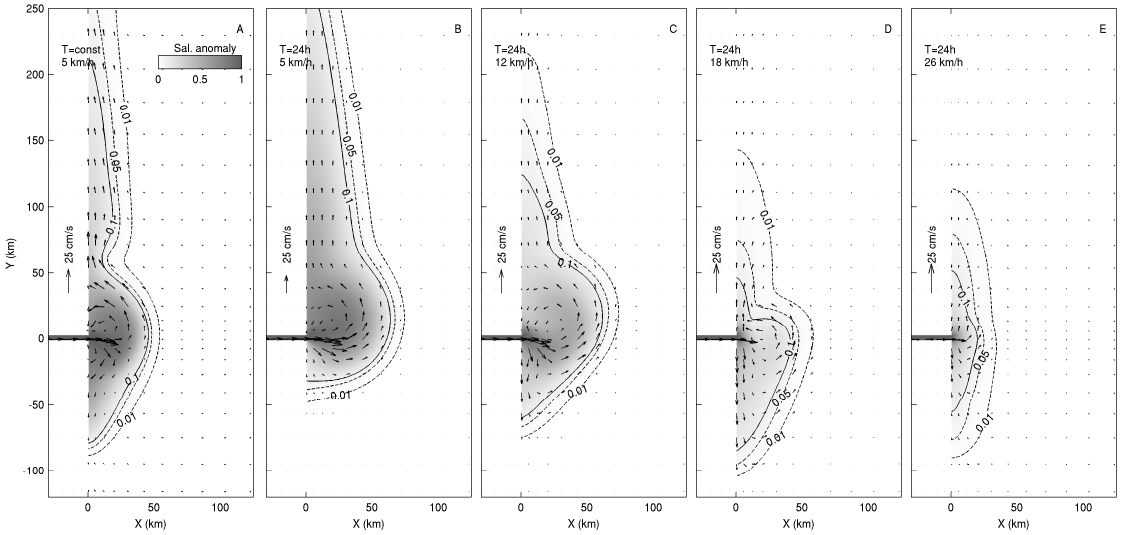

Figure 4.18: Surface views of salinity and velocity fields of plumes under different SE winds: constant intensity and direction (panel A), and sea-breezes of intensity 5, 12, 18 and 26 km/h. All cases present conditions averaged over 24 hours, and the predominant wind direction is 340^o.

downstream direction when the plume is forced by slight breezes, upstream direction when forced by moderate breezes, and it accumulates in front of the bulge when forced by gentle or fresh breezes.

The re-circulation that appears clearly visible in panels B, C, and D of Figure 4.18 is a background feature, obtained when the surface fields are averaged over a 24 hour period, and it does not appear in a snapshot view taken at an arbitrary time (result not shown). Another interesting feature apparent in the horizontal distribution of salinity and velocity is the variation in the length of the downstream penetration of freshwater, such that the stronger the sea-breeze the shorter the length of the current.

The vertical features of these plume are presented in Figure 4.19 . By comparing the structures in panels A, B, and C with those presented in Figure 4.17 for the case of a shift in the wind intensity, one finds that constant winds do a better job mixing the water column near the plume front. In addition, these results indicate that as the intensity of breezes strengthens, the stratification in offshore gets eroded resulting in a narrower bulge, just at the same time as the mixing in the near-shore region increases, deepening the plume and promoting the seaward movement of the base of the plume.

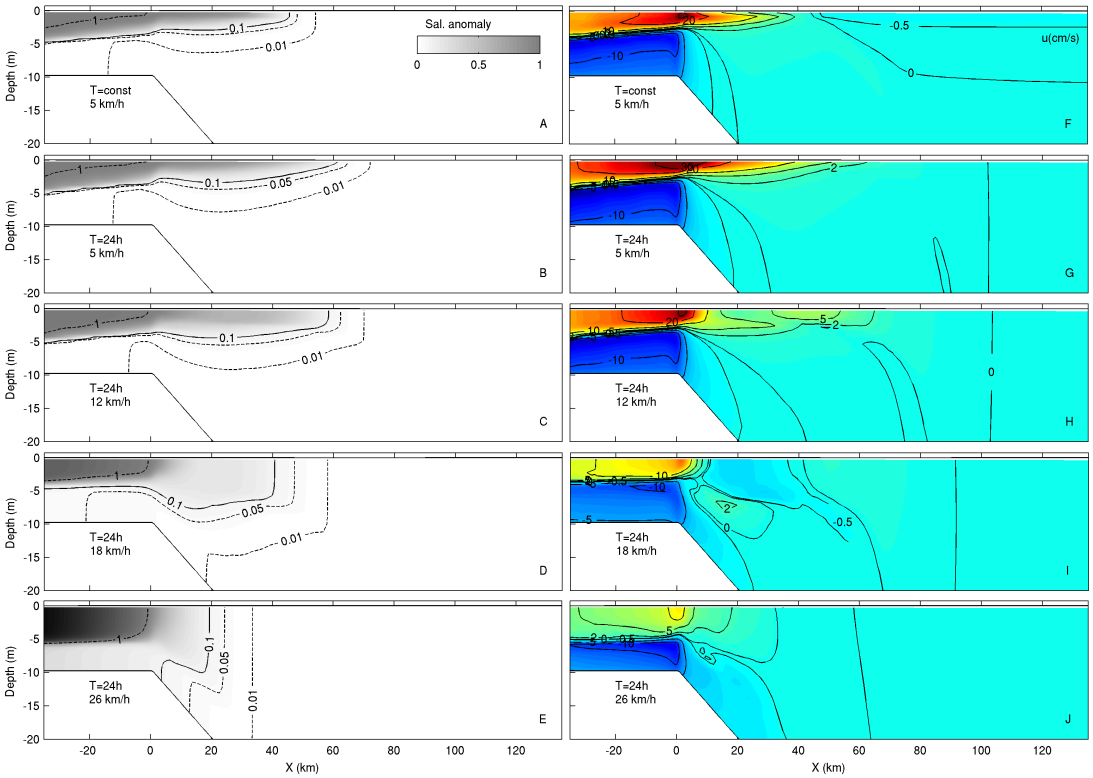

Figure 4.19: *Left:* same as the caption in the previous image, except for vertical features. *Right:* cross-shore velocity corresponding to each panel on the left-hand-side.

4.3 Discussion

The analysis presented in this chapter was focused on the description of plume structures, assuming that most complicating factors are *a priori* absent, and hence the plume comprised the spreading of brackish water released from a moderate freshwater source, attached to a straight coast of constant depth and parallel to the meridians. The plume in this study is located in the Southern Hemisphere and moves over a constant slope bottom. It was found that under this simplified scenario the plume does not reach a steady state, consistent with a number of previous investigations (Nof and Pichevin, 2001; Isobe, 2005), yet the $1000\,\mathrm{m^3 s^{-1}}$ freshwater discharge generated a plume confined to a surface layer not deeper than 4 m, with a downstream and offshore penetration of about 300 and 75 km, respectively.

The circulation in the bulge area consists of an anticyclonic (counter-clockwise) gyre, the diameter of which increases gradually and continually due to the momentum imbalance. The upstream penetration of plume waters is unlike to reach the regions beyond 50 km from the river mouth, regardless of the magnitude of freshwater transport by the river. Notice that what is called upstream penetration is in fact the southern part of the bulge circulation and should not be confused with the

upstream turning of the source inflow mentioned in Garvine (1999), Garvine (2001), Nof (2005), and others. The analysis of momentum terms within the bulge confirmed earlier findings of an imbalance. It was found that the lateral pressure-gradient term and the Coriolis acceleration account for most of the momentum balance within the bulge. The third term in the cyclostrophic balance is considerably smaller than these two, and it is almost the same magnitude as the radial acceleration term. However, a combination of all the remaining term in the momentum equation is either not sufficient to compensate the imbalance generated by the terms in the geostrophic balance, or too large to be neglected. On the other hand, it has been shown for the coastal current that, the cross-shore movement of plume waters is governed by the buoyancy forcing, which takes part in the geostrophic balance along with the pressure at the bottom of the plume and the Coriolis acceleration. The alongshore momentum at the coastal current is balanced by the geostrophic, diffusive, and advective terms, and the orientation of the flow is determined by the buoyancy and advection terms.

It was found that under a modest freshwater inflow of about $1000\,\mathrm{m^3 s^{-1}}$, half of the inflow contributes to the growth of the bulge, while 30% is mixed with the ambient water, and only 20% goes to the coastal current. This freshwater distribution does not resemble any previously reported distribution, but it was noticed that every type of plume is associated with a particular distribution for the inflow freshwater. For instance, Garvine (2001) found a distribution of 94% and 6% for the portions of plume that turned upstream and downstream, respectively in plumes whose main feature was the upstream penetration. Nof and Pichevin (2001) have postulated that high (low) vorticity outflows dumps $^2/_3$ of the freshwater flux into the bulge (coastal current) and vice-versa.

It was shown that considerable amounts of freshwater and even an upstream turn of the inflow can occur when the plumes are forced by winds blowing from the east, or southeast provided that the zonal component of the wind is much large in comparison with the longitudinal counterpart. The same dispersion pattern was found for plumes forced by gentle to moderate sea-breezes blowing predominantly in the southeast direction. Yet, none of the scenarios simulated so far is sufficient to explain the presence of brackish water in the offshore (as in detached from the coast) and upstream regions as revealed by the *in situ* data presented in Chapter 2.

Chapter 5

Process studies in a realistic plume

In this chapter, the dispersion of a plume produced by a moderate discharge source is investigated. Following the identification of the physical processes governing the plume spreading discussed in Chapter 4, the plume's response to external forcing is determined from a series of numerical model experiments. Apart from gaining a better understanding of the plume behaviour in a realistic model setting, this chapter addresses the following questions:

- What is the influence of the relatively large size of the delta on the plume features?
- How does the plume respond to impulsive forcing by local winds, and/or tides?

The first question is addressed by comparing the dispersion patterns produced by single and multiple sources of freshwater buoyancy. The second question is addressed by establishing the differences between a plume forced solely by the river discharge and that subjected to wind and tidal forcing. The lateral spreading of the plume was found to be primarily determined by the wind forcing, and the plume waters are transported along the shore by the Ekman drift. The vertical structure is strongly influenced by the relative magnitude of the buoyancy and tidal forcings. Northerly to northeasterly winds were found to be a plausible explanation for the great deal of brackish water observed poleward from the river mouth reported in Chapter 2.

5.1 Realistic geometry and Etopo2 bathymetry

The idealized model domain and grid presented in Section 3.1 were altered in order to reflect the realistic features of the region. To this extent, a rotating earth configuration is adopted (Coriolis parameter, f, varies with latitude, ϕ, according to $f = 2\Omega sin\phi$), as well as the realistic geometry and bathymetry of the region (Figure 5.1). Bathymetry data was extracted from the global 2 arc-minute (~ 4 km) resolution bathymetry/topography database, Etopo2, then re-sampled at 7.21 km resolution and filtered to avoid isolated high peaks and $2\Delta x$ noise using the algorithm in the ROMSTOOLS package (Penven et al., 2008). Since the model does not have wetting and drying cells, a minimum depth of 3 m is set at the coast (using as sigma coordinate parameters $\theta_b = 0.1$, $\theta_s = 3$, and $h_c = 3$), which overrides the minimum from the detailed bathymetry dataset. The realistic coastline is constrained near the coast by the uniform horizontal grid resolution, set to 4.2 km by 4.2 km, and the third (vertical) dimension is defined by 20 sigma layers with the resolution focused near to the surface. Therefore, the model equations (i.e., the full primitive equations; Hedström, 1997) were solved for a total of 186×163 horizontal gridpoints representing the area bounded by $15^o - 22^oS$ and $34^o - 40^oE$.

The western and northern boundaries are closed, while the southern and eastern are set open with the Orlanski radiation conditions applied for all variables. Initially, the ocean is at rest and homogeneous with salinity set to $S = 35.5$ psu and temper-

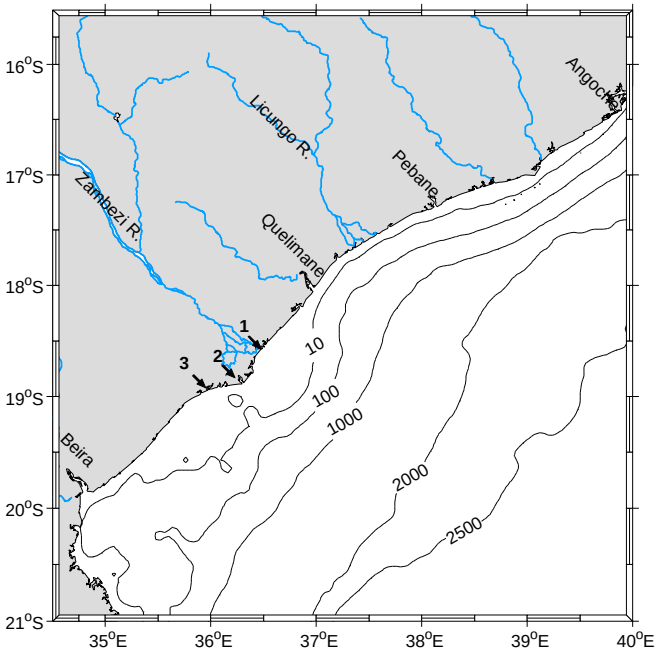

Figure 5.1: Bathymetry of the Sofala Bank, extracted from the etopo2 dataset, which has a spatial resolution of 2 arc-minute, and re-sampled at 7.21 km resolution, and filtered using the algorithm in the ROMSTOOLS.

ature $T = 29^oC$. The model is forced with a volume of brackish water introduced at the three point sources marked by the numbers around the Zambezi River delta in Figure 5.1. The salinity at the buoyancy source is set to 20.5 psu, slightly less than the historical minimum from hydrographic surface data recorded at the station E1 (refer to Figure 2.2), and for simplicity, temperature is kept constant and uniform throughout the simulation.

This configuration constitutes the spin-up run for a number of experiments with varying river discharge, as well as other external forcing (windstress imposed at the free-surface and tides imposed at the lateral boundaries). The spin-up lasts 50 days, and during this time, the total amount of freshwater input is set constant with its value varying between $q_{river} = 1000\,\mathrm{m^3 s^{-1}}$ and $3000\,\mathrm{m^3 s^{-1}}$ in different model runs. These values are a close approximation to the typical river discharges of the dry season and the annual mean, as indicated by gauge records from the past decade (Figure 2.3).

5.1.1 Spin-up run and the unforced buoyant plume

Apart from initializing the plume for various experiments, the objective of the spin-up was to evaluate the influence of the model geometry. The model geometry used differs from the real one only in the nature and location of the freshwater sources. In the real system, freshwater from the Zambezi River enters the ocean through an extensive delta, with three major branches and a number of small ones. The upstream point where the different branches separate from the main channel is located about 70 km from the largest river mouth at the coast, and the water level during spring tides follows the tidal oscillation. Since the distance between the three major river outlets is about ten times larger than the grid size, it is inappropriate to consider the river mouth as a single source. Therefore, in this initial experiment, two sets of model runs were performed in order to investigate the model sensitivity to the choice of buoyancy sources.

The first set consisted of three model runs, where the location of the buoyancy source was varied between the three sources indicated in Figure 5.1, while maintaining constant the freshwater discharge at $q_{river} = 1000\,\mathrm{m^3/s}$. The actual coordinates of the sources in the model were chosen to be as close as possible to the respective river mouths. On the map, the gridpoints used to introduce the freshwater correspond to the mouths of the Chinde River in the northern part of the delta, the Zambezi River (the main flow) at the centre, and Mucelo River to the south (Beilfuss and dos Santos, 2001).

For the second set of runs, apart from increasing the total amount of freshwater input, q_{river}, by a factor of 3, the freshwater was introduced concurrently through

the three source points, first using the same discharge, then differentiating between the mouths. Based on historical anecdotal information about the fluxes in the delta region, the proportion 3 : 5 : 2 for the sharing of discharge between the northern, central and southern sources was used, respectively. An additional run with a freshwater input of 3000 m^3/s introduced through the central source was performed for comparison purposes. Table 5.1 summarizes the discharge parameters used for these runs, where only the freshwater discharge and number of point sources were varied. The main difference between the sources is their location in relation to the central line of the delta, and the depth at each source, which influences the exit velocity of freshwater.

The evolution of plume during the spin-up time (Figure 5.2) is represented by the successive position of the 34 psu isohaline at 5, 15, 30, and 45 days. In analogy to previous chapters, the 34 psu isohaline corresponds to a salinity anomaly of 0.1 (Eq. 4.1), for an ambient salinity of 35.5 psu and source salinity of 20.5 psu. There is a clear difference in the horizontal spreading of the various plumes, which results from the interaction between the brackish water from the plume and either the local bathymetry or the shoreline. Some of the plume features that are distinctive for each source are still noticeable in the shape of the produced when all the three sources are considered. For instance, when freshwater is introduced through the northern source alone, the plume apparently ceases its alongshore spreading after reaching the region near the city of Quelimane, where the bathymetry changes more rapidly. This behaviour is indicated by the 34 psu contour that shows no progression between days 30 and 45 (*cf.* panels 1 and 4 or 5), during the same period, the plume still advances offshore in the bulge region near the source.

The shape of the plumes produced when the central source is considered alone is the least altered by the model geometry, given that the plume shape displays more similarities with the plumes produced in the case of a straight coast configuration (Chapter 4). The reason behind this pattern might be the position of the source in

Table 5.1: Parameters used in the spin-up (SUP) experiment

Run	Source	$q_{river}[m^3/s]$	Depth [m]
SUP-1	1	1000	3.35
SUP-2	2	1000	5.21
SUP-3	3	1000	3.36
SUP-4	1+2+3	3×1000	-
SUP-5	1+2+3	900+1500+600	-
SUP-6	2	3000	5.21

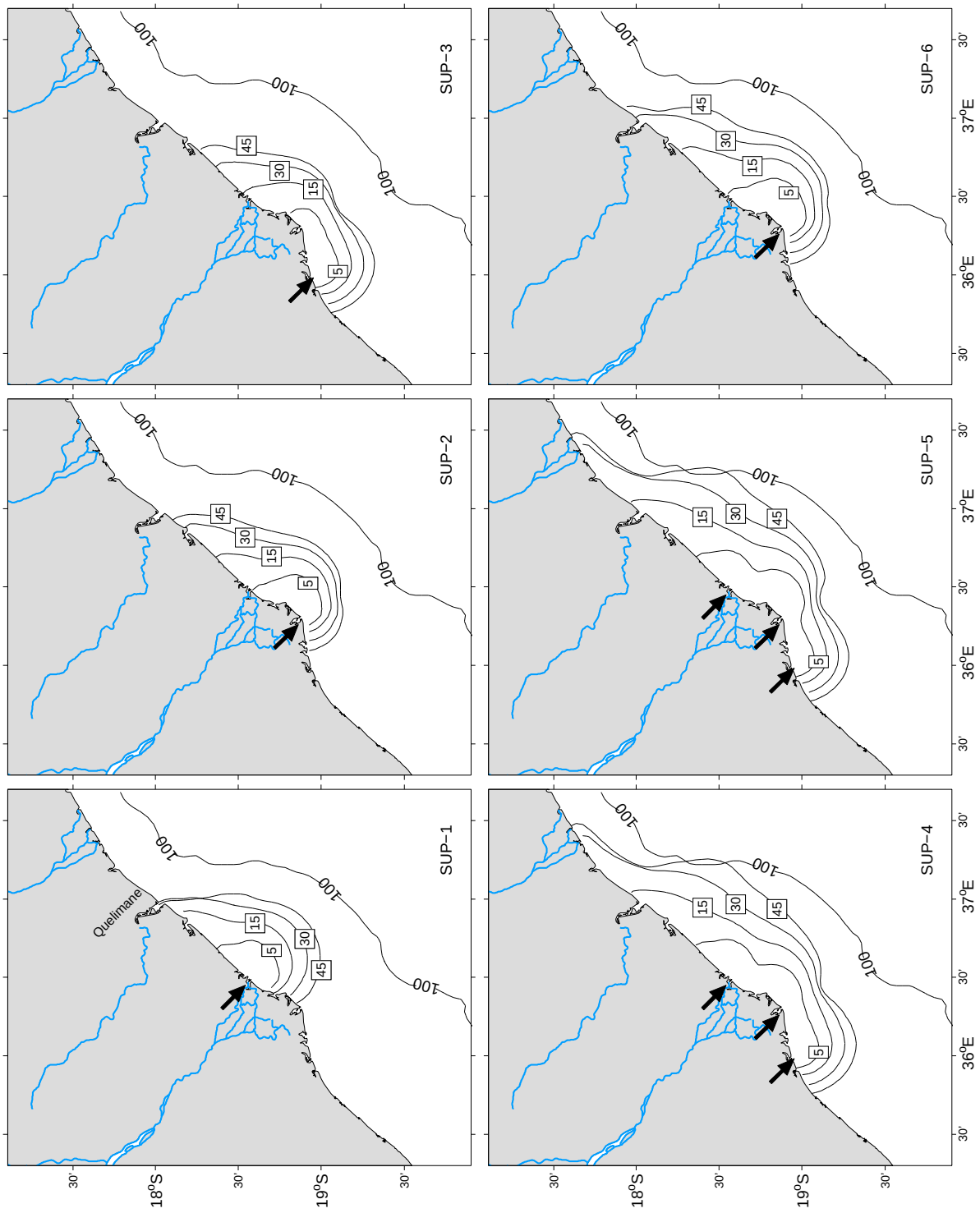

Figure 5.2: Location of isohaline 34 psu at day 5, 15, 30 and 45 for different conditions of buoyancy input, here characterized by the number of point sources and the total discharge. The dark arrows over land indicate the quantity and relative position of point sources. The 100 m isobath is plotted for reference.

relation to the headland (i.e., at the tip), which results in equivalent Bernoulli pressure fields in the southern and northern regions. For these plumes, the meridional component of the pressure gradient force at the source is relatively well-balanced because the flow is not constrained by the coast as it happens in the other two cases.

On the other hand, the southern source generates plumes that are greatly impacted by the geometry. The buoyant water spreads mostly in the alongshore direction by virtue of the seaward bending of the coastline downstream from the source, reaching the central and northern sources in approximately 5 and 15 days, respectively. The exit velocity of the freshwater particles could induce differences in the plume spreading during the early stages of plume formation, however, this is not the case since the differences in depth (Table 5.1) between sources is negligible. It appears that at day 45, the shape of the area bounded by the 34 psu isohaline is not directly affected by the presence of the headland, but instead the local topography acts in a way to produce a protuberance in the plume shape, a feature that will be discussed later.

The maximum alongshore extent attained by the plumes in these three cases is apparently unaltered, which translates to freshwater from the northern source penetrating further north as compared to the other two sources. The above mentioned differences in the plume shape associated with the geometry and topographic factors arising from the presence of a headland suggest that a misrepresentation of the location of the mouth could lead to totally different results, if the realistic bathymetry and geometry are employed. Therefore, the existence of a headland along the shore constitutes a potential source of errors, and it is the one feature present in the Zambezi delta that has not been sufficiently explored in previous river plume studies. The delta in this case protrudes into the coastal ocean to form a nearly symmetric headland of large proportions (about 30×60 km), and it complicates the near-shore dynamics to a great deal.

In summary, the shape of the plume resulting from the combination of the three sources is notably more elongated in comparison with the shapes of the single source plumes, however it contains signatures of each single-source plume. There is not a clear evidence of changes in the offshore plume extent in the region near the sources, but downstream from the river mouth, the combined-source plume is projected offshore and reaches the 100 m isobath. This offshore projection is not apparent in any of the shapes of single-source plumes, and it inhibits the identification of plume zones according to the offshore extent around day 45, as the bulge and coastal current appear to be merged together.

The plume shape produced under combined-sources with similar discharge rates has no significant difference with the shape produced under a differentiate discharge

rate (i.e., using the proportion 3 : 5 : 2). This feature suggests that the resulting plume structure is independent of the proportion of freshwater discharge. On the other hand, the salinity contours in panel 6 of Figure 5.2 indicate that plume structures differ to a great deal when a single source is considered instead of multiple sources, with the alongshore penetration length and offshore projection being considerably reduced in this case (compared to panel 4 or 5). This behaviour suggests that the amount and relative location of sources exerts more control over the structure of the resulting plume than the differences in the freshwater volume discharged in each source.

Density and velocity fields

The horizontal and vertical distributions of properties is examined here for a freshwater discharge of $1500\,\mathrm{m}^3/\mathrm{s}$. All model parameters are kept as described in the previous section. Note that the "point-source" algorithm in ROMS uses the prescribed discharge rate to compute the barotropic velocity at the freshwater source, which is then used to compute the surface level and the pressure gradient term due to buoyancy input. Using the true north orientation of the grid in ROMS, the model requires the river (or point sources) to enter the coastal ocean perpendicularly, since only one direction (either x or y) at a time can be specified for the orientation of the buoyant discharge, and hence the barotropic velocity at the source. This condition contributes to the under-estimation of the influence of river-inertia on the flow in oblique coastlines, in numerical simulations that use domains with true north orientation.

Figure 5.3 presents the simulated surface salinity and velocity fields 50 days after the model initialization. The left panel displays the results from an experiment with freshwater discharged from a single source located at the centre of the delta, while the panel on the right-hand-side shows the plume produced from the combination of the three sources. In both cases, the region nearer the sources consists of less saline water with negative vorticity and a current speed that hardly exceeds 10 cm/s. The salinity increases towards the plume offshore limit, and judging by the location of the 34 psu isohaline, the plume is highly asymmetric in relation to the position of the sources, with the major portion of freshwater found in the northern (downstream) region. It is evident that the plume water turns left and moves northeastwards (along the coast) by virtue of the Coriolis force. No gyre is present in the case of three sources in contrast to the single source case, which suggests that the resulting flow pattern is a consequence of the proximity between sources and the interaction of the flow from each source.

By inspecting the results from the shared-discharge case it was found that near

the sources, the freshwater spreads in all directions, i.e., the flow is radial due to the concentric pressure field arising from the point source parametrization of river discharge. For the central and southern sources, freshwater particles that follow the southward path after their release execute a left turn and join the rest of the plume water. The plume becomes markedly narrower in the region where these flows converge, and the curved isohalines of $31 - 34$ psu change from convex to concave in that stretch. This feature is present in both cases, although it is considerably more pronounced in the case of combined sources, an indication of the alterations to the plume shape brought about by the inclusion of the southern source in the computations.

Away from the source region, the flow tends to be unidirectional and parallel to the coast, in contrast to the region near the sources where the flow varies considerably with the distance offshore. Taking the alongshore flow as positive towards the north, it is found that the near-shore flow changes from negative between the southernmost reach and source #2, where the flow is mainly seaward, to positive in the northern part of the plume. In the central part of the plume (near source #1), the near-shore flow is characterized by weak intensity and high (negative) vorticity. Another striking feature of the dispersion pattern is the intense landward flow of

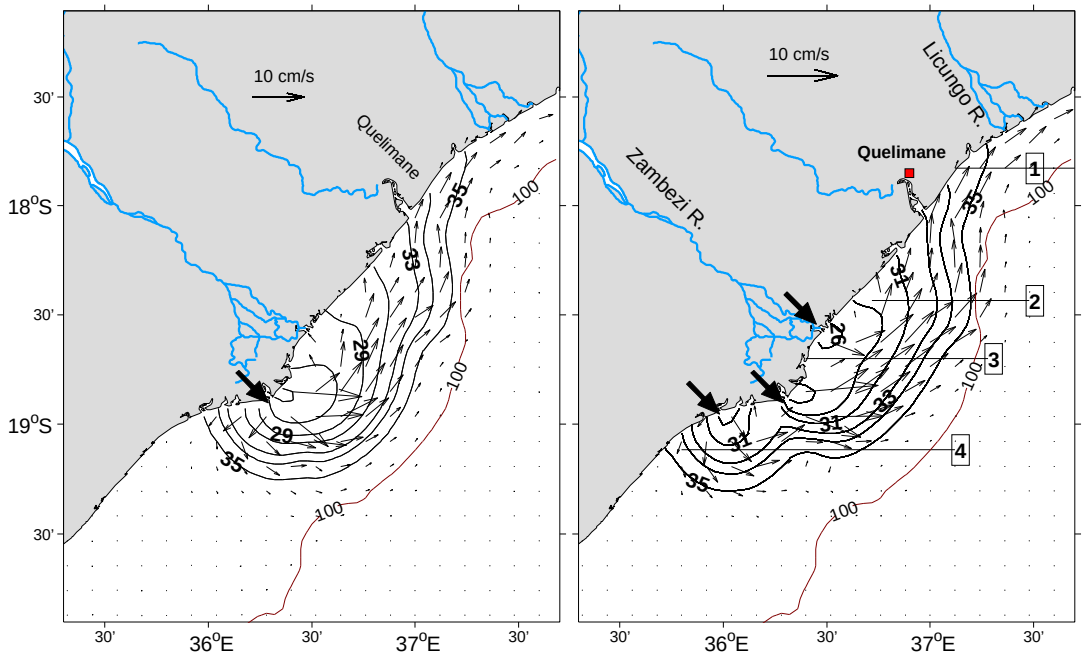

Figure 5.3: Horizontal distribution of surface salinity (contours) and velocity field (arrows) at $t = 50$ days, for the central source discharging $1500\,\mathrm{m^3 s^{-1}}$ (*left*), and the three sources sharing the same discharge using the proportion $3 : 5 : 2$ (right). Velocity vectors are plotted every third gridpoint. The numbered horizontal lines on the right panel indicate the position of sections mentioned in the text.

plume waters with impact angles varying between $45^o \sim 90^o$, occurring between the northern source and the city of Quelimane ($18^o - 18^o30'S$), nearly following the bathymetry contour. Outside the plume limits, the water is nearly quiescent.

The flow regimes mentioned above represent an advanced stage of the plume formation, and have evolved from the radial and symmetric flow resulting from the pressure gradient due to salinity difference near the sources, which is established soon after the buoyant discharge is released. In addition to the radial flow, each freshwater particle has a prescribed initial acceleration proportional to the discharged volume, chosen to be along the x-axis. Although the initial motion of the buoyant discharge occurs in the cross-shore direction, the Coriolis effect comes into play at the early stage of plume formation, causing the density-driven flow to veer northwardly. This behaviour then results in plume asymmetry in relation to the location of sources, as the buoyant waters are transported northeastwards along the coast.

In summary, the horizontal plume structure presented in Figure 5.3, which corresponds to the fully-developed stage (refer to the discussion of Figure 4.1), is characterized by freshwater that spreads radially, with portions that after leaving the source, execute a left turn and form a coastal current that ultimately moves northeastwards along the coast. The magnitude of the density-driven flow is almost invariant, in contrast with its orientation that changes from landward near the sources to parallel to the coast towards the leading nose.

The vertical distribution of salinity (contours in Figure 5.4) shows that there is not much difference between the vertical structure of the plumes produced in the single-source and combined-source configurations. However, in the southern region where the near-shore flow is directed mostly southwards, the plume is limited to a thin surface layer of lighter water, located further landward in the case of combined sources. This pattern constitutes the most significant difference in the vertical structures of the plume in the two cases, which can be explained by the presence and proximity to source #3. The plume waters occupy the entire water column near the coast, with the density shear decreasing seawards as indicated by the isohalines that extend from the surface to the bottom at the offshore plume limit. This structure is consistent with the *bottom-advected* plumes of Yankovsky and Chapman (1997), and owes its characteristics to the extensive and shallow shelf. A density front separating the plume from ambient water is apparently not present in any of the transects displayed, indicating a gradual mixing between the two environments.

The vertical structure of velocity indicates that the flow is in general weak, with the maximum cross-shore velocity ($\sim 6\,\mathrm{cm/s}$) occurring in the region nearer the sources (cf. transect taken along $18^o37.5'S$ and $18^o26.1'S$ in Fig. 5.4). In

the southern region of the plume where the flow executes the left (northwards) turn, there is a bottom layer of denser water flowing landwards by virtue of bottom friction, resulting from the interaction between the plume induced motion and the topography. The landward flow is limited to the depression zone, and reaches its maximum intensity at the depression side facing the ocean, as can be seen in the transects of either the single-source case or the combined-source case (bottom panels of Figure 5.4). In addition, vertical velocity shear is elevated in this region as well as in the region near the sources, and it is almost insignificant in the regions with landward flow (top panels in Figure 5.4).

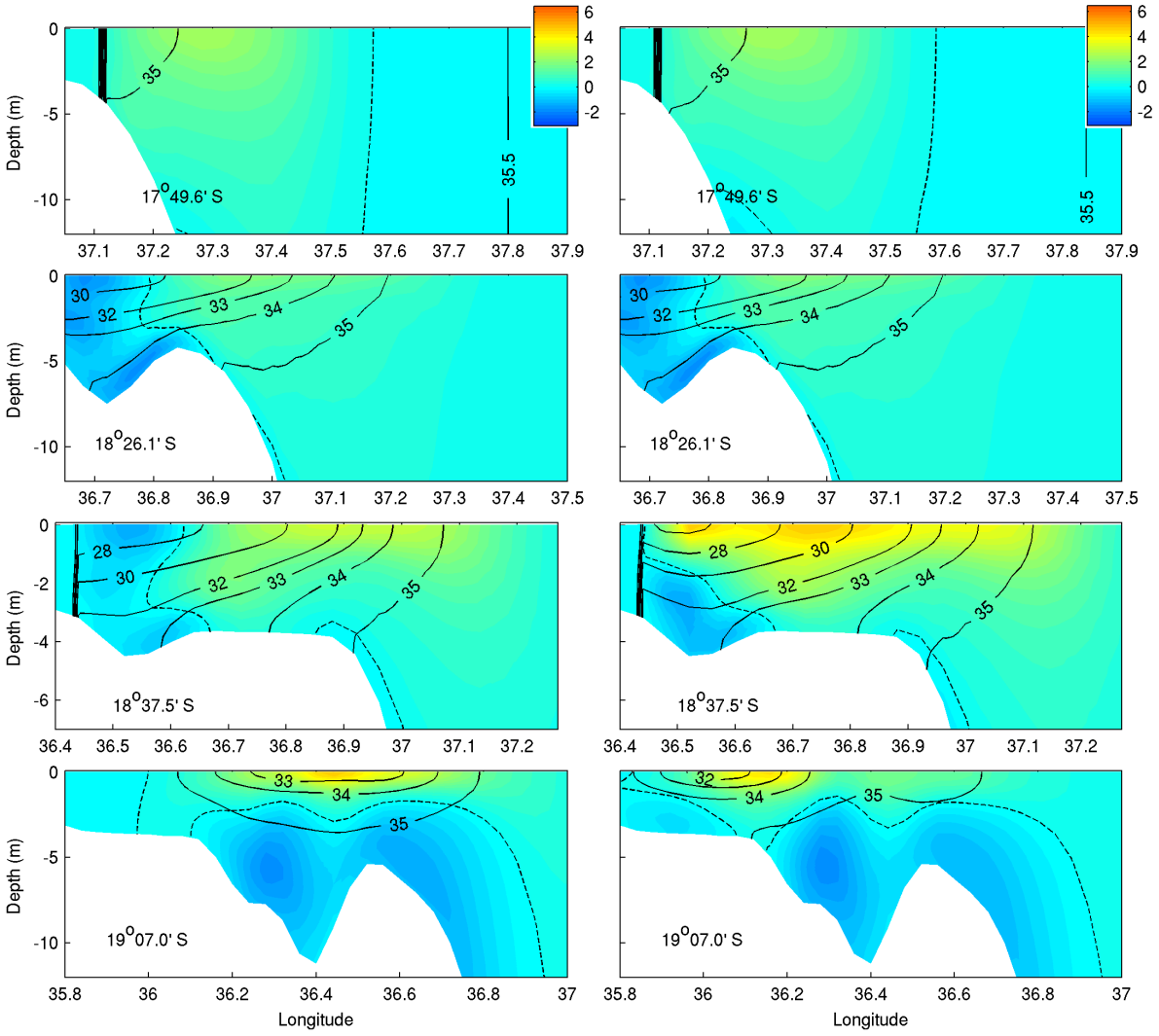

Figure 5.4: Vertical distribution of salinity (contours) and cross-shore velocity in cm/s (colors) for the central source alone (*left*); and for the three sources (right). In both cases the total discharge is $1500\,\mathrm{m^3 s^{-1}}$. From top to bottom, transects represent the region of positive coastal current, landward flow, radial flow near the sources, and negative flow (section marked in Fig. 5.3 by 1, 2, 3, and 4, respectively). Data was plotted from as close as possible to the coastline, and therefore the vertical and horizontal axes are different. The dashed contour represent the zero velocity.

Momentum balance

The default settings of the present model include an option that allows the computation and storing of the terms in the momentum balance equations for every grid point at every internal time-step, with and without the averaging of fields. Making use of this option, the momentum balance terms at the end of the spin-up run were computed for two transects located along the latitudes $18^o37.5'S$ and $19^o07.0'S$, and the results are presented in Figures 5.5 and 5.6. Shown are the zonal and meridional components of the Coriolis acceleration, pressure gradient, advection, and mixing terms. The latter two terms represent the combination of their horizontal and vertical counterparts, and the pressure term accounts for the effects of both buoyancy and bottom pressure (i.e., baroclinic and barotropic pressure gradient).

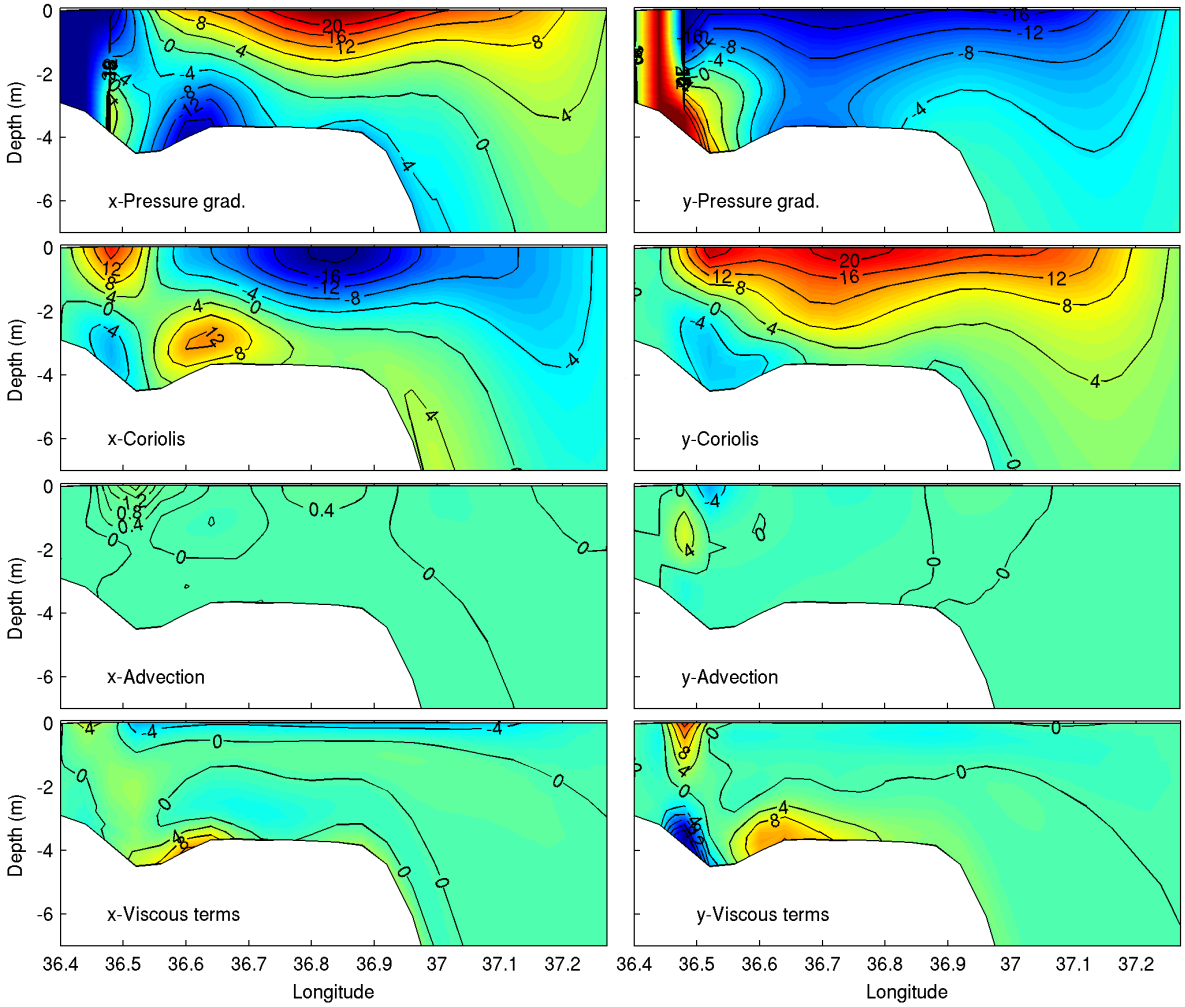

Figure 5.5: Vertical distribution of the east-west (*left*) and south-north (*right*) components of the momentum terms, computed at the end of the spin-up ($t = 50$ days) along the latitude $18^o37.5'S$, for the case of three point sources discharging $1500\,\mathrm{m^3 s^{-1}}$. Units are $10^{-7}\,\mathrm{m\,s^{-2}}$ for all terms. The sign notation is such that the local acceleration (not shown) balances all the other terms of the momentum equation.

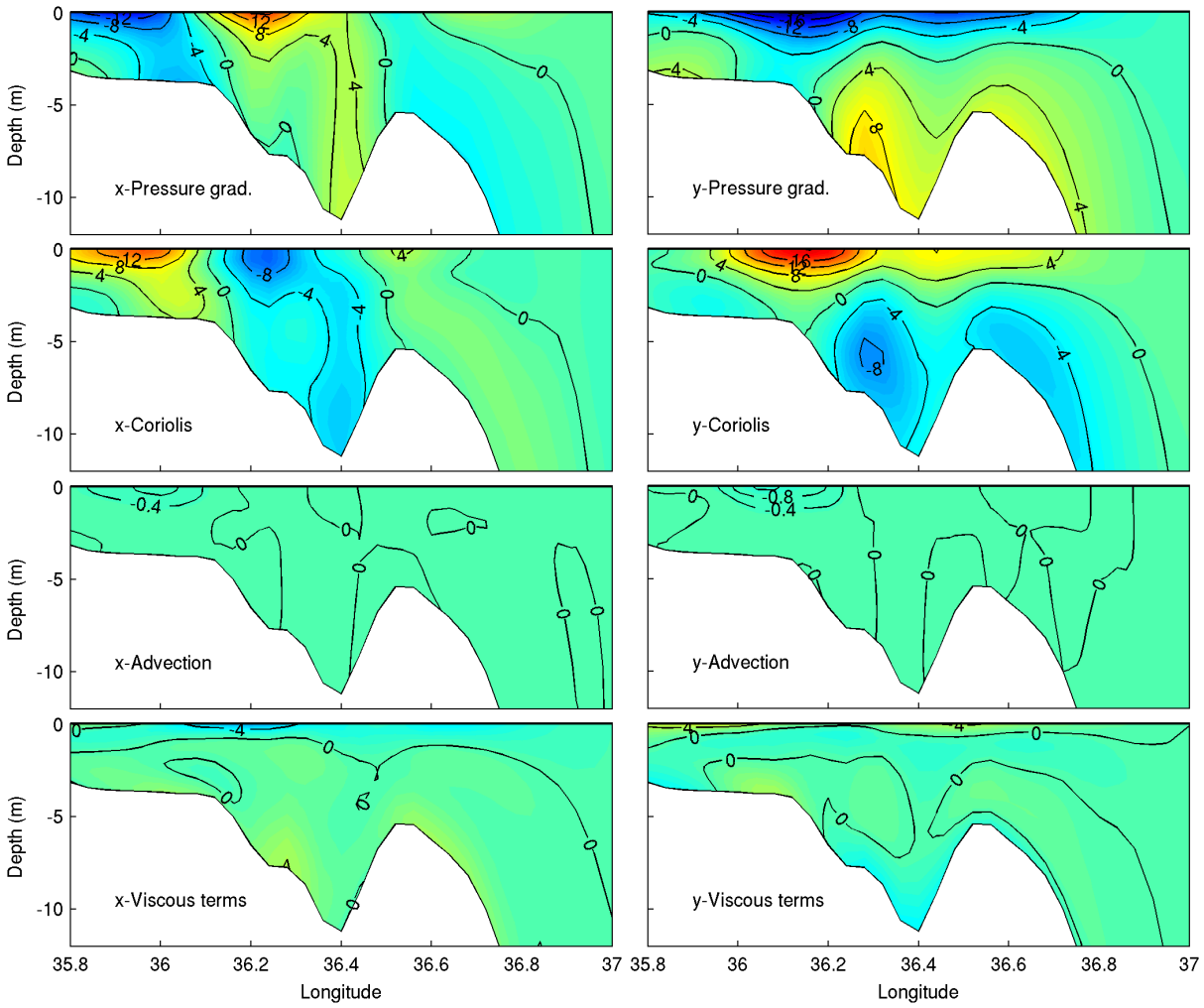

Figure 5.6: Same as in Figure 5.5, except for a transect along the latitude $19^o07.0'S$.

The flow is driven by the pressure gradient term, which is primarily balanced by the Coriolis term everywhere except at a few specific locations, as follows. Firstly, near the coast, the lighter water is transported upstream (opposing the sense of propagation of a Kelvin wave) by virtue of advective processes, as depicted in the vertical distribution of the advection terms in both directions. Secondly, in the bottom layer throughout the shelf zone, the bottom friction acts in a way to slow down the motion of plume waters. Thirdly, in the surface layer, the contribution of shear velocity to the viscous terms compensates the geostrophic imbalance. Lastly, in locations with irregular topography, the combination of advection and mixing accounts for the imbalance, and a different flow regime exists, which depends on the dimensions of the topographic irregularities which can modify the flow all the way from the surface to the bottom.

The surface flow along the transect at $18^o37.5'S$ is primarily oriented north-eastwards (see transect 3 in the left panel of Figure 5.3), which is a consequence

of the similar magnitudes of the zonal and meridional components of the Coriolis term (Figure 5.5). Also, there exists a depression in the bottom topography, deep enough to alter the pressure field near the bottom. Therefore, the zonal component of the pressure gradient term at the depression is positive in the downward slope and negative in the upward slope. This difference occurs because near the seabed, the buoyancy forcing in Eq. (4.8) is dominated by the bottom pressure, which increases with the depth. However, it is this difference in pressure gradient that results in opposite alongshore flows at each side of the depression, as evidenced in the zonal Coriolis term ($-fv$). The cross-shore flow in the bottom layer is oriented landwards as a result of the excess bottom friction in the upward slope generated by the seaward flow at the surface layer. Here, there is a clear separation of the effects of buoyancy and bottom friction, which determines the opposing flow regimes at the surface and bottom layers, respectively. Conversely, the Coriolis term at the transect taken along $19^o07.0'S$ (Figure 5.6) indicates a positive alongshore flow of the entire water column within the depression. This flow is purely geostrophic in nature, however buoyancy plays a major role in the surface layer, while the bottom pressure (through the topographic effects induced by the flow of denser water along the upward slope of the depression) is most significant in the bottom layer.

Summary of the buoyancy-driven motion of a plume

Very often, numerical simulations of unforced buoyant discharges over constant slope topography present a bulge of re-circulating flow connected to a coastal current, with the whole system being strongly influenced by river inertia and the Earth's rotation. This is the case of the numerical results presented in Chapter 4. In this section, realistic bathymetry and model geometry were used in the plume simulation and the results produced at the end of spin-up pointed to large differences between the structure of the current plume and that described in the previous chapter. For instance, no distinct separation was found between the bulge region and the coastal current, not to mention the absence of re-circulation in front of sources. Conversely, the plume consisted of brackish water that spread radially at the sources, and north-eastwards (along the coast) away from the sources. The merging of bulge and coastal current was attributed to the fact that freshwater enters the ocean through a delta, here represented as three point sources rather than a single outlet. However, apart from the re-circulation in front of the source, the plume structure produced by a single source discharge located at the centre of the delta presented many similarities with that produced when the discharges from three point sources were combined. Further analysis showed that the freshwater spreads as a *bottom-advected* plume (i.e., maintain contact with the bottom to a distance well offshore) regardless of the

choice of amount and location of the point sources. This contrasts the results from the straight coastline experiments, which produced a surface advected plume.

5.1.2 Wind effects on the plume structure

The objective of the next experiment is to examine the alterations brought about by the wind forcing on the above described plume structure. The wind-forced simulation starts from the end of the spin-up and lasts 10 days, hence all the model parameters described in the previous section were kept unaltered, except the windstress that was increased from the spin-up value ($\tau/\rho_0 = 0\,\mathrm{m}^2/\mathrm{s}^2$) to a maximum value corresponding to either the weak wind conditions (i.e., windspeed of 5 km/h), or the moderate wind conditions (i.e., windspeed of 12 km/h). It is worth mentioning that tests with strong wind conditions often resulted in model crash due to numerical instabilities, and for that reason, the response to strong winds are not discussed here. The windstress was imposed using a ramp function in time, which starts with zero windstress (i.e., the spin-up condition), reaches its maximum value over one inertial period ($T_i = 1.55$ days), and then becomes constant until the end of the simulation.

Two sets of 10-day simulations were undertaken, each consisting of 16 model runs that comprise 2 sets of wind strengths (weak and moderate), and 8 runs with different wind direction. The latter parameter was varied between the four major directions (i.e., north, west, south, and east), and the directions in a rotated system where the orientations correspond to a clockwise rotation (by 40^o) of the model coordinate system (positive in the true north and east directions) to a local "alongshore"-"cross-shore" coordinate system, (τ_l, τ_c, after Kourafalou et al., 1996b).

Under the action of weak or moderate winds, the buoyant discharge was spread downwind in all the 16 cases analyzed, resulting in a plume shape that can be categorized in two groups, namely the ones exhibiting a "*large bulge*", and those featuring a "*coastal current*". The groups were identified according to the horizontal distribution of surface salinity combined with the direction of the flow attained at the end of the 10-day wind forcing. Examples are presented in Figures 5.7 and 5.8, for each group respectively.

The downwind transport of plume waters is in good agreement with earlier studies on buoyant discharges over shallow and sloping topography (Chao, 1988b; Kourafalou et al., 1996b), as well as the theory of Ekman transport (Kampf, 2008; Cushman-Roisin and Beckers, 2009). None of the plumes featuring a coastal current extended as far north as the mouth of the Licungo river (refer to the panel A of Figure 5.7), except for the plumes forced by positive alongshore winds, and none of

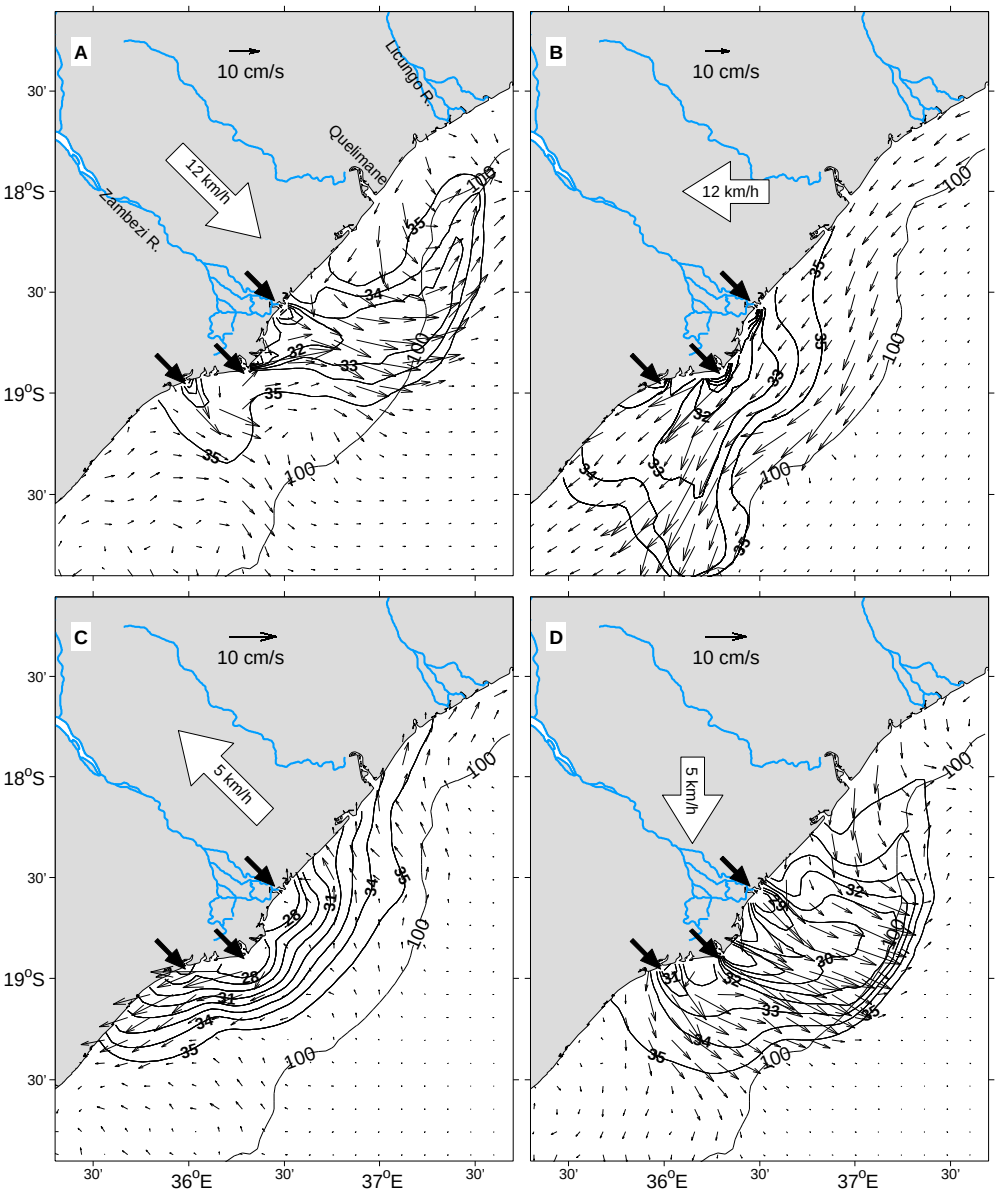

Figure 5.7: Simulated surface salinity (contour) and velocity (arrow) after 10 days of wind forcing for the three source points and different wind direction and magnitude, as indicated by the large arrow over land. Shown are some of the cases that resulted in a large bulge. The 100 m isobath is also showed.

the plumes featuring a large bulge near the sources extended offshore beyond the 100 m isobath.

The "*large bulges*" were formed under northerly, easterly, negative alongshore, moderate positive across-shore, and weak negative across-shore wind cases (Figure 5.9). Winds blowing in these directions induce a surface current in the vicinity of the freshwater sources that is either directed seawards, or directed along the coast towards the southern model boundary. These flows inhibit the development of a buoyant flow in the downstream direction (i.e., in the direction of propagation of a

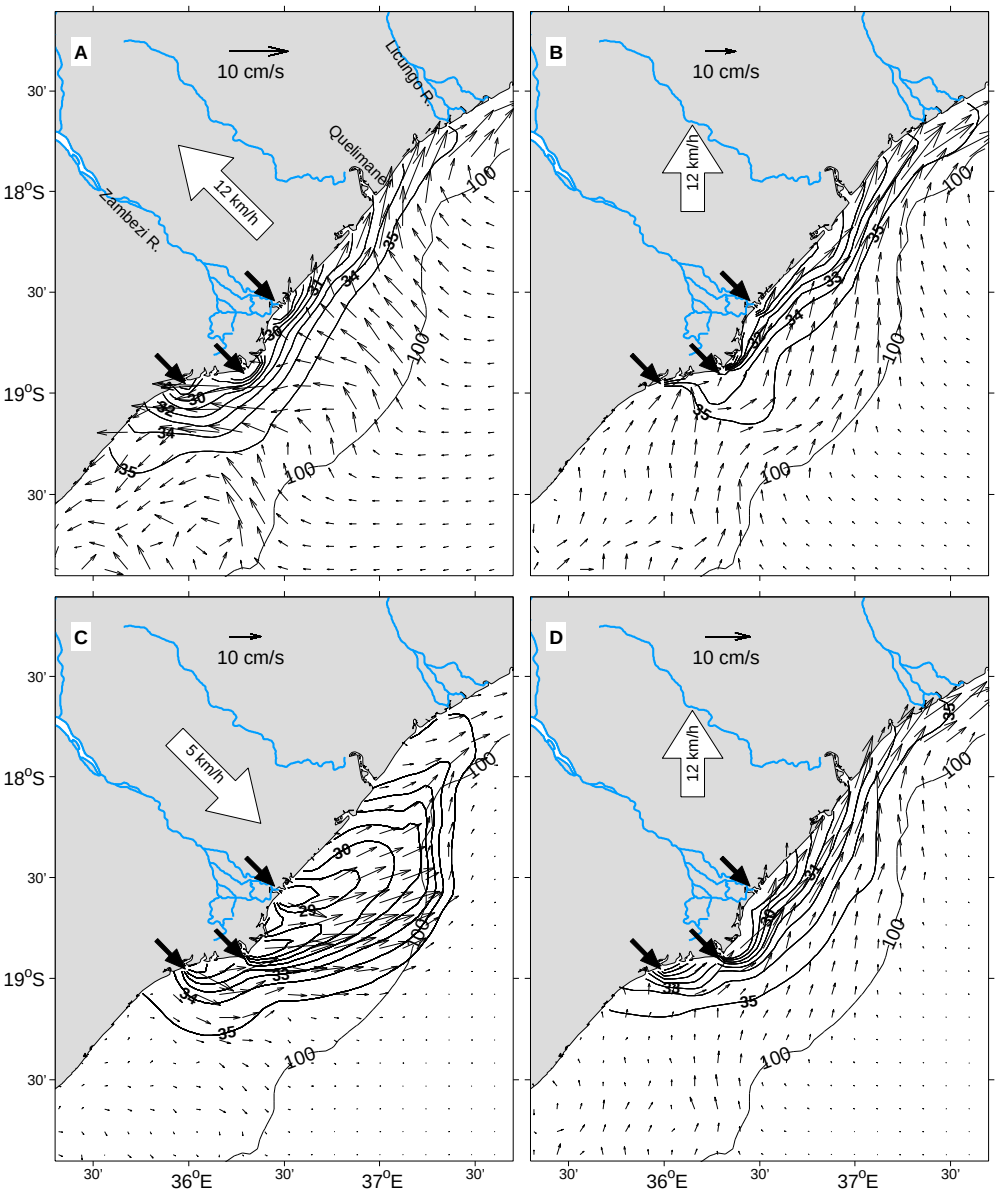

Figure 5.8: Same as in Figure 5.7, except for some of the cases that resulted in a coastal current connected to a small bulge.

Kelvin wave), and promote the accumulation of freshwater immediately in front of the delta. Depending on the windstress magnitude, the shape of the bulge changes from symmetric in relation to source #2, to distorted (displaced towards the south or north).

Plumes that feature a *"coastal current"* were produced under westerly, southerly, positive alongshore, moderate negative across-shore, and weak positive across-shore wind cases (Figure 5.9). The largest downstream penetration of the coastal current was found under the action of weak positive alongshore and moderate southerly winds, and it reached about 140 km downstream (measured from the source #1). However, the penetration distance in the remaining cases that resulted in a coastal

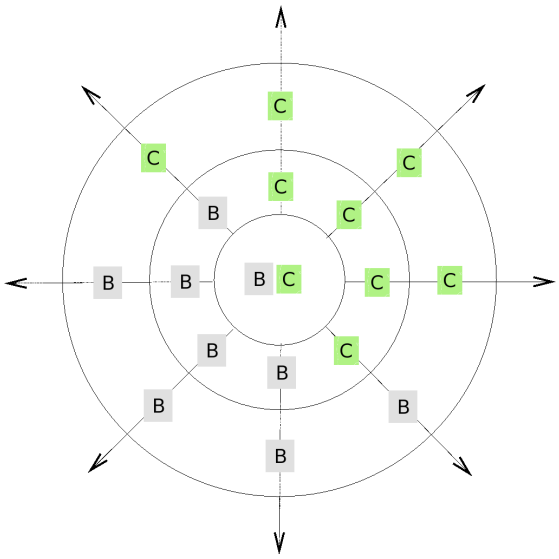

Figure 5.9: Shape of plume classified as bulge (B) or coastal current (C), as simulated for a discharge of $1500\,\mathrm{m^3 s^{-1}}$ under different wind conditions. The inner circle represents the spin-up results (no wind forcing), the middle circle represents the weak winds (5 km/h), and the outer circle represents the moderate wind conditions (12 km/h). Arrows indicate the direction of wind blowing.

current was not very different from this value, as the shortest penetration was about 110 km. On the other hand, the upstream penetration varied considerably from nearly no penetration to a few kilometers measured from source #3. The upstream penetration did not depend much on the intensity of windstress but rather on the strength of the wind-driven ambient current generated upstream from the plume (around $\sim 19^o30'S$). Similarly, the maximum width of the bulge was in the range of approximately $0.5 \sim 1.5$ times greater than the maximum width of the coastal current (measured half way to the nose of the current), which also indicates that in some cases, the bulge and coastal current could not be distinguished. According to the classification schemes of Chao (1988a) and Kourafalou et al. (1996b), these plumes can be classified as subcritical to diffusive-subcritical.

The inclusion of windstress in the computations caused the transport of buoyant water by the coastal current to occur primarily attached to the coast. This statement is based on the observation that the regions containing a uniform flow away from the coast and connected to a landward flow, which were prominent features in the unforced plume, do not appear in wind forced plumes. Overall, one finds that two types of plumes can be associated with the alongshore component of the wind, namely, a "*large bulge*" produced under a negative wind component, and a "*coastal current*" produced under a positive wind. An exception to these patterns comprises the plumes forced by across-shore winds (i.e., having zero alongshore component), for which the plume shape is defined by the wind orientation and intensity. In

this case, a strong negative or weak positive wind results in a coastal current, and the opposite results in a bulge. Here, a negative wind blows directly landwards while a positive blows seawards. This result is interesting mostly because the actual annual mean wind field in the study region is predominantly oriented northwestward (southeasterly), according to the data measured between 2002 and 2007 at a ground station located in the Quelimane city airport (data analyzed in a previous study, Nehama, 2008). The satellite derived winds presented in Figure 2.4 also indicate a predominance of southeasterly winds in the region. Based on this result, it is suggested that the shape of plumes observed at any particular time will strongly depends on the wind field (i.e., its magnitude, orientation, and possibly the timing).

It is worth mentioning that the identification of plume type as "coastal current" or "large bulge" for plumes under the action of across-shore winds was mostly based on the shape of the salinity contours rather than the flow field itself. In fact, landward winds induce a divergence of surface flow near the coast, with the northern part of the plume flowing northeastwards along the coast, and the southern part flowing towards the southwest. Hence, under weak winds, the bulge attains a considerably large size that suggested the designation of "large bulge" (*cf.* Figure 5.7.C), but it is strongly pressed against the coast under moderate winds, intensifying the flow in the northern part and gaining the appearance of a coastal current (Figure 5.8.A). Similarly, for the positive weak wind case, transport of brackish water occurs towards the northeast in what was previously termed "coastal current", in spite of the transport not being parallel to the coast. A moderate version of these winds promotes a similar transport but offshore, as in detached from the coast. These discrepancies highlight the importance of the wind field in the determination of plume dispersion patterns.

With a few exceptions, all the wind-forced plumes exhibited an irregular shape, particularly in the southern half of the bulge, where a protuberance is present. In the previous section, these small irregularities in the bulge shape were attributed to convergence in front of the bulge of selected parts of the flow that initially was radial. The results from the current experiments indicate that in some cases these features do not disappear after 10 days of wind forcing. In fact, some wind conditions even intensify the protuberances rendering an irregular plume shape. The cases in which the protuberances were completely washed out from the plume shape include, but are not limited to, the majority of plumes classified as coastal current.

The plumes produced under the action of moderate alongshore negative and westward winds displayed a feature that is worth discussing. The movement of plume waters was oriented upstream (i.e., opposite to the sense of a Kelvin wave), with the orientation of velocity vectors varying between 220^o (i.e., parallel to the coast) and 270^o. An example is displayed in panel B of Figure 5.7, which shows a

large bulge spreading southwards in a non-uniform velocity field. The near-shore flow is oriented primarily towards the southwest, and it intensifies seaward. The maximum southward penetration of brackish waters is in general comparable to half the length of a typical coastal current ($\sim 50 - 100\,\mathrm{km}$), but whenever this feature was present, the amount of freshwater present in the upstream coast exceeded that in the downstream. Although there is a considerable amount of freshwater in the region downstream from the sources, a coastal current is absent as indicated by the southwestward oriented velocity vectors.

Figure 5.10 displays the momentum balance along a zonal transect located south of source #3 recorded for a plume forced by moderate westward winds. Contrary to the unforced plume, the pressure gradient and the Coriolis terms do not balance each other, but rather contribute to a three-way balance between these two and the viscous term, which now incorporates the effects of wind mixing, bottom friction and velocity shear. The primary direction of plume spreading is not consistent with the numerical results obtained for a straight coast and gently sloping topography (Section 4.2), which predicted flow attached to the southern coast under the action of moderate winds. The reason for this discrepancy is the presence of a landmass downstream of the flow. Due to the coastline orientation in the current experiment, the near-shore flow in the region to the south of the sources is not completely obstructed by the landmass, which allows the development of a zonal velocity component that promotes the widening of the plume bulge. It then follows that, the seaward transport of plume waters is a process induced by the poleward flowing wind-driven current, and flow adjustment to changes in the bottom topography (i.e., a geostrophic adjustment with the Coriolis acceleration playing the major role, as illustrated in Figure 5.10).

Contrary to the case of a straight coast, the present results are not strictly consistent with either the theory of Ekman drift which predicts surface motion oriented at 45^o to the left of the wind in deep water, nor the field observations of flow in shallow waters that report surface flow parallel to the local winds Gelfenbaum and Stumpf 1993. In the current case, the surface velocity field in the region between the coast and the 100 m isobath computed for westward moderate winds (Figure 5.7.B) is oriented towards the southwest (i.e., corresponding to an angle of 45^o). In the regions where the water column shoals, the surface current intensifies and the angle between the wind and the surface flow increases, resulting in the brackish water being transported nearly southwards (i.e., corresponding to an angle $>45^o$). These flow modifications are driven by and can be explained by bottom processes associated with the topographic irregularities. It is then concluded that the upstream penetration of plume waters described above is a process intrinsically related to the local geomorphological features, namely the shallow and rough topography, and the

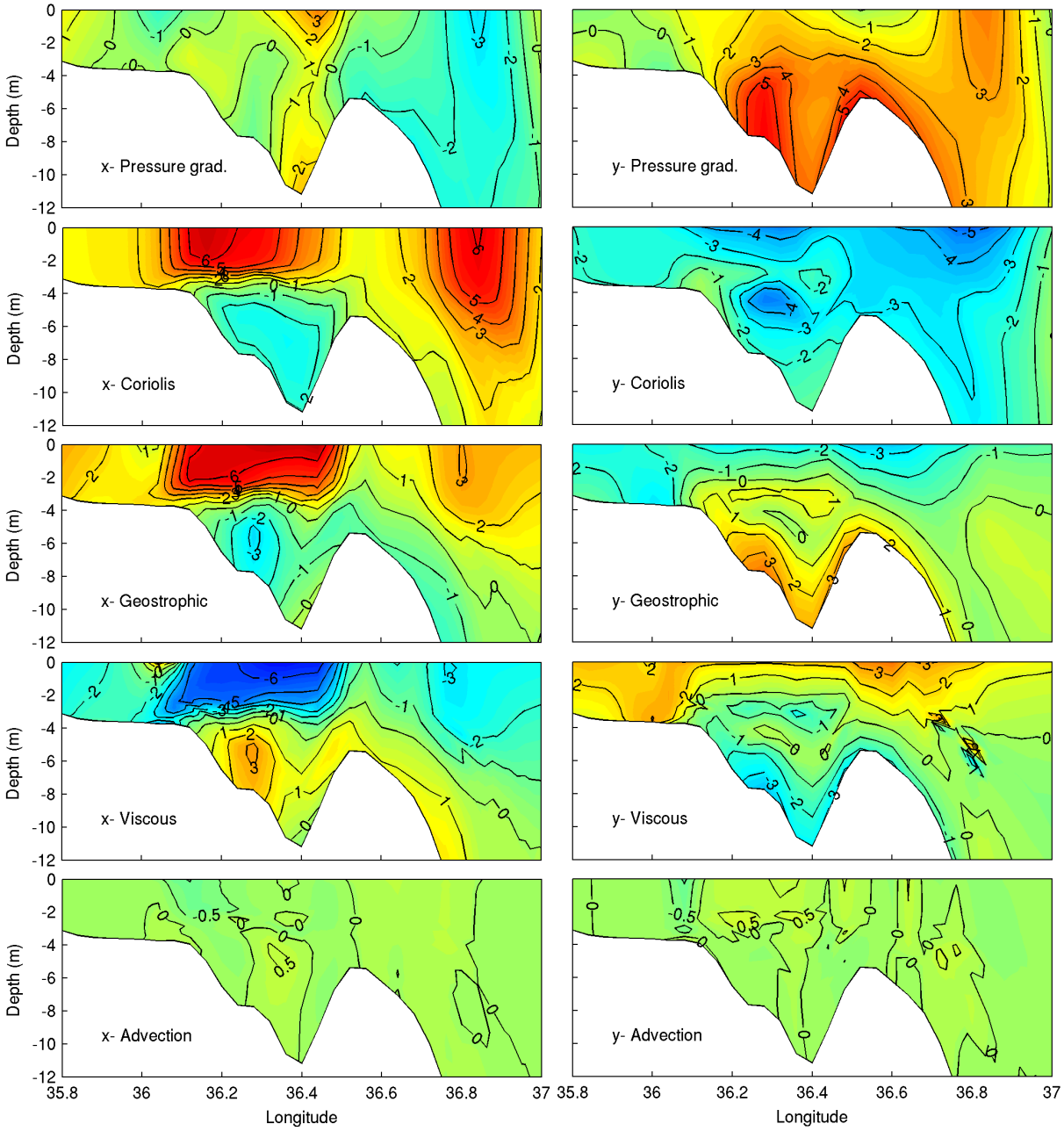

Figure 5.10: Vertical distribution of the zonal (*left*) and meridional (*right*) components of the momentum terms along the latitude $19^o07.0'S$, 10 days after an easterly moderate wind started blowing over a pre-existing plume. Contours are $10^{-7}\,\mathrm{m\,s^{-2}}$ for all terms. The sign notation is such that the local acceleration (not shown) balances all the other terms of the momentum equation.

details along the coastline (including the orientation relative to the true North).

Plume structure under an oscillating wind field

Coastal systems are often subjected to the action of sea-breezes in which, the wind direction and intensity change during the day, with its vector following a elliptical trajectory. In order to investigate the influence of this wind field on a pre-existing dry-season plume ($q_{river} = 1500\,\mathrm{m}^3/\mathrm{s}$), an experiment was conducted consisting of two sets of model runs, using the idealized sea-breezes described in Eq. (3.3), where the phase difference ϕ_τ, and the wind velocity components used to compute the mean magnitude, τ_0, and the sea-breeze amplitude, τ_1, were varied as indicated in Table 5.2. The sea-breeze was imposed from the end of the spin-up run and lasted 10 days.

The first set of model runs (runs 1-4 in Table 5.2) aimed at investigating the plume response to symmetric sea-breezes (i.e., centre of the windstress ellipsoid located at the origin). The magnitude of breezes for each run was chosen to match values corresponding to the Beaufort numbers 2 through 5 (light, gentle, moderate, and fresh breezes), and the phases were approximated to the average direction of QuikSCAT winds (computed for a $2^o \times 2^o$ box centred at the Zambezi delta).

The sign of the averaged wind velocity components in (Table 5.2) determines the quadrant in which the centre of the ellipsoid is located, and hence, the orientation of the wind forcing, while the phase difference between the x- and y- components determines the ellipse's orientation. Provided that the phase difference in runs 5-7 is nearly the same (i.e., it varies between 237^o and 259^o), the ellipses in these cases will have the same orientation. Their position in the Cartesian orthogonal system will vary as shown in panels B, C, and D of Figure 5.11 .

Table 5.2: Wind velocity components used in the experiment with sea-breezes. Subscript zero indicates the averaged wind velocity (km/h), while the subscript one indicates the sea-breeze amplitude (km/h). These parameters, along with the phase lag (ϕ_τ, in *degrees*), were incorporated into equations (3.2) and (3.3) to determine the windstress components, τ_x and τ_y.

Run	U_0 , V_0	U_1 , V_1	$\phi_{\tau x}$, $\phi_{\tau y}$
1	0.0 , 0.0	$5.0cos(\phi_{\tau y})$, $5.0sin(\phi_{\tau y})$	180 , 130
2	0.0 , 0.0	$12.0cos(\phi_{\tau y})$, $12.0sin(\phi_{\tau y})$	180 , 130
3	0.0 , 0.0	$18.0cos(\phi_{\tau y})$, $18.0sin(\phi_{\tau y})$	180 , 130
4	0.0 , 0.0	$26.0cos(\phi_{\tau y})$, $26.0sin(\phi_{\tau y})$	180 , 130
5	−5.67 , 10.15	7.49 , 7.15	115.9 , −142.9
6	1.41 , 8.54	5.64 , 4.75	142.7 , −108.3
7	−13.49 , 0.19	7.21 , 9.93	103.3 , −133.9

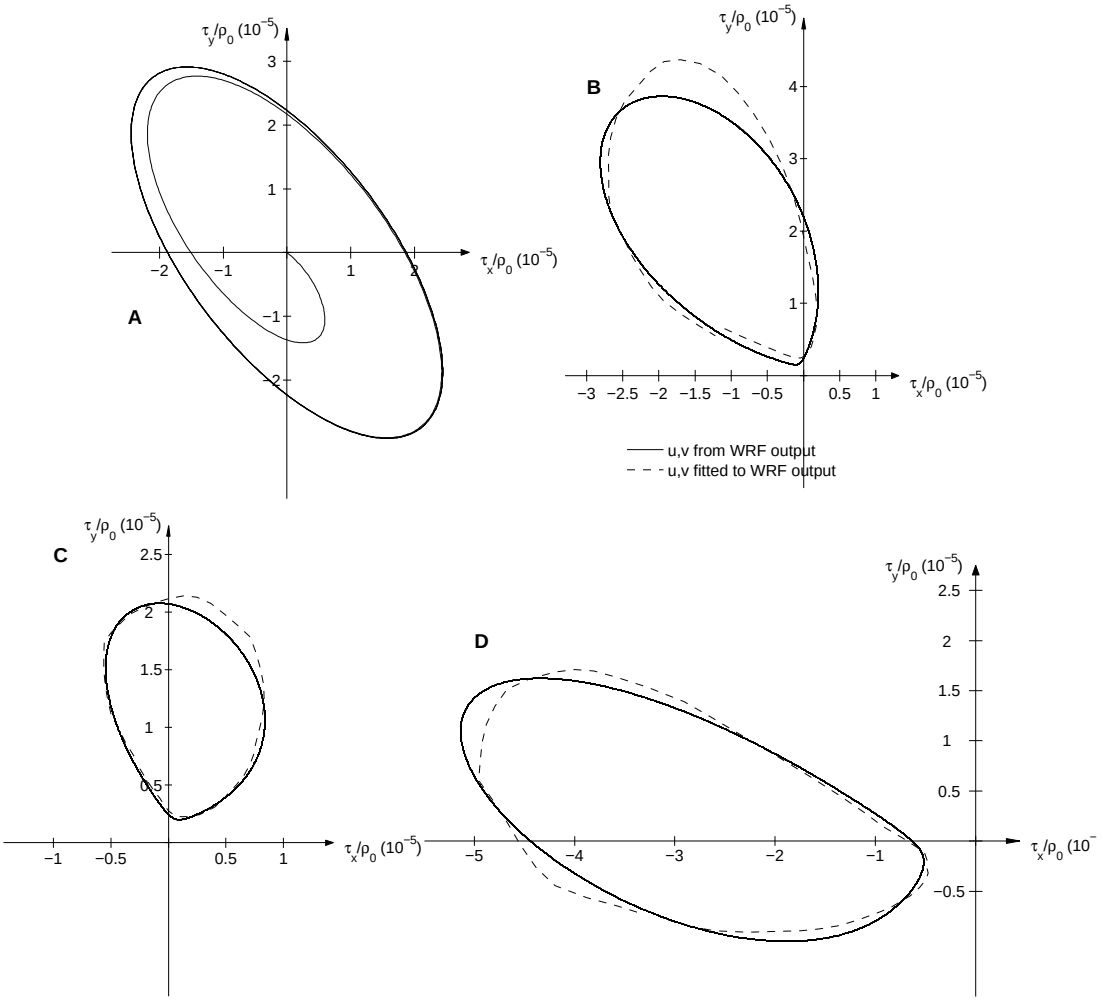

Figure 5.11: Windstress used in the experiment with sea-breezes. (A): analytical windstress computed from the average conditions in February; (B-D): windstress calculated from WRF simulated velocities fitted to a curve using the least-squares method.

High-frequency wind data

The wind conditions for the second set of runs (runs 5-7 in Table 5.2) were extracted from a 2-year long high-frequency data output from the Weather Research and Forecasting model (WRF) using the least-squares approach. WRF was set up and run specifically for this study and the data were made available by Mr Genito Maure (currently at CSAG). The model was forced with sea surface temperature (SST) extracted from the National Oceanic and Atmospheric Administration (NOAA) dataset, and boundary conditions from the NCEP Reanalysis. The data was simulated and recorded for the period 2006-2007 following a spin-up time of one year, and the computations were performed in a multicore workstation based at the Eduardo Mondlane University. Parallel studies using exactly the same model configuration have been validated satisfactorily against atmospheric conditions (i.e.,

precipitation) from the TRMM dataset (Maure, *pers. com.*). These data comprise two-year long time-series of wind velocity components sampled at 30 minutes interval over a large area that includes the Sofala Bank, at a spatial resolution of 30 km that is rather coarse compared with the 4.2 km used in the present oceanic model.

Plume features

Figure 5.12 presents the horizontal distribution of salinity and velocity averaged over one cycle of sea-breeze, 10 days from the turning of the wind forcing (panels C-F representing runs 1-4). The unforced plume at $t = 50$ days, and the plume forced by constant winds oriented along the negative alongshore direction are also shown. As can be seen, there is no significant difference in the maximum longshore and cross-shore extents between the unforced plume and those of the plumes forced by sea-breezes having magnitude of 5, 12, and 18 km/h, as depicted by the position of salinity contours. However, the spacing between the salinity contours increases considerably, and the position of contours is displaced landwards as the wind intensity increases from the "no wind" case to the case with 18 km/h breezes. This behaviour is a clear indication of the enhanced horizontal mixing associated with the periodic wind forcing.

The horizontal velocity field changes significantly from the "no-wind" case to the case of 26 km/h breezes. The magnitudes of the de-trended surface flow are very similar in the cases of "no-wind" and a sea-breeze of 5 km/h, suggesting that light breezes have only a minor effect on plume structure. On the other hand, the surface velocity of plumes forced by $12 \sim 26$km/h breezes (i.e., spanning gentle to fresh breezes) is considerably reduced in comparison with the "no wind" case, but not much difference is noticeable across these wind-forced plume cases.

Contrary to the de-trended flow, the transient flow presented in Figure 5.13 indicates that the amplitude of the surface flow increases with the sea-breeze intensity, as expected. In all cases, the trajectories in the offshore region are predominantly circular, changing to elliptic near the coast. The orientation of the semi-major axis of the ellipses along the coast changes from northward in the case of a 5 km/h wind magnitude, to northeastward in the remaining cases, while the eccentricity (the ratio of semi-major to the semi-minor axis) decreases with the intensity of sea-breezes. In addition, the surface flow in the plume region is not in phase with either the flow in the offshore region, or the wind forcing. This phase lag is depicted in the time series computed from the case of a 26 km/h sea-breeze, presented in Figure 5.14. Shown is a 2-day variation of the windstress (uniform over the model domain), and the surface velocity at two stations along the latitude $18^o28.39'S$, one located in the near-shore region within the reach of plume waters and the other in the offshore

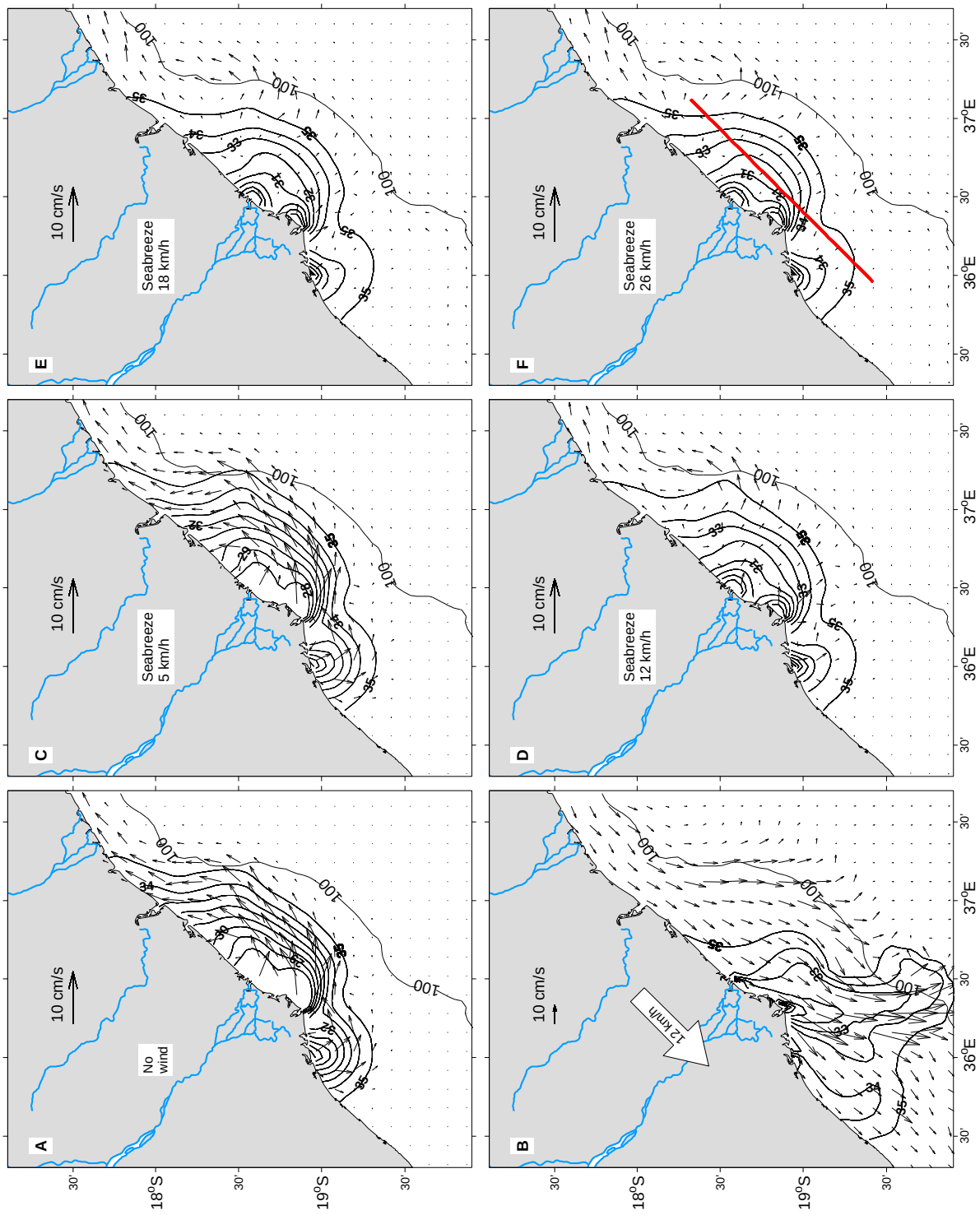

Figure 5.12: Horizontal view of surface salinity (contours) and velocity (arrows) fields averaged over one cycle, for the following wind conditions: (A) no wind forcing; (B) After 10 days of constant wind, starting from (A); (C-F) averages over a 24h period of conditions after 10-days of sea-breezes started from (A), with maximum wind intensity indicated textually in the centre of each panel. The 100 m isobath is also plotted. Salinity contours are 28 to 35 by 1 psu interval.

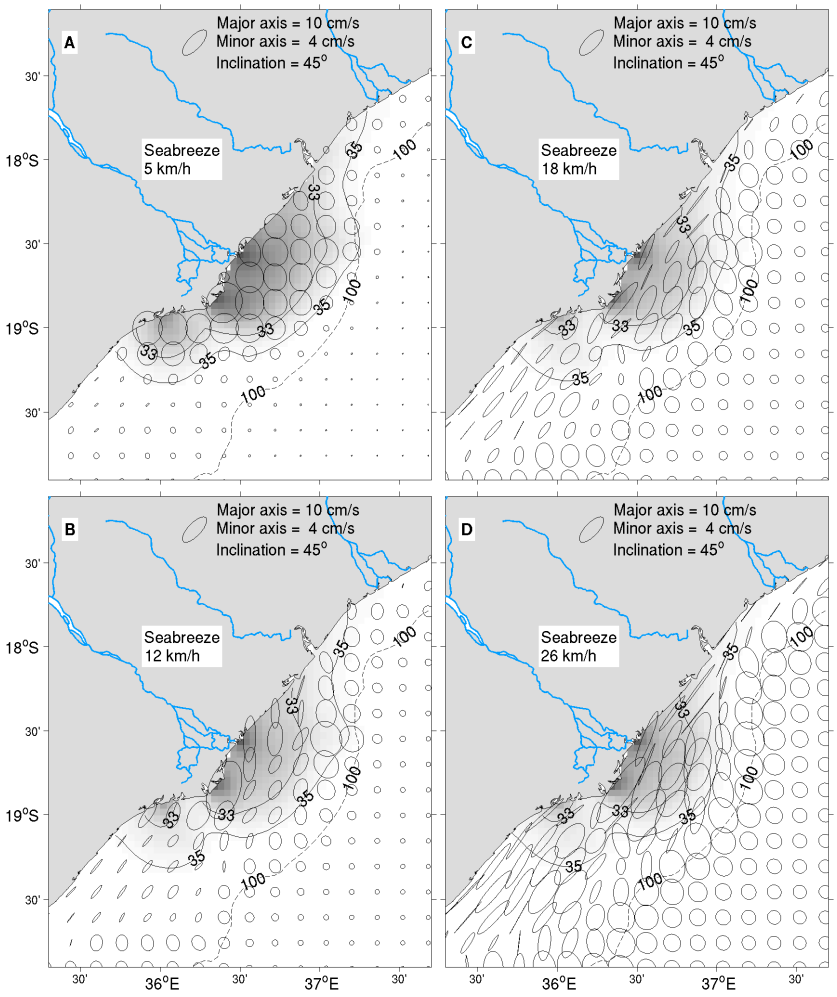

Figure 5.13: Same as in Figure 5.12, except for the transient velocity field at the top layer represented as ellipses estimated for one cycle of wind forcing, 8 days after the switching of wind. The different tones of gray represent averaged surface salinity with the contours for 33 psu and 35 psu plotted for reference.

region. In the zonal direction, the near-shore velocity component is 7.3 hours ahead of the wind, and the offshore component is lagged by about 5 hours in relation to the wind. In the meridional direction, both components of the surface velocity lagged by less than 2 hours in relation to the wind.

The effect of asymmetric sea-breeze forcing on a pre-existing plume is displayed in Figure 5.15. The top panels present plumes forced by constant winds, whose orientation is the best match to the orientation of the permanent component of sea-breezes used to force the plumes in the bottom panels (refer to the graphs B, C, and D of Figure 5.11). The similarity between the shapes of plumes produced by constant winds and an asymmetric breeze reveals that the magnitude and orientation of the permanent component of sea-breeze dictate the pattern of plume spreading.

In summary, the horizontal structure of plumes is only weakly influenced by the

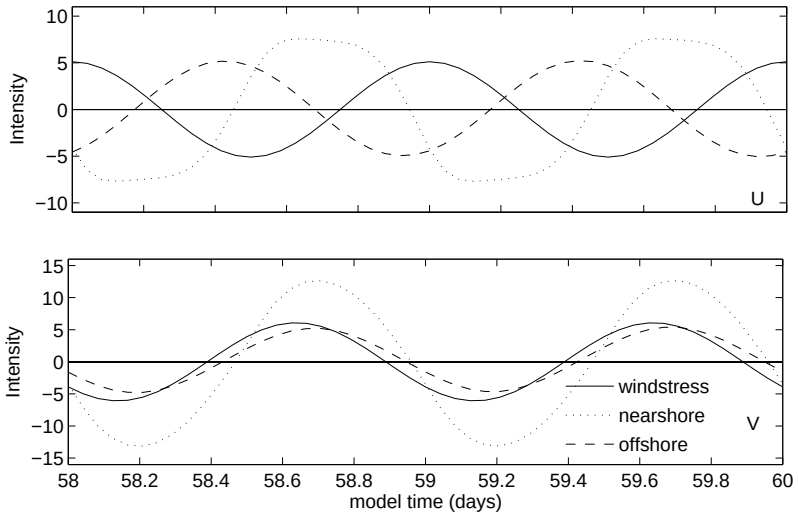

Figure 5.14: Windstress and surface velocity computed for a sea-breeze of 26 km/h intensity, at two stations. The top (bottom) panel presents the x- (y-) components of windstress and velocity expressed as $10^{-5}\mathrm{m}^2\mathrm{s}^{-2}$, and cm/s, respectively.

action of symmetric breezes, and the plume shape resembles that of an unforced plume in most respects. The most notable difference between these plume is the increased spacing between isolines, depicting the enhanced horizontal mixing brought about by the breezes. On the other hand, the primary direction of the dispersion of a plume forced by asymmetric breezes is similar to that of a plume forced by a constant wind oriented along the direction of the permanent component of the breeze.

The vertical structure of a plume under the action of light symmetric breezes (maximum intensity of 5 km/h) is identical to the structure of unforced plumes presented in Figure 5.4, with no exception. As the intensity increases, the structure gradually changes to a more vertically uniform, in response to the increased wind-induced mixing. For instance, the vertical structure of a plume forced by breezes having intensity of 26 km/h is depth-invariant (not shown) with salinity and velocity contours consisting of straight lines that extend from the surface to the bottom (i.e., without the portion of reverse flow at the bottom of the depression).

Figure 5.16 displays the vertical distribution of salinity and vertical mixing coefficient (K_h in $\mathrm{m}^2\mathrm{s}^{-1}$) recorded along the transect depicted by the red line in Figure 5.12-F. Shown is the unforced plume, along with plumes forced by a constant moderate wind (12 km/h of intensity oriented along the negative across-shore direction), a symmetric sea-breeze (12 km/h of intensity), and an asymmetric breeze with a permanent component similar to the constant wind. The distribution of salinity indicates that a weak symmetric breeze produces a plume with similar structure to the unforced plumes, except for the increased vertical mixing. For most of the

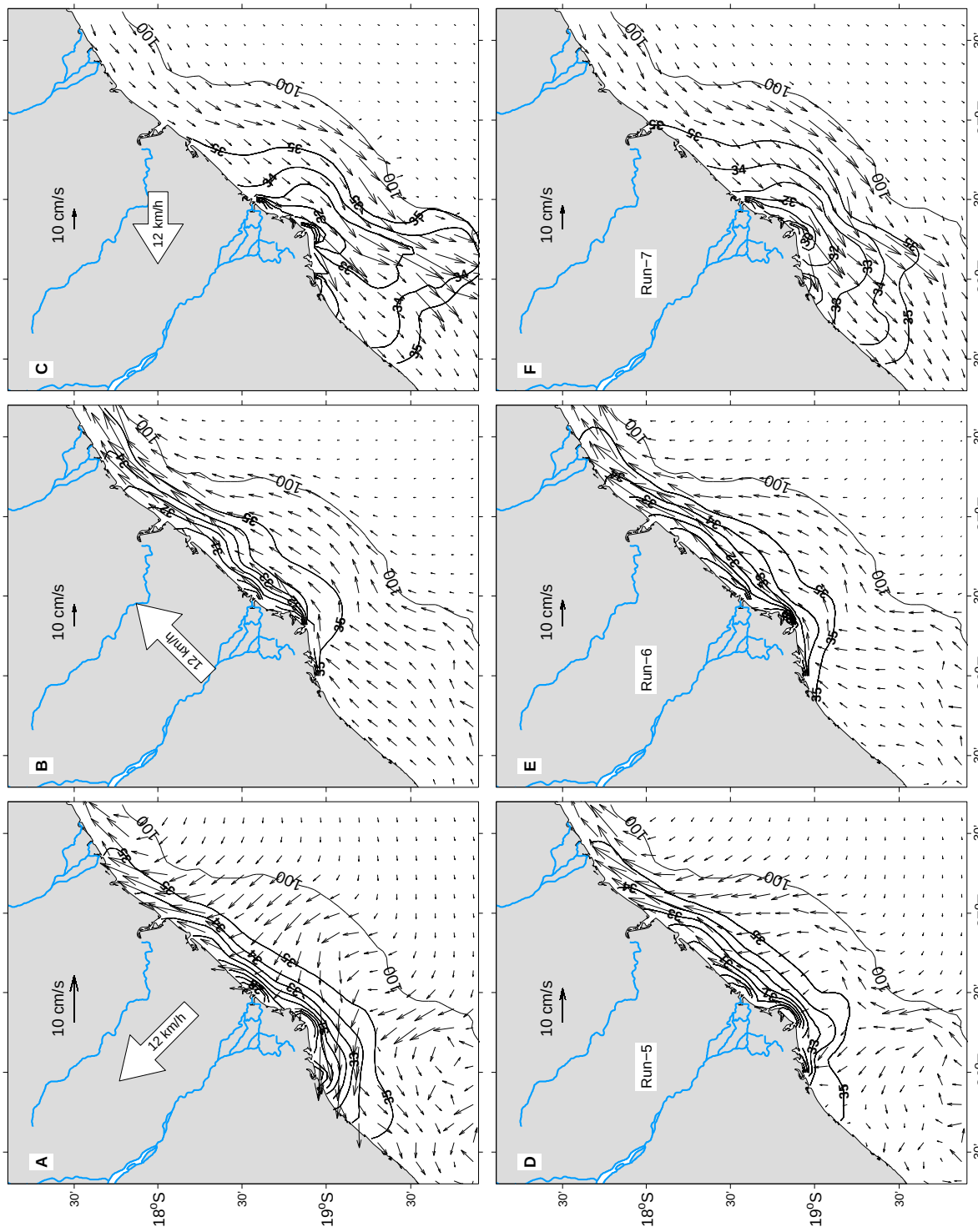

Figure 5.15: Same as in Figure 5.12, except for runs 5, 6, an 7. Panels A, B, and C display the fields simulated for constant winds with orientation being as close as possible to the orientation of the averaged sea-breeze that produced the plumes in panels D, E, and F, respectively.

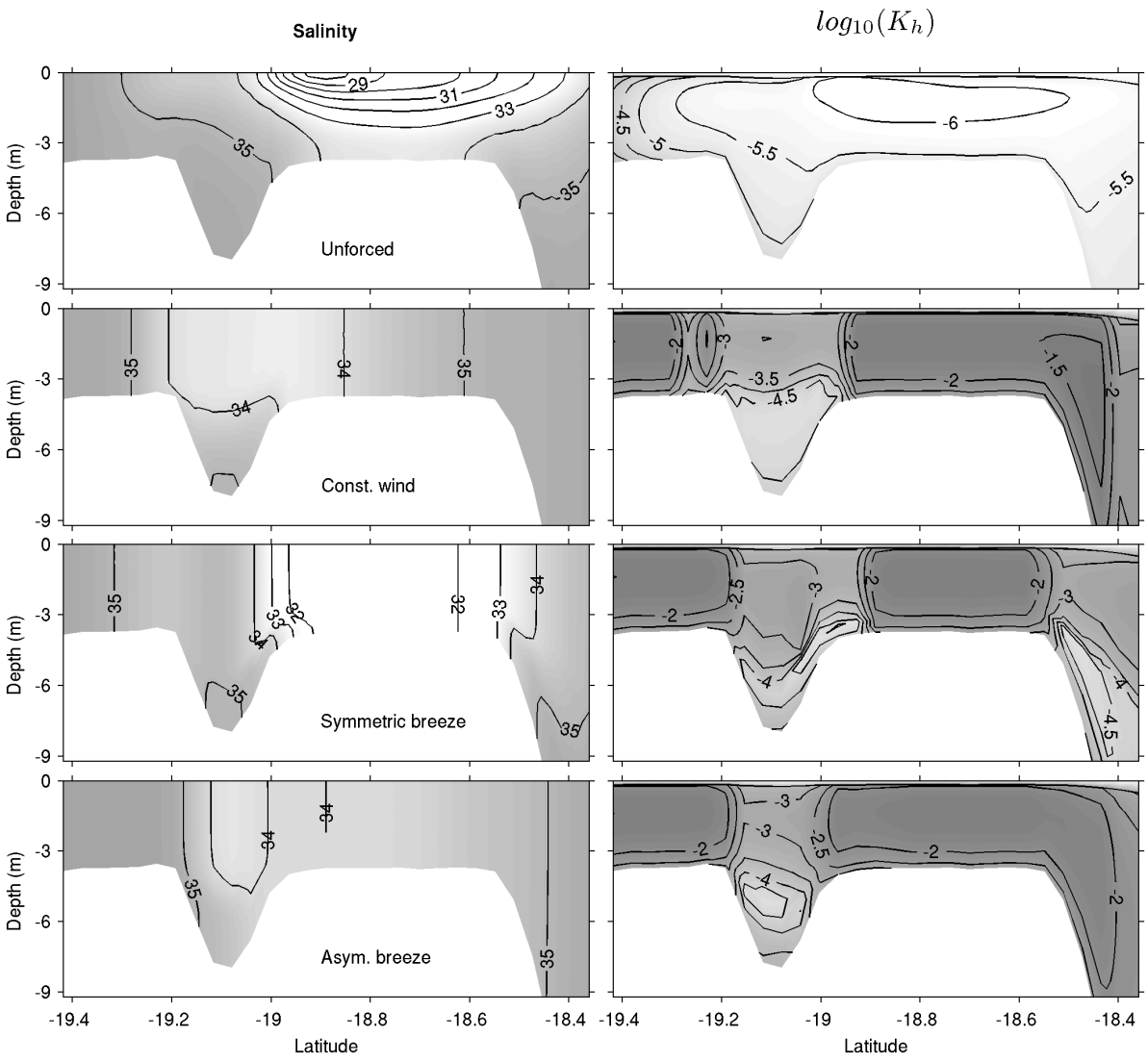

Figure 5.16: Vertical distribution of salinity, and vertical mixing coefficient (K_h in m^2s^{-1}) along the red line displayed in panel (F) of Figure 5.12, simulated for four different wind forcing. The data is presented for the model time $t = 50$ days in the case of unforced plume, and at 10 days from the beginning of the wind forcing (for the wind forced cases).

plume region, the distribution of the mixing coefficient values is similar in all wind forced cases, except at the depression where it appears to contain two well-defined layers in the case of a constant wind, while it increases gradually upwards in the sea-breeze cases. Judging by the location of the isoline of $log_{10}(K_h) = -4.5\,m^2s^{-1}$ at the depression in all the wind-forced cases presented in Figure 5.16, one might hypothesize that the sea-breezes promote a much higher vertical entrainment of the plume waters than the constant wind.

Summary of the wind-driven motion of a plume

The response of a pre-existing buoyant plume to intensive wind forcing is marked by either a change in the energy available for mixing, or by a movement of water perpendicular to the wind direction (i.e., the well-known Ekman drift). It was found that for a constant wind field, the most striking feature is the Ekman drift which combined with the local geomorphology and bathymetry results in plume waters being transported either offshore the location of the 100 m isobath, or downstream attached to the coast to approximately 17.5^oS, or even upstream in offshore up to 20^oS. The occurrence of upstream and seaward penetration of plume waters is associated with winds having a negative alongshore component, and/or winds that resulted in surface movement of water oriented seaward or southwestward. During wind conditions favourable to a downstream coastal current, the upstream transport is nearly insignificant, with extents varying from zero to few kilometers. In contrast, wind conditions favourable to the upstream transport often allowed the presence of significant amount of plume waters in the downstream region, despite the southwestward orientation of the surface velocity vectors.

Symmetric sea-breezes have been shown to be inefficient in advecting plume waters to large distances. This conclusion comes from the similarities found between the shape of the unforced plumes and those forced by symmetric breezes of different intensity. Hence, the response of the plume to these breezes was marked primarily by the enhancement of vertical and horizontal mixing, which translates to a depth invariant structure and a reduced seaward spreading of plume.

The asymmetric sea-breezes have non-zero magnitude when averaged over the cycle, and for this reason the response of the plume to this type of wind forcing comprises a mixture of the responses described above for constant winds and symmetric breezes. Given that these breezes most likely represent the actual wind conditions observed, one may expect the overall plume dispersion pattern to be strongly determined by the permanent component of the wind field, while the transient features as well as the vertical structure of the plume will be governed by the magnitude and orientation of the oscillatory part of the wind field.

However, the analysis of the response to sea-breeze forcing, with intensity maintained constant for over 50 days, indicated that the plume waters are transported upstream to 19.5^oS, downstream to 17.5^oS, and half way to the 100 m isobath offshore. The structures of these plumes were depth-invariant.

5.1.3 Tidal effects on the plume structure

The results presented in the previous section revealed that for a 24-hour period wind forcing that causes the velocity of plume waters to reverse continually in a symmetrical manner, the effects of the buoyancy forcing prevail over the effects of the wind forcing. Thus, the plume spreads laterally regardless of the windstress magnitude. This raises the question of what the shape of plumes would be in the presence of tides, which incidentally reverses the velocity field at a much higher frequency and induces a cyclic variation of the potential energy.

In order to investigate the influence of tidal forcing on plume spreading, an experiment was set up where, apart from buoyancy input, the model was forced with an hypothetical tide defined at either the eastern or the southern boundary, according to

$$\eta^{ext} = A \cdot \cos\left[\frac{2\pi}{T} \cdot t\right], \tag{5.1}$$

where η^{ext} is the sea surface elevation at the boundary (refer to Eq. 3.5), $A = 50\,\mathrm{cm}$ is the tidal amplitude maintained as constant along the boundary, and $T_p = 12\,\mathrm{h}$ is the tidal period, here chosen to be semi-diurnal. By making use of the Flather boundary conditions, it was possible to introduce tidal oscillations in the model, and it only required a switch between the passive and active regimes for the barotropic fields mentioned in Table 3.1, depending on which boundary was being used for the tides. All remaining model parameters follow the descriptions given in the preceding sections, except the boundary condition for the sea surface elevation that now uses the zero-gradient boundary condition. The tidal oscillations are imposed from the beginning of simulation ($t = 0$), and the amplitude at the active boundary is increased from zero to its maximum value within the first inertial period using a hyperbolic-tangent ramp function.

There is a need to keep the simulation as simple as possible, while representing correctly the physics of the processes involved. For that purpose, the tides were introduced through only one boundary at a time to avoid reflection inside the model domain. Given that the model domain contains two open boundaries, two model runs were performed in order to identify any possible spurious behaviour driven by the choice of the boundary, and hence, the tides were introduced from the eastern boundary in one run, and though the southern boundary in the other run. Figure 5.17 presents the resulting propagation of the tidal wave, and the associated surface velocity in the vicinity of the plume waters at the model time $t = 50\,\mathrm{days}$. As can be seen in panels A through D of Figure 5.17, there is no significant difference in the tide propagation and plume spreading produced when tides are introduced from

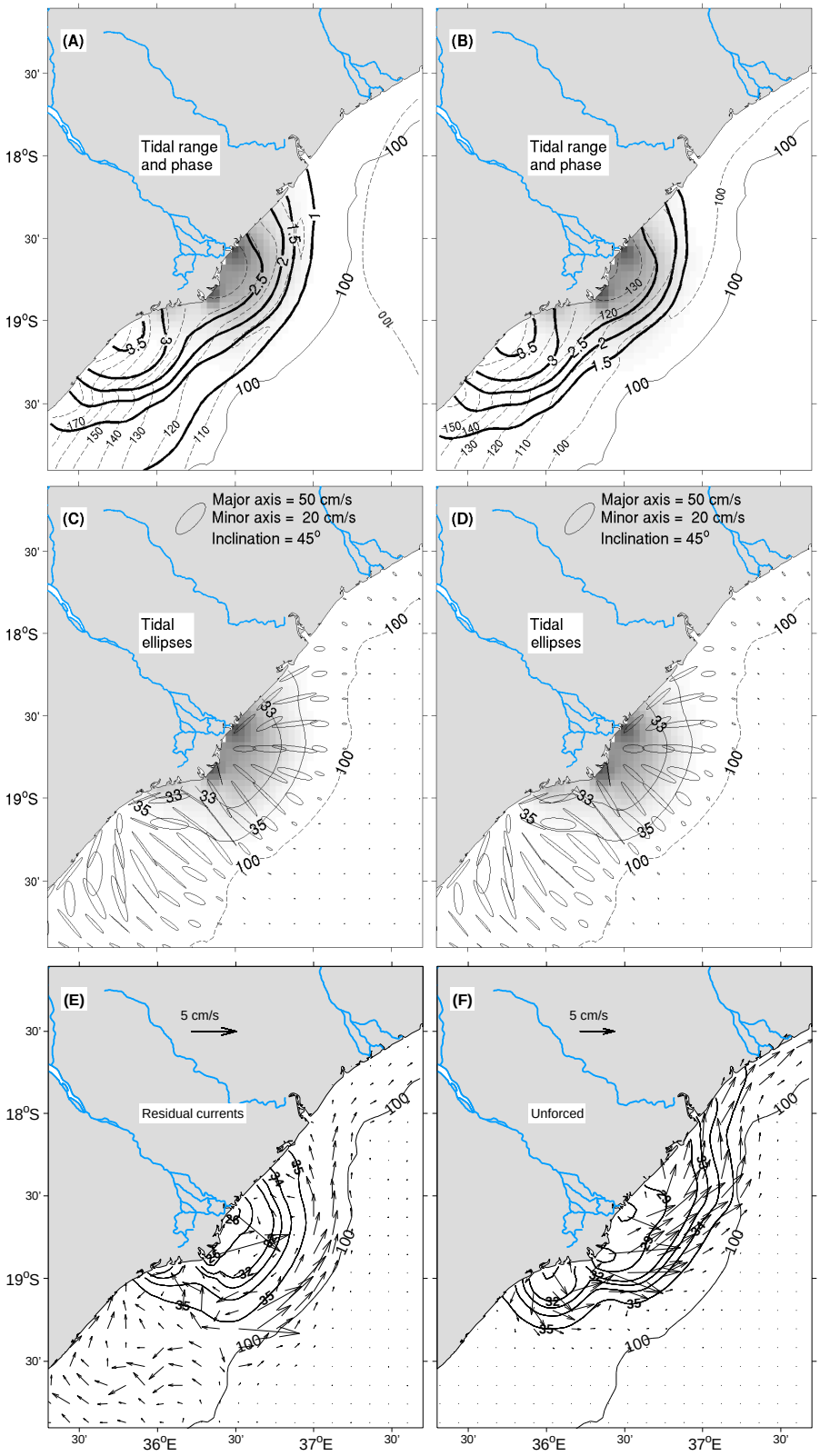

Figure 5.17: The panels on the right (left) represent the case of tides introduced from the southern (eastern) boundary, with the exception of panel (F). (A-B) Co-tidal lines indicated by the solid thick lines (phase in *hours*), and the co-range lines indicated by the dashed contours (range in *cm*). (C-D) surface salinity (shaded colours) and tidal ellipses. (E) surface salinity (contours) and tide-averaged currents (arrows). (F) same as in panel (E), except for the unforced plumes. All fields refer to the model time $t = 50$ days.

either the eastern or the southern model boundary. However, the distribution of co-tidal lines varies slightly between the two cases, given that the minimum tidal phase onshore from the 100 m isobath is less than 1.0 in the case of tides introduced from the eastern boundary, and only less than 1.5 in the other case. The tidal wave propagates shoreward with its amplitude being strongly amplified between the coastline and the 100 m isobath.

The co-range lines are roughly aligned with the coast or the 100 m isobath, but differences exist between the southern and northern parts relative to the delta region. The northern part appears to be homogeneous and synchronous, while in the southern part, the tidal range increases towards the coastal region between 19^oS and 20^oS, and the tidal phase increases towards the southern mouth. This increase is supposedly related to the local bathymetry and the offshore extension of the bank, which differ largely in the two locations. The offshore extension of the Sofala bank (or the continental shelf) is greater in the southern part of the domain, which translates to a higher amplification of the tidal wave amplitude in this region.

The surface tidal ellipses (panels C and D) indicate that the tidal excursion increases towards the plume waters, where the ellipse major axes are oriented predominantly towards the various mouths of the Zambezi River. An exception exists in the vicinity of the southern river mouth, where the tidal ellipses are greatly distorted, in some cases turning into a linear (bi-directional) trajectory. The region further south presents a different regime, which is probably caused by the high-energy tides (i.e., highest tidal range and retardation). The tidal ellipses in this region vary between the least distorted ellipsoids to straight lines.

Panel E presents the tide-averaged fields of surface currents and salinity for the case of tides introduced from the eastern boundary. As can be seen, the tide-averaged flow is relatively weak throughout the domain, hardly exceeding 5 cm/s. Within the plume limits (salinity < 35), this flow does not have a well-defined pattern, and it features a meander, landward flow in the near-shore, whereas at the coast, the flow is nearly parallel to the coast. This pattern indicates that, for a semi-diurnal tide of amplitude 50 cm, the resulting tidally-driven flow is very strong and any contribution from the buoyancy-driven flow on the de-trended flow is insignificant. Outside the plume limits (i.e., between the 100 m isobath and the plume), there exists a relatively strong and well-defined flow of saline waters parallel to the 100 m isobath. This flow constitutes the outer bound for the plume waters, it starts in the offshore region in front of the southern river mouth, and appears to be constrained by local bathymetry. It then weakens as it becomes attached to the coast in the region north of 18^oS.

By comparing the surface salinity distribution from the tide-forced (panel E) and the unforced (panel F) plumes, one finds that the alongshore extension of the plume

is substantially reduced in the case of a tidally-forced plume. It appears that the offshore extension of the plume (assuming the plume limit as, $S = 35\,\text{psu}$) is nearly unaffected by the tides, but differences in the horizontal salt gradient are noticeable, given that salinity contours are located much further apart in the tide-forced case. This pattern is a clear indication of the mixing effects of tides, which in this case precludes a sharp salinity/density front from forming at the plume boundary, as well as erodes the stratification within the reach of plume waters.

Overall, apart from being weak, the tide-averaged flow does not seem to be the driver of the spreading of the salinity plume, since the flow orientation within the plume limits is not aligned with the main direction of plume spreading. For this reason, it is now instructive to analyze the transient field of velocity, which is cyclic with period of 12 hours.

From the horizontal distribution of tidal range, it follows that at least two spots of maximum range can be identified along the coastline, the first one is located between the sources #1 and #2, ad the second one is located to the south of the source #3. From the snapshots of density and velocity field presented in Figure 5.18, it can be seen that during the ebbing tide (rising tide), the field of transient velocity is oriented radially from (towards) the two spots of maximum range. For most of the tidal cycle, the velocity vectors in the northern and central parts of the plume are observed crossing the isohalines, and suggesting a radial spreading of the freshwater. In contrast, the vectors in the southern part of the plume tend to be oriented along the isohalines, except during the periods of slack water. This behaviour is combined with the fact that tidal ellipses are considerably distorted to linear trajectories in the southern region of the plume, hence favouring the spreading of the less saline waters in the across-shore direction. The same argument accounts for the spreading in the northern region to be directed in both the alongshore and the across-shore direction. However, the horizontal dispersion of plume waters seems to be best explained by the buoyancy and the geostrophic balance.

In Figure 5.19, the vertical properties of the tidally-forced plumes for an along-shore transect (red line in Figure 5.12-F) are compared with the unforced plume. As can be seen, the local bathymetry is very shallow and features a depression that in both cases is associated with increased mixing and downward movement of water. The model-computed vertical mixing coefficient is considerably higher in the tide-forced case and it reaches a maximum of $0.032\,\text{m}^2\text{s}^{-1}$ (presented in presented in Figure 5.19 as $10^{-1.5}\text{m}^2\text{s}^{-1}$) compared to the maximum value of $10^{-5}\text{m}^2\text{s}^{-1}$ computed for the case of unforced plumes. The bottom boundary layer in the depression varies between 70 cm in the unforced case to full water column in the tide-forced case. The large vertical mixing coefficient observed in the tide-forced simulation leads to much

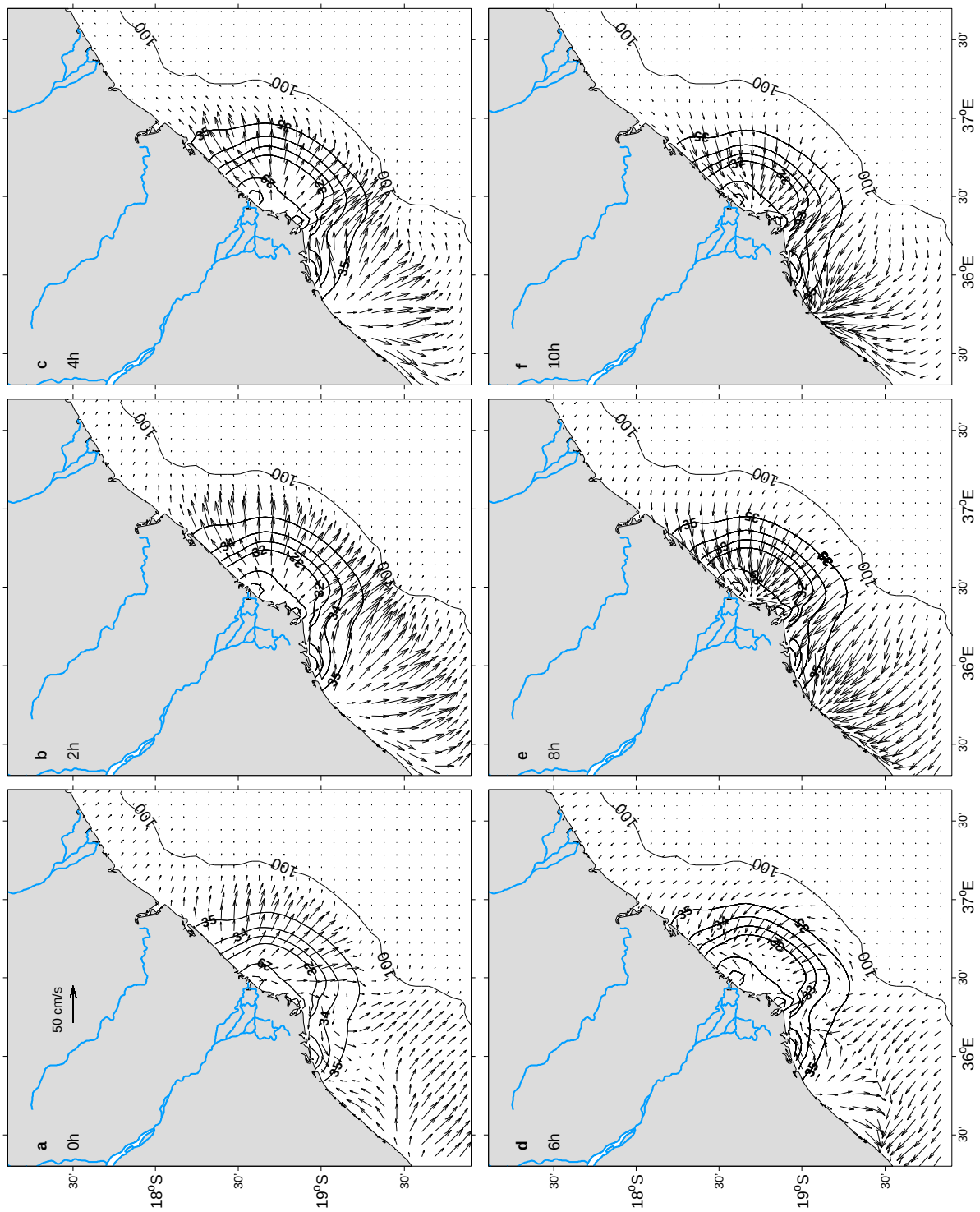

Figure 5.18: Snapshots of the surface velocity field (arrow), and salinity (contours) over a 12-hour cycle, taken at a 2-hour interval. The time-stamp in panel (a) refers to few minutes after the first high-water of the 50th day (model time). The contours indicate salinity of 29, 32, 33, 34, and 35 psu.

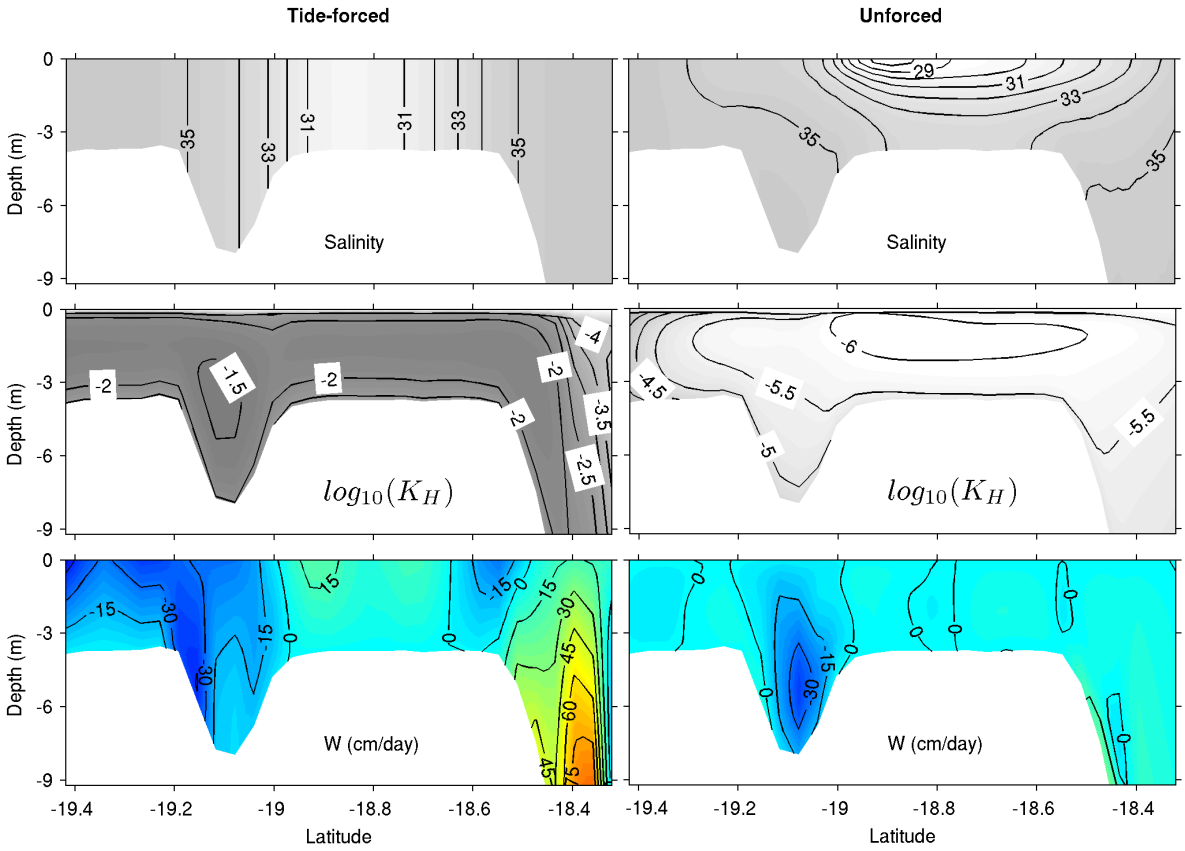

Figure 5.19: Vertical distribution of salinity, vertical mixing coefficient (K_H in m^2s^{-1}), and vertical velocity, averaged over one tidal cycle in the case of tide-forced plumes (*left*), and presented for the model time t = 50 days in the case of unforced plume (*right*).

stronger vertical velocities and consequently increased vertical mixing.

In summary, this analysis has shown that a 50 cm amplitude tide generates strong flows over the coast. But due to its periodicity, the de-trended component of the tidally-driven flow is very weak and inefficient for moving the plume water over large distances. As a result, the lateral dispersion of the plume is driven by the geostrophic component of the flow, as well as the interactions between the tidally-driven flow and the local topography. On the other hand, the tide promotes an increased mixing between the ambient and plume waters, and hence, an augmented vertical entrainment of brackish water. This behaviour explains the generally smaller alongshore penetration of the plume, the increased spacing between isohalines in the horizontal distribution of salinity, and the depth-invariant structure of the plume.

5.2 Higher resolution (Gebco1) bathymetry

The results presented in the previous sections were produced considering the 2 arc-minute (approx. 4 km) global bathymetry dataset (Etopo2), according to which the water column in the region immediately offshore from the delta is shallower than 10 m and has a depression in the region to the south of the river mouths. These features might well be an artifact of the above mentioned dataset, since they do not agree with the depth recorded in the CTD castings reported in Chapter 2, and neither appear in the higher spatial resolution (1 arc-minute; approx. 2 km) Gebco dataset. The difference between the two datasets (Gebco1 minus Etopo2) is displayed in Figure 5.20. As can be seen, the position of the 100 m isobath in relation to the coast is roughly similar everywhere in either data-sets, except in the region located seawards from delta. More importantly, the topography levels in the region between the coastline and the 100 m isobath are misrepresented in the Etopo1 dataset, with depth differences reaching $20 - 50$ m. The Gebco1 bathymetry in the area under consideration happens to be in a better agreement not only with the depths recorded in the CTD casts (which are referenced to the free-surface), but also with the bathymetry from charts used for navigation and reproduced from historical hydrographic soundings. Since the plume lateral dispersion is very sensitive to the local topography, it is instructive to analyze the differences imposed by the higher

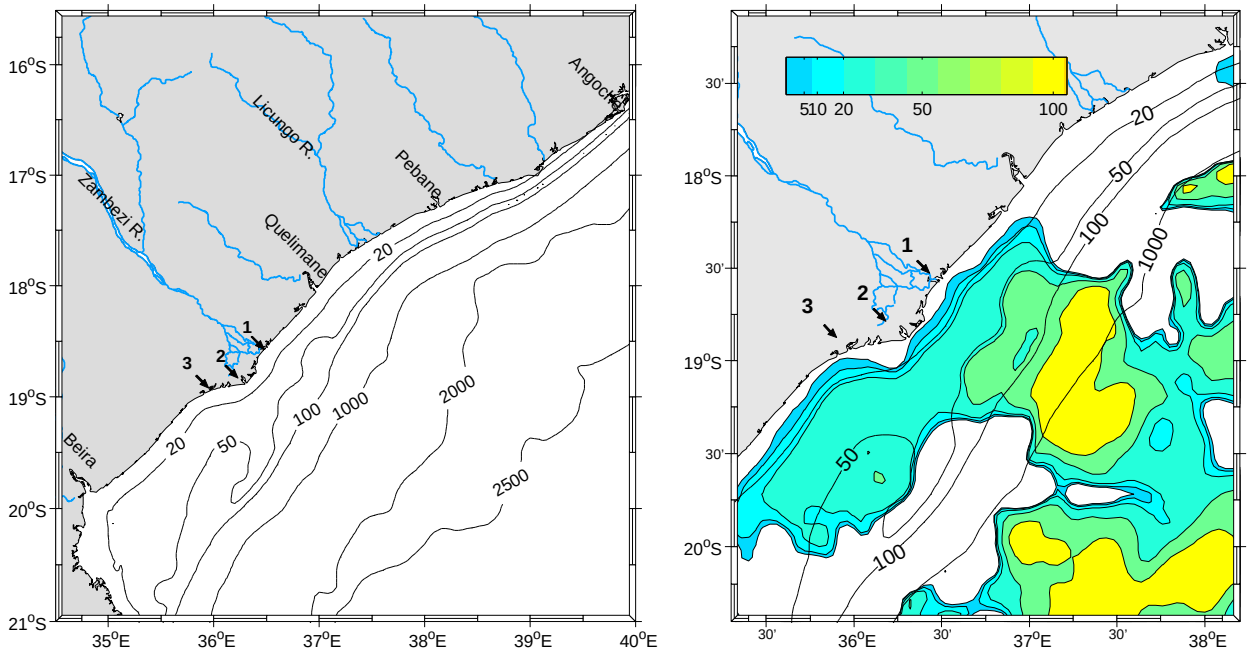

Figure 5.20: *Left:* bathymetry of the Sofala Bank, extracted from the Gebco1 dataset, which has a spatial resolution of 1 arc-minute, and re-sampled at 7.21 km resolution. *Right:* Difference in meters between the gebco1 and the etopo2 datasets near the Zambezi delta.

resolution and more accurate bathymetry to the plume structure discussed in the previous section.

To that extent, simulations of the unforced and wind-forced plumes were performed using the exact same model parameters described in the preceding sections, and the differences found in the results are described below. Then, the tide-forced plume was simulated using a slightly modified approach.

5.2.1 Unforced plume

In other to evaluate the model geometry, in particular the influence of each of the three main outlets of the Zambezi River on the dispersal and structure of the buoyant plume, an experiment was conducted using the parameters described in the Section 5.1.1, and the Gebco1 bathymetry. In short, the model settings include a freshwater discharge entering a homogeneous (non-stratified) coastal ocean, in the absence of additional external forcing, and Orlanski radiation applied at all open boundary for all fields. A total of 6 model runs were performed using the discharge rate (q_{river}) displayed in Table 5.3, and the evolution of resulting plumes is displayed in Figure 5.21.

The horizontal structure of the plume 5 days from the freshwater release is very similar in the case of the northern and central sources (panels 1 and 2), as well as in the cases with combined discharges (panels 4 and 5). For separate discharges, the plume consists of a circular bulge and a portion of freshwater extending northwards. The bulge is symmetric in relation to the source in the case of the northern source and asymmetric in the case of the central source. The southern source produces a narrower plume, which may be related with the northeastward transport of freshwater (around the headland). The early stages of the plume evolution in the case of multiple sources consists of a triple bulge that forms when the three bulges merge together. In all cases, the structure described above evolves continuously until day

Table 5.3: Parameters used in the spin-up experiment

Run	Source	$q_{river}[m^3/s]$	Depth [m]
SUP-1	1	1000	5.28
SUP-2	2	1000	7.05
SUP-3	3	1000	7.07
SUP-4	1+2+3	3×1000	-
SUP-5	1+2+3	900+1500+600	-
SUP-6	2	3000	7.05

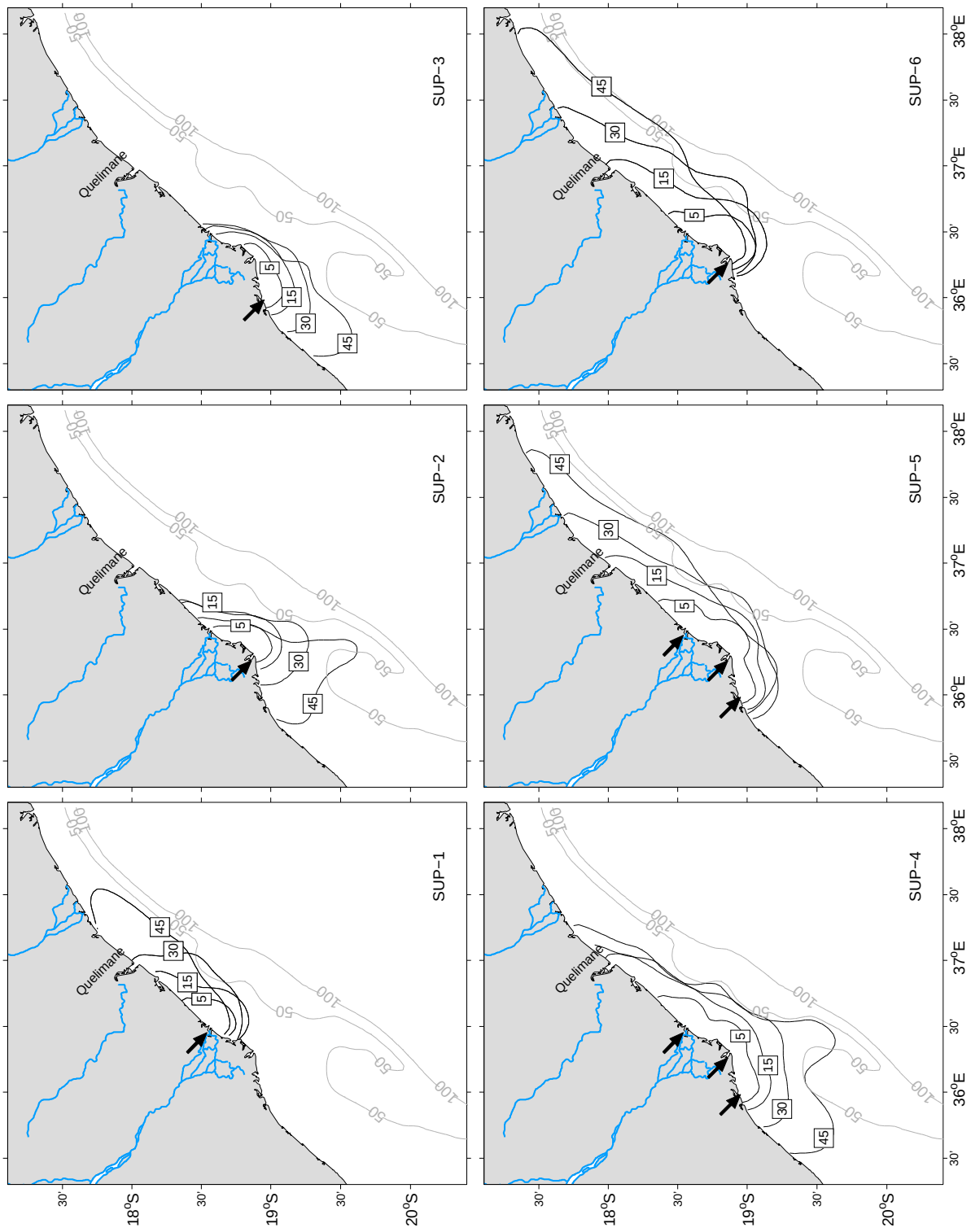

Figure 5.21: Location of isohaline 34 psu at day 5, 15, 30 and 45 for different conditions of buoyancy input, here characterized by the number and location of point sources, and the total discharge. The dark arrows over land indicates the quantity and relative position of point sources. The gray contours correspond to the 50 m and 100 m isobaths, here plotted for reference.

26, with the plume advancing mostly in the alongshore direction and most of the freshwater being transported downstream. According to the classification schemes of Chao (1988b) and Kourafalou et al. (1996b), all these plumes are characterized as "diffusive subcritical", given that the width of the bulge is comparable to the width of the coastal current. The only exception is the plume produced by the central source alone, whose bulge is projected well offshore and is considerably wider than the downstream flow.

Although the density-driven flow never reaches the open boundaries, a current is generated along the shelf edge (not shown), and from day 26 onwards it become strong enough to dramatically induce changes to the density-driven flow in the near-shore. For instance, in almost all the situations presented in Figure 5.21, the plume on day 45 retreats in relation to earlier stages, as depicted by the intersection of the isolines in selected regions of the plume. The shelf-edge current is remotely induced by the density-driven current through the volume conservation enforcement, employed to account for the changes in the volume of freshwater. This current showed to be very sensitive to the choice of number and position of the sources, since for example, the freshwater introduced from the central source resulted in a shelf-edge current oriented towards the southwest and northeast for a discharge rate of 1000 and 3000 m^3/s, respectively. These results reveal that the position of the river mouth in relation to the headland (delta) combined with the discharge rate have major implications for the plume spreading.

Based on this knowledge and aiming at evaluating the structure of an unforced plume, the model was run using a freshwater discharge of 1500 $m^3 s^{-1}$, introduced through multiple sources using the proportion 3 : 5 : 2 for the discharge rate of the northern, central, and southern river mouths. The horizontal distribution of salinity and velocity at the model time, $t = 15$ and $t = 22$ days is presented in Figure 5.22 . These results correspond to conditions at the end of spin-up (start of the upcoming experiments), and the unforced case, respectively. There is not much difference in the plume structure on these two days, apart from the increased alongshore and across-shore extents in the structure on day 22. No re-circulation is present at the bulge, which is only slightly wider than the coastal current measured half way to the leading edge (nose).

The vertical structure of the unforced plume at day 22 is presented in Figure 5.23, where salinity and velocity profiles are plotted against the distance from the coast in kilometers. As can be seen, in all transects, the bottom layer contains only ambient water, and the plume waters are limited to a thin layer at the surface, whose thickness varies between 2 and 4 meters at the coast. Near the river sources, the bottom layer moves landwards, opposing the flow of freshwater in the upper

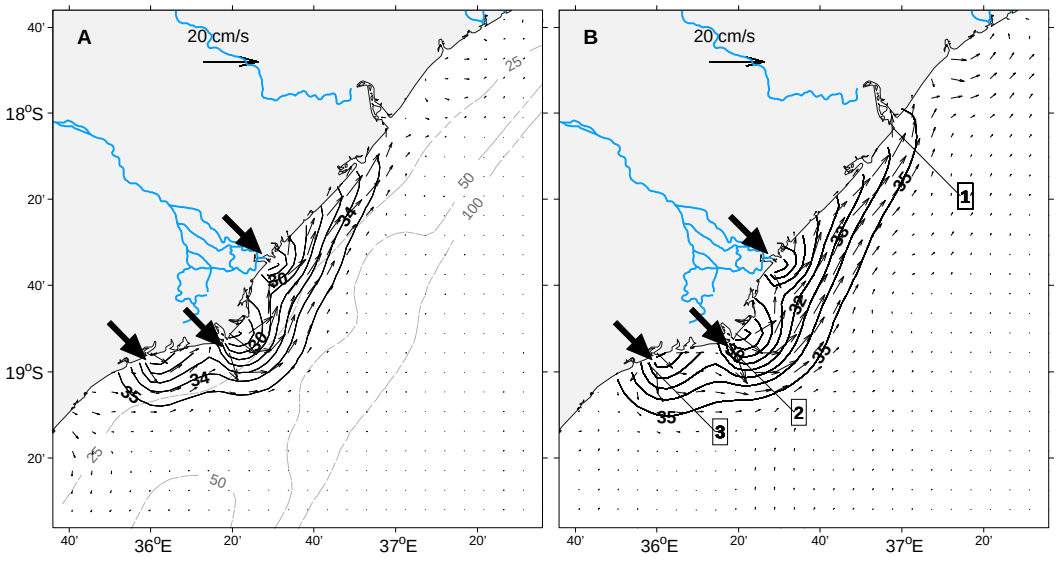

Figure 5.22: Horizontal distribution of surface salinity (contours) and velocity field (arrows) simulated for a discharge of $1500\,\mathrm{m}^3 s^{-1}$. (A) Initial conditions for the experiments with external forcing, $t = 15$ days. (B) Unforced plume at $t = 22$ days. Velocity vectors are plotted every other gridpoint, and contours are 28 to 35 by 1 psu.

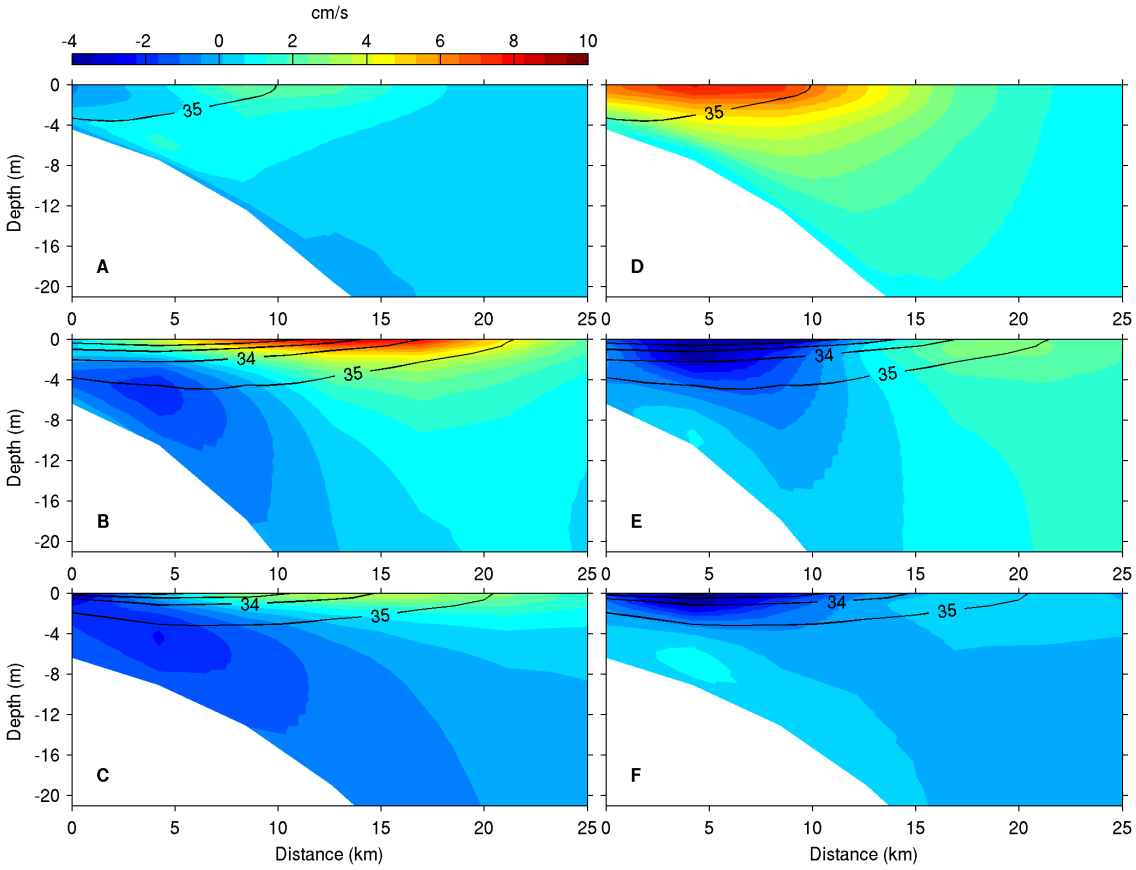

Figure 5.23: Vertical distribution of the zonal (*left*) and meridional (*right*) velocity components overlaid by salinity contours (C.I. is 1 psu) computed for the model time $t = 22$ days. From top to bottom, transect 1, 2, and 3 illustrated in Figure 5.22-B.

layer. The coastal current has a relatively intense flow, and weak vertical gradient of salinity compared with the rest of the plume.

In summary, in the absence of additional external forces, a moderate and constant freshwater discharge generates a surface-advected plume, in contrast with the bottom-advected found when the Etopo-2 bathymetry was employed. In 22 days, the plume spreads over the area comprehended between the latitudes $18^oS - 19.1^oS$ and the 50 m isobath. The maximum plume thickness is smaller than 5 m in the entire plume extension, and a shoreward oriented undercurrent exists in the periphery of the sources.

5.2.2 Plume response to wind forcing

The structure of freshwater plumes under the action of an intensive wind field was studied. Two cases were analyzed, namely (i) constant winds blowing over a pre-existing plume, and (ii) oscillating winds with a period of 24 hours, both starting from the end of spin-up (day 15). Specifications of the model runs and results are described below.

Constant wind field

Following the spin-up, a constant windstress was turned on and sustained for 7 days. Two wind magnitudes (5 and 12 km/h) representing weak and moderate conditions were tested, along with eight wind directions characterizing the four major directions in the standard coordinate system and that of the "alongshore"-"across-shore" system (rotated clockwise by 40^0). It is worth mentioning that tests with strong wind conditions often resulted in model crash due to numerical instabilities, and for that reason, the response to strong winds are not discussed here.

The horizontal structure of the plume fully agrees with that found in the simulation with coarse resolution bathymetry. According to these results (described in Section 5.1.2), a constant wind field acting over a moderate-discharge plume can alter the plume structure to become either a "*large bulge*" that spreads progressively offshore if the alongshore component of the wind is negative, or a "*coastal current*" flowing northeastwards along the downstream coast, which occurs when the alongshore component of the wind is positive (see Figure 5.9). In contrast with results found with the coarser resolution bathymetry, the winds blowing in the cross-shore direction generate a large bulge when oriented seawards, and a coastal current if oriented landwards.

The main difference between the two simulation approaches lies in the fact that

under the coarser resolution bathymetry, the plumes forced by cross-shore winds are greatly influenced by the magnitude of the winds, while under finer resolution bathymetry, they only depend on the orientation of the windstress. Notice that the water column in the finer resolution dataset is in general deeper than in the other case, and that it is this greater depth which causes the differences in the results.

The horizontal and vertical structures of the wind-forced plumes are presented in Figures 5.24 and 5.25, respectively, where only the most predominant wind direction observed in the Sofala Bank in the period January to March are shown. The plume structure produced under the positive alongshore winds was excluded due to its similarity with the plume produced under the northward winds, not to mention the weak intensity of these winds. The resulting primary orientation of plume spreading does not always coincide with the predominant orientation of the surface flow, as indicated by the velocity vectors in panels B and F in Figure 5.24. In these specific cases, the part of the surface flow directed southwestwards, which favours the existence of a large bulge, is as strong as the part of the flow directed northeastwards, which favours the coastal current. Below, a description of the plume's response to impulsive winds is given, following the discussion of Chao (1988b), however, only for a few wind fields chosen by their importance to the study site.

Northward (southerly) winds, as well as the northeastward (downwelling favourable) winds, induce a motion of plume waters oriented primarily northeastwards along the coast, similar to the orientation of the flow in the unforced plume case. Near the coast, the Ekman drift is constrained by the landmass, thereby causing the whole circulation to be oriented downwind. During weak winds, the circulation is similarly weak everywhere, except in the plume region downstream from the river mouth where the wind-induced and the buoyancy-driven flows interact and ultimately form a strong coastal jet along the coast (characterized by an intense two-layer flow of plume waters flanked by relatively slower flow of ambient waters). Under the action of moderate winds, the coastal jet is replaced by a wind-driven coastal current, whose width increases towards the plume leading nose. The moderate winds inhibit the upstream penetration of plume waters, as well as the across-shelf motion, resulting in massive deepening of the plume near its sources. Hence, the plumes forced by moderate winds have a region near the coast where the plume is connected with the bottom (i.e., plume base). Therefore, these plumes are classified as bottom-advected.

Landward (northwestward) winds induce the movement of plume waters oriented towards both the southwest and the northeast direction (i.e., along the coast). Ekman drift near the coast is directed shoreward, which inhibits the seaward export of plume waters. Apparently, the interaction between the model geometry (presence of a headland) and the shoreward flowing Ekman drift results in flow

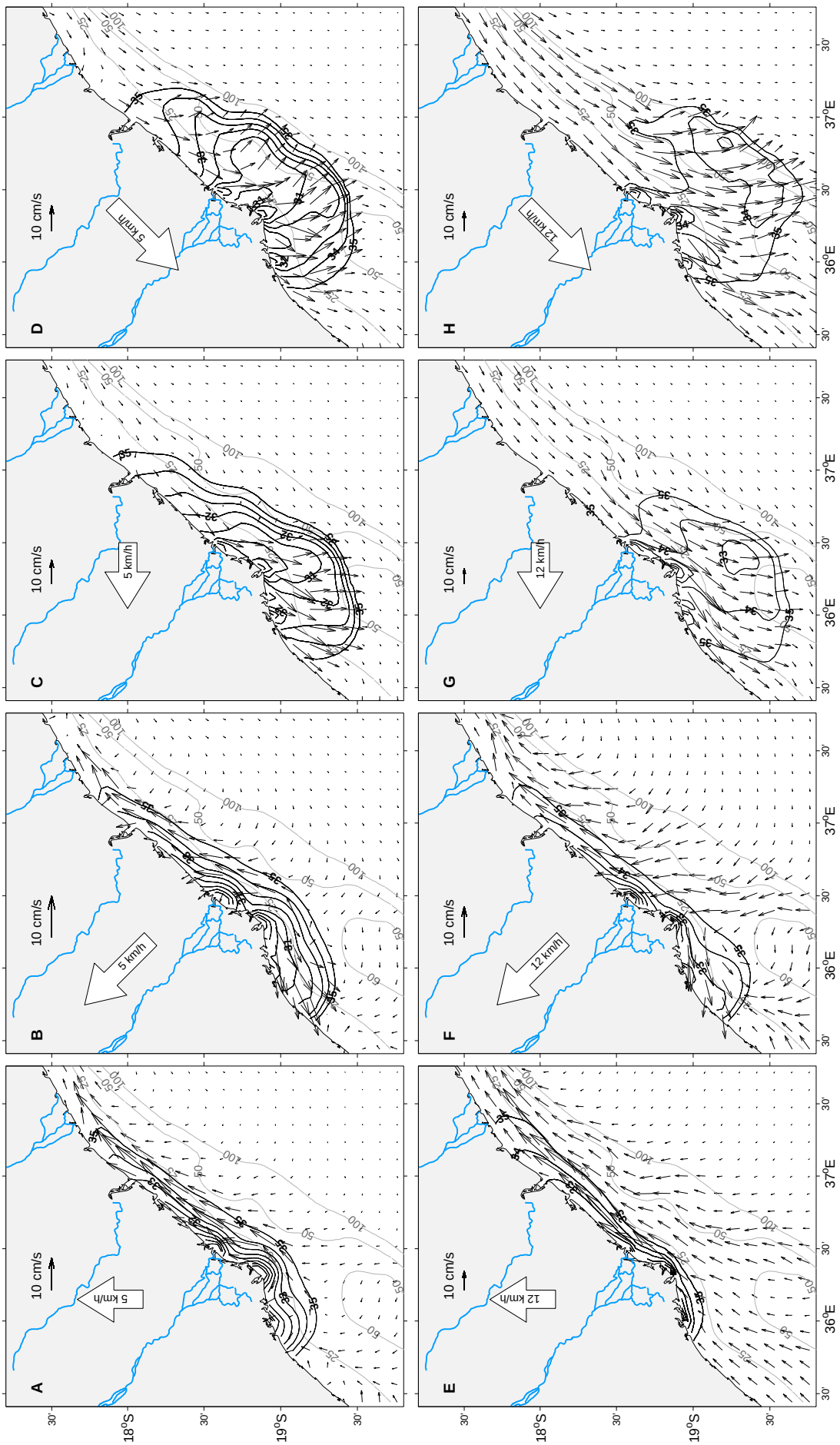

Figure 5.24: Horizontal distribution of surface salinity (contours) and velocity field (arrows) simulated for a discharge of $1500\,\mathrm{m^3 s^{-1}}$ at the time $t = 22$ days. Velocity vectors are plotted every other gridpoint, and contours are 28 to 35 by 1 psu. The large arrow over land and its inscription indicate the wind direction and magnitude, respectively.

separation offshore from the headland. Plume waters then flow along the coast and away from the sources in both directions (downstream and upstream). There is also a possibility that the coastal set-up also contributes to the flow separation in front of the headland tip. Either way, the part of the plume flowing upstream become wider than its downstream counterpart by virtue of the geostrophic forces.

Westward (easterly) winds drive the movement of near-shore water (Ekman drift) towards the southwest, i.e, opposing the direction of a Kelvin wave. Hence, within the reach of plume waters, stratification weakens the wind-driven flow and the freshwater is projected offshore by virtue of the Coriolis force. Under impulsive winds, intense vertical mixing occurs near the sources resulting in portions of the freshwater that were advected at earlier stages being disconnected from the sources, giving the appearance of a pool of lighter water at the centre of the plume in the

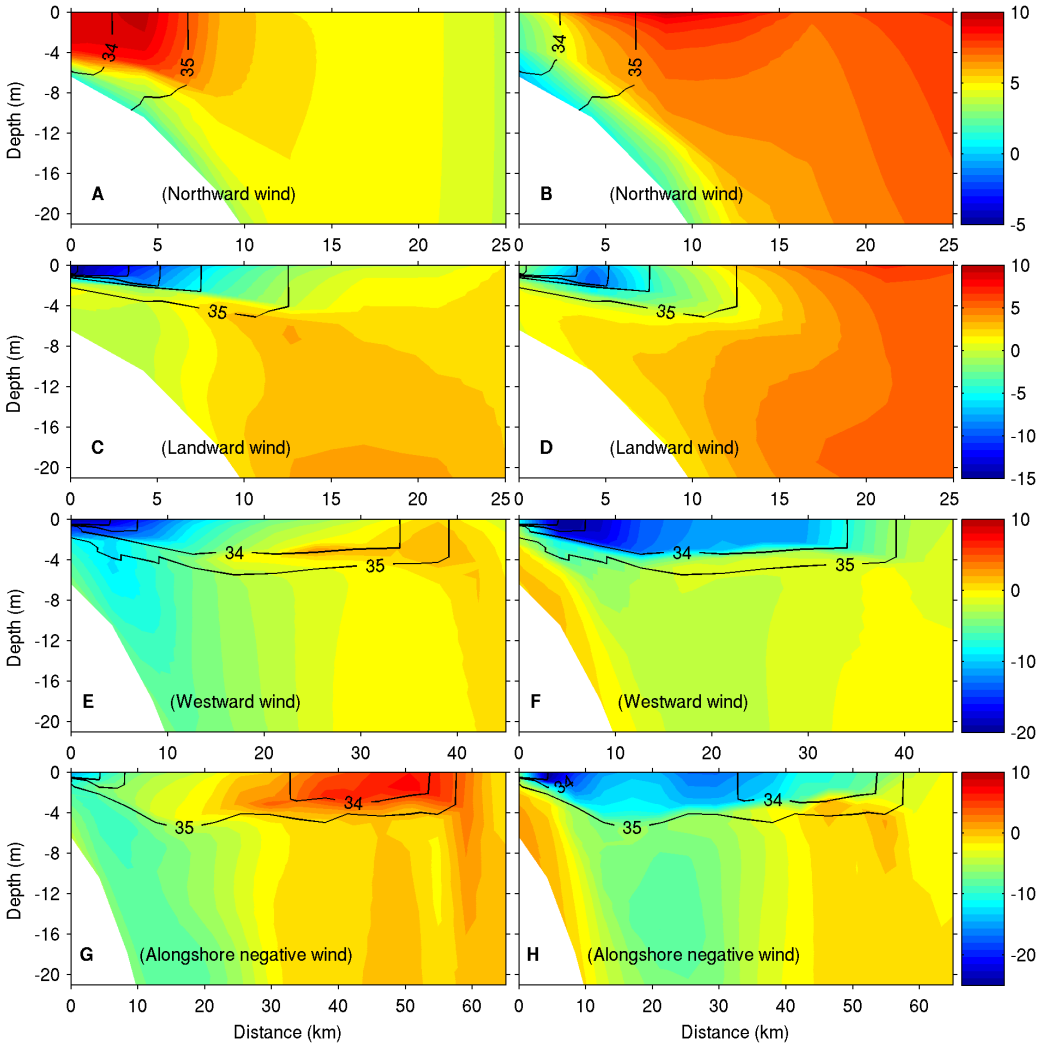

Figure 5.25: Vertical distribution of the zonal (*left*) and meridional (*right*) velocity components overlaid by salinity contours (C.I. is 1 psu) computed for a 12 km/h wind at the model time $t = 22$ days, at the across-shore transect leaving the central source.

horizontal views.

Southwestward (upwelling-favourable) winds also termed negative alongshore winds, produce a plume response similar to the westward winds, except for the greater seaward intrusion of plume waters, as well as the enhanced horizontal mixing between the plume and ambient waters. Since the plume does not feel the bottom, it is transported seaward by the wind as if there was no friction between plume and ambient waters and the plume had no influence from the land mass or coastline.

24-hour period oscillating wind-field (sea-breeze)

Starting from the end of the spin-up run, the plume was subjected to the analytical sea-breeze fields illustrated in Figure 5.11. Following the experiments with coarse resolution bathymetry, two sets of model runs were performed, each using a wind forcing defined by either symmetric or asymmetric breezes. Details of each type are presented in Table 5.2 and Figure 5.11, but in short they read as follows. The symmetric breezes are centered at the origin of the Cartesian system, the major axis is oriented landwards, and the amplitude was varied between 5, 12, 18, and 26 km/h. For asymmetric breezes, the centre is other than zero, and the position of the centre indicates the magnitude and orientation of the permanent component, which according to the data presented in Table 5.2 (*cf.* runs 5 to 7), the winds used in this experiment correspond to either one of ~ 10 km/h landward breezes, ~ 7 km/h northeastward breezes, or ~ 12 km/h westward breezes. The asymmetric breezes were extracted from the numerical weather prediction model (WRF), discussed in Section 5.1.2.

The horizontal structure of plumes under the action of oscillating wind fields is presented in Figure 5.26. These results agree with the overall findings for the coarser resolution bathymetry experiment, according to which the symmetric sea-breeze is ineffective in driving the motion of plume waters, but it does induce a considerable increase in the horizontal as well as vertical mixing in the entire system. Likewise, the response to asymmetric breezes is similar to the corresponding constant wind field in most of the aspects of the plume structure. The most relevant difference between the plume's response to the constant wind and that of the asymmetric sea-breeze is the enhanced vertical mixing noticeable mainly in the results for the finer resolution bathymetry.

In connection with the enhanced vertical mixing, the plumes under the action of landward and northeastward breezes were found to spread as bottom-advected plumes, at least in the region nearer to the sources, while a westward breeze produced

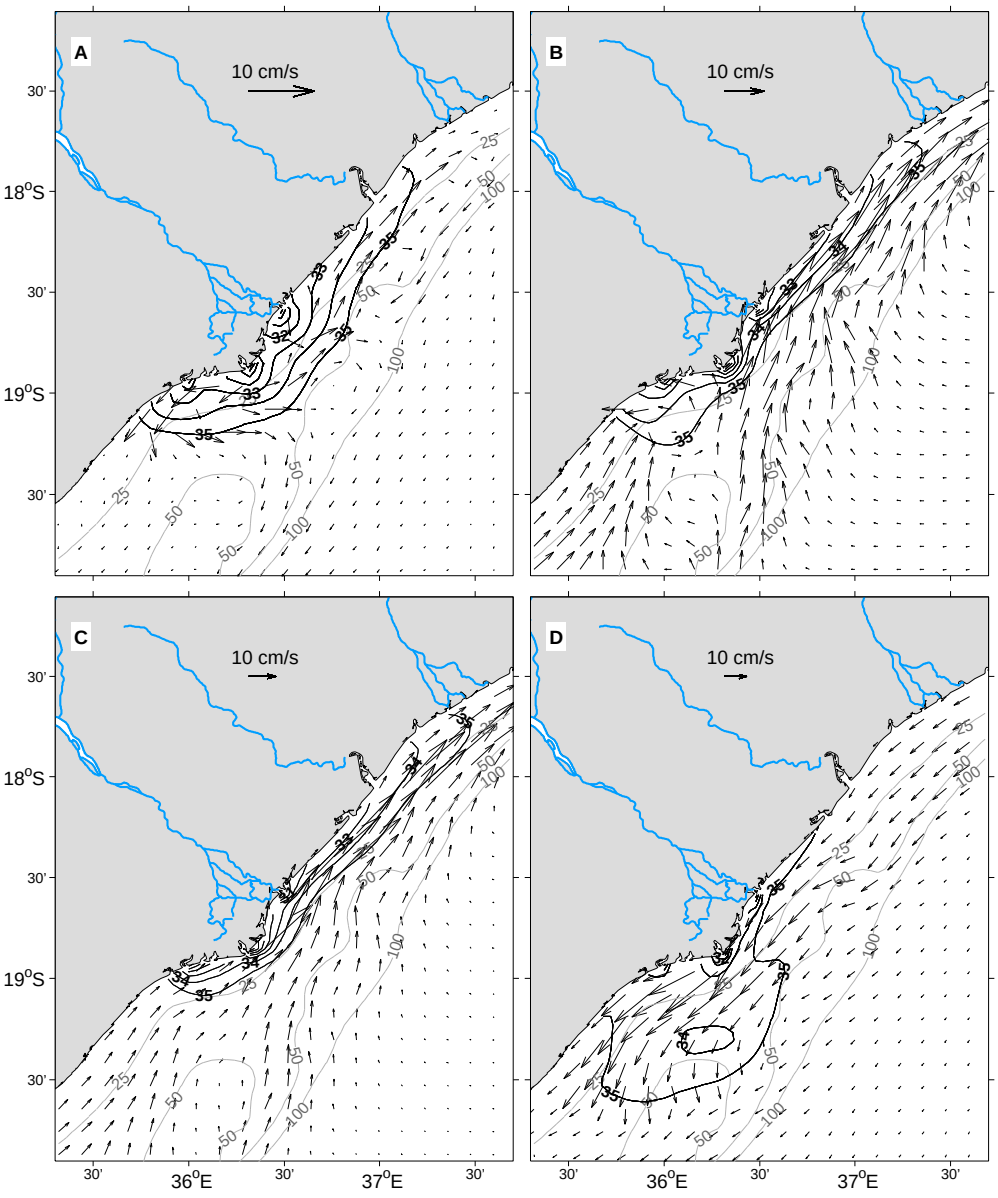

Figure 5.26: Horizontal views of surface salinity and velocity fields at $t = 23$ days, for the following conditions of sea-breeze forcing: symmetric breezes of 12 km/h (A), and sea-breeze having a constant component oriented landwards (B), northeastwards (C), and westwards (D).

a surface-advected plume with a maximum thickness of about 8 m, which represents nearly the double of the thickness of the plume forced by a constant westward wind (Figure 5.27). In this case, the 35.0 isohaline has been used as the plume boundary, which also allows the characterization of the plume's horizontal features as presented above. In contrast to the unforced plume, the structure of the current plumes did not feature a landward movement of ambient waters in the bottom layer, underneath the lighter water, with the exception of plumes forced by westward breezes for which the two velocity components are both negative.

This behaviour is illustrated in Figure 5.28, which presents the time series of the

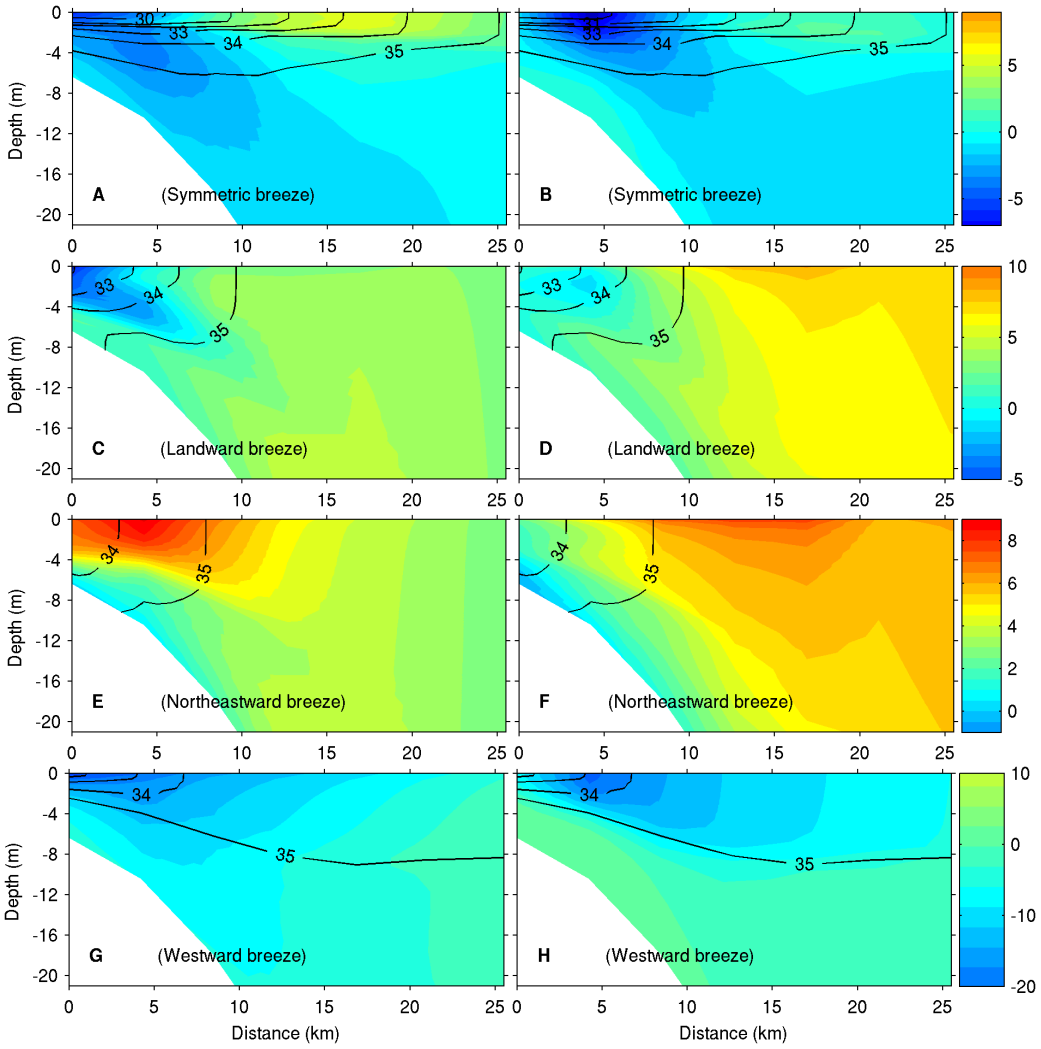

Figure 5.27: Vertical distribution of the eastward (*left*) and northward (*right*) velocity components overlaid by salinity contours (C.I. is 1 psu) computed for different sea-breeze configurations at the model time, $t = 23$ days, along the across-shore transect leaving the central source. Velocity is given in cm/s.

sea-breezes and current at selected depths. The time-series of velocity components can be approximated to the Lissajous curve for two signals having the same frequency, for which the trajectory is always elliptic, except in the case of an unitary aspect ratio (same magnitude) with phase shift of $\pi/2$ that result in a circular orbit, or the case of phase shift of π or 0 (irrespective of the magnitude), which results in a rectilinear trajectory. By these means, the circulation throughout the water column is primarily elliptic, but it changes from nearly circular within the plume in the upper layer, to elliptic elongated at about 3 m depth, and finally to nearly rectilinear at the bottom layers.

In summary, the results of experiments with a finer resolution bathymetry indicate that plume waters are primarily transported by the winds in what is known as

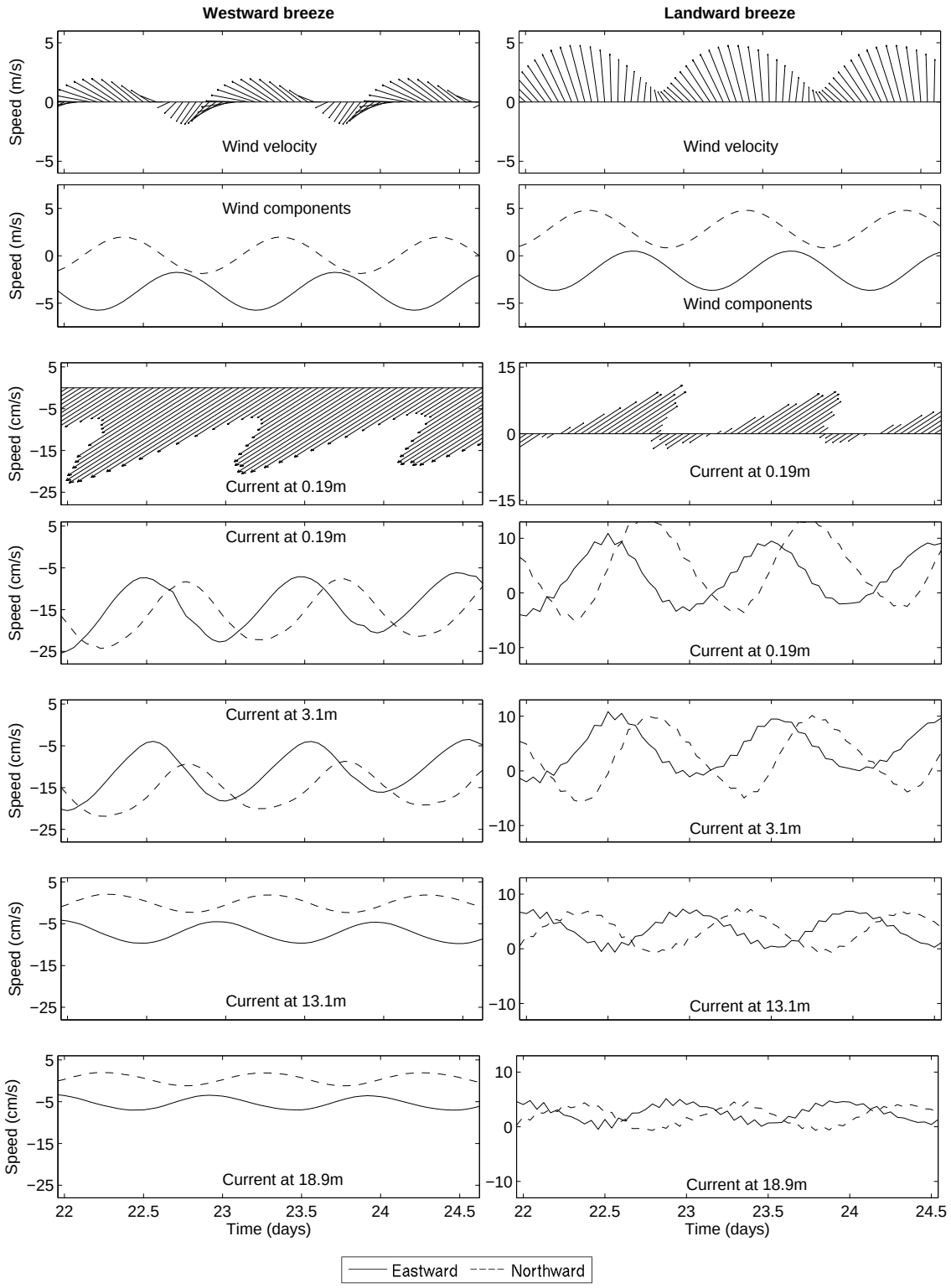

Figure 5.28: Time series of wind velocity and components, as well as the current at four depths (surface layer, two intermediate layers, and the bottom layer) between days 22 and 24.5 counted from the the beginning of simulation, recorded at a station located 8.4 km from the coast along the transect leaven the central source (see Figure 5.27).

Ekman drift, with the landmass and shoreline playing an important role in the determination of the plume shape. This behaviour confirms the overall results found for the coarser resolution bathymetry, except that the plumes produced in that experiment were subjected to a much stronger influence of bottom friction and bottom boundary layer processes, which is a direct consequence of the notably shallower water column.

5.2.3 The tide-forced plume

The implications of tidal forcing on the otherwise unforced plume is studied next. A semi-diurnal oscillation of the free-surface is imposed at the open boundaries and allowed to propagate over the model domain. The experiment consisted of two sets of model runs where the tides were introduced to the model domain through the eastern boundary in the first set, and through the southern boundary in the second set. The amplitude of the free-surface oscillation was varied between 50, 100, and 200 cm in the first set, and the corresponding model runs were termed TE1, TE2, and TE3, respectively. It is worth mentioning that the amplitude used in the experiment TE3 is only slightly larger than half the values reported for the Port of Beira ($\sim 20^o S$). For the second set, only an amplitude of 50 cm was considered and the run was termed TS1. The period of the tidal wave was set to 12 hours in all the cases, and the remaining parameters followed the specifications in the previous experiments. As for the experiment with the coarser resolution bathymetry and tidal forcing, the tides were introduced to the domain using the Flather boundary conditions, specified for the normal component of barotropic velocity at the eastern/southern boundary. The constraints for the baroclinic velocities and tracers were expressed in terms of the Orlanski radiation conditions, and a zero-gradient condition was imposed for the free surface.

The propagation of the tidal wave 23 days from the beginning of the simulation is presented in Figure 5.29. The tides propagate from south to north, regardless of the boundary used to introduce the perturbation, as shown by the progression of the co-tidal lines that indicate the time and location of the passage of wave crest. High-water occurs first at the coast around $21^o S$ in all cases, from where it travels seawards as well as towards the coast between the Zambezi delta and the Pungoe River estuary (located about $19^o 45' S$). The tidal wave is considerably slower in the shelf zone than offshore, and in contrast, the tidal range decreases gradually seawards from the vicinities of the Pungoe River estuary. Another feature present in all the cases is the massive increase in the tidal range onshore from the 100 m isobath, mainly in the region south of the Zambezi delta where the shelf has its widest extension.

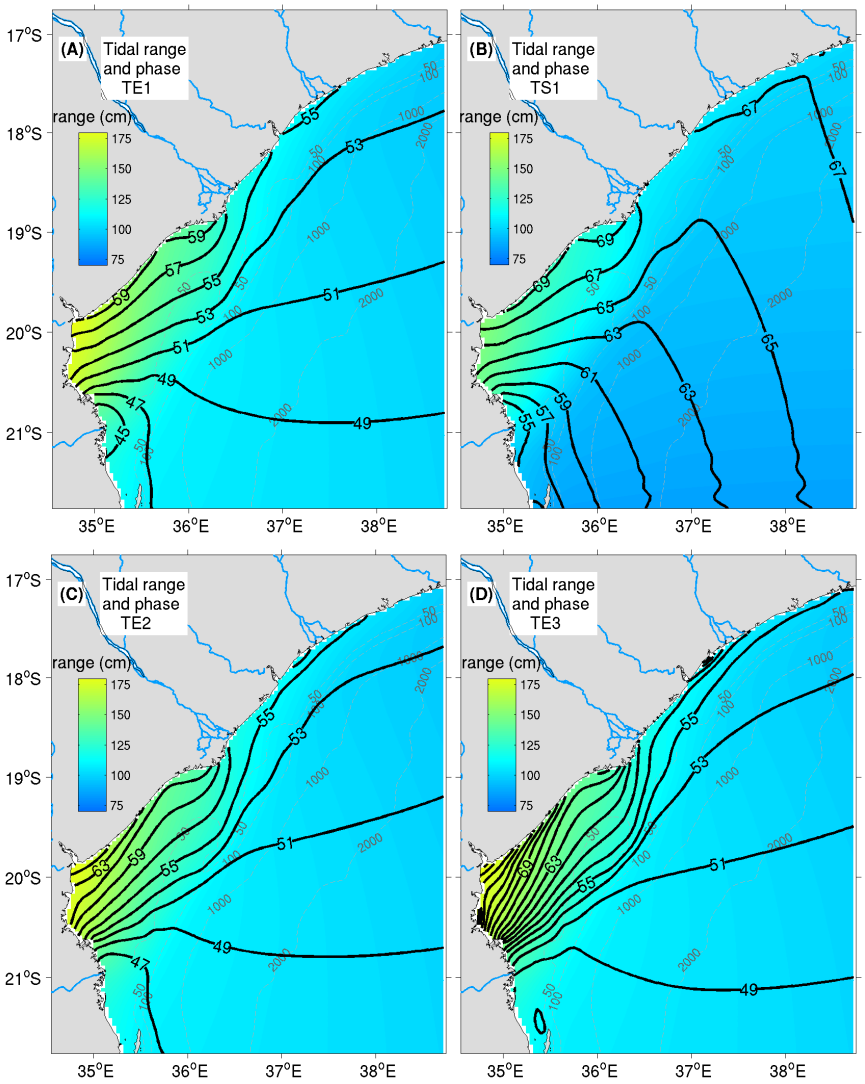

Figure 5.29: Propagation of the tidal wave at the model time, $t = 23$ days, as illustrated by the tidal range (colours, range in cm) overlaid by co-tidal lines (thick lines, phase in *minutes*). The different panels present a tidal wave of amplitude 50 cm introduced through the eastern (A) and southern (B) boundaries, as well as a wave of 100 cm (C) and 200 cm (D) introduced through the eastern boundary.

Despite the small differences in the wave propagation between cases TE1 and TS1, the transient velocity field at the surface layer (tidal ellipses presented in Figure 5.30), as well as the residual velocity, does not display an appreciable difference, and consequently the plume dispersion patterns are similar in both cases. This means that having the tides introduced from either open boundary does not qualitatively influence the resulting plume structure. This behaviour is consistent with the results from the coarser resolution experiments, except the fact that, due to the increased depths in the current configuration, the tide travels faster towards the coast, as evidenced in the phase lines presented in Figures 5.17 and 5.29. Consequently, the following analysis of plume structure will be based on the simulation with tides

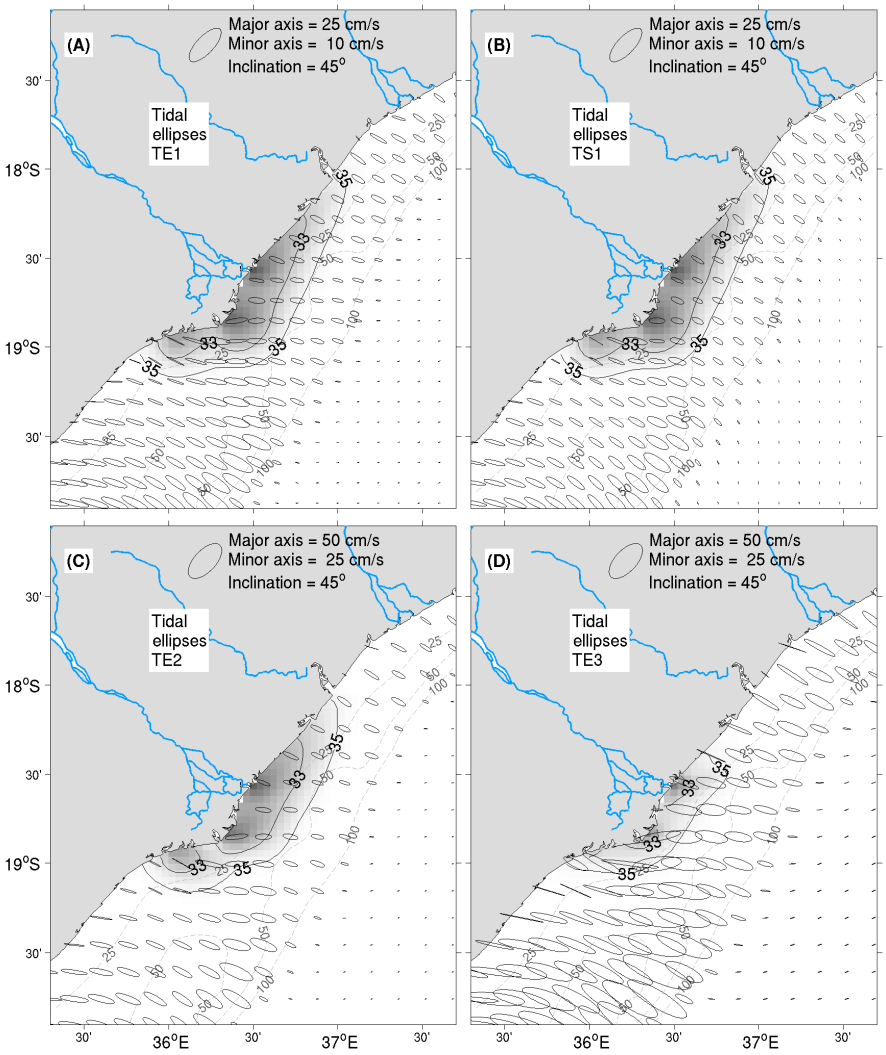

Figure 5.30: Horizontal distribution of surface salinity averaged over one tidal cycle (shaded colours) and ellipses of the tidal current presented for one tidal cycle centered at the time $t = 23$ days, for the case of a tidal wave with 50 cm amplitude introduced through the eastern (A) and the southern (B) boundary, as well as a wave having amplitude of 100 cm (C) and 200 cm (D) introduced from the eastern boundary.

introduced from the eastern boundary.

The orientation of the tidal current ellipses (Figure 5.30) is similar in every case, and it does not seem to be much affected by the buoyancy-driven flow in the plume zone. Conversely, the magnitude of the current increases considerably within the reach of plume waters, as indicated by the size of ellipses that is comparatively larger within the plume than away from the region of river influence. The size of ellipses decreases shoreward from the shelf edge in the region between $19^o - 20^oS$, and some variation in the orientation of ellipses is noticeable. These changes are very likely caused by bottom friction and bottom boundary layer processes that seem to have minimum effect in the plume region.

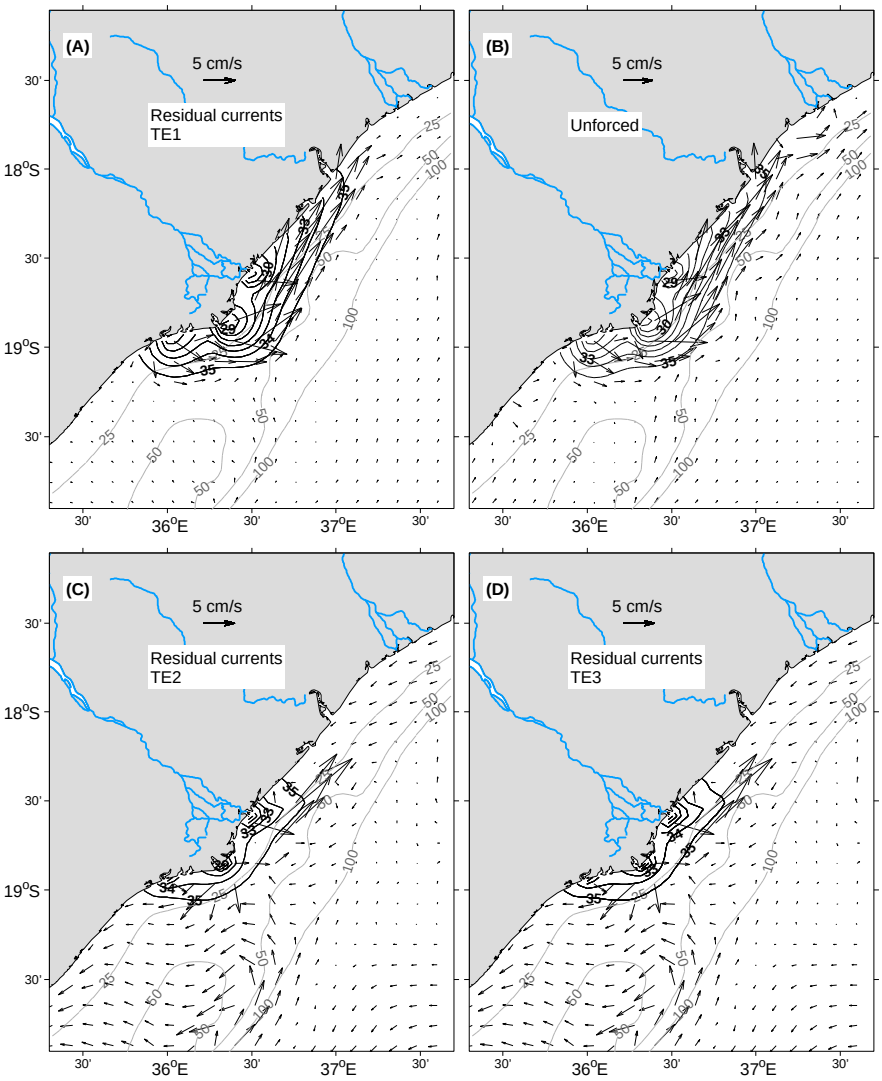

Figure 5.31: A, C, and D: Same as the previous figure, except for the velocity averaged over one tidal cycle. In panel (B), the surface salinity and velocity fields are presented for time, $t = 23$ days, to allow an easy comparison. C.I.'s are 28 to 35 by 1 psu.

Figure 5.31 presents the surface salinity and residuals of the tidal currents for the simulations with tide amplitude of 50, 100, and 200 cm, which correspond to the experiments TE1, TE2, and TE3. The experiments TE1 and TE2 resulted in a surface velocity field (residuals) that in general are comparable to the unforced plume (displayed in panel B of Figure 5.31), for which the magnitude of buoyancy-driven flow lies closely between $2 - 10$ cm/s and has a mean value of 6.3 cm/s. The average of the residual current within the plume waters (salinity < 35.00) is 4.5, 9.3, and 17.5 cm/s in the experiments TE1, TE2, and TE3, respectively. These tidal current amplitudes are smaller than the realistic conditions, judging by the recent estimates of Leal et al. (2009) that reported flooding and ebbing values in the range $20 - 25$ cm/s. When compared with the unforced plume, the cases TE1, TE2,

and TE3 can be thought of as a situation where the tide-induced flow is weaker, comparable, and stronger than the buoyancy-driven flow, respectively.

According to Chao (1990), the amplitude of the tidal current can be used to estimate the characteristic length scale of the tidal excursion, through the expression

$$\int_0^{T/2} V_0 \sin \frac{2\pi t}{T} dt = TV_0/\pi \,,$$

where V_0 is the amplitude of the tidal current. This equation resulted in a length scale of 0.6, 1.3, and 2.4 km for the cases TE1, TE2, and TE3, respectively. Note that in all cases, the tidal excursion is considerably smaller than the horizontal grid spacing of the model ($max \triangle x \approx max \triangle y = 4.2$ km), suggesting that the model might fail to capture some vital aspects of the tide influence on the plume spreading, a fact that arises from the choice of model grid resolution and/or the tidal wave amplitude.

Nonetheless, the plume produced in the TE1 experiment, for which the tidal-induced flow is weaker than the buoyancy-driven flow, exhibits a horizontal structure that is nearly identical to that of the unforced plume. A closer inspection to the position of the 35 psu isohaline reveals that near the sources and particularly offshore from the central source the tide-forced plume extends offshore up to the 50 m isobath, while the brackish water in the unforced is transported to very close, but never really crosses the 50 m isobath. There is almost no difference in the alongshore extension of the plume in these two cases, however looking at the plume as a whole (panels A and B of Figure 5.31), one finds that the most striking feature is the resemblance of the plume shapes, including the spacing between the isohaline contours.

In the case TE2, the residuals of the tide-induced flow are somewhat comparable to the buoyancy-driven flow in the unforced plume, and the main difference in the horizontal features is the noticeably shorter alongshore plume extent, in relation to the unforced plume (panels B and C), as well the increased spacing between isohalines that indicates higher mixing. The offshore extent of the plume in the region near the sources is identical to the unforced plume, but it is slightly larger along the coastal current in the downstream coast.

The plume structure in the case TE3 with a tide-induced flow stronger than the the buoyancy-driven flow, is greatly modified from that of the unforced plume. The downstream as well as offshore penetration of the plume waters is strongly reduced, the coastal current is absent, the spacing between isohalines have increased even more, and the 33.0 isohaline and fresher waters are limited to few kilometers offshore from the sources.

In addition, the vertical distributions of the physical properties in tide-forced plumes differ considerably from the unforced case presented previously, and the

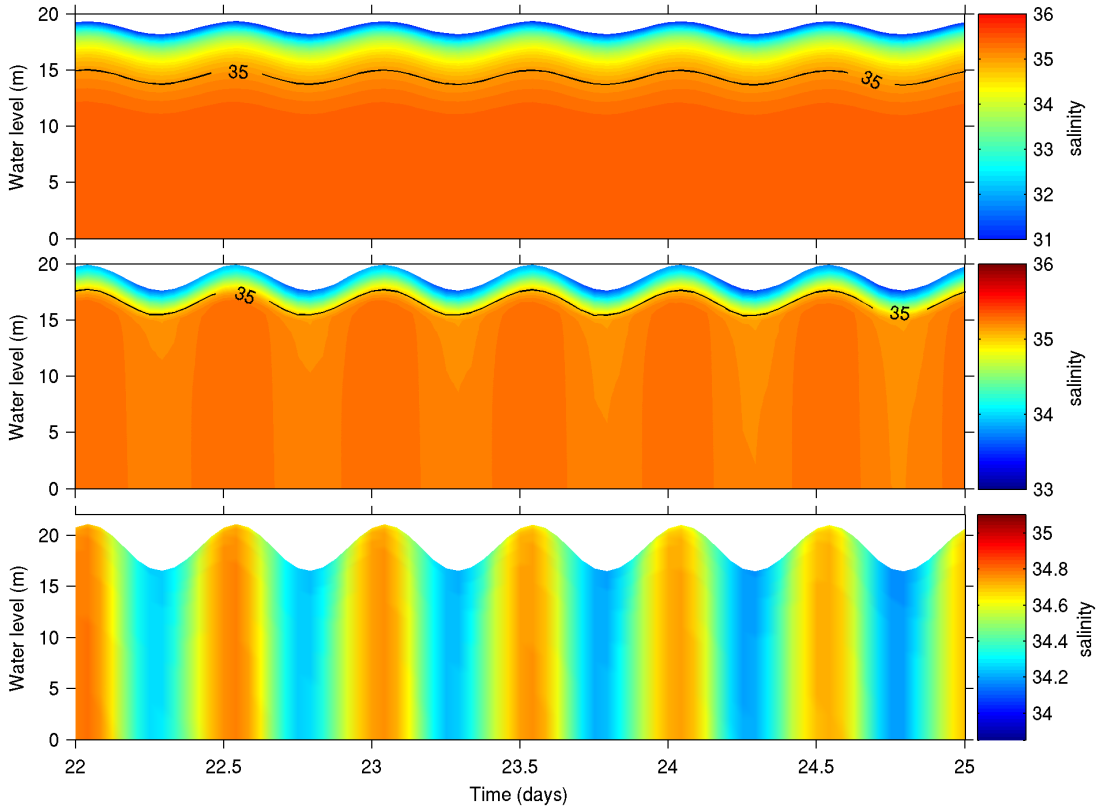

Figure 5.32: Time series of salinity during days 22 and 25 for a station located 8.4 km offshore from the central river mouth. From top to bottom it is shown the results for the run TE1, TE2, and TE3.

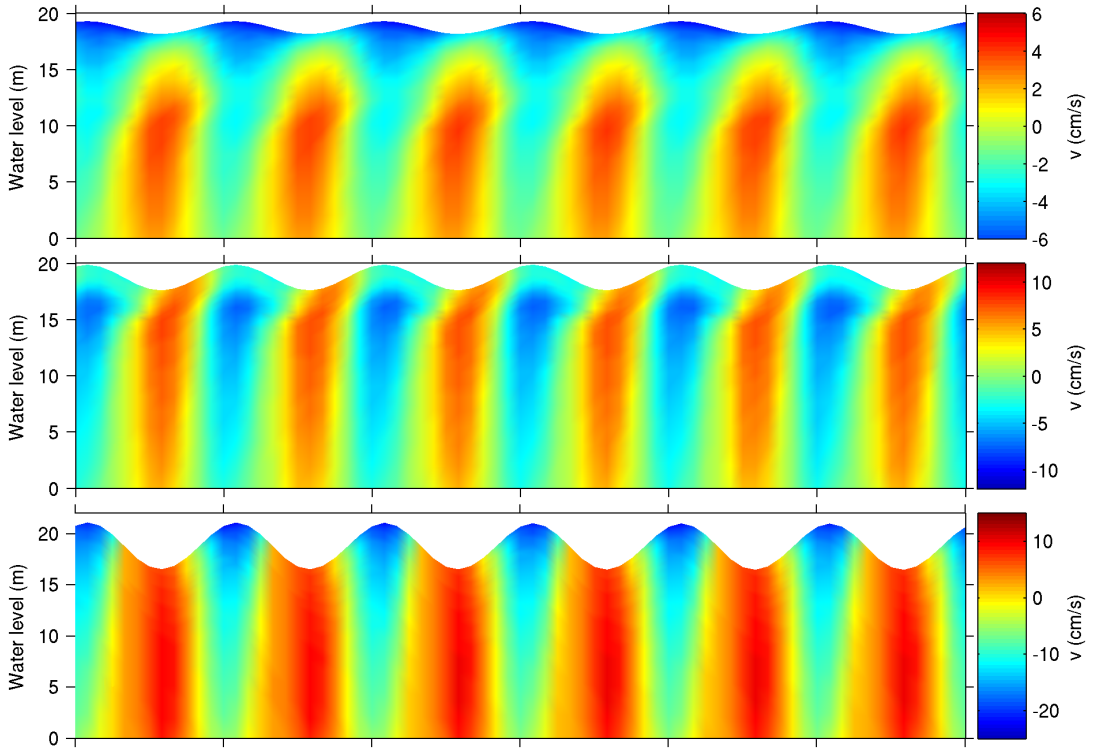

Figure 5.33: Same as Figure 5.32, except for the northward component of velocity.

differences can be characterized according to the time scale in which their occur. Some sub-tidal features measured at a station located 8.4 km offshore from the central source are presented in Figures 5.32 and 5.33. The water column in the cases simulated with tidal amplitude of 50 and 100 cm is stratified throughout the tidal cycle, and the thickness of the surface layer containing brackish water is about 4 and 2.5 m in each case, respectively. The salinity increases gradually downwards from the surface to the plume limit, and the salinity in the layers underneath the plume is constant throughout the tidal cycle in the experiment TE1, while it undergoes a tidally variation in the case TE2. Conversely, plume waters occupy the entire water column in the case TE3, and the salinity distribution is vertically uniform and it varies tidally, with peak salinities occurring at high-water.

The eastward velocity component is identical in the three tide-forced cases (results not shown), except that the magnitude is larger for higher tidal wave amplitudes, and it is characterized by the tendency to be vertically homogeneous, and the continuous change in orientation at the tidal frequency. However, the flow in the layers occupied by plume waters is slightly more intense than the layers below, and this feature is more noticeable in the case TE1. The magnitude of the eastward velocity is significantly larger than the northward counterpart, displayed in Figure 5.33. Conversely, the northward velocity component presents large differences between the different experiments. For the case TE1, no reversal was observed at the surface layer, and the reversal in the interior layers was delayed in relation to the bottom layers. The flow in the cases TE2 and TE3 reversed in all layers, but only in the former case the flow exhibited a phase lag between plume and ambient waters since the entire water column is occupied by plume waters in the case TE3. The phase lag gives an indication of the horizontal velocity shear, which has a maximum value during high-water.

The super-tidal features can be visualized in Figure 5.34. The plume structure for the case TE1 resembles that of the unforced case, and is marked by a relatively strong positive eastward velocity and a negative northward velocity in the nearshore. The maximum plume thickness is about 4 m, which is slightly less than the unforced plume. In contrast, the unforced plume features a landward flow of saltier water underneath the brackish water, which is not evident in any of the tide-forced plumes. Due to the additional horizontal and vertical mixing induced by the tides, the seaward excursion of the plume is progressively reduced, such that the larger the tidal wave amplitude the shorter the plume excursion. With the increase in the tide wave amplitude, and hence increase in tidal energy available for mixing, the structure of the plume went from surface-advected in the case TE1 to bottom-advected in the case TE3. According to Yankovsky and Chapman (1997), the plume

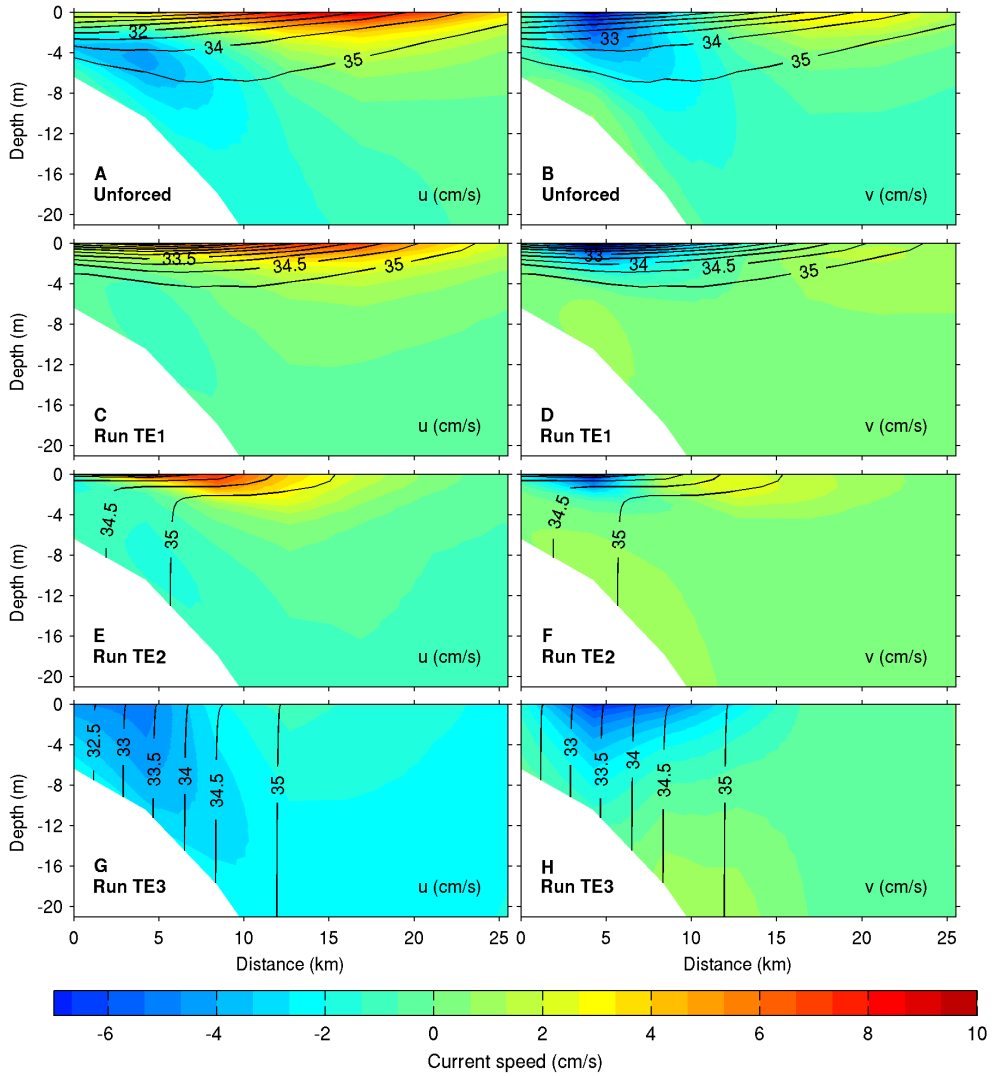

Figure 5.34: Vertical distribution of the eastward (left) and northward (right) velocity components overlaid by salinity contours at the across-shore transect leaving the central source. All the fields in the tide-forced runs TE1, TE2, and TE3 were averaged over one tidal cycle, and the unforced structure was averaged over 24 hours, both centered at the model time $t = 23$ days.

in case TE2 falls under the "intermediary" classification.

In summary, the tide-forced plume presented in this section compares well with that simulated using a coarser resolution bathymetry. In fact, the main characteristics found in the previous analysis that includes no stratification within the plume and short penetration (in comparison with the unforced plume), represent a better match to the findings for a plume forced by a high-energy tide whose residual current surpasses the buoyancy-driven flow.

The tests with different wave amplitudes revealed that the primary effect of tides on a freshwater plume is the shortening of the plume's offshore and alongshore

penetration, along with the mixing of the water column. This enhanced mixing is more prominent in the mouth region, where a plume base that moves laterally to-and-fro with the tides is created. In fact, the tide-induced lateral movement is not limited to the plume base, but it occurs in the entire plume region when enough energy is supplied by the tides, eroding completely the stratification everywhere in the plume.

The residual current is greatest within the plume where buoyancy strongly contributes to determine the velocity field. Although the residual current represents only a small fraction of the transient flow, it is the main driver of the plume's lateral spreading.

5.2.4 Wind-driven motion of a tide-forced plume

The response of a pre-existing tide-forced plume to impulsive wind forcing is investigated next. A number of model runs were performed where the plumes described in the previous section were subjected to an oscillating wind field for 10 consecutive days. The numerical experiments comprise three different situations characterized by the initial degree of stratification, namely, a surface advected plume $\sim 4\,\mathrm{m}$ thick, an intermediary plume with its base displaced offshore by $6 \sim 7\,\mathrm{km}$, and a bottom advected plume with no stratification. In order of appearance, these correspond to the tide-forced plumes produced for a wave amplitude of 50, 100, and 200 cm, respectively. In terms of circulation, it has been shown that considering the constant river discharge of $1500\,\mathrm{m}^3/\mathrm{s}$, these plumes represent a situation where the buoyancy-driven flow dominates over the tide-induced residual flow (case-1), a situation where the two flows are comparable (case-2), or a situation where the tidal flow dominates (case-3). The wind field in each case comprised a moderate constant wind blowing in three different direction (landward, westward and southwestward), and the three asymmetric sea-breezes derived from the weather forecast model (see Figure 5.11). The structure of the plume obtained in each case is as follows.

Case-1: buoyancy forcing dominates over the tide forcing

Despite the difference in the wind fields, the transient circulation outside the plume waters did not vary much between the various cases analyzed, as displayed in Figure 5.35. Within the plume, the differences in the velocity appear to be insignificant and they are limited to the size of ellipsoids denoting the magnitude of the flow. In fact, the transient flow in all these cases compares very well with the flow driven solely by tides and river discharges (prior to wind forcing) presented in Figure 5.30-A.

Conversely, the residual flow (Figure 5.36), computed by averaging the instan-

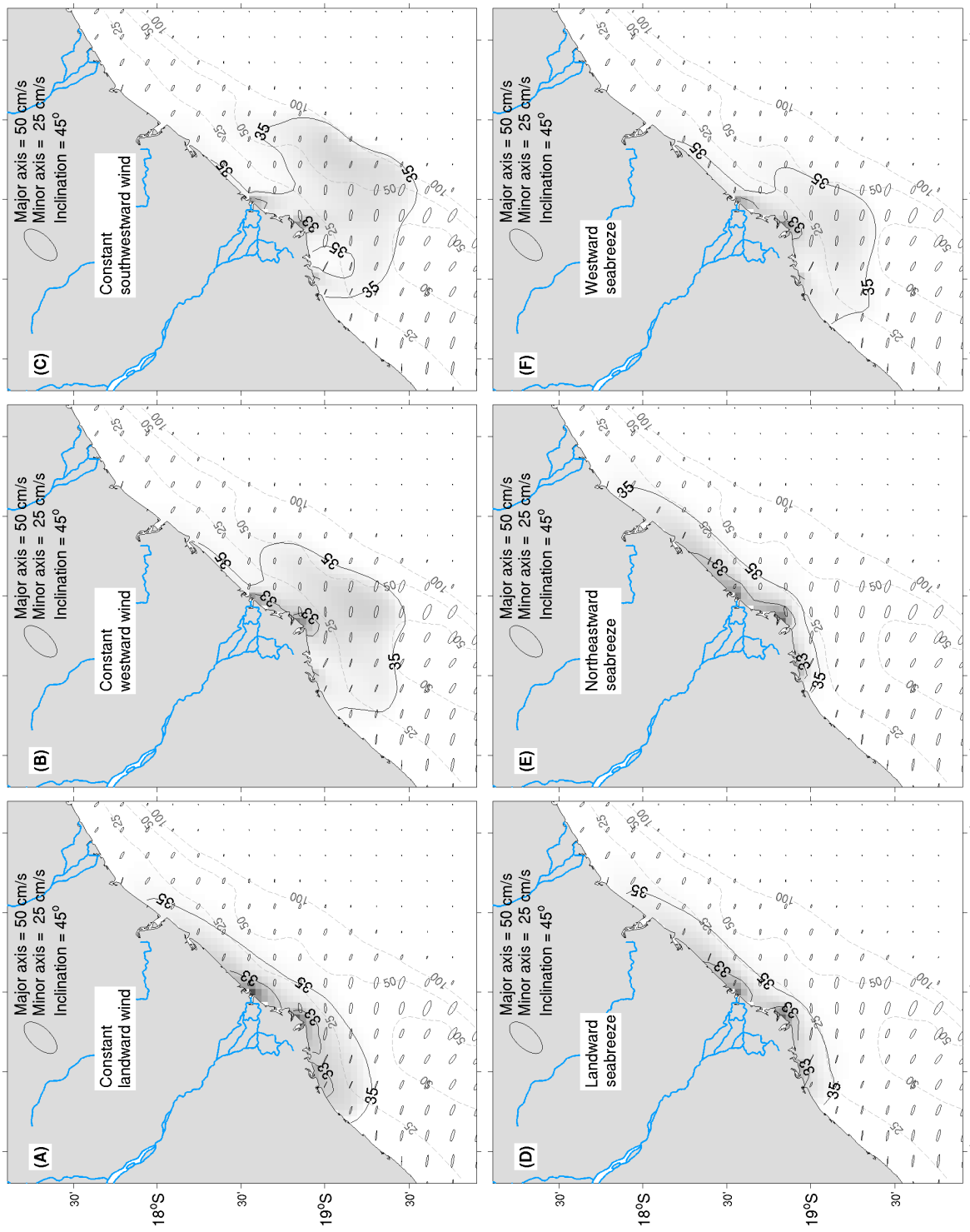

Figure 5.35: Ellipses of the surface current and salinity (shaded colours) at the model time, $t = 31$ days, simulated for a tidal forcing corresponding to a wave amplitude of 50 cm.

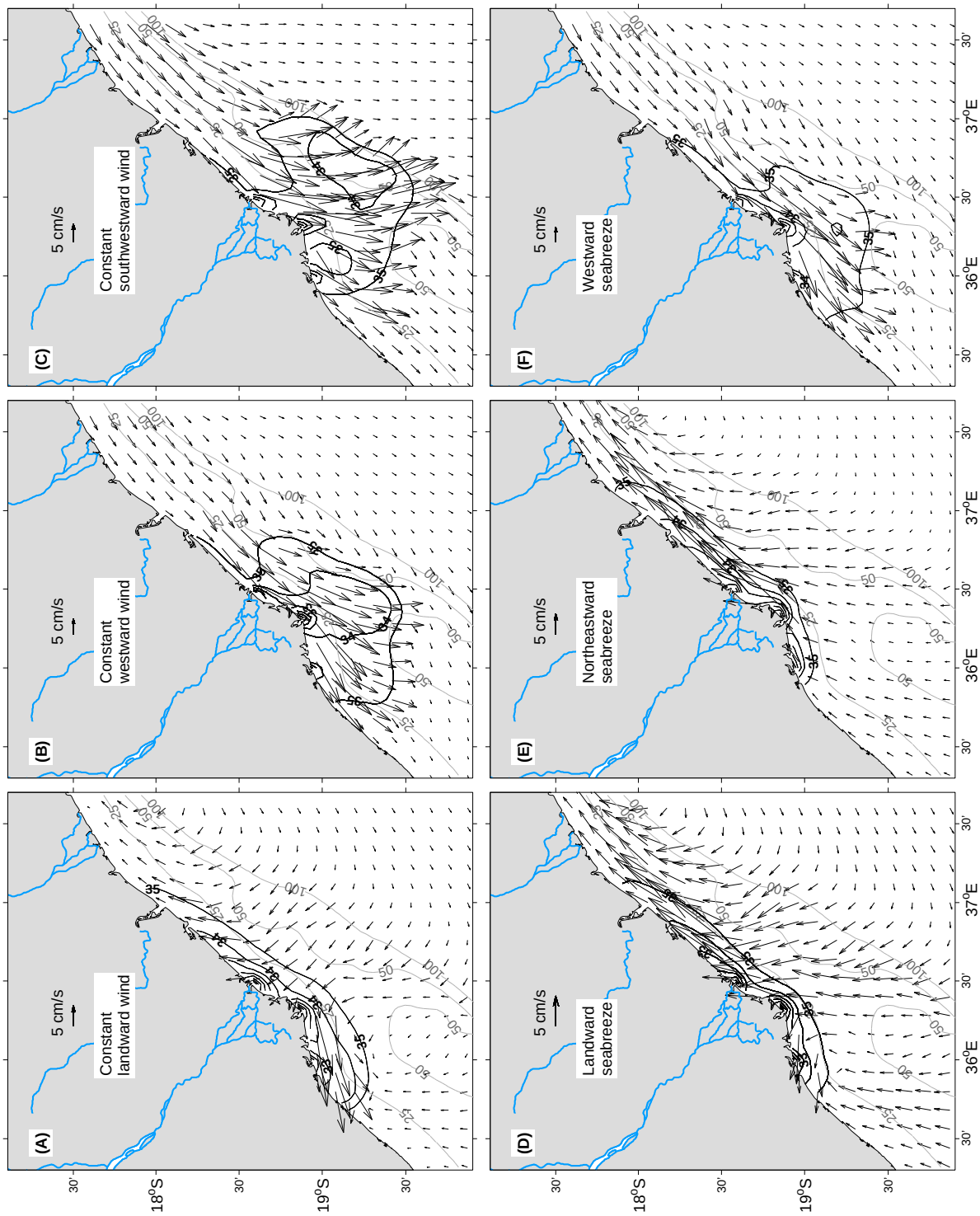

Figure 5.36: Same as previous image, except for the residual current (averages over one tidal cycle). Salinity contour is 28 to 35 by 1 psu.

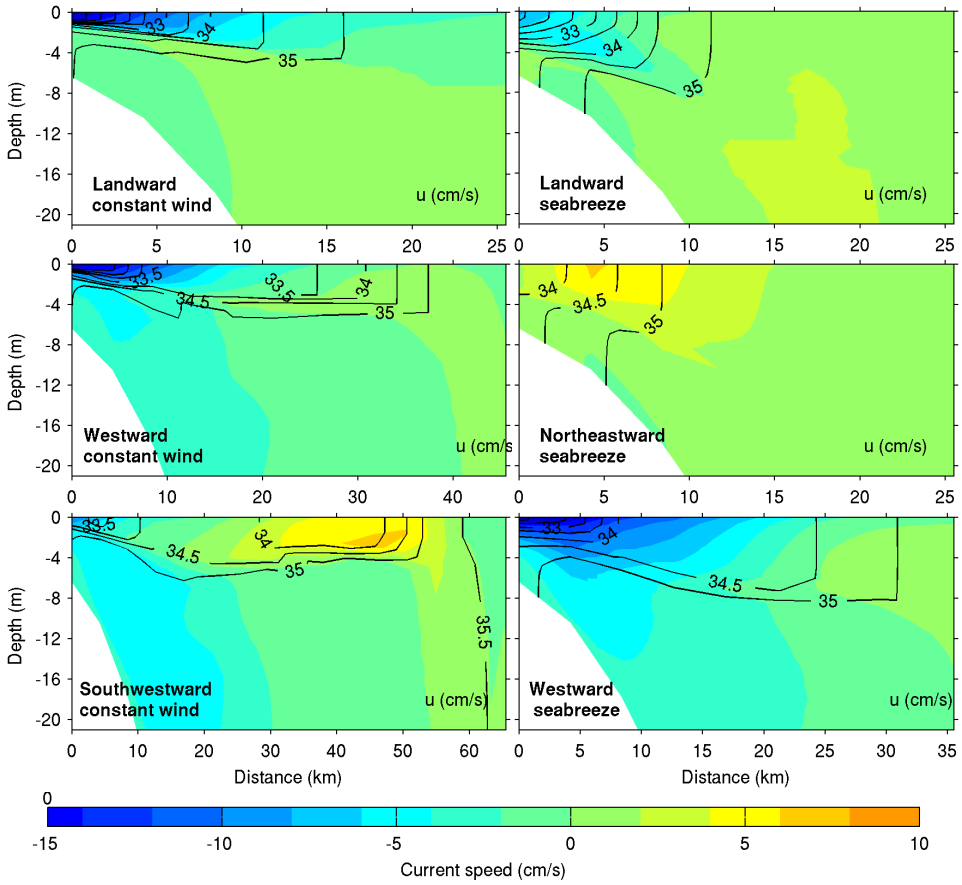

Figure 5.37: Vertical distribution of the eastward velocity component overlaid by salinity contours for different wind conditions (as indicated by the text in each panel), averaged over one tidal cycle at day 31 (8 days from the start of wind forcing).

taneous velocity field over a 24 hour period, is now notably stronger in comparison with the flow in the no-wind case, and it is dominated by the wind-induced circulation. The resulting plumes spread in a similar manner to the plumes forced solely by an impulsive wind, with the exception that due to the additional tide-induced mixing, both the offshore and alongshore extents are reduced. Also, the vertical distribution of salinity and the eastward velocity component (Figure 5.37) suggests a plume structure that is deeper than the corresponding no-tide (Figure 5.27) and no-wind cases (Figure 5.34). The combination of the tide- and wind-induced mixing in all cases with sea-breeze resulted in bottom advected structures, with the base of the plume (where it connects to the bottom) extending a few kilometers offshore, as indicated by the position of the 35.0 psu contour.

Case-2: comparable buoyancy-driven and tide-induced flows

Tidal ellipses for the surface velocity are presented in Figure 5.38 . The eccentricity of the tidal current ellipses, as well as the orientation of the ellipse axis tends to

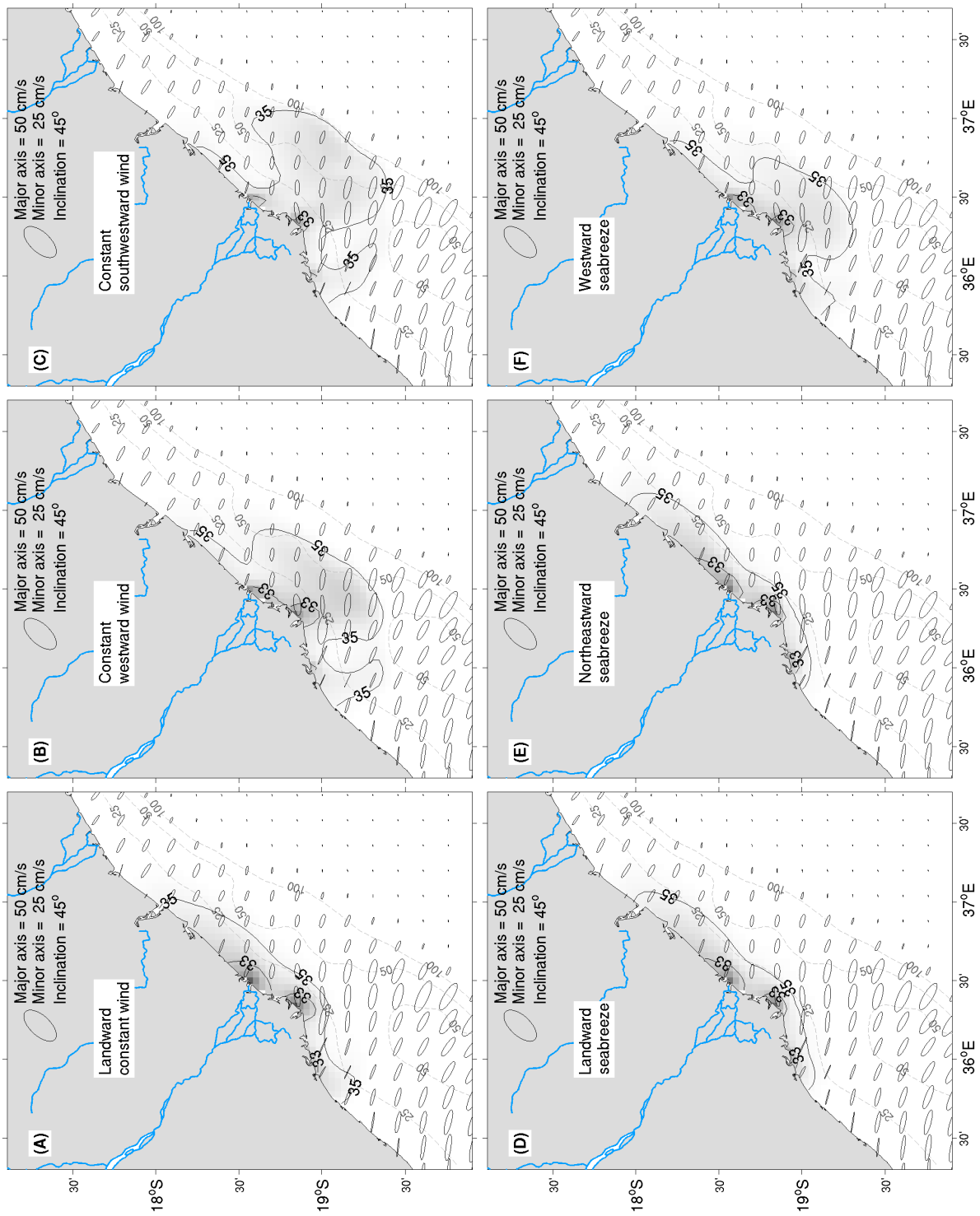

Figure 5.38: Same as Figure 5.35, except for a tidal forcing corresponding to a wave amplitude of 100 cm.

remain unaltered as the amplitude of the tidal wave is increased from 50 to 100 cm, however the magnitude of the amplitude of the tidal current (indicated by the size of ellipsoids) increases significantly. By comparing the residual flows in case-1 and the current case (Fig. 5.39), one finds that the orientation is in general the same and the differences in magnitude noticeable in the horizontal distributions are subtle. However, the vertical distributions indicate a reduction in the residual flow, which is still dominated by the winds. The super-tidal structure presented in Figures 5.38 and 5.39 indicates that the plume in every case analyzed spreads in the exact same fashion as its correspondent in case-1, except the plume extension is reduced, particularly in the alongshore direction.

It is interesting to note that even in the cases where the wind-induced motion of the plume is primarily seawards (i.e., constant westward and southeastward winds, and westward breezes), the offshore plume extension did not change significantly. This behaviour is in excellent agreement with the spreading patterns reported by Garvine (1999) and Isobe (2005). These studies have indicated that little or no additional offshore penetration was observed in the simulations forced by tides.

The main difference in the vertical structure of the current plume in relation to the case-1 is the enhanced vertical mixing near the coast in all cases, which is denoted by both the existence of a plume base in contact with the bottom in the cases of constant wind, and the seaward movement of the base or the complete erosion of the stratification in the cases of sea-breeze.

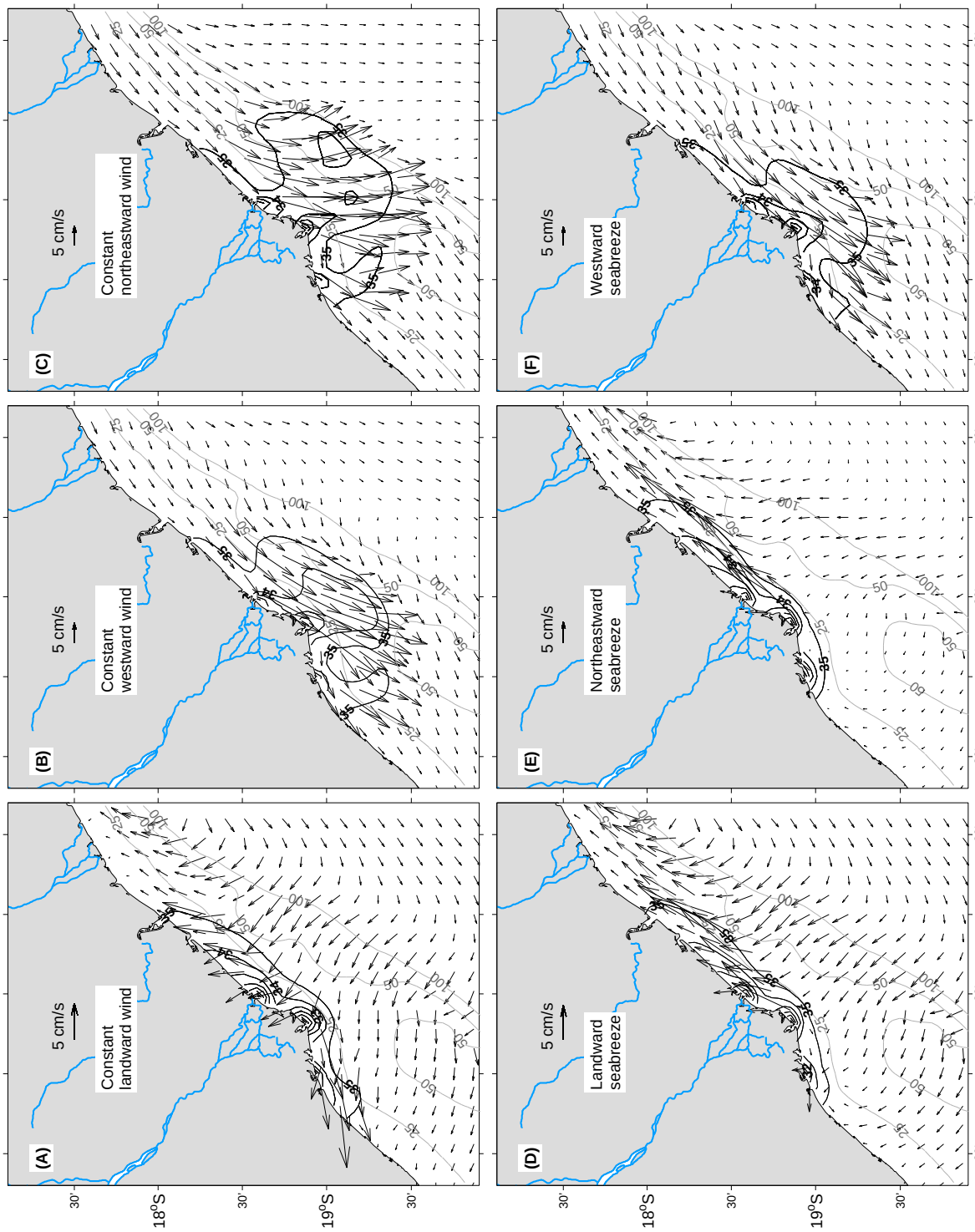

Figure 5.39: Same as previous image, except for the residual current (averages over one tidal cycle). Salinity contour is 28 to 35 by 1 psu.

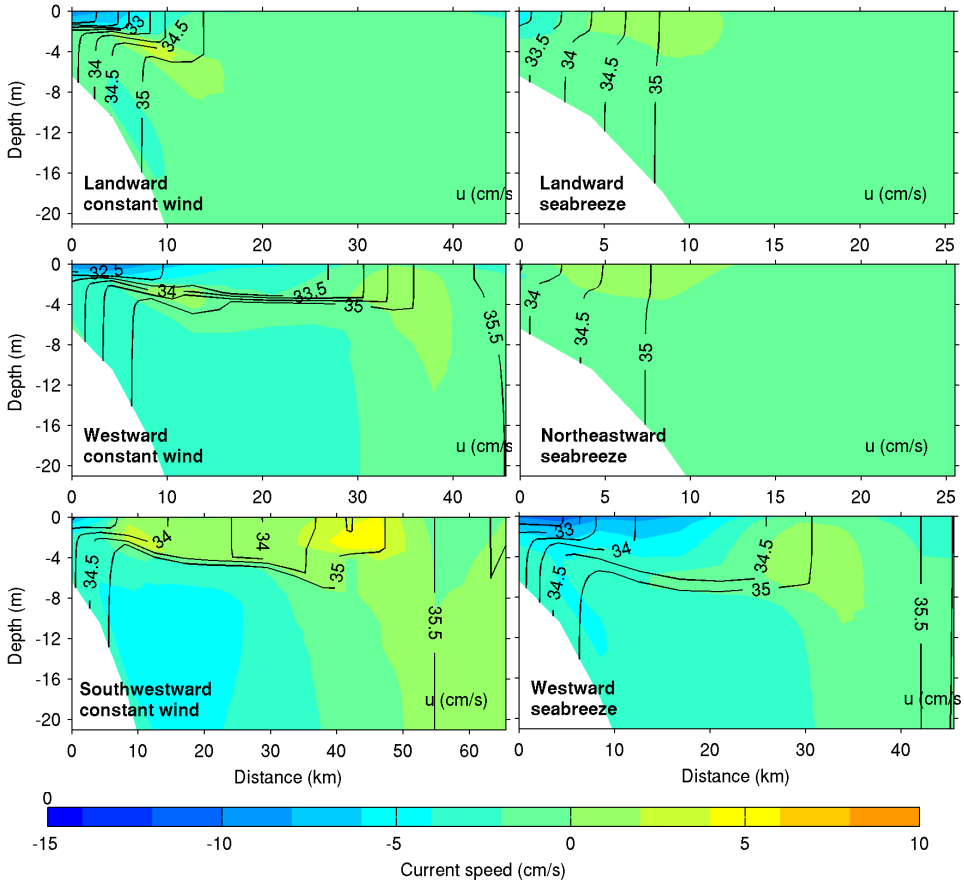

Figure 5.40: Same as Figure 5.37, except for the case of a tidal wave of 100 cm amplitude.

Case-3: tide forcing dominates over the buoyancy forcing

For a tidal wave of 200 cm amplitude, the resulting transient flow (Figure 5.41) exceeds 50 cm/s in some regions of the domain, and it is similar for all wind conditions analyzed. That flow intensity is a few times higher than the buoyancy-driven and wind-driven flows estimated when no other external forcing is applied to the plume. In consequence, the residual flow appears to be insensitive to small differences in the wind forcing, since a northeastward breezes produced the surface flow pattern similar to that produced by landward breezes and constant wind. Common features of these wind fields include an associated Ekman drift oriented primarily downstream in the near-shore region (Figure 5.43). Given that the same argument holds true for the experiments using the other three wind fields analyzed, namely the westward breezes, and constant winds oriented either westwards or southeastwards, one may expect that in general, under a tide-driven flow stronger than the buoyancy-driven flow, the primary orientation of the resulting surface flow will depend on whether the Ekman drift at the coast is oriented primarily downstream (northeastwards) or upstream (southwestwards).

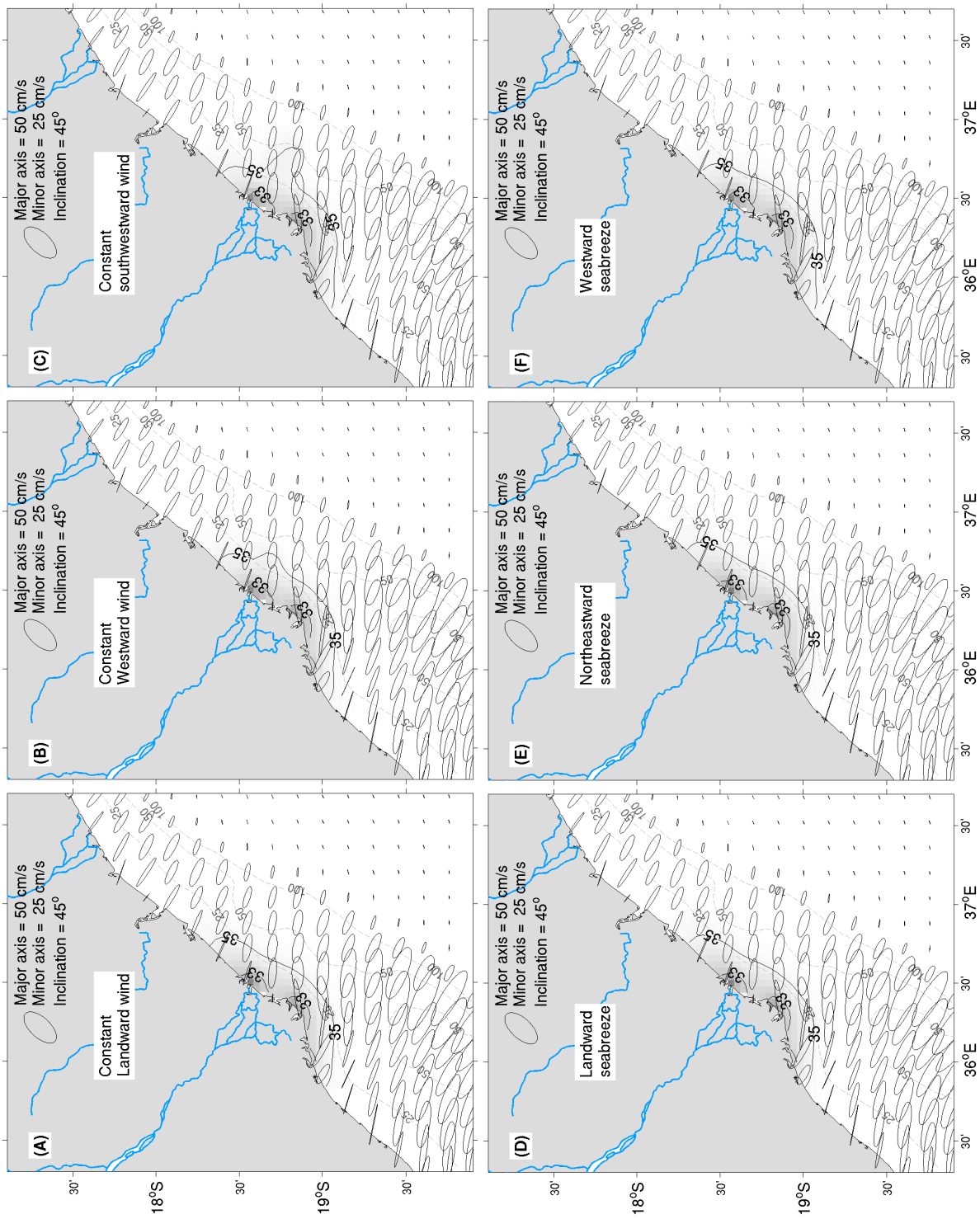

Figure 5.41: Same as Figure 5.35, except for a tidal forcing corresponding to a wave amplitude of 200 cm.

Conversely, the plume spreading is very similar in every case, with some differences that appear to be too small to detail. The plume in this case is limited to a small region of brackish water in the vicinity of the sources. Likewise, the vertical super-tidal structure is very similar in all cases, and comprises a fully mixed water column with very weak speeds. According to the position of the salinity contour 35.00 in Figure 5.42 , the offshore extension varies between 12 and $\sim$ 14 km in all cases. Notice the constant salinity gradient onshore from the 20 m isobath.

In summary, the plume's lateral spreading and vertical entrainment will depend largely on the amount of tidal energy available for mixing, and it will dictate the plume dynamics in coastal regions with strong tides. However, for plumes having the buoyancy-driven part of the flow weaker or comparable to the tide-induced flow, the spreading of the plume is governed by the Ekman drift and the plume attains considerable longshore and offshore extensions. It was found that most of the experiments with combined tide and wind forcing resulted in bottom-advected plumes, regardless of the orientation of the winds.

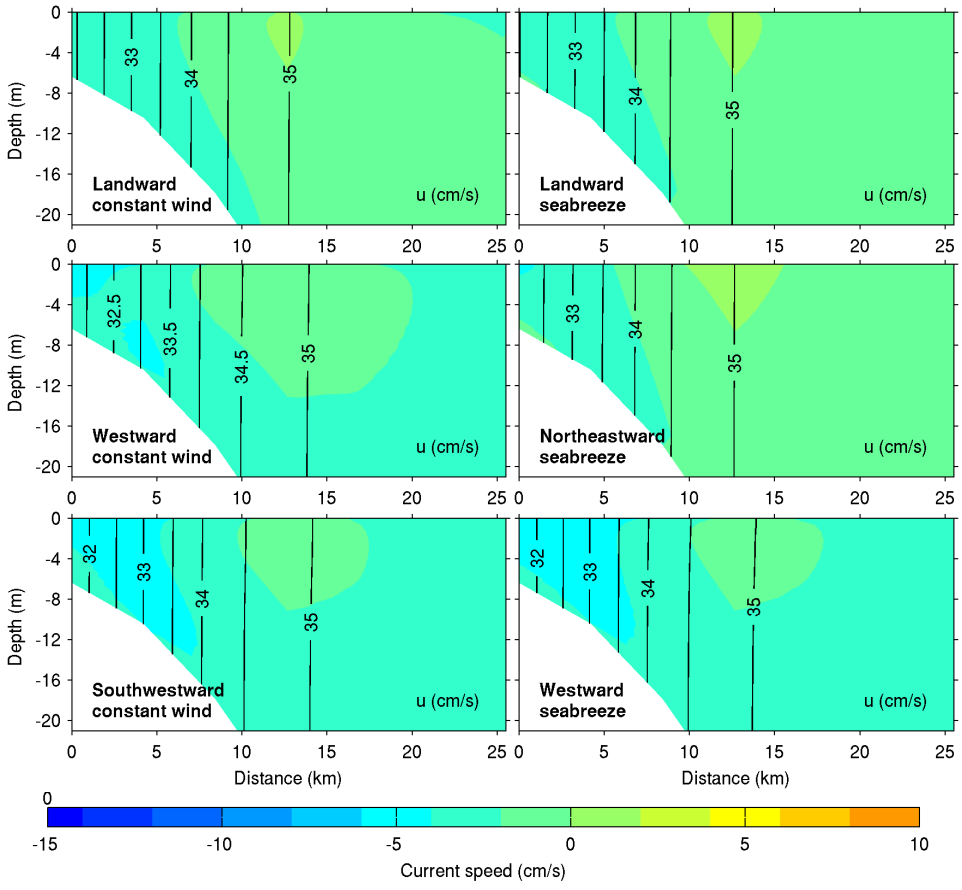

Figure 5.42: Same as Figure 5.37, except for the case of a tidal wave of 200 cm amplitude.

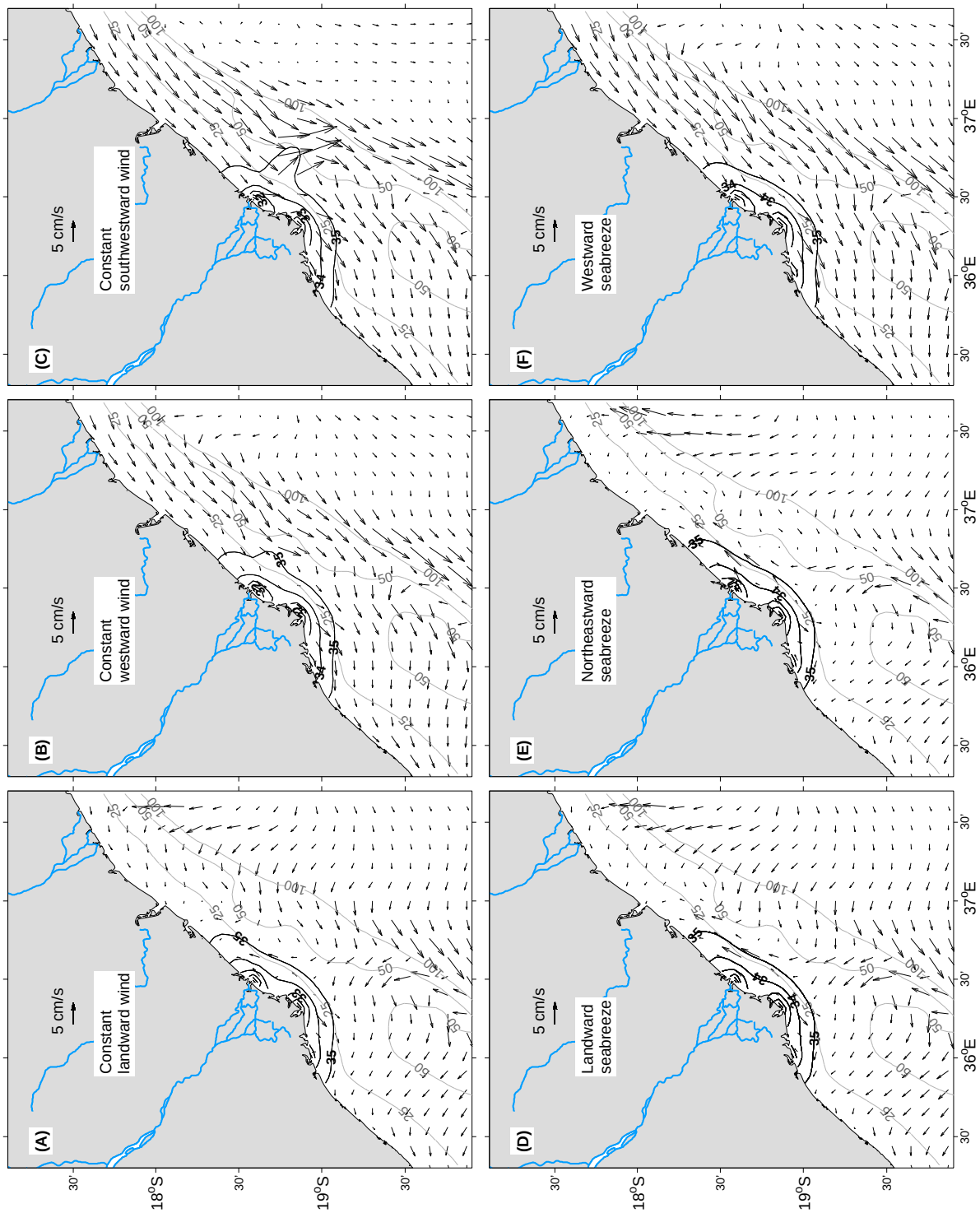

Figure 5.43: Same as Fig. 5.41, except for the residual current (averages over one tidal cycle). Salinity contour is 28 to 35 by 1 psu.

5.3 Discussion

Very often, numerical simulations of unforced buoyant discharges over constant slope topography present a bulge of re-circulating flow that is strongly affected by river inertia and the Earth's rotation. In this chapter, the structure of a freshwater plume was investigated through a series of numerical simulations that aimed to identify the roles played by wind and tide forcing on the plume structure. Realistic geometry and bathymetry were adopted, as a first step towards a realistic simulation of the Zambezi River plume.

One of the main characteristics of the Zambezi River is the deltaic form of its mouth, and most importantly, the fact that the delta constitutes a sizable headland with potential impacts on the near-shore circulation. A basic test was performed on the choice of the amount and location of the river mouths in relation to the centre of the headland, and some major differences were found. They are summarized as follows. Each of the three sources located either at the northern limit, at southern limit, or at the centre of the delta (i.e., the headland tip), produces a plume with a dispersion pattern completely different from the other two, as a consequence of the dissimilar distribution of surface pressure at the coast. By the fifth day of computation, the plumes from the northern and central sources spread radially, while the southern river mouth generates a plume bent northeastwards. This curved shape of the plume from the southern mouth is somewhat consistent with the observations of the Elwha River plume along the Strait of Juan de Fuca (west coast of the U.S.) reported by Warrick and Stevens (2011), the difference being that the bending is induced by the ambient flow in the Elwha River plume, and induced by the buoyancy-driven flow from the southern mouth of the Zambezi River. As the plume evolves, the differences in the spreading between the outflows from the different mouths endures, given that accumulation of brackish water tends to be proportional to the position of river mouths in relation to the centre of the headland. To avoid ambiguity in the choice of a particular source, the description of the Zambezi Plume structure in subsequent analysis relied on the plumes resulting from the combination of the three sources.

In the absence of external factors such as winds, tides, and/or ambient currents, a modest discharge of freshwater forms an estuary plume trapped to the coast that propagates northeastwards along the coast, in agreement with the downstream propagating plumes of Chao (1988a) and Garvine (1999). Two concurring simulations using different bathymetry datasets were performed, and no major differences in the above described dispersion pattern were found. The two datasets differed mainly in two aspects, firstly, the depth difference at the sources was about 2 m in average, and, secondly, the maximum depth difference in the periphery of the river mouth

(i.e., onshore from the 100 m isobath) was about 50 m. Part of Garvine's (2001) analysis included testing the impact of shelf configuration on the plume structure, and in particular he tested the minimum depth at the coast (i.e., a coastal wall) in a single inlet model. His overall findings indicated that the type of the predicted plume is very sensitive to the choices of model parameters. Following that line and comparing the two bathymetries, the largest difference found is the vertical plume structure that was surface-advected under the high resolution (and probably more accurate) bathymetry that features a deeper shelf, and bottom-advected otherwise.

No clear distinction between the bulge and coastal current regimes were found, which is a typical result for numerical simulations employing realistic geometry and bathymetry (Pimenta et al., 2005; Kourafalou et al., 1996b), and re-circulation in front of the river mouth was not apparent in the present results. However, due to the initially radial dispersion, a portion of freshwater was found south (upstream) of the river mouths just before it turned towards the downstream direction. The circulation patterns and the length scale associated with this portion of freshwater do not seem enough to explain the upstream flow of brackish water beyond 20^oS found in the observations presented in Chapter 2. In connection with this pattern, a number of experiments were conducted to explore the role of winds and tides in the plume structure. Two types of wind field were tested, constant winds blowing from eight different directions and sea-breezes that continuously vary their intensity and orientation within a period of 24 hours, both acting on a pre-existing plume.

It was found that regardless of the initial stratification set by the choice of bathymetry dataset, the wind forced simulations produced two distinct patterns of plume dispersion, which due to their shapes were termed "*large bulge*" and "*coastal current*". Large bulges were produced whenever the Ekman drift resulted in a fairly strong southwestward (alongshore upstream) motion of coastal waters inducing a seaward motion of the plume as a whole. The plumes are then characterized by a large portion of freshwater projected offshore to a distance equivalent or less than the position of the 100 m isobath. The surface flow within the plume waters varied from seaward to southwestward depending on the orientation and intensity of the windstress. On the other hand, a coastal current was produced whenever the Ekman drift resulted in a northeastward (downstream) motion of near-shore waters. Similarly, the maximum downstream penetration and the ratio of plume width at the source to the width of the current varied depending on the orientation and magnitude of the windstress.

In general, the Ekman drift governed the movement of coastal waters, which occurred at some angle to the left of the wind, as predicted for water over deep topography. Onshore from the 100 m isobath, this movement was constrained by the presence of landmass, resulting in (alongshore) flow oriented either northeastwards or

southwestwards. The plume waters were then transported to the left of this modified Ekman drift, whose orientation at the surface varied between $>15^o$ and 90^o in the case of large bulges, and between 0^o and 180^o in the case of coastal current. The plume response to impulsive constant winds has been examined before by Kourafalou et al. (1996b) and Chao (1988b), and the dispersion patterns presented in this chapter agree with these previous studies.

The wind conditions that resulted in a large bulge comprise both weak and moderate winds whose alongshore projection is negative, as well as seaward winds. It was noted that the large bulge constitutes a plume shape that fairly resembles the ship-based in-situ observations reported in Chapter 2, although with a few exceptions. For instance, the present simulation reproduced reasonably well the spreading transport of plume waters, reaching regions beyond 20^oS in some cases, but it failed to produce a concurrent downstream transport of freshwater in a coastal current significantly narrower than the upstream counterpart. It is speculated here that, in contrast to the portion of brackish water moving downstream, the upstream transport is a process purely driven by the winds. Based on results from numerical simulation and references to observational evidence, Kourafalou et al. (1996b) pointed out that a downstream buoyancy-driven current near the coast might very likely coexist with an upstream wind-driven flow, during periods of strong river discharges and light upwelling-favourable winds.

To study the plume response to oscillating winds, a number of simulations were conducted including either an uniform and symmetric sea-breeze of varying magnitude oriented predominantly landward, or a "realistic" and asymmetric sea-breeze with varying predominant orientation, both blowing over a pre-existing plume fed by a constant discharge of $1500\,\mathrm{m^3s^{-1}}$. The resulting plume response to the diurnal oscillation of winds can be summarized as follows:

(1) Uniform symmetric breezes are ineffective in driving a synoptic-scale (in the ocean viewpoint, here corresponding to $2 \sim >4$ days) variability of the plume, giving that every effort to move the plume is compensated 14 hours later by an effort to bring the plume to its initial position. In other words, the integral of shear stress exerted by the wind field in 24 hours reduces to zero. However, in real systems, the breezes are hardly symmetric because the land/sea temperatures and hence the atmospheric pressure fields vary significantly during the 24-hr period.

(2) Asymmetric breezes (i.e. consisting of a synoptic and a diurnal component) induce motions of plume waters in the same fashion as a constant wind having the same magnitude and orientation of the synoptic (or permanent) component of the breeze. The only similarity between the responses is the enhanced (or reduced) mixing that results from the shear instability (Stumpf et al., 1993; Piñones et al., 2005) between the plume and the underlying ambient waters under asymmetric (or

symmetric) breezes. The simulation-based responses described above are supported by the in situ observation of Piñones et al. (2005) who found that the Maipo River plume propagates upstream off the central coast of Chile during periods of intense sea-breeze activity (predominantly oriented landwards). This analysis suggests that in spite of the small scale (few kilometers) variability noticed throughout the day, it is the difference in the windstress between day and night (i.e., spinning up and relaxing regimes) that ultimately drives the synoptic dispersion of the plumes.

It is worth mentioning that the simulation forced by asymmetric westward breezes resulted in a horizontal distribution of salinity much closer to observations, and it consisted of a massive bulge of brackish water propagating upstream, and a portion of water in a narrow segment downstream from the river mouths. The plume exhibited a surface-advected structure, contrasting the observed bottom-advected structure presented in Section 2.3.

Garvine (1999) studied the effects of tides on a buoyant plume and found that shelf tides have moderate influence on the horizontal plume spreading, which is most pronounced in the alongshore penetration of freshwater. It was found that in the presence of tides, both the upstream and the downstream penetrations are noticeably decreased, while the across-shelf plume extension is nearly unchanged. Simpson (1997) has recognized the importance of the role played by tidal stirring in the vertical stability of freshwater-influenced coastal waters, and noted that these regions undergo periods of alternated mixing and stratification.

The plume response to tidal forcing was simulated for three different scenarios that consisted of a tide-driven flow greater (A), comparable (B), and smaller (C) than the buoyancy-induced flow. For the real plume during spring-tide, these might correspond to periods of extremely high, moderate, and extremely low discharges, respectively. The calculations suggest a weak response of the plumes to the forcing during the scenario (A), which translates to plumes spreading without significant influence of the tidal flow, as observed in the Maipo River plume (Piñones et al., 2005) in central Chile where the diurnal modulation of shelf salinity is more coherent with local land-sea breezes than the tides (tidal range $< 1\,\mathrm{m}$). During periods characterized by scenario (B), the plume response is likely to be moderate, in agreement with the above mentioned findings of Garvine (1999) for a generalized plume. In this case the plume will have a shorter alongshore penetration compared to scenario (A), and there will be permanent contact with the seabed near the river mouth. Lastly, during periods characterized by scenario (C), tidal stirring will promote homogeneity of the water column throughout the plume and the lateral spreading (both alongshore and across-shore) will be greatly inhibited.

It was found that when the tide-driven flow of plume waters is forced additionally

by moderate asymmetric breezes, the resulting lateral spreading is determined by the winds through the Ekman drift, while the vertical structure of the plume is determined by the tidal forcing. An exception to this behaviour is the case of a tide-driven flow greater than the buoyancy-driven flow, where due to enhanced mixing, plume waters do not spread laterally far from the river mouth. However, following the analysis of Kourafalou et al. (1996b), it is suspected that for wind conditions other than those reported in this study, the plume lateral and vertical spreading will be dictated by the relative magnitude of the three forcings.

Chapter 6

Variations in surface plume patterns

Having established the characteristics of the plume's response to wind and tidal forcing in the previous two chapters, it is now time to investigate the typical patterns of the Zambezi River plume. In this chapter, the horizontal distribution of salinity in the periphery of the Zambezi River mouth is analyzed using three different approaches, each using as input the results from a hindcast simulation. Firstly, the plume patterns computed for February 2007 are investigated through visual analysis of surface fields during selected wind events. Then, self-organized maps and principal component analysis are applied to a subset of the data.

The questions being addressed are related to the structure of the Zambezi River plumes, as well as the effect of ambient factors on this structure. Specifically, the effect of ambient current is investigated in this chapter, along with patterns of low-frequency variability of the plume.

The model-derived monthly-averaged surface salinity for February 2007 compared reasonably well with remotely-sensed salinity for the same period, in contrast with the distribution of surface temperature that reflected the climatological forcing flux of heat. On the other hand, the main features of the salinity distribution observed in 2007 by the Mozambican National Institute of Fisheries Research were fairly well reproduced by the hindcast model. Principal component analysis revealed that a strong ambient current ($\sim 50\,\mathrm{cm/s}$) is capable of advecting the plume waters down along the current, regardless of the orientation of the buoyancy-driven flow and the the Ekman drift.

6.1 Model configuration

The Regional Ocean Modelling System (ROMS_AGRIF version 2.1) described in Chapter 3 was used in the current analysis, with the following modifications. The model domain comprises an area bounded by the limits $14^o - 23^oS$, and $33^o - 46^oE$, and the numerical grid consists of a stretched spherical grid with horizontal resolution of $^{1^o}/_{12}$, and 32 sigma-layers defining the vertical dimension (stretching parameters $\theta_b = 0.1$, $\theta_s = 5.0$, and $h_c = 5\,\mathrm{m}$). The model is initialized and one-way offline nested within the Simple Ocean Data Assimilation Reanalysis (SODA; Carton and Giese, 2008). Forcing of the model includes daily river discharge (based on measurements from the Tete gauge station introduced in the model via three point sources discharging in the proportion 3 : 5 : 2), tides (10 constituents from TPX7.0; Egbert and Erofeeva, 2002), hourly winds (extracted from the Weather and Research Forecast model, WRF, discussed in Section 5.1.2), and climatological surface fluxes of heat and freshwater (from the Atlas of Surface Marine Data, COADS; da Silva et al., 1994). The salinity and temperatures at the freshwater sources is kept constant ($S = 3.0\,\mathrm{psu}$, $T = 29\,^{\circ}\mathrm{C}$) throughout the simulation, while changing the volumetric discharge rate realistically.

The imposed boundary conditions comprise the Flather radiation conditions applied for the normal barotropic fluxes of momentum, and Orlanski conditions (outward radiation combined with nudging towards clamped external values) for the tangential component of the barotropic momentum fluxes and the remaining fields (sea surface elevation, baroclinic velocities and tracers). Vertical mixing is achieved through the K-profile parametrization (Large et al., 1994) with a linear formulation for the bottom friction (drag coefficient, $C_D = 3 \times 10^{-4}\mathrm{m/s}$). The model was run for the years 2006 and 2007, the last two years for which CTD was collected and hourly wind data was made available. The time-stepping for the baroclinic and barotropic modes are 6 minutes and 6 seconds, respectively.

6.2 Temporal patterns of the surface fields

6.2.1 Monthly-averaged patterns

The results from the first year of the hindcast model were excluded from the analysis that follow, and only results for 2007 are reported. Figure 6.1 presents model-derived SST for February 2007 alongside observed SST extracted from two global datasets. The model-derived SST is based on twice-daily records from the surface layer averaged over the month. The observed SST's comprise the standard monthly SST product from the AVHRR sensor onboard the MODIS-Aqua satellite (both

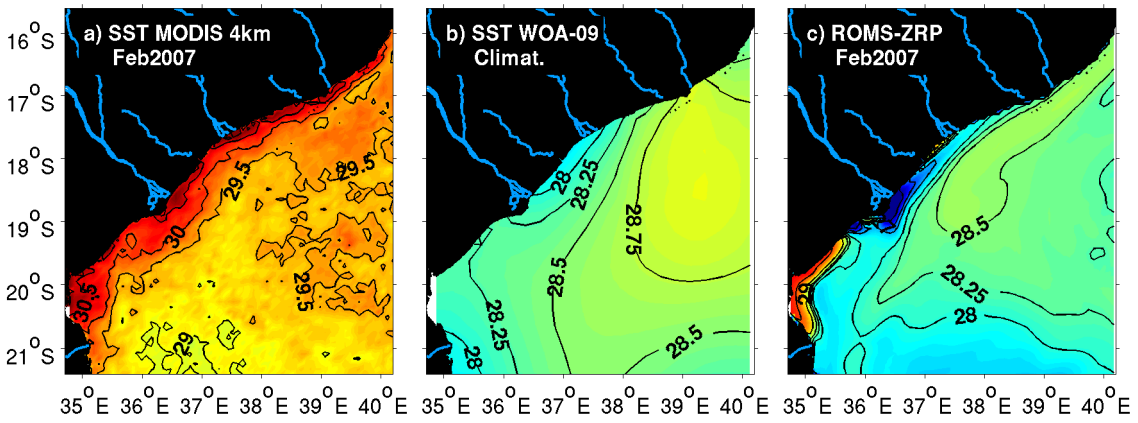

Figure 6.1: Sea surface temperature in the periphery of the Zambezi delta, computed for the month of February using (a) monthly composites from MODIS-Aqua, (b) monthly climatologies from the World Ocean Atlas 2009, and (c) ROMS simulated monthly averages.

daytime and nighttime passes), consisting of data observed during February 2007 and distributed with 4-km resolution, as well as SST climatologies from the World Ocean Atlas (WOA09) which represent a blend of a great deal of historical data (Locarnini et al., 2010). When compared to the single-cruise SST data presented in Figure 2.15b, one finds that the satellite-derived SST's are a better match. As can be seen, both datasets indicate a lateral gradient of surface temperatures with the warmest waters occurring at the coast, particularly near the mouths of the rivers. The patchiness in this thermal signature of the plume suggests a northward spreading of plume waters, although it is only evident in averages of nighttime and daytime SST's. We found no evidence of a thermal signature of the plume in daily composites (results not shown), and neither in separate distributions of daytime and nighttime temperatures, in agreement with the observations of Siddorn et al. (2001).

Away from the coast the surface temperatures increase equatorward (as it would be expected), a feature also reproduced by the model. However, the model failed to reproduce the thermal signature of the Zambezi plume, since it was substituted by a pool of cold waters in the vicinity of the delta. The model-derived temperature for this region is approximately 2^oC lower than in the offshore region. A similar pattern is present in the climatological data (panel B of Figure 6.1), except with smaller differences in the temperature of the near-shore and offshore regions. The similarity between the model-derived SST and the climatological observations, as well as the great discrepancies with the MODIS monthly composite, suggests that the simulated distribution of SST reflects the (climatological) heat flux used to force the model. However, it is possible that these discrepancies have other sources, since the model-derived SST did not compare well with other satellite-based climatological data (results not shown), as for instance, MODIS-Aqua and Pathfinder 4-km

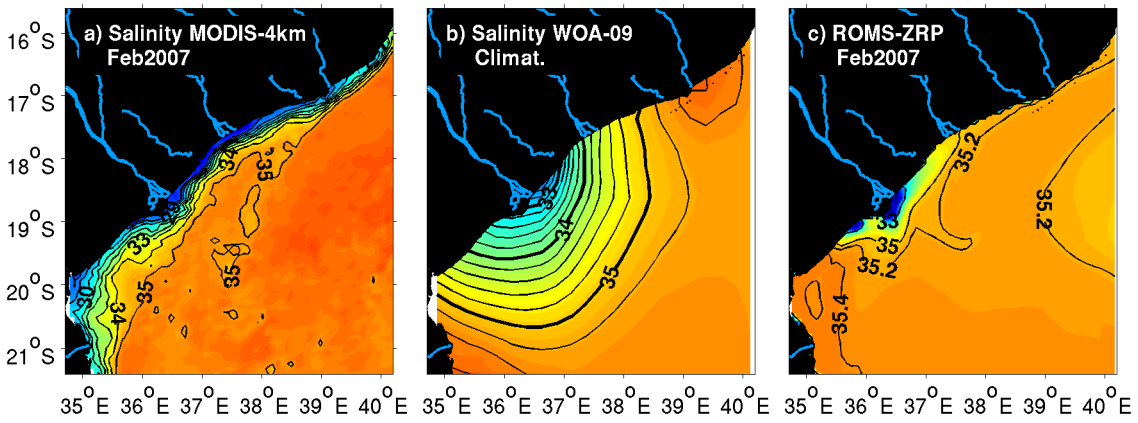

Figure 6.2: Surface layer salinity computed for the month of February using (a) monthly composites from MODIS-Aqua, (b) monthly climatologies from the World Ocean Atlas 2009, and (c) ROMS simulated monthly averages. The C.I. is 1.0 psu in the MODIS data and 0.2 psu in the WOA-09 data.

climatological SST products.

The horizontal distribution of model-derived salinity at the surface layer (averaged over February 2007) is presented in Figure 6.2, along with an estimate of salinity based on monthly composites of reflectance ratio from the MODIS-Aqua 4-km products, and monthly climatologies from the WOA dataset (Antonov et al., 2010). The salinity estimate from the MODIS product was computed using the algorithm offered by Siddorn et al. (2001), which has the form of a linear relationship ($S = 37.45 - 7.07\frac{R555}{R490}$) between the near surface salinity and the ratio of reflectances at two wavelengths. The algorithm was conceived specifically for the Zambezi influenced waters and its accuracy is believed to be subjected to the temporal variations in the water contents, and also the instantaneous chlorophyll concentration (i.e., the lower the chlorophyll concentration more accurate are the salinity estimates).

The salinity distribution observed by these means indicates that the brackish water ($S < 35.0$) from the Zambezi River spreads primarily seaward and downstream (northeastwards) along the coast. This feature, which was seemingly well reproduced by the model, is consistent with the *in situ* observations presented in Figure 2.15a, except for the differences in the offshore extension of the plume near the river mouth. The orientation of the 35.2 psu contour in the model-derived data, as well as the 34.0 psu contour in the observed salinity for February 2007, suggests that low-salinity water is removed from the far-field region of the plume and transported seaward, probably by ambient currents flowing polewards or by south-going anticyclonic mesoscale eddies.

At about 20^oS, there is a region of low-salinity water at the coast noticeable in the satellite-derived data, which neither it is present in the *in situ* data (Fig.

2.15a), nor it was reproduced by the model (Fig. 6.2c). There is a chance that these low-salinity waters are simply an artifact of the algorithm discussed above, since the shallow depths and the fairly high turbidity in that region (Fig. 2.15c) could have contributed negatively to the salinity estimation as explained above, but then the peak turbidity was found right at the Zambezi River mouth, therefore this region is more prone to miscalculations. On the other hand, the model-derived salinities could be wrong in that region, as is the case of the downstream region where the northeastward penetration of brackish water does not reach 17^oS. The reason for these differences is likely the exclusion from the computation of the freshwater buoyancy input from the other rivers indicated by the lines over land in Figure 6.2.

Nevertheless, in contrast with the distribution of temperature, the model-derived and the observed climatological salinities do not share many similarities, except for the seaward increase of the salinity values and weak or absent influence from the other rivers that meet the ocean in the region displayed in Figure 6.2. The 35.0 contour in the distribution of model-derived salinity averaged over February depicts a plume that extends primarily along the downstream direction, while it indicates a more radial distribution of brackish water (i.e., nearly symmetric in relation to the river mouth), in the climatological data. Also, the alongshore and across-shore extensions of brackish water are considerably smaller ($\sim$ 100 km shorter) in the model-derived salinity, in comparison with the climatological data.

In summary, the distribution of the model-derived temperature computed from monthly averages of the surface layer values in February 2007 shows great similarities with the observed climatological temperatures, and weak correspondence with the temperatures observed during the same period. This behaviour has been attributed to the climatological fluxes used to force the model. In contrast, the salinity simulated for February 2007 shows more similarities with the values observed for that period than with the climatological observations. For this reason, the analysis of plume variation that follow will be restricted to the surface salinity. It was found that the Zambezi plume has a thermal signature that is clearly noticeable in the monthly composite of both daytime and nighttime values, and same as the salinity distribution, it indicates a northward spreading of the plume waters.

6.2.2 Sub-tidal patterns

In order to investigate the horizontal structure of the plumes during short (sub-tidal) timescales, the model-derived surface velocity and salinity fields were averaged during specific periods depicted by shaded areas in Figure 6.3. These periods represent a number of selected wind events that marked the February 2007 wind conditions, which include a moderate northward wind corresponding to a maximum windstress

intensity of $\tau/\rho = 5 \times 10^{-6}\,\mathrm{m^2 s^{-2}}$ (around day 7), a notably weak wind with its orientation alternating between southward and northward (between days 10 and 12), a short ($\sim$ 1-day) event of strong winds oriented northward (day 13), and a gentle wind blowing predominantly southeastwards (between days 18 and 19). The corresponding river discharge is present in the upper panel of Figure 6.3, and letters are used to discriminate the events. The resulting plume features are presented in Figure 6.4, and discussed below.

Following a number of days of predominantly northwestward to northward winds, the horizontal distribution of salinity on February 7th (panel A of Figure 6.4) displayed a tongue indicative of southward movement of freshwater (S<35.00) induced by the southwestward flowing strong ambient current. It was noted that, near the coast and mainly within the reach of plume waters, the surface flow is oriented northeastwards along the coast, in agreement with the plumes forced by northward winds simulated in the absence of ambient current (presented in the previous chapters). In contrast, the orientation of the flow offshore from the bank region appears to be determined mostly by the large-scale circulation in the channel.

During days 10 and 12, the winds were expected to have little or no influence on the plume dispersion, given the rather small intensity of the winds. The surface salinity field (panel B) depicts a plume that spreads progressively along the downstream coast with maximum offshore extent attained in the region between the Zambezi River mouth and the city of Quelimane. No upstream offshore penetration is present, which is very likely connected with the fact that the ambient current

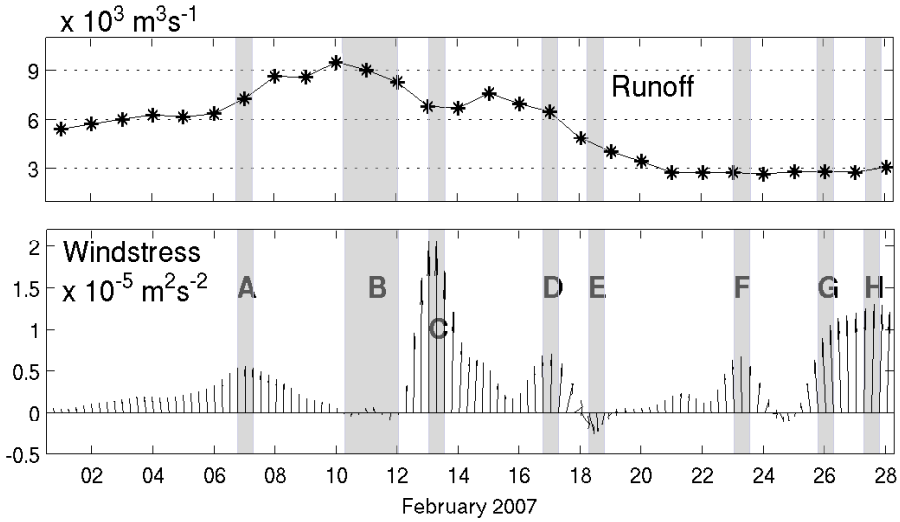

Figure 6.3: *(Top)*: daily run-off measured at the Tete gauge station during February 2007. *(Bottom):* 36-hr low-pass filtered time series of wind stress (simulated by WRF model, and divided by the mean water density) spatially averaged over a $2^o \times 2^o$ box centred at the Zambezi River mouth.

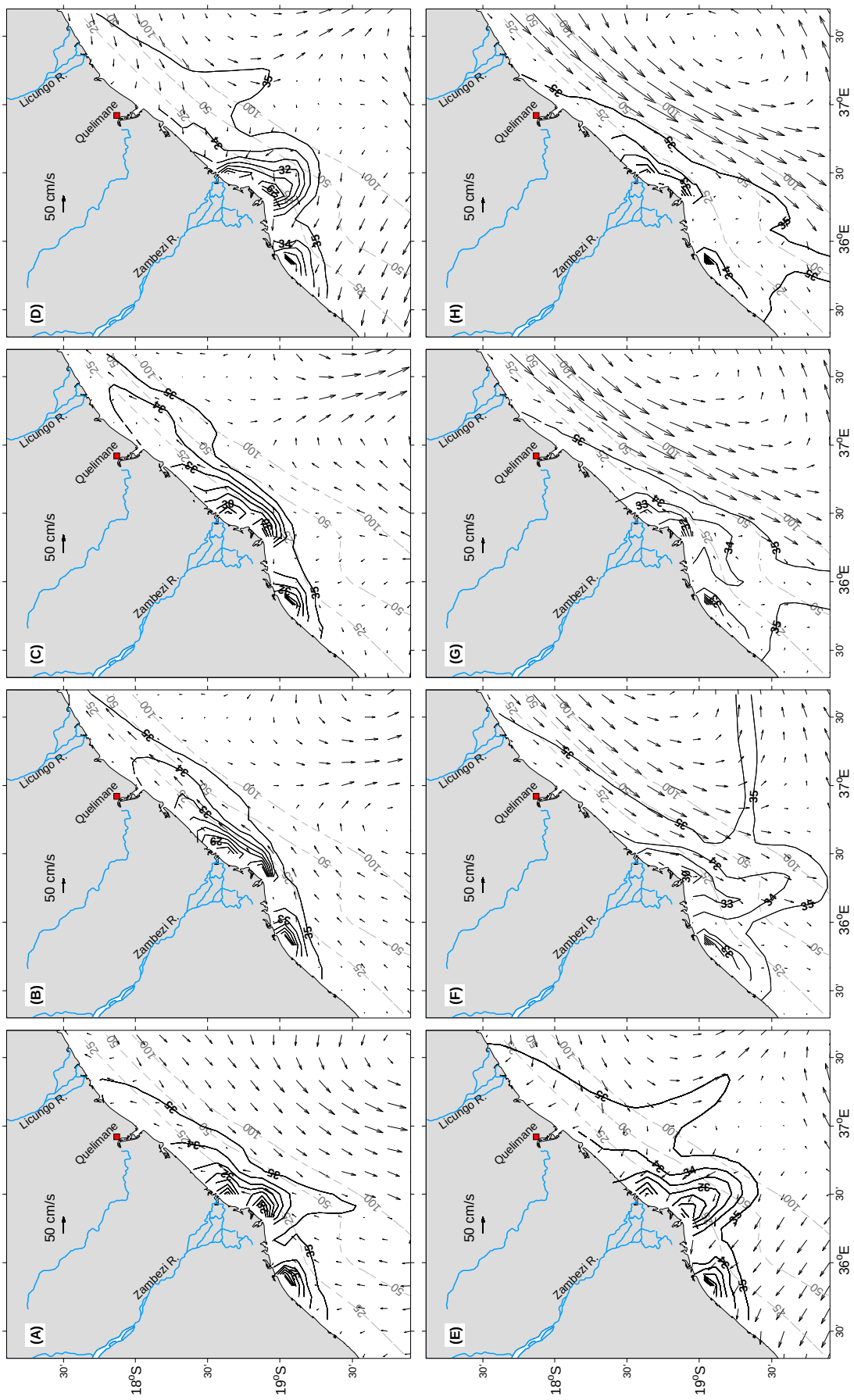

Figure 6.4: Simulated surface salinity and velocity fields during wind conditions highlighted in the previous figure, which includes a moderate northward wind (A), a weak wind (B), a short event of strong northward winds (C), and a gentle southeastward wind (E). The bathymetry contours of 25, 50, and 100 m are also plotted. The salinity contour interval is 28 to 35 by 1 psu.

immediately seaward from the plume region is generally weak. Also, this current is particularly oriented northeastwards in the region south of 19^oS, which favours the downstream advection of plume waters. The velocity vectors indicate a much more intense northeastward flow within the plume compared to the flow seaward from the plume limit. Notice that this flow behaviour was preceded by a 3-days period of gradual wind relaxation and river discharge intensification, suggesting that these plume features (panel B) are a consequence of the excess buoyancy during times of fading windstress and ambient current.

During the strong wind event that lasted about 24 hours on February 13th, the distribution of water of salinity $S < 33.00$ (panel C of Figure 6.4) did not vary significantly from that displayed in panel A (i.e., plume patterns ~ 48 hours earlier). In contrast, portions of the plume having salinity between $33.0 \sim 35.0$ spread further downstream, as depicted by the location of the 34.00 isohaline. This behaviour indicates that although the discharge rate has decreased significantly between the two scenarios, the action of winds and the freshwater released in previous few days could be responsible for the additional downstream penetration of plume waters. It appears that the surface flow did not change in general, as a consequence of the intensified windstress, at least not within the plume, where a slight reduction in the magnitude of the surface flow is noticeable. This flow behaviour is not consistent with the wind-driven motion of plume discussed in previous chapters.

Prior to days 18 and 19, the winds were moderate and oriented northeastwards. Between days 18 and 19, the winds changed to gentle strength and predominantly from the northwest. The river discharge (Figure 6.3) was about $5000\,\mathrm{m^3s^{-1}}$, which is above the annual mean discharge. The orientation of the surface flow within the plume (panel E of Figure 6.4) varied between northwestwards to southwestwards, and a similar pattern existed in the region seaward from the plume boundary, except with a region of greatly reduced flow in front of the mouths. The slack water seaward from the plume limit is a consequence of the convergence of ambient current away from the coast. The shape of the associated plume contains two protuberances marked by seaward departures of low salinity water. One is the bulge located immediately in front of the mouths, characterized by salinity gradients oriented towards the freshwater source. The second is a tongue of brackish water ($S < 35.0$) transported seawards beyond the 100 m isobath by virtue of the ambient current. In contrast to the plume displayed in panels A, B, and C, the bulge in this case is projected well offshore reaching the 100 m isobath, apparently due to a combination of two factors, as follows. Firstly, the volume of freshwater discharged in the previous few days is favourable for an unusual stratification near the mouths. Secondly, the alongshore component of surface flow within the plume is noticeably weak, which is then likely to be affected by the background poleward flow. It should

be noted that, although southeastward winds acting on a buoyancy-enhanced plume promote the offshore transport of plume waters (in agreement with the results from Section 5.2.4), these winds are not the main driver of the transport in the current case. This conclusion arises from the fact that the seaward projection of the bulge is also present in the plume computed for days 17 and 23, prior and posterior to the southeastward winds.

By comparing the plume patterns in panels C through H of Figure 6.4, one finds that, firstly, the surface flow within the plume is reasonably strong and oriented equatorward when the ambient flow (which determines the background flow) is weak. Secondly, as the poleward ambient flow strengthens, the equatorward motion of plume waters weakens and eventually reverses following the orientation of the ambient flow. Here, portions of the plume having high salinity are progressively transported seawards by virtue of the ambient flow that has a strong seaward (i.e., zonal) component. Thirdly, when the plume water ceases to flow equatorward, the near-field region of the plume is projected offshore beyond the 100 m isobath, in consequence of the seaward transport of low-salinity waters. Lastly, under sufficiently strong poleward flow near the offshore plume limit, the shape and location of plume waters become largely deviated from the predictions of a plume in absence of ambient current. The examples shown in panels F through H of Figure 6.4 show large amounts of freshwater ($S < 35.0$) in the upstream direction.

Overall, the plume dispersion patterns simulated for daily varying forcings reveal some degree of dependence of the plume evolution on the forcing fields prior to the time the plume was recorded (ocean memory - the forcing is integrated through time). Also, they suggest a much higher influence of the ambient current on the plume when compared to the findings in previous chapters.

6.2.3 Typical plume patterns identified by SOMs

Through the illustrations of sub-tidal plume features presented in the previous section, the plume response to a specific event of winds, ambient currents, or river discharge can be evaluated accurately, yet the choice of a particular sub-tidal period for averaging the data is rather subjective. The identification of characteristic plume patterns that occur at a certain frequency can be performed using classification tools like for instance the Self-Organizing Maps (SOMs).

The SOM is an artificial neural network method that performs the identification and unsupervised classification of data by projecting the input data space, which can be high-dimensional, to a set of units (neural network nodes) on a low-dimensional (typically 2-d) space. SOMs have been recognized to be excellent tools for feature

extraction in many fields, including oceanography. Examples in the latter field include, but are not limited to, the identification of SST and wind patterns in various time scales from satellite-derived data performed by Richardson et al. (2003), as well as the analysis of occurrence of a bi-directional river plume on the Washington/Oregon shelf conducted by Liu et al. (2009). In SOMs, the number of units (map size) determines the level of detailed information in the final classification patterns, so that a large (small) map results in more detailed (generalized) patterns (Vesanto et al., 2000). During the training of the SOM, each unit is linked to each input data through weights, and the least Euclidean distance between the weights and the input vector determines the Best-Matching Unit (BMUs).

In order to apply the SOM to the ROMS simulated surface plume fields, the data was organized following the scheme displayed in Fig. 2 of Richardson et al. (2003), where each sample image comprised the area limited by $17^o - 20^oS$ and $34.6^o - 39.0^oS$ (corresponding to a 38×52 grid). In total, 730 images were used for this analysis representing the twice-daily records throughout 2007, each having 1130 data pixels after removing the land. The exclusion of land points in the computations reduces data amount and improves the clustering performance, since a land-masked dataset with "no-data" points in general results in additional clusters being formed in land (Eom, 1999). For each image, the salinity and velocity components were concatenated into a single raw vector, and the final input matrix to SOM consisted of 3390 columns (1130 gridpoints $\times$ 3 variables) $\times$ 730 rows (record length). Prior to concatenation, the three variables were normalized to the range [-1; 1] to avoid miscalculations of the Euclidean distances since the salinities and velocities have different scales. Normalization parameters were recorded for posterior re-assembling of the variables to aid the interpretation of findings. After a few tests, a map size of 3×3 SOM units was selected, and training was performed. The SOM toolbox (Vesanto et al., 2000) is used and the parameter choice follows the suggestion of (Liu et al., 2006) for a small map size, namely, a neural lattice of "*sheet*" shape (i.e., flat or 2D), linear initialization, "*ep*" neighborhood function (i.e., Epanechikov function), and batch training algorithm. After the SOM was performed, images of plume patterns were recreated (from the node weights for each variable), and land mask reinserted.

Plume patterns

Figure 6.5 presents the summary of the SOM analysis of plume patterns, where similar patterns are gathered next to each other. The distribution of surface salinity hardly varies between the different general patterns. The most notable difference is the length of downstream penetration that diminishes from unit #1 through unit

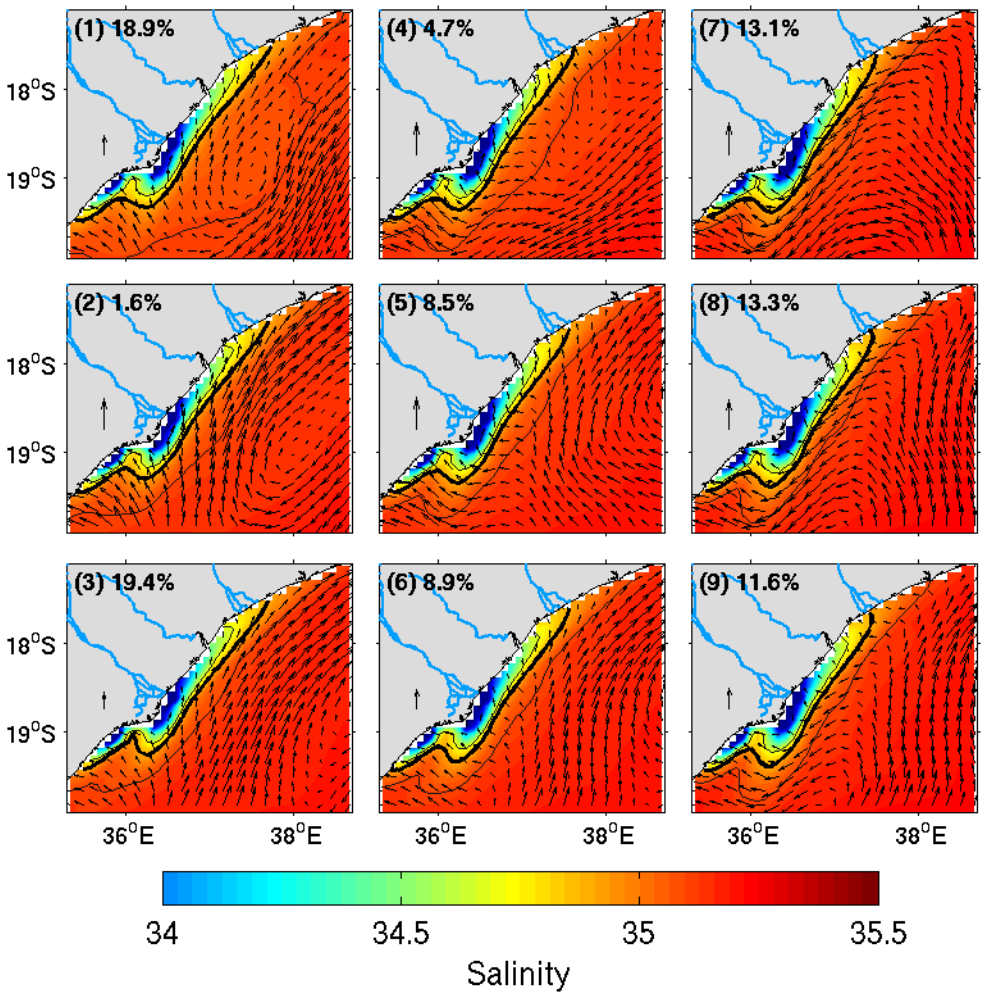

Figure 6.5: A 3×3 SOM of 730 twice-daily surface salinity and velocity fields of the Zambezi River plume. The SOM unit number and the frequency of occurrence (percentage relative to all year) of each pattern is shown in the top left corner of each plot. The arrow over land indicates a surface flow of 30 cm/s in each plot. The three contours indicate salinity of 34.7, 34.9 (thick line), and 35.1.

#9, as indicated by the position of the salinity contour $S = 34.9$. According to these patterns, the Zambezi River freshwater often turns left and proceeds downstream regardless of the orientation of the ambient flow, with a non-negligible portion of freshwater found upstream attached to the coast. Another subtle difference in the salinity distribution between the SOM patterns is related to the protuberance in the northern part of the plume, which is indicative of the tendency for poleward transport of plume waters. The protuberance becomes more visible from the top three units (#1, #4, and #7) towards the bottom units (#3, #6, and #9), which account for about 40% of the occurrence. Similarly, the surface flow within the plume region (in the downstream reach) varies only slightly, from northeastward in units 1-3 to landward (northwestward) in units 7-9.

The ambient flow in units #1 to #3 is oriented northeastwards immediately seaward from the plume and southwestwards further offshore. Units #7 to #9 display the opposite pattern, southwestward flow immediately seaward from the plume, and northward to northeastward flow further offshore. Units #4 to #6, located in the centre of the SOM exhibit an intermediary pattern of ambient circulation, and have the smallest frequency of occurrence.

In general, the patterns simulated for 2007 can be grouped in two clusters, the most frequent (38.3% without unit #2) consisting of plume waters penetrating downstream beyond the Licungo River mouth and bounded by northeastward ambient flow (units #1 and #3). The second cluster has a frequency of occurrence of 38%, and consists of plume waters with a slightly shorter downstream penetration bounded by southwestward ambient flow (units #7, #8, and #9).

Figure 6.6 presents the distribution of frequency of occurrence throughout the year. As can be seen, the different clusters or plume patterns are reasonably well distributed throughout the year, meaning that the patterns identified in the SOM occur irrespective of the known seasonal fluctuations in the river discharge and wind conditions. With only a few exceptions, all clusters occur with different frequency every month. It is worth noting that only the second cluster occurred in February when the discharges were maximum. However, the annual distribution of frequency indicates that forces other than buoyancy and windstress (or combination of forces) determine the occurrence of a specific pattern.

To further investigate this relationship, the time-series for the BMU has been plotted against the windstress and river discharge observed during January to March 2007 (Figure 6.7). As mentioned above, the largest downstream penetration occurs in unit #1 and it decreases gradually towards pattern #9, hence, the BMUs in the plot can be thought as sorted according to the penetration length (shorter first). Units #1 to #3 having larger penetration are not linked to a specific event of wind of discharge, given that similar condition do not produce similar patterns. Similarly, the occurrence of patterns #3, #6, and #9, which features a more distinct protuberance in the northern part, does not seem to be associated with a particular wind/discharge event.

Overall, the patterns of plume variability identified with the aid of self-organizing maps indicate that plume dispersion occurs generally along the downstream coast, with little or no upstream penetration of freshwater in the offshore region. This structure is consistent with the single-cruise surface data collected in 2006 and presented in Chapter 2, as well as the with cruise data reported by Siddorn et al. (2001). The magnitude and orientation of the ambient flow immediately seaward from the plume limit determines the weak variability of plume patterns. The most prominent difference in the patterns of spatial distribution of salinity suggested by the SOM

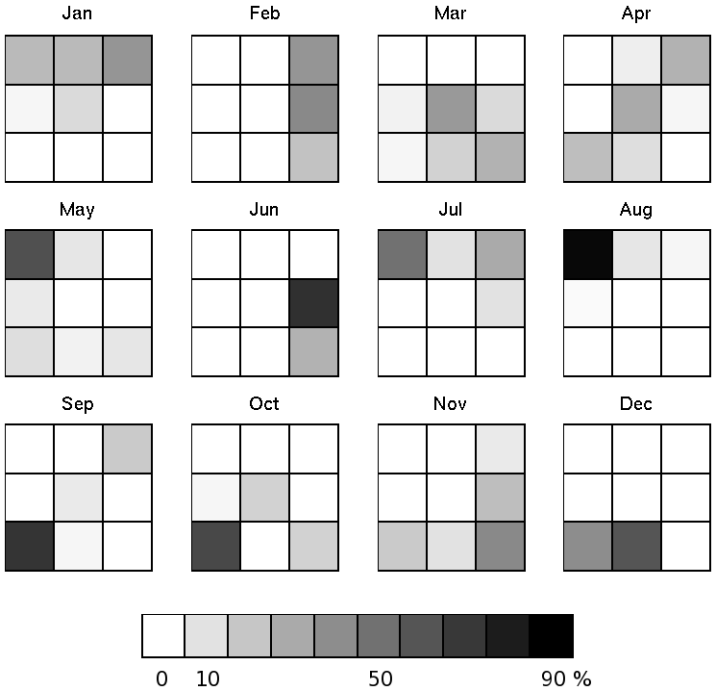

Figure 6.6: Annual frequency maps of the 3×3 SOM of surface salinity and velocity fields.

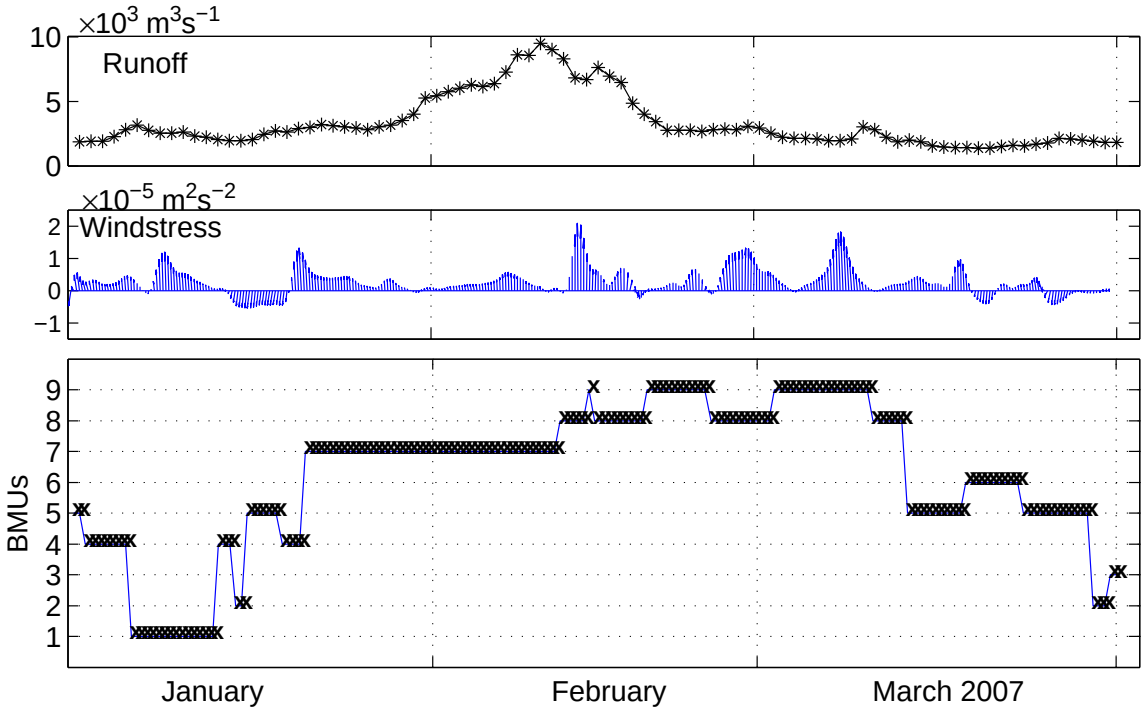

Figure 6.7: (Top) Daily run-off measured at the Tete gauge station between January and March 2007. (Middle) 36-hr low-pass filtered time-series of wind stress (divided by the mean water density) spatially averaged over a $2^o \times 2^o$ area centred at the Zambezi mouth. (Bottom) Time-series of the Best-Matching Units of the simulated plume patterns (Jan-Mar 2007).

analysis includes the length of the downstream penetration, which is greater for an equatorward flowing ambient current immediately seaward from the plume bound. However, further analysis is needed to establish the linkages between the plume patterns and the geophysical parameters used in the plume simulation.

6.2.4 PC analysis of plume variability

Many studies have revealed event-scale coherent patterns of plume variability worldwide. For instance, the analysis of MODIS satellite imagery combined with HF radar current meters and drifters (Warrick et al., 2007) indicates that plumes in the Southern California Bight often detach from the coast and turn left, the opposite direction of the Coriolis influence, during exceptionally episodic river discharges. Outputs of the POM model have showed that the distribution of brackish water discharged from the Rio de Plata in South America was more sensitive to the orientation of wind forcing than the variability of river outflow (Pimenta et al., 2005). On the other hand, long-term variability of plume size has been found to be intrinsically related to precipitation rate (Nezlin et al., 2005; Nezlin and DiGiacomo, 2005), through correlation analysis of remotely-sensed maps of sea-spectral reflectance in the Southern California Bight.

The use of empirical orthogonal function (EOF) and principal component (PC) analysis in oceanography allows for the extraction of important patterns/structures from data, as well as the assessment of relative variance explained by these patterns. A number of examples of the application of this method are presented in Luo and Yamagata (2002) and Ramos et al. (2010). In general, the method consists of the decomposition of the time-series into PC, or empirical orthogonal modes, each having an associated variance, a spatial pattern, and a PC time series.

The time-series in the current study consists of 1-year long, 36-hr low-pass filtered records of surface salinity sampled twice-daily in the same subset area used for SOM analysis (previous section, limits $17^o - 20^oS$ and $34.6^o - 39.0^oS$). The EOF analysis resulted in the leading 15 PC modes of low-frequency variability amounting to 90% of the total explained variance.

The space-domain of the first PC mode is shown in Figure 6.8. Since the three subsequent modes account for 7.8%, 5.5%, and 4.7% of the total variance, respectively, the first mode with 56.23% is clearly the dominant one. The mode changes its sign within the reach of the plume waters, and it has two positive maxima at the sources and a negative maximum in the offshore region. In addition, the orientation of contours of the mode loadings/variance resembles to some extent the distribu-

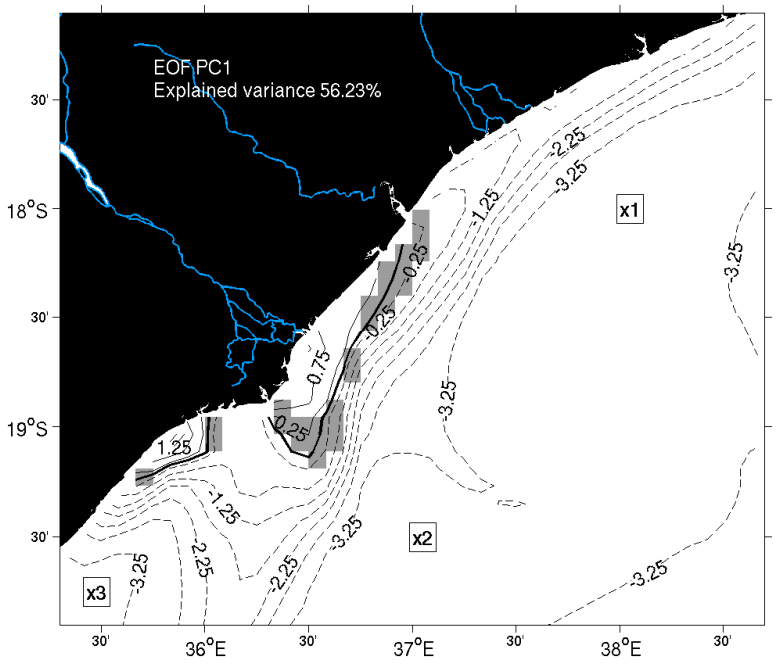

Figure 6.8: Spatial pattern of the first leading PC from 1-year long model outputs of surface salinity. Loadings have been multiplied by 100. Dashed (solid) line indicates negative (positive) values, and the shaded area indicates regions where the mode is not statistically significant at the 95% confidence level. Explained variance (in percentile) for the mode is indicated by text in the image.

tion of surface salinity evaluated for February 2007 (Section 6.2.2). This pattern of the leading PC mode suggests the existence of a bi-modal structure varying at low-frequency. It is then assumed from the geometry of the seesaw-like structure that one mode is likely to be strongly influenced by the river runoff, while the other comprises the ambient water.

Spatial patterns for the PC modes 2 through 4 are presented in Figure 6.9. These modes are considered "least important" by the fact that their eigenvalues (i.e., fractions of data total variance) are less than 0.1. The second leading PC mode displays a spatial pattern with two maxima, one negative along the downstream coast, and another positive in the upstream offshore region. The time dependence for this mode (not shown) is predominantly high-frequency when compared to the first mode, and has period of about a month, while the first mode period is about 230 days.

In order to investigate the importance of the various forcing fields on the structure of salinity variability, the PC time-series was correlated with the forcings, and results are presented in Table 6.1. For each PC mode, the best correlation is marked by an underbar, and insignificant correlations are marked by an asterisk near the r values. It was found that the first leading mode correlates best with the runoff, while the second and third modes correlate best with the ambient current and windstress, res-

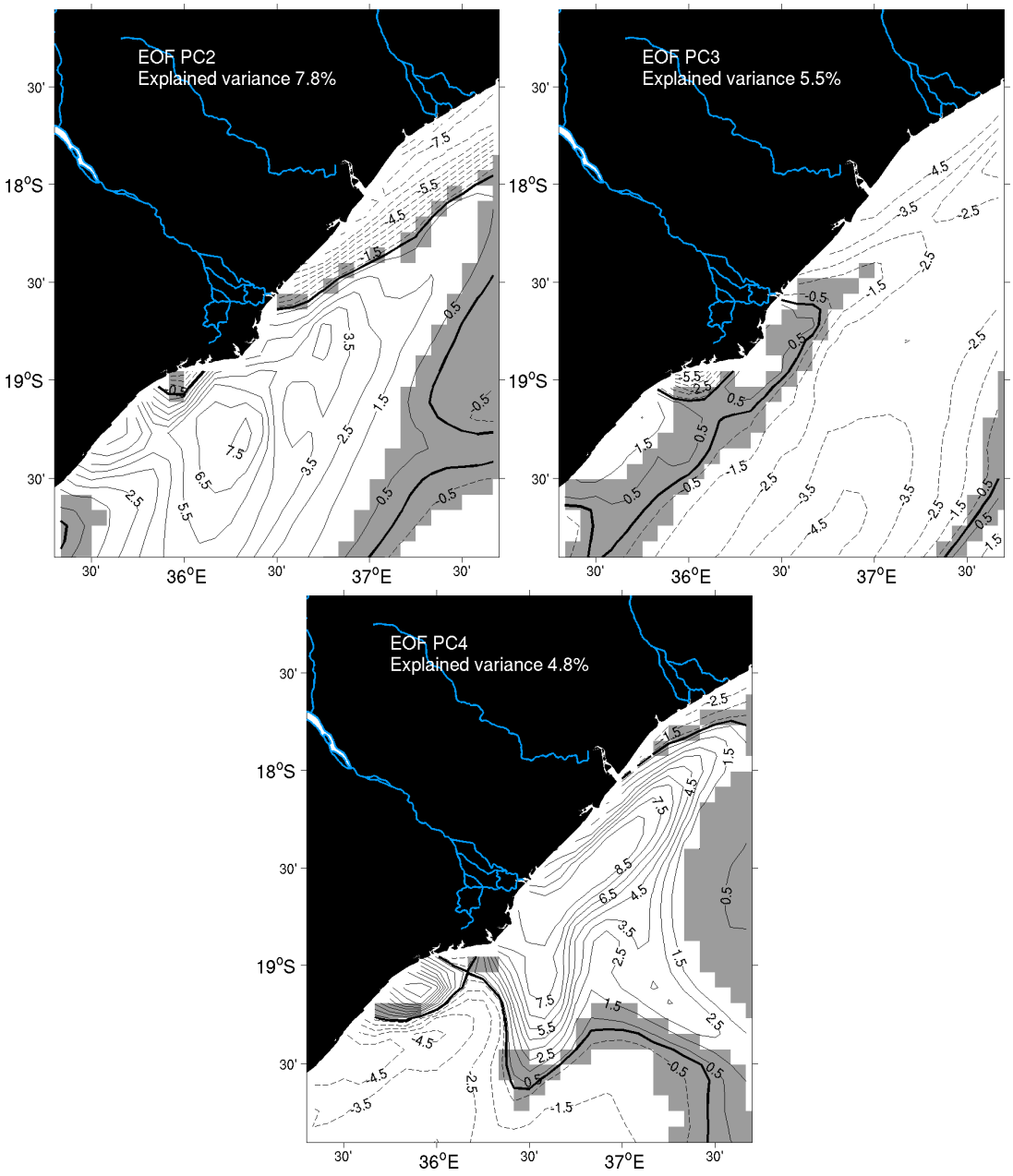

Figure 6.9: Same as the previous image, except for the second (top-left), third (top-right), and fourth (bottom) modes.

Table 6.1: Correlation (r) between the amplitude of EOF and forcings, with the underbar indicating the best correlation for each EOF mode. Each column under windstress and ambient current correspond to the zonal component, meridional component, and the magnitude of the forcing, respectively. Refer to Figure 6.8 for the locations of points x1, x2, and x3. Asterisks near r values indicate insignificant correlations at the 95% significance level.

	Windstress			**Runoff**	U_{amb}, $x1$			U_{amb}, $x2$			U_{amb}, $x3$		
eof-1	.07	.07	.07	<u>-.44</u>	-.09	-.16	.20	.17	.15	-.10	.07*	.03*	-.03*
eof-2	-.12	-.12	-.12	.11*	<u>.61</u>	.58	.39	.28	.54	.22	.01*	.06	.04*
eof-3	.20	.21	<u>.21</u>	.05	-.10	-.07	.002*	-.05*	-.07*	.09	.10	.06*	.06*
eof-4	.10	.10	.10	<u>-.57</u>	.27	.26	.16	-.05*	.11	.06*	-.04*	-.12	-.04*

pectively. It is interesting to note that, from the three stations used to compute the correlation with ambient current, only the two stations located downstream and immediately seaward from the mouths presented significant results. However, in general these best correlations are weak (corresponding to a r^2 of 20%, 36%, and 4% for the case of runoff, current, and windstress, respectively), which could be an indication of a non negligible degree of non-linearity between the geophysical variables.

A common technique to test the robustness of the PC eigenvectors, and to see whether the "most important" pattern of the PC modes is domain-dependent is the orthogonal rotation of the PC (for which a number of methods are available, including the Varimax). However, rotation is mainly applied when the variance is fairly well distributed amongst eigenvectors, which is not the case in the current analysis. Nonetheless, a rotation of the first two modes were performed motivated by the fact that most "rules of thumb" in statistic seem to work well in one situation, and not so well in others. The choice of two modes was based on a different "rule of thumb" which considers the components having a "fraction of variance greater than 0.1" as "*most important*". A scree test approach (Cattell, 1966) failed here, mainly because most of the variance is incorporated in the first leading mode.

The variances of the first and second PC modes correspond to a fraction of 0.6 and 0.1, respectively, and the subsequent modes have smaller fractions. After applying the rotation, the explained variance of the first and second PC modes became 56.1% and 8.0%, and the spatial patterns were identical to the unrotated modes. By these means, no improvements were achieved when the orthogonality constraint was removed from the first two leading modes. A test including the rotation of the first three and four PC modes did not produce any better results, since the rotated spatial patterns were significantly similar to the unrotated ones.

However, the seesaw-like structure of salinity variability was further tested by constructing a point correlation map (which is the shared correlation between a selected gridpoint and all the other grid points) of the original model output data. For the maps in Figure 6.10, two gridpoints in the periphery of the mouth were chosen both located within the reach of plume waters, one gridpoint located onshore from the line of zero variance (refer to Figure 6.8), and another gridpoint located offshore from this line. These results show that correlation in the opposite domain relative to the contour of zero variance is in general weak, with a maximum of about -0.25, which lies within the limit of insignificant correlations at the 95% significance level. There seems to exist a region in the downstream coast, between the Zambezi mouth and the city of Quelimane, where the spatial pattern of correlation contradicts the above described pattern. Despite all these contrasting results, it is concluded that the structure produced by the unrotated EOF is an accurate representation of

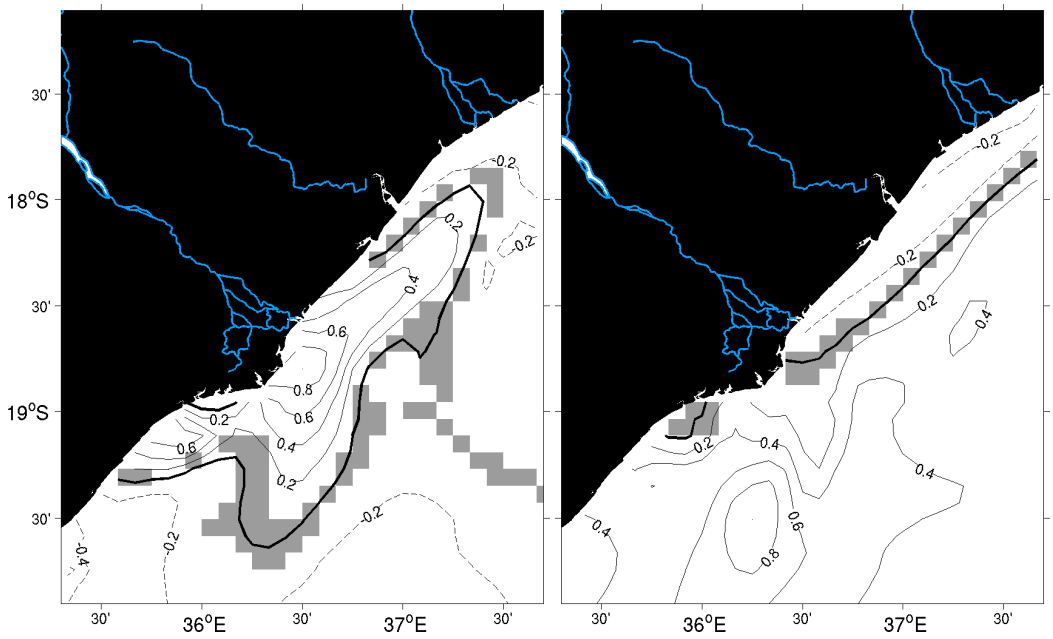

Figure 6.10: Point correlation map of surface salinity with respect to 18.75^oS, 36.5^oE (*left*), and 19.5^oS, 36.25^oE (*right*). Shaded areas indicate regions with correlation statistically not significant at the 95% significance level. Thick (dashed) contours indicates zero (negative) correlation.

the model outputs, and that a statistically significant bi-modal (i.e., a seesaw-like structure having two regions with opposing sign variance) low-frequency pattern is incorporated into the first leading PC mode. The implications of these patterns are discussed in the next section.

6.3 Discussion

The hindcast simulations employed in this analysis use climatological fluxes of heat and freshwater for the entire model domain, but salinity in the region of interest (i.e., subset area used to present results) is further influenced by daily freshwater discharge from the Zambezi River. Due to the nature of the forcing fluxes, the model failed to reproduce accurately most features of the temperature distribution observed in February 2007. In addition, these temperature observations revealed a thermal signature of the plume not reported in previous studies of the Zambezi influenced waters. On the other hand, features in the satellite-based observations of salinity were found to be appropriately represented in the model-derived distribution of surface salinity. Here, it is found that in order to reproduce accurately the alongshore extension of the penetration of low-salinity waters, a correct parametriza-

tion of the buoyancy input from the other rivers in the region has to be considered. Overall, the monthly-averaged structure of the Zambezi plume in February 2007 was characterized by plume waters (i.e., low salinity and high temperature) being transported equatorward along the coast.

The analysis of sub-tidal plume features recorded during selected wind events has showed that the shape of the plume or the dispersion pattern is highly susceptible to changes in the ambient current immediately seaward from the plume's offshore bound. Under a large river discharge and a weak to moderate ambient current, the plume waters are transported equatorward regardless of the orientation of the ambient flow. When the ambient flow is stronger than the local Ekman drift, the plume is transported according to the orientation of the ambient flow, which in some cases translates to portions of the plume being carried seawards beyond the 100 m isobath. However, the example presented in Figure 6.4 shows that, even when the ambient flow is very strong and the majority of the plume waters is transported poleward, the freshwater still penetrates downstream beyond the city of Quelimane.

Nevertheless, the analysis of plumes during a particular period is only useful for the assessment of the plume's response to a specific wind or discharge event, and not the typical dispersion pattern, given that plume properties during the chosen period might not be representative of the universe of events. To that extent, SOM and PC analyses were conducted where attempts were made to extract the plume's typical patterns of dispersion, based on 1-year long model-derived time-series. The patterns retrieved by SOM indicate that the Zambezi plume typically spreads equatorward along the coast, with the length of downstream and upstream (offshore) penetration strongly determined by the intensity and orientation of the ambient flow. Here, cases of strong poleward ambient flow resulted in the plume spreading as far north as the mouth of the Licungo River, and a large and discernible protuberance occurred in the upstream direction. This structure is identical to the in situ observations made in 2004, 2005, and 2007 and presented in Chapter 2, while the observations made in 2006 are more consistent with the SOM cases of a moderate to strong equatorward motion of ambient waters immediately seawards from the plume.

In analogy to the sub-tidal plume features computed for February 2007, the patterns retrieved by SOM using 1-year long time-series showed little or no relationship with the local windstress and runoff. Similarly, no clear pattern of occurrence of a specific SOM structure throughout the year was found. It is worth noting that in order to take advantage of the SOM capabilities, the plumes were represented in terms of their salinity and velocity distributions, however similar patterns of salinity distribution were found when only salinity was employed. The nine patterns retrieved by SOM, which exhibit many similarities between them, represent the plume's general patterns. When compared with the sub-tidal features in the February plumes, one

finds a number of plume features not accurately represented in the SOM patterns. This behaviour constitutes a disadvantage of the method and arises from the need to keep the number of output patterns to as small as possible, while incorporating most of the variability of the plume. In tests using a larger number of output patterns (not shown), more features could be discerned, but they appeared at extremely low frequencies making it hard to interpret. It was also noted that more discernible patterns were retrieved when shorter records (few weeks $\sim$ months) were used, consistent with results presented by Liu et al. (2009). In that study, the plume patterns retrieved by SOM were based on a 2.5 months long data record, sampled at 4-hr interval. However, the use of shorter record contradicts the objective of the current analysis, as the patterns become representative of a particular period of time, and subject to the forcing fields occurring during that time.

The PC analysis allowed for the identification of three regions, which according to the loadings/variance of the first leading mode, can be interpreted as the plume's near-field region (at the coast where the variance is positive and loadings increase towards the mouths), the far-field region (where there is a strong horizontal gradient of the loadings/variance; *see* Figure 6.8), and ambient waters (where the variance is nearly constant in space). It turns out that the shape of the near-field region is consistent with a plume structure comprised by a wide bulge and a narrower coastal current in the downstream coast, but the shape of the far-field region is indicative of upstream (poleward) transport of freshwater beyond 20^oS, as well as a downstream current that penetrates beyond 17^oS.

Through correlation analysis it was found that each leading PC mode correlates better with a particular forcing, for example, PC-1 correlates better with river runoff, PC-2 with the zonal component of ambient flow, and PC-3 with windstress. These results suggest that correlations between salinity and both runoff and ambient current promote the damping of the plume response to windstress, hence they determine the patterns of horizontal dispersion. These patterns contradict most plumes observed worldwide, but similar results results have been reported in the literature, in which the effect of ambient current on the plume dispersion surpasses that of the local winds. For instance, the North Brazil Current forces the Amazon River plume (Brazil) to move permanently northwestward (Nikiema et al., 2007), under a negligible effect of the Coriolis deflection and a moderate effect of the local wind field.

The horizontal structure of PC-2 shows larger variability of surface salinity in the southern part of the region of interest, as well as along the downstream coast. However, similarly to PC-1, this mode has a sign change within the plume limits, which translates to a positive correlation between the mode time-series in the southern part of the region and the ambient current measured at a downstream offshore station,

and consequently a negative correlation for the northern (downstream) region along the coast. This pattern implies that increased poleward transport by the ambient current promotes not only a reduction of downstream transport of freshwater, but also an enhanced upstream transport of freshwater. The same argument applied to the PC-3 supports the concept discussed by Hetland (2005) of larger wind-induced mixing effects in the far-field region, compared to the near-field region, where the third PC mode is either small or statistically insignificant at the 95% confidence level.

It was shown through point correlation maps, that salinity variability in the near-field plume is not correlated with the far-field zone, despite the fact that both the unrotated and the rotated PC analyses indicate the existence of a seesaw-like structure. Based on the combination of the correlation results and the sub-tidal plume patterns, it is suggested that the seesaw-like structure of the dominant mode indicates the occurrence of a strong buoyancy-driven flow oriented downstream during the rise period of river discharge (and hence decreased salinity in the near-field), that also induces the equatorward transport and removal of plume waters in the far-field. This behaviour would ultimately trigger the increase of surface salinity in the far-field at the exact same low-frequency, at which high discharges are observed. In addition, the seesaw-like structure implies that during the fall period of river discharge, salinity increases (decreases) in the near-field (far-field), which is only possible if ambient water is allowed to penetrate the near-field region through lateral mixing processes.

Generally speaking, the sub-tidal plume patterns computed for February 2007 (Section 6.2.2) are satisfactorily well-represented in the salinity variability patterns identified with the aid of PC analysis, in spite of the difference in the record length used in each analysis (1 month, and 1 year time-series, respectively).

Chapter 7

Synthesis

The results of the modeling exercises described in this thesis will be discussed with reference to the objectives that were set out in the opening chapter. The research was aimed at examining the dispersion patterns of the Zambezi River under a number of idealized and realistic scenarios, and to investigate relevant processes that influence:

- the typical cross-shore and alongshore penetration lengths of the freshwater plume,
- the typical depth of the plume,
- the distribution of water properties within the plume zone,
- and ultimately, the changes to these distributions driven by winds, tides, and ambient current.

In an effort to attain these objectives, two different approaches were used that comprise the collation and analysis of *in situ* hydrographic data (Chapter 2), and numerical simulation of the plume development and evolution (Chapters 4, 5, and 6). The hydrographic data consisted of single-cruise shipboard measurements of salinity, temperature and turbidity collected by the Mozambican National Institute of Fisheries Research, around periods of maximum discharge between 2004 and 2007. The water properties assessed by these means were combined with discharge data from an inland gauge station and QuikSCAT wind data to identify patterns of dispersion of freshwater over the shelf.

The numerical experiments were conducted through the Regional Ocean Modeling System (ROMS), which was run in a number of different configurations that employ either an idealized geometry, a realistic geometry and bathymetry, or a realistic forcing (i.e., hindcast configuration). The overall simulation strategy was to first analyze the physical mechanisms that control the development and evolution

of the plume in a simplified model setting, and then represent them realistically obeying the numerical limitations of the model.

A number of methodological constraints have contributed negatively for the achievement of the goals of this study, and the first constraint is related with the cruise data. The sampling effort varied from year-to-year due to weather conditions and external factors. Given that the primary purpose of the cruises was to evaluate the shrimp recruitment prior to the onset of the fishing season, it is found that the sampling approach is not well suited for tracking the freshwater plumes. The sampling plan called for sampling 73 CTD stations each year, as often as possible, but since these stations were interspersed with sampling of shrimp recruitment, it took 15 days on average to sample all CTD stations. During the 15-day period, the wind and runoff conditions varied substantially, along with unmeasured variations in the ambient current, which when combined altogether, might introduce large inaccuracies to the patterns of horizontal plume dispersion. Conversely, an effort was made to sample every transect on the same day, which indicates that the vertical profiles presented here are more consistent than the horizontal ones. In addition, the forcing fields also varied considerably across plume observations (in different years), so that, a rough analysis of the forcing suggests that there exists a large inter-annual variability of the forcing. This variability has made it impossible to link coherently the plume features generalized across the observations, to the forcing fields.

The complexity and nonlinearity of the phenomena being investigated required a numerical model capable of accommodating the different forcings, which cover a wide range of length and time scales. For this reason, the ROMS model was adopted in this study, and despite all the effort put in place in recent years to make it suitable for coastal oceans (i.e., inclusion of improved schemes of vertical mixing), the parametrization of rivers is still inadequate to accurately resolve the transformation of river water into oceanic water. This constraint affected the whole range of simulations conducted and presented throughout the report, either when a boundary condition parametrization was used (Chapter 4) or when a point source scheme was used (Chapters 5 and 6). To this extent, the results presented so far are related to the values set for the density and momentum of the river at the mouth or at the riverhead.

The summary of findings and conclusions about the structure of the Zambezi River plume (ZRP) is presented next. These include the majority of findings from Chapters 2 and 6.

The plume is in general distributed along both the downstream and the upstream coasts (Figure 2.6 and similars, as well as Figure 6.4). The downstream portion of

the plume is attached to the shoreline and confined to a distance from the coast equivalent to approximately the location of the 50 m isobath. The plume naturally penetrates downstream beyond the City of Quelimane, but only under a strong buoyancy input or an ambient current oriented equatorwards do the plume waters spread northward beyond the mouth of the Licungo River. The upstream portion of the plume is not exactly detached from coast, but it consists of a tongue of brackish water leaving the mouth and spreading poleward in offshore, beyond the 50 m isobath, which is located further apart from the shoreline in this region.

Plume waters occupy the entire water column in the region immediately seaward from the delta, to a distance that varies between 15 to 30 km. North of this region, the plume loses contact with the bottom in everywhere, while the contact with the bottom is maintained in the region to the south of the delta, where the shallow continental shelf is wider. Away from the coast, where the brackish plume waters move atop dense ambient waters, the plume thickness is about 10 to 20 m, except under considerably large discharges that result in the projection of the plume base all the way to the shelf edge, and the plume waters occupy the entire water column.

Near-surface temperature decreases gradually seaward from the maximum value occurring at the coast (Figure 6.1). Warmer temperatures along the shoreline occur near the City of Beira, where the shallows of the Sofala Bank are the widest. While the horizontal distribution of temperature from *in situ* measurement offers no clear basis for the inference of plume limits, the vertical distribution gives an indication of the length scales associated with vertical motion of dense ambient waters induced by topographical effects as the return flow runs up-shelf underneath the plume. Near-surface turbidity is in general higher at the coast, particularly in the region nearer the Zambezi River delta (Figure 2.6 and similars). Strong gradients of turbidity are found seaward from this region, with directionality of contours indicating a spreading of river-borne suspended materials in the same fashion as the freshwater, although with shorter offshore penetration length.

As the plume waters are transported equatorward along the coast, the spreading of the plume becomes obstructed by low salinity waters discharged by the Licungo River, which might limit the equatorward movement when the Zambezi discharge are lower than the annual mean, or simply change the plume shape by inducing a seaward bending of the isohalines.

Regarding the effects of ambient factors on the plume structure, the summary of findings and conclusion are taken from Chapters 4-6, and it reads as follows. The simplest of scenarios for the ZRP system was represented by a river of constant and moderate discharge emptying into a constant-slope ocean separated from the land by a 10 m deep straight coastal wall. Under these conditions and assuming that

winds, tides and ambient flow are absent, a sizable unsteady plume is formed, consisting of a bulge that grows continually as it re-circulates anti-cyclonically (counter-clockwise) in front of the river mouth, connected to a density-driven coastal current that flows equatorward along the coast. It was noted that from the 100% of freshwater discharge that generates this simplified plume, half contributes to the continuous growth of the bulge, while the remaining 20% goes to the coastal current and 30 % is mixed with the ambient water and eventually becomes oceanic water (Section 4.3).

In the real system, the outflow from each of the various mouths of the Zambezi River produces a corresponding number of plumes with small proportions, in which, the proximity between mouths leads to loss of individual plume identity, and a merging together to form the ZRP, shortly after the freshwater enters the coastal ocean (Figure 5.21). The dynamical mechanisms that determine the spreading of plumes generated in the northern part of the delta differs considerably from those in southern part of the delta, but it is the central plume that dictates the spreading and structure of the combined ZRP.

Even when no external forcing is applied to the plume, freshwater from the combined-source ZRP (i.e., plume from multiple mouths) penetrates upstream by virtue of lateral pressure gradient (Figures 4.8 and 5.21), and the band of low-salinity waters extends poleward along the coast up to $19^o10'S$. Re-circulation in front of the bulge as well as the continuous growth of the bulge is totally absent in the plumes formed under realistic geometry and bathymetry.

The spreading of an unforced plume was found to be driven by the pressure-gradient term, which is primarily balanced by the Coriolis acceleration when realistic bathymetry is employed (and hence re-circulation is absent). For these plumes, the geostrophic balance does not hold true in a few specific locations, as follows (Figures 5.5 and 5.6). Firstly, wherever the plume waters are transported upstream (opposing the sense of a Kelvin wave) by virtue of advective processes. Secondly, near the seabed wherever the bottom friction is strong enough to slow down the buoyancy-driven flow. Thirdly, geostrophy also breaks down in the surface layers in spots where the viscous terms dominate through the shear velocity. Lastly, in locations with irregular topography, where the combination of advection and mixing accounts for the imbalance.

In response to impulsive and constant wind forcing, the shape of the plumes changed into either a "*coastal current*" or a *"large bulge*", depending on whether the alongshore projection of the wind field is oriented equatorward or poleward, respectively (see Figure 5.9). Plumes having the shape reduced to a coastal current were found to spread downstream and the bulge (i.e., protuberance in front of the mouths) was either strongly reduced in size or not present at all. On the other hand,

plumes having their shape reduced to large bulges spread essentially seaward to the location of the 100 m isobath and poleward beyond $19^o30'S$.

Asymmetric breezes consisting of a synoptic and a diurnal component induce motions of plume waters in a similar fashion as the constant winds do (Section 5.2.2), except that the breezes induce an enhanced mixing that results from the shear instability between the plume and the underlying ambient waters. In connection with the enhanced mixing, the downward penetration of brackish water increases considerably, and in some cases, the plume water reaches and remains connected to the seabed. For instance, plumes forced by landward and northeastward breezes were found to spread in contact with the bottom well offshore while westward breezes produced plumes with relatively larger thickness than those produced under constant westward winds.

When river plumes were forced by tides in the simulations employing realistic geometry and bathymetry (Section 5.2.3), the plume's alongshore and across-shore extents became slightly smaller, with the horizontal plume shape nearly unaltered (when compared to the unforced plume). In contrast, the vertical entrainment of brackish water increased considerably, given that large extensions of the plume, if not the whole plume, were found to be in contact with the seabed. Also, the vertical structure was found to be governed by the relative magnitude of the buoyancy (or freshwater discharge) and tidal forcings. Winds forcing tended to support this behaviour, producing deeper plumes transported either downstream or seaward, depending on the orientation of the wind field and the resulting Ekman drift, with the lateral penetration length scale strongly determined by the relative magnitude of the forcings.

Strong poleward ambient currents advect high-salinity regions of the plume (far-field) downstream of the current resulting in a plume shape that features the upstream penetration of plume waters, which reaches as far south as 20^oS (Figure 6.4), while an equatorward ambient current forces the downstream transport of freshwater to far beyond the mouth of the Licungo River ($\sim 17^o30'S$). Simulations considering the transport of ambient waters driven not only by local factors revealed little influence of the local winds on the plume's averaged (typical) structure. In fact, the river discharge integrated through the delta and ambient currents simulated for the region around 18^oS were found to explain the horizontal plume structure relatively better than the windstress (Table 6.1). Also, the upstream transport of plume waters away from the coast was found to be highly correlated with the poleward transport of dense ambient waters.

The analysis of low-frequency variability of surface salinity revealed the existence of two plume regions, characterizing the near- and far-field regions of the plume (Figure 6.8). Salinity in the near-field region is negatively correlated with runoff,

while the correlation is positive in the far-field region. This pattern of variability in the far-field implies an increased downstream removal of brackish water from the plume during the runoff rise period, as well as a seaward transport of freshwater or enhanced mixing between plume and ambient waters during the runoff fall period.

References

Antonov, J. I., Seidov, D., Boyer, T. P., Locarnini, R. A., Mishonov, A. V., Garcia, H. E., Baranova, O. K., Zweng, M. M., and Johnson, D. R., 2010: World Ocean Atlas 2009, Volume 2: Salinity. Tech. rep., NOAA Atlas NESDIS 69, U.S. Government Printing Office, Washington, D.C.

Asplin, L., Skogen, M. D., Budgell, W. P., Gammelsrød, T., Dove, V., Andre, E., and Hoguane, A. M., 2006: Numerical modelling of currents and hydrography in Mozambique Channel. *Rev. Inv. Pesq.*, **25**.

Avicola, G., and Huq, P., 2003: The characteristics of the recirculating bulge region in coastal buoyant outflows. *Journal of Marine Research*, **61**, 435–463.

Backeberg, B., and Reason, C. J. C., 2010: A connection between the South Equatorial Current north of Madagascar and Mozambique Channel eddies. *Geophysical Research Letters*, **37**, L04604.

Beardsley, R. C., Limeburner, R., Yu, H., and Cannon, G. A., 1985: Discharge of the Changjiang (Yangtze) River into the East China Sea. *Continental Shelf Research*, **4(1-2)**, 57–76, get paper from UCT lib.

Beilfuss, R., and dos Santos, D., 2001: Patterns of hydrological change in the Zambezi Delta, Mozambique. Tech. rep., Program for the Sustainable management of Cahora Bassa dam and the lower Zambezi valley, Working Paper #2.

Blumberg, A. F., and Mellor, G. L., 1987: A description of a three-dimensional coastal ocean circulation model. N. S. Heaps, Ed., *Three Dimensional Coastal Ocean Models*, Amer. Geophys. Union, 1–16.

Bourgeois, S., Kocher, T., and Schelander, P., 2003: ETH Seminar: Science and politcs of international freshwater management 2003/04. Case study: Zambezi River basin. Tech. rep., ETH and EAWAG.

Brakel, W. H., 1984: Seasonal dynamics of suspended-sediment plumes from the Tana and Sabaki Rivers, Kenya: Analysis of Landsat Imagery. *Remote sensing of environment*, **16**, 165–173.

Carter, G. S., and Merrifield, M. A., 2007: Open boundary conditions for regional tidal simulations. *Ocean Modeling*, **18**, 194–209.

Carton, J. A., and Giese, B. S., 2008: A reanalysis of ocean climate using simple ocean data assimilation (soda). *Mon. Wea. Rev.*, **136**, 2999–3017.

Cattell, R. B., 1966: The scree test for the number of factors. *Multivariate Behav. Research*, **1**, 245–276.

Chant, R. J., Wilkin, J. L., Zhang, W., Choi, B.-J., Hunter, E., Castelao, R., Glenn, S. M., Jurisa, J., Schofield, O., Houghton, R., Kohut, J., Frazer, T. K., and Moline, M. A., 2008: Dispersal of the Hudson River Plume in the New York Bight: Synthesis of Observational and Numerical Studies During LaTTE. *Oceanography*, **21(4)**, 148–161.

Chao, S.-Y., 1988a: River-forced estuarine plume. *Journal of Physical Oceanography*, **18**, 72–88.

Chao, S.-Y., 1988b: Wind-driven motion of estuarine plumes. *Journal of Physical Oceanography*, **18(8)**, 1144–1166.

Chao, S.-Y., 1990: Tidal modulation of estuarine plumes. *Journal of Physical Oceanography*, **20(7)**, 1115–1123.

Chapman, D. C., and Lentz, S. J., 1994: Trapping of a coastal density front by the bottom boundary layer. *Journal of Physical Oceanography*, **24**, 1464–1479.

Chelton, D. B., deSzoeke, R. A., Schlax, M. G., el Naggar, K., and Siwertz, N., 1998: Geographical variability of the first baroclinic rossby radius of deformation. *Journal of Physical Oceanography*, **28**, 433–460.

Cheng, R. T., and Casulli, V., 2004: Modeling a three-dimensional river plume over continental shelf using a 3D unstructured grid model. L. Spaulding M., Ed., *Eighth International Conference on Estuarine and Costal Modeling*, 1027–1043.

Cushman-Roisin, B., and Beckers, J.-M., 2009: *Introduction to Geophysical Fluid dynamics*. Academic Press.

da Silva, A. M., Young, C. C., and Levitus, S., 1994: Atlas of surface marine data 1994, vol. 1, algorithms and procedures. technical report. Tech. rep., U.S. Department of Commerce, NOAA.

da Silva, J., New, A., and Magalhaes, J., 2009: Internal solitary waves in the Mozambique Channel: Observations and interpretation. *Journal of Geophysical Research*, **114**, C05001.

de Ruijter, W. P., Ridderinkhof, H., Lutjeharms, J., Schouten, M. W., and Veth, C., 2002: Observations of the flow in the Mozambique Channel. *Geophysical Research Letters*, **29(10)**, 1502.

Durski, S. M., Glenn, S. M., and Haidvogel, D. B., 2004: Vertical mixing schemes in the coastal ocean: Comparison of the level 2.5 Mellor-Yamada scheme with an enhanced version of the K profile parameterization . *Journal Geophysical Research*, **109**, C01015.

Egbert, G. D., and Erofeeva, S., 2002: Efficient inverse modeling of barotropic ocean tides. *Journal of Atmospheric and Oceanic Technology*, **19**, 183–204.

Eom, K. B., 1999: Fuzzy clustering approach in unsupervised sea-ice classification. *Neurocomputing*, **25(1-3)**, 149–166.

Fong, D. A., and Geyer, W. R., 2002: The alongshore transport of freshwater in a surface-trapped river plume. *Journal of Physical Oceanography*, **32**, 957–972.

Fong, D. A., Geyer, W. R., and Signell, R. P., 1997: The wind-forced response on a buoyant coastal current: Observations of the western Gulf of Maine plume. *Journal of Marine Systems*, **12(1-4)**, 69–81.

Gammelsrød, T., 1992: Variation in shrimp abundance on the Sofala Bank, Mozambique, and its relation to the Zambezi River runoff. *Estuarine, Coastal and Shelf Science*, **35**, 91–103.

Garvine, R. W., 1995: A dynamical system for classifying buoyant coastal discharge. *Continental Shelf Research*, **15**, 1585–1596.

Garvine, R. W., 1999: Penetration of buoyant coastal discharge onto the continental shelf: A numerical model experiment. *Journal of Physical Oceanography*, **29**, 1892–1909.

Garvine, R. W., 2001: The impact of model configuration in studies of buoyant coastal discharge. *Journal of Marine Research*, **59**, 193–225, Artifacts in buoyant coastal discharge models: An observational and model study.

Gelfenbaum, G., and Stumpf, R. P., 1993: Observations of currents and density structure across a buoyant plume front. *Estuaries*, **16(1)**, 40–52.

Geyer, W. R., Hill, P., Milligan, T., and Traykovski, P., 2000: The structure of the Eel River plume during floods. *Continental Shelf Research*, **20**, 2067–2093.

Geyer, W. R., Signell, R. P., Fong, D. A., Wang, J., Anderson, D. M., and Keafer, B. A., 2004: The freshwater transport and dynamics of the western Maine coastal current. *Continental Shelf Research*, **24(12)**, 1339–1357.

Hedström, K., 1997: *Draft - Users manual for an SCRUM model v3.0*.

Hetland, R. D., 2005: Relating river plume structure to vertical mixing. . *Journal of Physical Oceanography*, **35**, 1667–1688.

Hetland, R. D., and Signell, R. P., 2005: Modeling coastal current transport in the Gulf of Maine. *Deep Sea Research Part II: Topical Studies in Oceanography*, **52(19-21)**, 2430–2449.

Hickey, B. M., Kudela, R. M., Nash, J., Bruland, K. W., Peterson, W. T., MacCready, P., Lessard, E. J., Jay, D. A., Banas, N. S., Baptista, A. M., Dever, E. P., Kosro, P. M., Kilcher, L. K., Horner-Devine, A. R., Zaron, E. D., McCabe, R., Peterson, J. O., Orton, P. M., Pan, J., and Lohan, M. C., 2010: River influences on shelf ecosystems: Introduction and synthesis . *Journal of Geophysical Research*, **115**, C00B17.

Hoguane, A. M., 1997: Shrimp abundance and river runoff in Sofala Bank - The role of Zambezi. .

Hoguane, A. M., 2007: Perfil diagnóstico da zona costeira de Moçambique. *Revista de Gestao Costeira Integrada*, **7(1)**, 69–82.

Horner-Devine, A. R., 2009: The bulge circulation in the Columbia River plume. *Continental Shelf Research*, **29(1)**, 234–251.

Horner-Devine, A. R., Fong, D. A., Monismith, S. G., and Maxworthy, T., 2006: Laboratory experiments simulating a coastal river inflow. *Journal of Fluid Mechanics*, **555**, 203–232.

Huisman, S., 2006: *Kelvin and Rossby wave interactions at Midlatitudes: The cause for decreasing dominant mesoscale frequency in the Mozambique Channel*. Master's thesis, Institute for Marine and Atmospheric Research, Utrecht.

Hyder, P., Simpson, J., and Christopoulos, S., 2002: Sea-breeze forced diurnal surface currents in the Thermaikos Gulf, North-west Aegean. *Continental Shelf Research*, **22(4)**, 585–601.

IMR, 1977: Cruise report No. 1 of R/V DR. FRIDTJOF NANSEN. Joint NORAD/ Moçambique/FAO project to investigate the fish resources off the coast of Moçambique. Tech. rep., Institute of Marine Research.

IMR, 1978a: Cruise report No. 3 of R/V DR. FRIDTJOF NANSEN, January-March 1978. Joint NORAD/Moçambique/FAO project to investigate the fish resources off the coast of Moçambique. Tech. rep., Institute of Marine Research.

IMR, 1978b: Cruise report No. 4 of R/V DR. FRIDTJOF NANSEN, April-June 1978. Joint NORAD/Moçambique/FAO project to investigate the fish resources off the coast of Moçambique. Tech. rep., Institute of Marine Research.

Isobe, A., 2005: The ballooning of river-plume bulge and its stabilization by tidal currents. *Journal of Physical Oceanography*, **35**, 2337–2351.

Kampf, J., 2008: *Ocean modelling for beginners*. Online Publication.

Kourafalou, V. H., Lee, T. N., Oey, L.-Y., and Wang, J. D., 1996a: The fate of river discharge on the continental shelf. 2: Transport of coastal low-salinity waters under realistic wind and tidal forcing. *Journal of Geophysical Research*, **101(C2)**, 3435–3455.

Kourafalou, V. H., Oey, L.-Y., Wang, J. D., and Lee, T. N., 1996b: The fate of river discharge on the continental shelf. 1: Modelling the river plume and the inner shelf coastal current. *Geophysical Research*, **101(C2)**, 3415–3434.

Kundu, P. K., 1990: *Fluid mechanics*. Academic Press. London.

Langa, J. V., 2002: Gestão integrada dos recursos hídricos em Moçambique: Caso da bacia hidrográfica do Rio Licungo. Tese de Licenciatura em Geografia. Univesidade Eduardo Monglane. Maputo.

Large, W. G., McWilliams, J. C., and Doney, S. C., 1994: Oceanic vertical mixing: A review and a model with a nonlocal boundary layer parameterization. *Reviews of Geophysics*, **32(4)**, 363–403.

Leal, M. C., Sa, C., Nordez, S., Brotas, V., and Paula, J., 2009: Distribution and vertical dynamics of planktonic communities at Sofala Bank, Mozambique. *Estuarine, Coastal and Shelf Science*, 1–12, in press.

Lentz, S. J., Elgar, S., and Guza, R. T., 2003: Observations of the flow field near the nose of a buoyant coastal current. *Journal of Physical Oceanography*, **33(4)**, 933–943.

Li, M., Zhong, L., and Boicourt, W. C., 2005: Simulations of Chesapeake Bay estuary: sensitivity to turbulence mixing parameterization and comparison with observations. *Journal Geophysical Research*, **110**, C12004.

Li, X., Chao, Y., McWilliams, J. C., and Fu, L.-L., 2001: A comparison of two vertical-mixing schemes in a Pacific Ocean General Circulation Model. *Journal of Climate*, **14**, 1377–1398.

Lill, C. C., 1979: Upwelling over the shelf break. *Journal of Physical Oceanography*, **(9)**, 1044–1047.

Liu, Y., MacCready, P., and Hickey, B. M., 2009: Columbia River plume patterns in summer 2004 as revealed by a hindcast coastal ocean circulation model . *Geophysical Research Letters*, **36(L02601)**, 1–6.

Liu, Y., Weisberg, R. H., and Mooers, C. N. K., 2006: Performance evaluation of the self-organizing map for feature extraction. *Journal of Geophysical Research*, **111(c05018)**, c05018:1–14.

Locarnini, R. A., Mishonov, A. V., Antonov, J. I., Boyer, T. P., Garcia, H. E., Baranova, O. K., Zweng, M. M., and Johnson, D. R., 2010: World Ocean Atlas 2009, Volume 1: Temperature. Tech. rep., NOAA Atlas NESDIS 68, U.S. Government Printing Office, Washington, D.C.

Lu, X., Qiao, F., Xia, C., Zhu, J., and Yuan, Y., 2006: Upwelling off Yangtze River estuary in summer. *Journal of Geophysical Research*, **111**, C11S08.

Luo, J.-J., and Yamagata, T., 2002: Four decadal ocean-atmosphere modes in the North Pacific revealed by various analysis methods. *Journal of Oceanography*, **58**, 861–876.

Lutjeharms, J., 2006: *The coastal oceans of south-eastern Africa*, vol. 14B, 783–834. Harvard University Press, Cambridge, MA.

Magome, S., and Isobe, A., 2003: Current structure and behavior of the river plume in Suo-Nada. *Journal of Oceanography*, **59**, 833–843.

Manikiam, B., Gowda, H. H., Manavalan, P., Jayaraman, V., and Chandrasekhar, M. G., 1993: Study of sediment dynamics using satellite remote sensing. *Adv. Space Research*, **13(5)**, (5)75–(5)78.

Mann, K. H., and Lazier, J. R. N., 1996: *Dynamics of marine ecosystems - Biological-physical interactions in the oceans*. Oxford: Blackwell Science Limited, Boston.

Marchesiello, P., McWilliams, J. C., and Shchepetkin, A. F., 2001: Open boundary conditions for long-term integration of regional oceanic models. *Ocean Modelling*, **3(1-2)**, 1–20.

Marsaleix, P., Estournel, C., Kondrachoff, V., and Vehil, R., 1998: A numerical study of the formation of the Rhone River plume. *Jounal of Marine Systems*, **14**, 99–115.

Mavume, A. F., Rydberg, L., Rouault, M., and Lutjeharms, J., 2009: Climatology and landfall of tropical cyclones in the south-west indian ocean. *Western Indian Ocean Journal of Marine Science*, **8(1)**, 15–36.

McCreary, J. P., Zhang, S., and Shetye, S. R., 1997: Coastal circulations driven by river outflow in a variable-density 1Âœ-layer model. *Journal of Geophysical Research*, **102(C7)**, 15535–15554.

Mestres, M., Sierra, J. P., and Sánchez-Arcilla, A., 2007: Factors influencing the spreading of a low-discharge river plume. *Continental Shelf Research*, **27**, 2116–2134.

Münchow, A., and Garvine, R. W., 1993: Buoyancy and wind forcing of a coastal current. *Journal of Marine Research*, **51**, 293–322.

Nehama, F. P., 2008: *Dynamics of the Zambezi River plume*. Master's thesis, University of Wales Bangor, School of Ocean Sciences, U.K.

Nezlin, N. P., and DiGiacomo, P. M., 2005: Satellite ocean color observations of stormwater runoff plumes along the San Pedro Shelf (Southern California) during 1997–2003. *Continental Shelf Research*, **25**, 1692–1711.

Nezlin, N. P., DiGiacomo, P. M., Stein, E. D., and Ackerman, D., 2005: Stormwater runoff plumes observed by SeaWiFS radiometer in the Southern California Bight. *Remote Sensing of Environment*, **98**, 494–510.

Nikiema, O., Devenon, J.-L., and Baklouti, M., 2007: Numerical modeling of the Amazon River plume. *Continental Shelf Research*, **27**, 873–899.

Nof, D., 2005: The momentum imbalance paradox revisited. *Journal of Physical Oceanography*, **35**, 1928–1939.

Nof, D., and Pichevin, T., 2001: The ballooning of outflows. *Journal of Physical Oceanography*, **31**, 3045–3058.

Penven, P., Marchesiello, P., Debreu, L., and Lefèvre, J., 2008: Software tools for pre- and post-processing of oceanic regional simulations. *Environmental Modelling & Software*, **23(5)**, 660–662.

Pichevin, T., and Nof, D., 1997: The momentum paradox. *Tellus*, **49(A)**, 298–319.

Pimenta, F. M., Campos, E. J. D., Miller, J. L., and Piola, A. R., 2005: A numerical study of the plata river plume along the southeastern south american continental shelf. *Brazilian Journal of Oceanography*, **53(3/4)**, 129–146.

Piñones, A., Valle-Levinson, A., Narvaez, D. A., Vargas, C. A., Navarrete, S. A., Yuras, G., and Castilla, J., 2005: Wind-induced diurnal variability in river plume motion. *Estuarine, Coastal and Shelf Science*, **65**, 513–525.

Pugh, D. T., 2004: *Changing sea levels. Effects of tides, weather and climate*. Cambridge University Press, 280pp.

Ramos, A., Lorenzo, M., and Gimeno, L., 2010: Compatibility between modes of low-frequency variability and circulation types: A case study of the northwest Iberian Peninsula. *Journal of Geophysical Research*, **115(D02113)**, D02113.

Richardson, A. J., Risien, C., and Shillington, F. A., 2003: Using self-organizing maps to identify patterns in satellite imagery. *Progress in Oceanography*, **59**, 223–239.

Sætre, R., and da Silva, A. J., 1984: The circulation of the Mozambique Channel. *Deep-Sea Research*, **31(5)**, 485–508.

Schouten, M. W., de Ruijter, W. P., van Leeuwen, P. J., and Ridderinkhof, H., 2003: Eddies and variability in the Mozambique Channel. *Deep-Sea Research II*, **50**, 1987–2003.

Schumann, E. H., 1998: *The coastal ocean off southeast Africa, including Madagascar*, vol. 11, chap. 19, 557–581. John Wiley & Sons.

Shchepetkin, A. F., and McWilliams, J. C., 2005: The regional oceanic modeling system (ROMS): a split-explicit, free-surface, topography-following-coordinate oceanic model. *Ocean Modeling*, **9(4)**, 347–407.

Siddorn, J. R., Bowers, D. G., and Hoguane, A. M., 2001: Detecting the Zambezi River plume using observed optical properties. *Marine Pollution Bulletin*, **42(10)**, 942–950.

Simpson, J., 1997: Physical processes in the ROFI regime. *Journal of Marine Systems*, **12(1-4)**, 3–15.

Stumpf, R. P., Gelfenbaum, G., and Pennock, J. R., 1993: Wind and tidal forcing of a buoyant plume, Mobile Bay, Alabama. *Continental Shelf Research*, **13(11)**, 1281–1301.

Vesanto, J., Himberg, J., Alhoniemi, E., and Parhankangas, J., 2000: Som toolbox for matlab 5. Tech. rep., Helsinki Universit of Technology.

Walford, H., White, N., and Sydow, J., 2005: Solid sediment load history of the Zambezi Delta. *Earth and Planetary Science Letters*, **238**, 49–63.

Walker, N. D., Fargion, G. S., Rouse, L. J., and Biggs, D. C., 1994: The great flood of summer 1993: Mississipi river studied. *EOS Trans AGU*, **75**, 409.

Warrick, J. A., DiGiacomo, P. M., Weisberg, S. B., Nezlin, N. P., Mengel, M., Jones, B. H., Ohlmann, J. C., Washburn, L., Terrill, E. J., and Farnsworth, K. L., 2007: River plume patterns and dynamics within the Southern California Bight. *Continental Shelf Research*, **27**, 2427–2448.

Warrick, J. A., Mertes, L. A. K., Washburn, L., and Siegel, D., 2004a: A conceptual model for river water and sediment dispersal in the Santa Barbara Channel, California. *Continental Shelf Research*, **24**, 2029–2043.

Warrick, J. A., Mertes, L. A. K., Washburn, L., and Siegel, D., 2004b: Dispersal forcing of southern California river plumes, based on field and remote sensing observations. *Geo-Marine Letters*, **24**, 46–52.

Warrick, J. A., and Stevens, A. W., 2011: A buoyant plume adjacent to a headland - observations of the Elwha River plume. *Continental Shelf Research*, **31**, 85–97.

Weingartner, T. J., Danielson, S., Sasaki, Y., Pavlov, V., and Kulakov, M., 1999: The siberian coastal current: A wind- and buoyancy-forced artic coastal current. *Journal of Geophysical Research*, **104(C12)**, 29,697–29,713.

Yankovsky, A. E., and Chapman, D. C., 1997: A simple theory for the fate of buoyant coastal discharges. *Journal of Physical Oceanography*, **27**, 1386–1401.